Design of Selective *Plasmodium falciparum* Kinase Inhibitors using Computer-Aided Drug Discovery

Stephanie Gathoni Kamunya

Supervisor: Professor Kelly Chibale
Co-Supervisor: Dr. Lauren Arendse

Thesis presented for the degree of

DOCTOR OF PHILOSOPHY

In the Department of Chemistry
University of Cape Town

August 2022

Table of Contents

Table of Contents i

Dedication vii

Declaration viii

Acknowledgements ix

List of Abbreviations xi

Abstract xvii

List of Figures xix

List of Tables xxvii

CHAPTER ONE: Introduction 1

1.1. Background 1

1.2. The life cycle of the malaria parasite 1

1.3. Current antimalarials 3

1.3.1. Quinine 4

1.3.2. Chloroquine 4

1.3.3. Proguanil and pyrimethamine 5

1.3.4. Mefloquine 6

1.3.5. Artemisinin 6

1.4. Next generation antimalarials 7

1.5. Kinases 8

1.5.1. cGMP-dependent protein kinase (PKG) 11

1.5.2. Phosphatidylinositol-4-kinase (PI4K) 17

1.6. Application of polypharmacology 20

1.7. Computer-aided drug design (CADD) 21

1.8. Role of CADD in AIDS Drug Discovery 26

1.8.1. Saquinavir 27

1.8.2. Nelfinavir 29

1.8.3. Kaletra 32

1.9. Libraries available for Kinase Drug Discovery 34

1.10. Research question, aims, and objectives 35

1.10.1. Research question 35

1.10.2. Objective 35

1.10.3. Specific aims 35

1.11 References 36

CHAPTER TWO: Pyrazolo[3,4-d]pyrimidines (MLN0128 Series) 58

2.1. Introduction 58

2.2. Aims and specific objectives 60

2.2.1. Aims 60

2.2.2. Specific objectives 61

2.3. *Pf*PI4K homology modeling 62

2.3.1. Introduction 62

2.3.2. Identification and selection of templates 63

2.3.3. Sequence alignment 65

2.3.4. Model building and loop modelling 68

2.3.5. Model optimization and validation 68

2.4 Design of MLN0128 analogues 73

2.4.1. Molecular docking of MLN0128 74

2.4.2. Design of MLN0128 analogues 77

2.5. Synthesis of MLN0128 analogues 88

2.6. Characterization of key intermediates and target compounds 92

2.7. Biological evaluation of MLN0128 analogues 96

2.7.1. Introduction 96

2.7.2. Rationalization of *Pv*PI4K inhibition 96

2.7.3. Rationalization of *Pf*PKG inhibition 101

2.7.4. *In vitro* asexual blood-stage antiplasmodium activity and solubility profiling 110

2.7.5. Target selectivity with regards to mTOR and HuPI4KIIIβ 113

2.8. Conclusion and Future Work 120

2.9. References 123

CHAPTER THREE: Imidazopyridazines 132

3.1. Introduction 132

3.1.1 Imidazopyridazines as *Pf*CDPK1 and *Pf*PKG inhibitors 133

3.1.2. Imidazopyridazines as *Pf*PI4K inhibitors 135

3.1.3. Imidazopyridazines as dual inhibitors of *Pv*PI4K and *Pf*PKG 136

3.2. Aims and specific objectives 137

3.2.1. Aims 137

3.2.2. Specific Objectives 137

3.3. Compound prioritization using chemoinformatics 137

3.4. Rationalization of *Pf*PKG inhibition using molecular docking 144

3.5. *In silico* binding predictions and *Pf*PKG inhibition data 146

3.6. Molecular dynamics 159

3.7. Chemical Space Analysis 162

3.8. Conclusion and future work 164

3.9. References 165

CHAPTER FOUR: Pandemic response box (PRB) screening for hit identification of *Plasmodium* PI4K and PKG inhibitors 170

4.1. Introduction 170

4.2. Aim and specific objectives 171

4.2.1 Aim 171

4.2.2. Specific Objectives 171

4.3. Compound prioritization 172

4.3.1 Introduction 172

4.3.1. Target criteria 173

4.3.2. Compound prioritization via molecular docking 173

4.4. *Pf*PKG inhibition 180

4.4.1. Introduction 180

4.4.2. *In vitro Pf*PKG assay 180

4.4.3. Rationalization of *Pf*PKG inhibition 184

4.5. *Pv*PI4K inhibition..192

4.5.1. Introduction 192

4.5.2. *In vitro Pv*PI4K assay 192

4.5.3. Rationalization of *Pf*PI4K inhibition..196

4.6. Literature review of hit compounds 198

4.6.1. MMV00043 (tafenoquine)...198

4.6.2. MMV1580844 199

4.6.3. MMV1580482 (URMC-099-C) 200

4.6.4. MMV009948 (imatinib) 201

4.7. Conclusion..203

4.8. References 205

CHAPTER FIVE: Summary, conclusions, and recommendations for future work...209

5.1. Summary and conclusion 209

5.2. Recommendations for future work...212

CHAPTER SIX: Materials and methods...215

6.1. *In silico* methods 215

6.1.1. Homology modeling...215

6.1.2. Molecular docking 215

6.1.3. Molecular dynamics (MD) 216

6.2. Biological methods 217

6.2.1. *In vitro* antiplasmodium assays 217

6.2.2. Turbidimetric-based kinetic solubility 217

6.2.3. Kinetic Solubility using the HPLC-based DMSO “dry-down” method 218

6.2.4. Kinase inhibition assays 219

6.2.5. RBC HotSpot kinase assay protocol 225

6.3. Chemistry 226

6.3.1. Reagents, solvents, and equipment 226

6.3.2. Synthesis and Characterization 227

6.4. References 252

Dedication

This work is dedicated to my remarkable Mother, Father, and brothers for their unwavering support throughout this journey. To my mother, Elizabeth Ouma, for always believing in me; my father, John Kamunya, for always lending a helping hand and my brothers, Carlos and Thamo, for their unceasing sense of humor.

Declaration

I, **Stephanie Gathoni Kamunya**, hereby:

a) grant the University of Cape Town free licence to reproduce this thesis, in whole or in part, for the purpose of research;

b) declare that:

    i. this thesis is my own unaided work, both in concept and execution, and that apart from the normal guidance from my supervisor, I have received no assistance except that which has been acknowledged;

    ii. neither the substance nor any part of this thesis has been in the past, or is being, or is to be submitted for a degree at this University, or any other University.

Signature: Signed by candidate Date: **28/07/2022**

Print Name: **STEPHANIE GATHONI KAMUNYA**

Acknowledgements

I would first like to thank the Lord Almighty for His amazing grace and strength during this trying journey.

To my supervisor, the world-renowned Professor Kelly Chibale, I am eternally grateful for your guidance and endless support, not to mention, this opportunity to learn from your years of experience in the drug discovery world. I would also like to thank Dr. Lauren Arendse, my co-supervisor; your patience, continued support and encouragement truly helped in the realization of this thesis. I would also like to acknowledge Professor Matilu Mwau who believed in me from the very beginning.

I would like to acknowledge the Holistic Drug Discovery and Development Centre (H3D) for graciously sharing not only their research facilities but also their expertise throughout this project. Especially, both the Parasitology and Drug Metabolism and Pharmacokinetics (DPMK) teams who performed the asexual blood stage antiplasmodial and solubility assays, respectively. A special thanks to Tando Ntsabo and Dr. Andani Mulelu who were very instrumental in me settling into the biology lab where I carried out the enzymatic assays. Additionally, it is with a grateful heart that I acknowledge the academic group who were quite helpful all through this journey: specifically, Samuel Gachuhi for his crucial advice; Dr. Lebu Taleli and Dr. Godwin Dziwornu for their expertise in the synthetic lab; Mokhitli Morake for being a brother in Christ; Dr. Stephen Fienberg for introducing me to the Schrodinger software and Radwan Alnajjar for helping me interpret the molecular dynamic simulations.

Excitedly, I would like to extend my gratitude to Novartis Pharma AG who granted me the opportunity to be part of the 10th cohort of the Next Generation Scientist (NGS) program in

2020. A special thanks to Akiko Keller, Paul Ashigbie and their team who, despite the COVID-19 pandemic, still conducted this esteemed program. In addition, I heartfully thank my NGS mentor, Dr. Binesh Shrestha who played a critical role in the progression of my career.

Due to the hard work and dedication of the administration team: Elaine Rutherfoord-Jones, Saroja Naicker and Deidre van Rooyen, I was allowed to focus on my research. Their assistance in ordering of chemicals together with consumables and in executing administration obligations was invaluable.

Finally, I would like to hugely thank my funders: Merck, Medicines for Malaria Venture (MMV) and H3D. Their financial support was immeasurable.

List of Abbreviations

^{13}C-NMR	Carbon-13 Nuclear Magnetic Resonance
^{1}H-NMR	Proton Nuclear Magnetic Resonance
3D	Three Dimensional
ACT	Artemisinin-based Combination Therapy
ADME	Absorption, Distribution, Metabolism, Excretion
ADP	Adenosine Diphosphate
AIDS	Acquired Immunodeficiency Syndrome
AMBER	Assisted Model Building with Energy Refinement
APCI	Atmospheric Pressure Chemical Ionization
aPKs	Atypical Protein Kinases
Ar/HA	Aromatic Indicator
Ar-sp3	Aromatic balance
ATP	Adenosine Triphosphate
BLAST	Basic Local Alignment Search Tool
BSA	Bovine Serum Albumin
CADD	Computer-aided Drug Design
CBDs	cGMP-binding domains
CDPK4	calcium-dependent protein kinase 5
CDPKs	calcium-dependent protein kinases
cGMP	cyclic Guanosine Monophosphate
CHARMM	Chemistry at Harvard Macromolecular Mechanics
chEMBL	chemical database maintained by European Molecular Biology Laboratory
CHO	Chinese Hamster Ovarian

CK1	casein kinase 1
cKD	Conditional knock-down
cKO	Conditional knockout
CLK3	CDC-like Kinase 3
CML	Chronic Myeloid Leukemia
COMPASS	Condensed-phase Optimized Molecular Potentials for Atomistic Simulation Studies
CRK5	Cyclin-dependent protein kinase 5
CSD	Cambridge Structural Database
d	doublet
DCM	Dichloromethane
dd	doublet of doublets
DEL	DNA-encoded library
DHFR	Dihydrofolate Reductase
DIPEA	*N*, *N*-diisopropylethylamine
DMF	*N*, *N*-Dimethylformamide
DMSO	Dimethylsulphoxide
DND*i*	Drugs for Neglected Diseases Initiative
dt	doublet of triplets
dTMP	deoxythymidine monophosphate
DTT	Dithiothreitol
EGTA	Ethylene Glycol-bis(β-aminoethyl ether)-N,N,N′,N′-tetraacetic acid
ePKs	Eukaryotic Protein Kinases
ESI	Electrospray Ionization
E-value	Expectation value

FASTA	FAST-All
FBS	Fragment-based Screening
FDA	US Food and Drug Administration
Fsp^3	Aliphatic Indicator
GROMOS	Groningen Molecular Simulation
GSK	GlaxoSmithKline
GUI	Graphic User Interface
H3D	Holistic Drug Discovery and Development Centre
HEPES	4-(2-hydroxyethyl)-1-piperazineethanesulfonic acid
hERG	human *ether-a-go-go*-related gene
HIV	Human Immunodeficiency Virus
HPLC	High-Performance Liquid Chromatography
HTD	High-Throughput Docking
HTS	High-Throughput Screening
Hz	Hertz
IC_{50}	Half-maximal Inhibitory Concentration
J	Coupling Constant
LBDD	Ligand-based Drug Design
LBVS	Ligand-based Virtual Screening
LC-MS	Liquid Chromatography-Mass Spectrometry
m	multiplet
MD	Molecular Dynamics
MHz	Megahertz
min	minutes
MLK3	Mixed Lineage Kinase 3

MLM	Mouse Liver Microsomes
MMGBSA	Molecular Mechanics with Generalised Born and Surface Area solvation
MMV	Medicines for Malaria Venture
MoA	Mechanism of Action
MSD	Mean Survival Days
mTOR	mammalian Target of Rapamycin
NCE	New Chemical Entity
NIS	*N*-Iodosuccinimide
NMR	Nuclear Magnetic Resonance
NPT	Normal Temperature and Pressure
OPLS	Optimized Potentials for Liquid Simulations
OPLS3e	Extended Optimized Potentials for Liquid Simulations
PBS	Phosphate-Buffered Saline
PDB	Protein Data Bank
PDGF	Platelet-derived Growth Factor
Pf	*Plasmodium falciparum*
PFI	Property Forecast Index
PI3K	Phosphatidylinositol-3 Kinase
PI4K	Phosphatidylinositol-4 Kinase
PI4KIIIβ	Phosphatidylinositol-4 Kinase, type III beta
PIKs	Phosphoinositide Kinases
PIP5K2β	Phosphatidylinositol-5-phosphate-4 kinase, type II beta
PK5	Protein Kinase 5
PKA	Protein Kinase A
PKG	Protein Kinase G

PKIS	Published Kinase Inhibitor Set
PlasmoDB	*Plasmodium falciparum* genome Database
PRB	Pandemic Response Box
ps	picosecond
PUMA	Platform for Unified Molecular Analysis
Pv	*Plasmodium vivax*
q	quartet
QSAR	Quantitative Structure-Activity Relationship
RESPA	Reference System Propagation Algorithm
RLU	Relative Luminescence Units
RMSD	Root Mean Square Deviation
RP	Recursive Partitioning
s	singlet
SAR	Structure-activity relationaship
SBDD	Structure-based Drug Design
SBVS	Structure-based Virtual Screening
SP	Sulphadoxine-Pyrimethamine
t	triplet
TCPs	Target Candidate Profiles
td	triplet of doublets
TDR	Tropical Diseases Research
THF	Tetrahydrofuran
TIP4P	rigid planar four-site interaction potential for water model
TLC	Thin-Layer Chromatography
TR-FRET	Time-resolved Fluorescence Resonance Energy Transfer

UCT	University of Cape Town
UV	Ultraviolet
VEGFR2	Vascular Endothelial Growth Factor Receptor 2
VSGB	Surface Generalized Born Model and Variable Dielectric solvation model
WHO	World Health Organization
XP	Extra Precision

Abstract

The discovery of antimalarials with novel mechanisms of action able to circumvent resistance is crucial. This target-based drug discovery campaign is based on the following *Plasmodium* kinases: *Plasmodium falciparum* phosphatidylinositol 4-kinase (*Pf*PI4K) and *Plasmodium falciparum* cyclic guanosine monophosphate (cGMP)-dependent Protein Kinase (*Pf*PKG). The aim of this study was to use computer-aided drug design (CADD) methods to rationally design and accelerate the identification of *P. falciparum* kinase inhibitors. The foremost part of this project was focused on the design and synthesis of novel analogues of the anticancer human mammalian target of rapamycin (mTOR) inhibitor MLN0128 as dual *Pf*PI4K/*Pf*PKG inhibitors. Using structure-based drug design methods, several strategies were used to design potent dual *Pf*PI4K/*Pf*PKG inhibitors with reduced activity against human kinases specifically mTOR and human type III beta phosphatidylinositol-4 kinase (HuPI4KIIIβ). Selected compounds were prioritized for synthesis and were screened against the whole-cell parasite and the respective kinases: *Plasmodium* PI4K and PKG. Compound **46h** demonstrated high *Pv*PI4K potency with an IC_{50} of 0.002 nM. The most potent *Pf*PKG inhibitors, **46b** (0.12 µM**)** and **46g** (0.18 µM) also exhibited relatively good whole-cell activity with *Pf*NF54 IC_{50} values of 0.66 µM and 0.4 µM, respectively. High selectivity was also maintained relative to the human ortholog, HuPI4KIIIβ, and moderate selectivity was achieved relative to the mTOR kinase.

MMV652103, an imidazopyridazine lead compound showed potent inhibition of *Pv*PI4K (*Pv*PI4K IC_{50}: 0.0008 µM) but moderate *Pf*PKG inhibition with a *Pf*PKG IC_{50} of 0.12 µM. Therefore, the second part of this project was focused on optimising *Pf*PKG inhibition by compounds belong to this chemotype. Using chemoinformatic approaches, compounds from an in-house imidazopyridazine library were prioritised for *Pf*PKG inhibition assays to validate

molecular docking findings and understand protein-inhibitor interactions important for *Pf*PKG inhibition. These findings were then used to select more compounds from the in-house library for *Pf*PKG screening which demonstrated IC_{50} results ranging from 0.007 to >30 μM. These data, coupled with molecular docking and molecular dynamics studies, provided valuable insight into structural features driving *Pf*PKG inhibition.

The final part of this project was to virtually screen the Pandemic Response Box (PRB) for potential *Pf*PI4K and/or *Pf*PKG inhibitors. Of the 400 compounds in the PRB, 21 were selected for enzymatic screening after virtual screening using the *Pv*PKG crystal structure and the *Pf*PI4K homology model. Four hits were identified against *Pf*PKG (approximately 20% success rate) and two against *Pv*PI4K (approximately 10% success rate). Hence, the novel chemotypes (1H-pyrrolo[2,3-b]pyridine and pyrimidine-2,4-diamine) may be optimized for increased dual *Pf*PKG/*Pv*PI4K inhibition potency.

In summary, using CADD methods, this project identified analogues of various chemotypes as *Pf*PI4K and *Pf*PKG inhibitors.

List of Figures

Figure 1.1: The life-cycle of the *Plasmodium* parasite, with various stages highlighted[5]........3

Figure 1.2: Structure of antimalarial drugs discussed. Quinine (**1.1**), Chloroquine (**1.2**), Proguanil (**1.3**), Pyrimethamine (**1.4**), Mefloquine (**1.5**) and Artemisinin (**1.6**). 4

Figure 1.3: The kinase binding site with bound ATP. Important residues and pockets have been indicated.[60]..10

Figure 1.4: Crystal structure of *Plasmodium vivax* cGMP-dependent protein kinase (PDB code: **5F0A**) 12

Figure 1.5: ML10, a *Pf*PKG inhibitor with *Pf*PKG IC_{50} = 0.16 nM and *Pf* EC_{50} = 2.1 nM...14

Figure 1.6: *Pv*PKG-ML10 crystal structure complex (PDB ID: **5EZR**) with interacting residues shown. 15

Figure 1.7: Trisubstituted thiazole *Pf*PKG inhibitor with *Pf*PKG IC_{50} = 2 nM and *Pf* EC_{50} = 113 nM..16

Figure 1.8: MMV030084, a *Pf*PKG inhibitor with *Pf*PKG IC_{50} = 0.4 nM and *Pf* EC_{50} = 120 nM..16

Figure 1.9: MMV390048, a *Plasmodium* PI4K inhibitor with *Pv*PI4K IC_{50} = 3.4 nM and *Pf* EC_{50} = 28 nM..18

Figure 1.10: Homology model of *Plasmodium falciparum* phosphatidylinositol-4 kinase (*Pf*PI4K) with **MMV390048** bound into the active site. Hinge residue: **Val1357**, gatekeeper residue: **Ile1354** and catalytic lysine: **Lys1308**. 19

Figure 1.11: Drug discovery process. SBDD, structure-based drug discovery; NCE, new chemical entity..21

Figure 1.12: Illustration of Computer-Aided Drug Discover (CADD).[113] **SBVS**: Structure-based virtual screening; **PBVS**: Pharmacophore-based virtual screening; **LBVS**: Ligand-based virtual screening..23

Figure 1.13: Structure of HIV-1 PR peptidic inhibitor, Ro 31-8588 28

Figure 1.14: Structure of FDA-approved anti-HIV drug, Saquinavir (Ro 31-8959) 28

Figure 1.15: Crystal structure of wild-type HIV-1 Protease in complex with the antiviral drug, Saquinavir. (PDB Code: **3OXC**)[171] 29

Figure 1.16: Structure of Agouron hit compounds, AG-1002 (**A**) and AG-1004 (**B**) 30

Figure 1.17: Structure of FDA-approved anti-HIV drug, Nelfinavir (Viracept, Ag-1343)....30

Figure 1.18: Crystal structure of wild-type HIV-1 Protease in complex with the antiviral drug, Nelfinavir. (PDB Code: **3EKX**)[173] 31

Figure 1.19: Structure of the components of the FDA-approved anti-HIV drug, Kaletra: Lopinavir (**A**) and Ritonavir (**B**) 32

Figure 1.20: Crystal structure of wild-type HIV-1 Protease in complex with the antiviral drug, Nelfinavir. (PDB Code: **1MUI**)[174]..33

Figure 2.1: Structure and enzymatic activities of **MLN0128** determined via kinobead binding studies. 59

Figure 2.2: Structure of NCATS-SM3710, a *Pf*PI4K inhibitor. This compound also exhibited activity against multiple stages of the *P. berghei* life cycle. 60

Figure 2.3: Cascade followed for the design of MLN0128 analogues. Using the GSK published kinase inhibitor set (PKIS)[29], scaffold-hopping was used to design MLN0128 analogues. These were then docked into the targets of interest: *Pf*PI4K, *Pv*PKG, and the off target mTOR. The binding poses and conformation of the ligand were then analyzed to select a final list of compounds for synthesis. 62

Figure 2.4: (**A**) Parameters used to calculate the BLAST score, (**B**) mathematical equation used to calculate the BLAST score 64

Figure 2.5: (**A**) The ATP-binding site of HuPI4KIIIβ (PDB ID: 4D0L) with the co-crystallized ligand PIK93. The interacting residues are labelled and shown. (**B**) The 2D structure of PIK93. 65

Figure 2.6: Alignment of globally conserved residues in the ATP binding site. HuPI4KIIIβ is shown in green (PDB ID: 4D0L) while the cyan and purple ribbons are part of the *Pf*PI4K homology model. Pink and brown residues belong to HuPI4KIIIβ and *Pf*PI4K, respectively. 66

Figure 2.7: Illustration showing that the mismatch of the Ala692/Pro1448 is far from the active site 67

Figure 2.8: Ramachandran plot of the *Pf*PI4K homology model 69

Figure 2.9: KAI715 (**A**) and KDU691 (**B**) docked into *Pf*PI4K (purple) to validate the homology model. 72

Figure 2.10: Co-crystallized ligands of *Pv*PKG (**A**: PDB ID: 5F0A) and mTOR (**B**: PDB ID: 4JT5). These are both pyrazolo[3,4-d]pyrimidine analogues. 73

Figure 2.11: Mammalian target of rapamycin (mTOR; red) binding with MLN0128 (magenta). mTOR, red; MLN0128, magenta. Interacting residues and hydrogen bonds are shown. 75

Figure 2.12: Phosphatidylinositol-4 kinase **(**PI4K; purple) binding with MLN0128. PI4K, purple; MLN0128, magenta. Interacting residues and hydrogen bonds are shown 76

Figure 2.13: cGMP-dependent protein kinase (PKG) binding with MLN0128. PKG, green; MLN0128, magenta. Interacting residues and hydrogen bonds are shown. 77

Figure 2.14: (A) *Pf*PI4K homology model (pink) and (**B)** *Pv*PKG crystal structure (pink) aligned to mTOR (brown). 78

Figure 2.15: Illustration of the scaffold decomposition process involved in the design of MLN0128 analogues. 80

Figure 2.16: MLN0128 analogues docked into (**A**) *Pf*PI4K (cyan) and (**B**) *Pv*PKG (orange) with the respective analogues also docked into mTOR to demonstrate favorable and unfavorable poses 81

Figure 2.17: MLN0128 analogues selected for synthesis. cLogP, calculated partition coefficient; MW, molecular weight 88

Figure 2.18: ^{1}H-NMR spectrum of 4-((4-amino-3-iodo-1H-pyrazolo[3,4-d]pyrimidin-1-yl)methyl)-N,N-dimethylbenzenesulfonamide (**45f**) 93

Figure 2.19: ^{1}H-NMR spectrum of a target compound, 4-((4-amino-3-(2-aminobenzo[d]oxazol-5-yl)-1H-pyrazolo[3,4-d]pyrimidin-1-yl)methyl)-N,N-dimethylbenzenesulfonamide (**46f**) 94

Figure 2.20: ^{13}C-NMR spectrum of 4-((4-amino-3-(2-aminobenzo[d]oxazol-5-yl)-1H-pyrazolo[3,4-d]pyrimidin-1-yl)methyl)-N,N-dimethylbenzenesulfonamide (**46f**) 95

Figure 2.21: Scatter plot showing no correlation between *Plasmodium* PI4K docking score and enzymatic data 98

Figure 2.22: (**A) 46h** (0.002 µM) and **(B) 46e** (0.013 µM) docked into the *Pf*PI4K homology model (purple) 100

Figure 2.23: Scatter plot showing no correlation between *Plasmodium* PKG docking score and enzymatic data 103

Figure 2.24: (**A**) **46b** (0.12 µM) and **(B) 46a** (0.8 µM) docked into the *Pv*PKG (green) crystal structure (PDB ID: 5F0A) 105

Figure 2.25: (**A) 46h** (0.22 µM) and (**B**) **46e** (0.25 µM) docked into the *Pv*PKG (green) crystal structure (PDB ID: 5F0A) 107

Figure 2.26: (**A**) **46g** (0.18 µM) and (**B**) **46f** (0.8 µM) docked into the *Pv*PKG (green) crystal structure (PDB ID: 5F0A) 109

Figure 2.27: **(A)** MLN0128 docked into the mTOR (red) crystal structure (PDB ID: 4JT5), **(B)** HuPI4KIIIβ (PDB ID: 4D0L; green) aligned with mTOR (PDB ID: 4JT5; red)............116

Figure 2.28: Aligned residues in the back pockets of mTOR (red) and residues in HuPI4K (green)..........118

Figure 2.29: MLN0128 docked into wildtype (**A**) and computationally mutated HuPI4KIIIβ (**B**)..........119

Figure 2.30: MLN0128 analogue with mTOR IC_{50} of >10 μM. 120

Figure 2.31: *Pv*PKG co-crystallised with potent and selective *Pf*PKG inhibitor, ML10. 121

Figure 2.32: Examples of MLN0128 analogues with decreased mTOR inhibition.[67]..........122

Figure 3.1: Imidazopyridazine core………………………………………………… 132

Figure 3.2: Parent compound (MMV652103) ^{a}MSD, mean survival days; hERG, human *ether-a-go-go*-related gene; *Pv*PI4K, *P. vivax* phosphatidylinositol 4-kinase; *Pf*PKG, *P. falciparum* cGMP-dependent kinase..........133

Figure 3.3: Potent *Pf*CDPK1 inhibitor (*Pf*CDPK1 IC_{50} = 0.013 μM) with imidazopyridazine core *In vivo P. berghei* (po) at 4 × 50 mg/kg, 46%, 7 mean survival days..........133

Figure 3.4: *Pf*CDPK1 inhibitor with *Pf*CDPK1 IC_{50} = 0.02 μM..........134

Figure 3.5: *Pf*CDPK1 inhibitor with imidazopyridazine core. MLM, mouse live microsomes 134

Figure 3.6: KAI715, a *Pf*PI4K inhibitor with *Pf*PI4K IC_{50} = 11 nM..........136

Figure 3.7: Frontrunner imidazopyridazine analogue studied by Cheuka et al.[14]..........136

Figure 3.8: Heatmap of the calculated physicochemical properties of SFK52 library compounds. The red color showed positive correlation while the blue color demonstrated negative correlations. 140

Figure 3.9: Property forecast index (PFI) distribution of imidazopyridazines..........141

Figure 3.10: Aliphatic indicator (Fsp^3) distribution of imidazopyridazines..........142

Figure 3.11: The favorable pose of **2** (**A**) and the unfavorable pose of **9** (**B**) when docked into *Pf*PKG (PDB ID: 5F0A). The negatively charged regions (red), positively charged region (green), and hydrophobic regions (green) are represented on the surface. 145

Figure 3.12: Scatter plot of the imidazopyridazine analogues showing the lack of correlation between the *Pf*PKG IC_{50} values and the calculated binding energy. 150

Figure 3.13: **11** (pink) and the parent compound (brown) docked into *Pv*PKG with interacting residues showed as lines 151

Figure 3.14: **16** (magenta) docked into *Pv*PKG (green) with interacting residues labeled and showed as lines 152

Figure 3.15: **44** (pink) and **42** (brown) docked into *Pv*PKG with interacting residues labeled and showed as lines.. 153

Figure 3.16: **28** (brown) docked into *Pv*PKG with interacting residues labeled and showed as lines 154

Figure 3.17: **39** (pink) and **38** (brown) docked into *Pv*PKG with interacting residues showed as lines. 156

Figure 3.18: **32** (red) and **35** (purple) docked into *Pv*PKG with interacting residues labeled and showed as lines.. 157

Figure 3.19: **34** docked into *Pv*PKG with interacting residues labeled and shown as lines. 158

Figure 3.20: Structure of the parent compound and **29** with corresponding *Pf*PKG IC_{50} values 159

Figure 3.21: Distance between **Asp675** and the parent compound (brown) and **29** (pink).. 160

Figure 3.22: Distance between **Asn578** and the parent compound (brown) and **29** (pink).. 161

Figure 3.23: Distance between **Asn575** and the parent compound (brown) and **29** (pink).. 161

Figure 3.24: Chemical space analysis of the tested Imidazopyridazine analogues. 163

Figure 4.1: Screening cascade followed for pandemic response box compounds...............172

Figure 4.2: The kinase active site with bound ATP. The adenine region forms the hinge interaction with the kinase.[3]..174

Figure 4.3: **MMV000043** (blue) docked into *Pv*PKG (green) with interacting residues shown as lines...185

Figure 4.4: **MMV1580844** (purple) docked into *Pv*PKG (green) with interacting residues shown as lines 186

Figure 4.5: Structure of vemurafenib and **MMV1580482**. The 1H-pyrrolo[2,3-b]pyridine core common to both in shown in pink...187

Figure 4.6: Co-crystallized ligand with a 1H-pyrrolo[2,3-b]pyridine core docked into a human kinase (PDB ID: 3OG7). The hinge is colored purple. 188

Figure 4.7: **MMV1580482** (red) docked into *Pv*PKG (green) with interacting residues shown as lines...189

Figure 4.8: **MMV009948** (imatinib) co-crystallized with the human Abl kinase (PDB ID: 2HYY). The hinge is colored purple..190

Figure 4.9: **MMV009948** (orange) docked into *Pv*PKG (green) with interacting residues shown as lines 191

Figure 4.10: **MMV1580844** (pink) docked into *Pf*PI4K (purple) with interacting residues shown as lines 197

Figure 4.11: **MMV1580482** (red) docked into *Pf*PI4K (purple) with interacting residues shown as lines and hydrogen bonds shown in yellow 198

Figure 4.12: Structure of tafenoquine 199

Figure 4.13: Structure of MMV1580844 (*Pf*PKG and *Pv*PI4K IC_{50} = 1.92 µM and 3.71 µM, respectively)..199

Figure 4.14: Structure of **MMV1580482** 200

Figure 4.15: Structures of 1H-pyrrolo[2,3-b]pyridine analogues as *Pf*CLK3 inhibitors......201

Figure 4.16: Structure of **MMV009948** (imatinib) 201

Figure 4.17: Human Abl kinase domain (PDB ID: 2HYY) in complex with MMV009948 (imatinib, purple). The hinge (cyan), gatekeeper (Thr315, magenta), and interacting residues are labelled. 202

Figure 4.18: Novel chemotypes with dual *Pf*PKG/*Pv*PI4K inhibition 203

Figure 5.1: Front-runner MLN0128 analogues with associated biological data 210

Figure 5.2: Parent compound and front-runner SFK52 analogue with associated biological activity..211

Figure 5.3: Front-runner Pandemic Response Box compounds that exhibited dual *Pf*PKG/*Pv*PI4K inhibition...211

Figure 5.4: MLN0128 analogue, **46b**, with its associated biological data. 212

Figure 5.5: **46b** docked into *Pv*PKG (**A**) and **MLN0128** docked into mTOR (**B**) showing important amino acid interactions...213

Figure 5.6: Front-runner SFK52 analogues with associated biological data.......................214

Figure 5.7: Novel chemotypes that exhibited dual *Pf*PKG/*Pv*PI4K inhibition. 214

Figure 6.1: Kinase-Glo® reaction mechanism. 219

Figure 6.2: ADP-Glo™ kinase assay...220

Figure 6.3: Comparison of positive (orange) and negative (blue) controls for Kinase-Glo® (A) and ADP-Glo™ (B) assays. The high signal-to-background ratio of ADP-Glo^{TM} is preferred. 221

Figure 6.4: A, ATD/ADP conversion standard curve; B, *Pf*PKG enzyme titration 223

Figure 6.5: IC$_{50}$ of MLN0128 against *Pf*PKG 224

List of Tables

Table 2.1: Ligands used to validate the *Plasmodium falciparum* phosphatidylinositol-4 kinase (*Pf*PI4K) homology model 70

Table 2.2: Selected ligands with favorable poses in *P. vivax* cGMP-dependent protein kinase (*Pv*PKG) 82

Table 2.3: Selected ligands with favorable poses in *P. falciparum* phosphatidylinositol 4-kinase (*Pf*PI4K) 85

Table 2.4: Isolated yields for target compounds synthesized according to **Scheme 2.1** 91

Table 2.5: Results from *Pv*PI4K screening with respective calculated binding energy 97

Table 2.6: Results from *Pf*PKG screening and calculated binding energy 102

Table 2.7: *In vitro* activity against asexual blood-stage *P. falciparum* NF54 and K1 strains, *Pv*PI4K and *Pf*PKG IC_{50} values, and solubility data 111

Table 2.8: Results from mTOR and HuPI4K screening and *Pv*PI4K inhibition data 114

Table 3.1: Whole-cell and enzymatic activity and calculated binding energy data of imidazopyridazine analogues 143

Table 3.2: Enzymatic activity, docking score, and calculated binding energy data of imidazopyridazine analogues 147

Table 4.1: Compounds prioritized for enzymatic screening 175

Table 4.2: *Pf*PKG enzymatic data for PRB compounds 181

Table 4.3: *Pf*PKG IC_{50} values of PRB hit compounds 184

Table 4.4: *Pv*PI4K enzymatic results for PRB compounds 192

Table 4.5: PRB hit compounds against *Pv*PI4K 195

Table 6.1: ATP/ADP standard curve dilutions 222

Table 6.2: HPLC gradient used for determining the purity and mass (mass-to-charge, m/z) of compounds via LC-MS 227

CHAPTER ONE: Introduction

1.1. Background

As a preventable and curable life-threatening disease malaria was responsible for 241 million cases and caused 627,000 deaths worldwide in 2020. Of these, an estimated 501,600 were in children under the age of 5 years. The African region is the most vulnerable and accounted for 95% of the total number of cases worldwide.[1] Malaria is a blood-borne disease caused by the *Plasmodium* parasite and is transmitted through the bite of an infected female *Anopheles* mosquito. There are five *Plasmodium* species of human interest: *P. falciparum*, *P. vivax*, *P. malariae*, *P. ovale*, and *P. knowlesi*.[2] *P. falciparum* and *P. vivax* are the most harmful of these. *P. falciparum* causes the most severe form of disease and is responsible for 99.7% of infections in the most burdened region, Africa. It also accounts for 50%, 65%, and 71% of cases in the South-East Asia, Western Pacific, and Eastern Mediterranean regions, respectively. In the Americas, *P. vivax* is the prominent parasite and is responsible for 75% of reported cases of malaria. This *Plasmodium* species is also responsible for the relapsing form of malaria.

1.2. The life cycle of the malaria parasite

During the blood-meal of a female *Anopheles* mosquito (**Stage 1**), sporozoites are injected into the bloodstream of the first host, the human, triggering the human liver-stage cycle (**Stage 2**) (**Figure 1.1**). In *P. ovale* and *P. vivax* infections, hypnozoites are formed and may remain dormant for several months or years (**Stage 3**). This particular feature is not observed for *P. falciparum* infections. Therefore, an episode of malaria relapse may occur in the absence of a mosquito bite.[3] The parasites then form schizonts which eventually develop into thousands of merozoites (**Stage 4**).

When liver cells rupture, merozoites are released into the bloodstream and rapidly invade the host red blood cells. This is the onset of the human blood stage malaria infection. Clinical symptoms are brought about by the destruction of infected red blood cells associated with the rapid asexual replication of merozoites. A small percentage of merozoites differentiate into male and female gametocytes and are taken up by the second host, the female *Anopheles* mosquito, as part of a blood-meal, thus beginning the mosquito stage (**Stage 5**). Diploid zygotes form in the mosquito through the fusion of male and female gametes and develop into ookinetes. These in turn form oocysts as ookinetes migrate to the midgut and pass through the gut wall of the insect. The cycle then continues when sporozoites are formed through meiotic division of oocysts, which migrate to the salivary glands of the mosquito.[4]

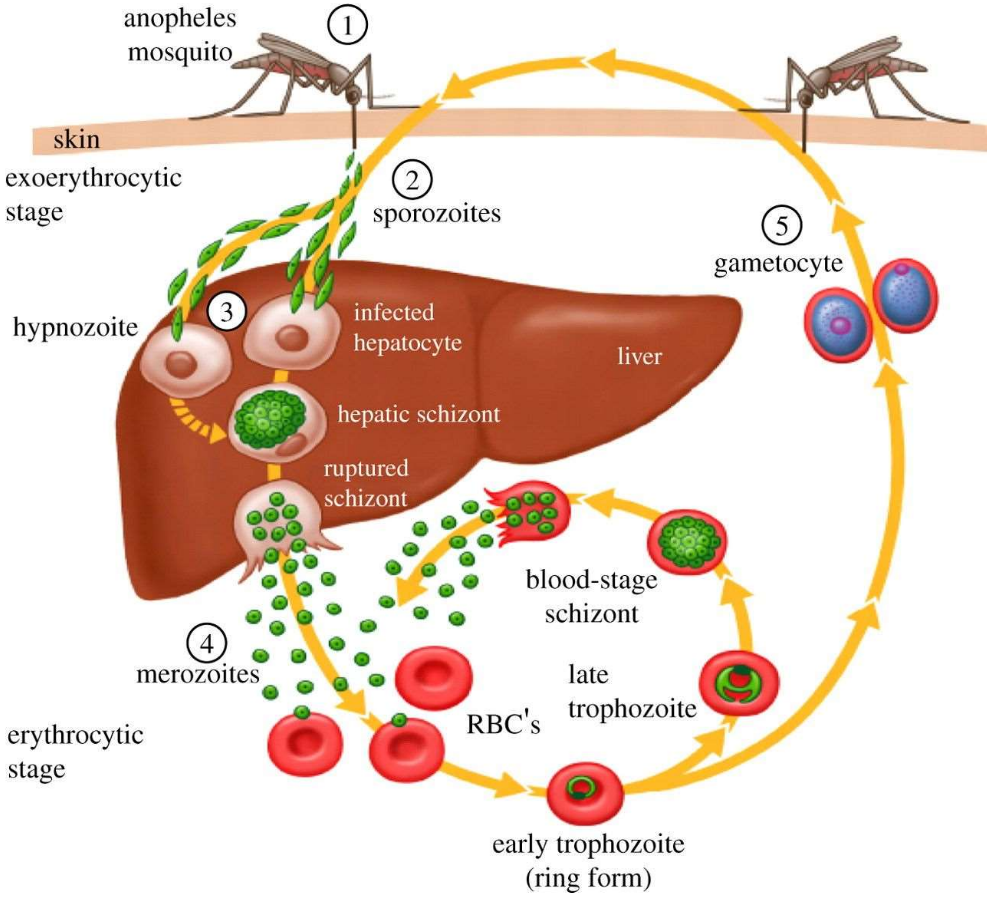

Figure 1.1: The life-cycle of the *Plasmodium* parasite, with various stages highlighted[5]

1.3. Current antimalarials

In addition to vector control, the most effective strategy employed to reduce disease burden is chemotherapy in which the efficacy of the antimalarial is crucial. Some of the antimalarial drugs used historically are discussed in the following sections (**Figure 1.2**).

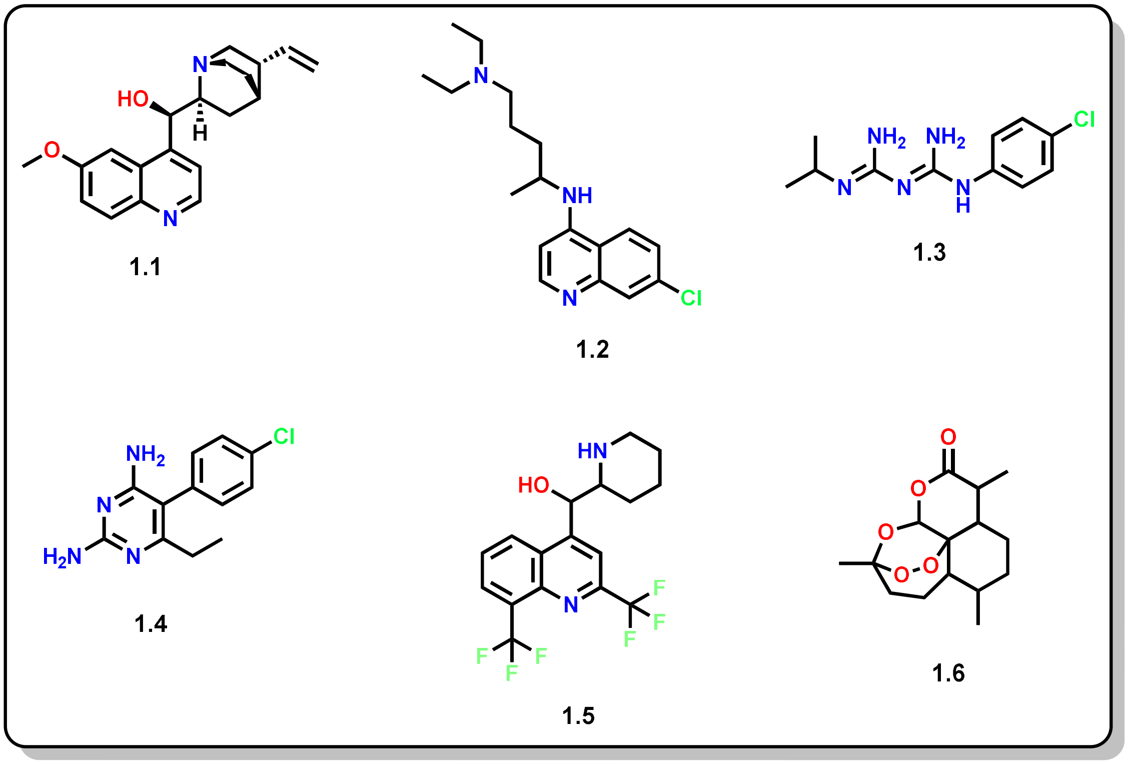

Figure 1.2: Structure of antimalarial drugs discussed. Quinine (**1.1**), Chloroquine (**1.2**), Proguanil (**1.3**), Pyrimethamine (**1.4**), Mefloquine (**1.5**) and Artemisinin (**1.6**).

1.3.1. Quinine

Quinine (**1.1**) was isolated by two French chemists from the bark of a cinchona tree in 1820. Evidence suggests that this quinoline interferes with the hemoglobin degradation pathway.[6] Using a cellular thermal shift assay, *Plasmodium falciparum* Purine Nucleoside Phosphorylase (*Pf*PNP) is the suggested protein target.[7] It continues to play a crucial role as an antimalarial, especially in the first trimester of pregnancy. Quinine resistance has been observed occasionally.[8]

1.3.2. Chloroquine

The pivotal story of chloroquine (**1.2**) spans from 1934 to 1946 and involves its discovery, the work of investigators in six countries on five continents, its rejection, re-discovery, evolution, and ultimately, its acceptance.[9] The need for a quinine substitute led to the synthesis of this 4-aminoquinoline; chloroquine (then known as Resochin) and 3-methyl-chloroquine (Sontochin) by German scientists. During World War II, a stockpile of Sontochin abandoned by the Germans was discovered by French soldiers in North Africa, who handed it over to American researchers. After some structural changes to Sontochin, the new formulation was given the name: Chloroquine. Resochin was assumed to be toxic but after comparing its structure to that of chloroquine, the two were found to be identical.[10] Owing to its safety and efficacy, chloroquine has since been used as a frontline antimalarial in the fight against malaria. Chloroquine leads to the accumulation of toxic heme, through inhibition of the conversion of heme to hemozoin, leading to the death of the parasite.[11, 12]

Unfortunately, *Plasmodium* strains resistant to chloroquine were documented in four locations: the Thai-Cambodian border in 1957, parts of Colombia and Venezuela in 1960, Papua New Guinea in the 1970s, and in Eastern and Southern Africa in the late 1970s and early 1980s.[13-16] This presented challenges and has led to a delay in the global eradication of malaria, particularly in Africa.[17] It was shown that mutant forms of *Pf*CRT, *Plasmodium falciparum* Chloroquine Resistance Transporter, mediates resistance to chloroquine.[18]

1.3.3. Proguanil and pyrimethamine

Proguanil (**1.3**), a pyrimidine derivative, was discovered during World War II. By targeting the dihydrofolate reductase (DHFR) of the various *Plasmodia* species, the Proguanil metabolite inhibits the purine and pyrimidine biosynthesis pathway necessary for DNA synthesis.[19, 20] Proguanil has shown activity in both the pre-erythrocytic and erythrocytic stages of *P. falciparum*, providing both causal and suppressive prophylaxis, respectively.[21]

Pyrimethamine (**1.4**) was later developed based on the success of proguanil's chemical class. Consequently, a similar mechanism of action was observed.[22] However, resistance to proguanil and pyrimethamine was observed quite rapidly.[23] This led to the development of combinations of these antimalarials with sulphonamide and sulphones to prevent further resistance and increase efficacy. Unfortunately, resistance to sulphadoxine-pyrimethamine (SP) antimalarial treatment prevailed, challenging its success.[24, 25]

1.3.4. Mefloquine

In an effort to combat the emergence of multidrug-resistant *Plasmodium* strains, a collaboration between Hoffman-La Roche, the US Army Medical Research and Development Command, and the World Health Organization's (WHO) Tropical Diseases Research (TDR) led to the development of mefloquine (**1.5**). It has been suggested that through the inhibition of the 80S ribosome, this quinoline negatively affects *Plasmodium* schizonts. However, the definite mode of action of mefloquine is still elusive.[26] This compound is active against the intraerythrocytic stage of the *Plasmodium* parasite[27] and is therefore used in both prophylaxis and treatment.[28] Unfortunately, mefloquine resistance was first recorded in Asia in 1985.[29]

1.3.5. Artemisinin

Artemisinin (**1.6**) has been known to Chinese herbalists for more than 2000 years as Qinghao and was isolated from sweet wormwood (*Artemisia annua*) in 1972 by Chinese scientists.[30] Qinghao extracts showed efficacy similar to that of quinine and chloroquine in clearing parasites in malaria-infected mice, and later in humans, when first tested in 1975.[31] *In vivo* studies showed that artemisinin could kill parasites within the erythrocyte of the host and remove the killed parasite in the spleen.[32] Studies showed the rapid inhibitory effect of artemisinin and demonstrated its efficacy against both schizonts and rings.[33, 34] By compromising the parasite's proteasome function and causing protein damage, the parasite burden of the *Plasmodium* infection is greatly reduced by artemisinin or its derivatives.[35]

Partnering artemisinin derivatives with other long half-life antimalarials improved its efficacy and highlighted the value of artemisinin-based combination therapy (ACT).[36, 37] Treatment duration and resistance development were reduced during drug combination. This combination is the first-line treatment for uncomplicated *P. falciparum* malaria in approximately 80 countries.[38]

1.4. Next generation antimalarials

As previously noted, resistance has plagued some of the antimalarials currently on the market. This has slowed down progress towards the eventual eradication of the disease. Antimalarial resistance usually emerges in low-burdened areas (e.g., South-East Asia) and spreads into the high-burdened region of Sub-Saharan Africa.[39] This implies that the recent resistance to ACT chemotherapy observed in South-East Asia may pose a threat to treatment in Sub-Saharan Africa, with *in vitro* resistance to artemisinin recently recorded in Rwanda causing great concern.[40, 41]

An additional concern to resistance is the fact that most marketed drugs target the blood stage of the parasite life cycle. This has increased the need for the development of antimalarials with novel modes of action and a low propensity for resistance. In response to this, Medicines for Malaria Venture (MMV) has developed target candidate profiles (TCPs) to guide the development of the next generation antimalarials.[42] With the second target candidate profile (**TCP2:** long lasting compounds) retired[43], the remaining profiles are defined as follows:

- **TCP1:** blood-stage treatment, in which the molecule clears asexual blood-stage parasites

- **TCP3:** relapse treatment, in which the molecule shows activity against hypnozoites
- **TCP4:** liver prophylaxis, in which the molecule shows activity against hepatic schizonts
- **TCP5:** gametocyte transmission blockade, in which the molecule targets gametoctyes
- **TCP6**: mosquitocidal activity, in which the molecule blocks transmission by targeting the insect vector.

These TCPs provide guidelines for the development of antimalarials with a novel mechanism of action (MoA) and multistage activity, thus reducing the potential for resistance development. This may be achieved by identifying antimalarials that target enzymes which play a vital role in the survival of the parasite and are expressed at multiple stages of its life cycle.

1.5. Kinases

An ideal drug target is one that is structurally and functionally characterized. It should also participate in a biological process known to be critical to the disease.[44] Kinases are enzymes that catalyze the transfer of a phosphate group from ATP to substrates such as lipids (e.g., phosphatidylinositol kinases), proteins (e.g., serine/threonine or tyrosine-specific kinases), nucleic acids, and carbohydrates. Phosphorylation of the substrate modulates its interaction with other enzymes and/or its activity, eventually contributing to different physiological responses and therefore playing a vital role in cell signaling.[45, 46] As they are involved in specific signaling pathways, kinases regulate cell functions such as cell adhesion, cell cycle progression, and metabolism.[47]

Kinases were not initially considered to be favorable drug targets because of competition with the millimolar concentrations of ATP in cells and selectivity issues associated with conserved binding sites in case of competitive inhibitors. However, once the first kinase inhibitor, imatinib (marketed as Gleevac®/Glivac®) was approved by the US Food and Drug Administration (FDA), kinases became an attractive group of drug targets. Nearly two decades after the discovery of imatinib, over 70 kinase inhibitors have been approved by the FDA with approximately 300 human kinase inhibitors currently in clinical trials.[48, 49]

The success of marketed kinases from the cancer field makes this gene family attractive for drug targeting in the field of malaria. Indeed this success has highlighted the importance of *Plasmodium* kinases as attractive antimalarial drug targets.[50,51-53] The success of *Plasmodium* kinase inhibitors is in turn illustrated by MMV390048 reaching the second phase of clinical trials. This antimalarial is a *Plasmodium* phosphatidylinositol-4 kinase type 3 beta (PI4KIIIβ) inhibitor. Additionally, the *Plasmodium* cGMP-dependent protein kinase (PKG), essential in the cGMP pathway, is crucial in key development stages. Therefore, *Plasmodium* PKG inhibitors have demonstrated activity against various stages of the parasite's life cycle.[54]

Sequencing of the *P. falciparum* genome has played a critical role in the identification of *P. falciparum* targets.[55] This led to the establishment of various databases, such as PlasmoDB and the WHO/TDR database (http://TDRtargets.org), which consequently provided efficient *in silico* tools for the identification, evaluation, comparison, and later selection of potential drug targets.[56]

The *P. falciparum* kinome comprises 85–99 enzymes.[57] Eukaryotic protein kinases (ePKs) form the main class, while atypical protein kinases (aPKs) lack sequence similarity with ePKs. *Plasmodium* kinases fall into one of these two groups with approximately 73% classified as ePKs. The *Plasmodium* kinome is largely conserved between different *Plasmodium* species. However, considerable divergence was revealed between the *P. falciparum* kinome and that of other eukaryotes, including the mammalian host.[58] Specifically, most *Plasmodium* kinases do not have a human orthologue, thus increasing the chance of attaining selectivity over human kinases.[59]

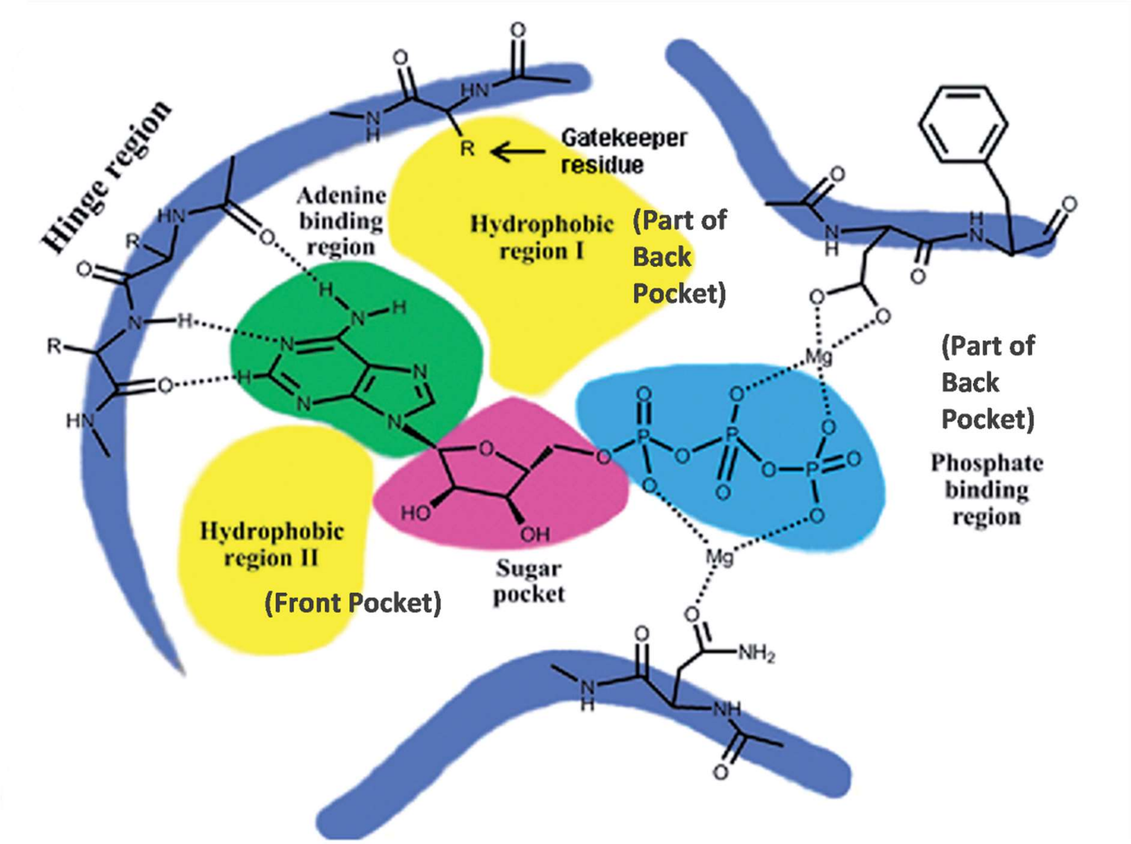

Figure 1.3: The kinase binding site with bound ATP. Important residues and pockets have been indicated.[60]

Figure 1.3 illustrates the ATP binding site of the kinase. The adenine of ATP binds to the hinge region of the active site. The gatekeeper plays a crucial role as it allows access to hydrophobic region I and the phosphate binding region which are jointly known as the back pocket. The ribose pocket is the region where the sugar motif of ATP binds. Therefore, it is also referred to as the sugar pocket. The front pocket (or hydrogen region II) is the solvent accessible region.

The *Plasmodium* kinases of interest and focus on this thesis project are the cGMP-dependent protein kinase (PKG) and PI4KIIIβ.

1.5.1. cGMP-dependent protein kinase (PKG)

As a serine/threonine protein kinase, *Plasmodium* PKG belongs to the established ePK group. This enzyme plays a crucial role in several stages of the parasite's life cycle. These roles include dissemination of the parasite through cellular motility, merozoite egress from hepatocytes and red blood cells, transmission of the parasite to the mosquito during a blood-meal, and gametogenesis.[61-67] With *Plasmodium* PKG essential to both the human and mosquito stages, inhibition of this enzyme is expected to translate to activity against various stages of the parasite's life-cycle.[68-70]

Understanding the structural features of *Plasmodium* PKG will provide great insight into the design of PKG inhibitors through elucidation of the interactions required for potent inhibition. The binding site of *Plasmodium vivax* cGMP-dependent protein kinase (*Pv*PKG) with a pyrazolo[3,4]pyrimidine derivative as the bound ligand was used for this structure investigation (**Figure 1.4**). The catalytic αC-helix and five-stranded β-sheets (β1-β5) make up the N-terminal lobe, whereas the C-terminal lobe is the larger α-helix.[71] There are four cGMP-binding domains (CBDs) in the N-terminal regulatory region: CBD-A, CBD-B, CBD-C, and CBD-D. The absence of cGMP leads to inhibition of the enzyme. Moreover, allosteric binding of cGMP to the regulatory region activates the catalytic domain.[72-74] The binding affinity of cGMP to different domains varies, with CBD-D demonstrating the highest binding affinity.[73-76] With the support of experimental data, molecular dynamic simulations identified key cGMP-CBD-D amino acid interactions that may be exploited in the design of allosteric *Plasmodium* PKG inhibitors.[77] The catalytic domain containing ATP and substrate binding sites follows the regulatory domain.[76]

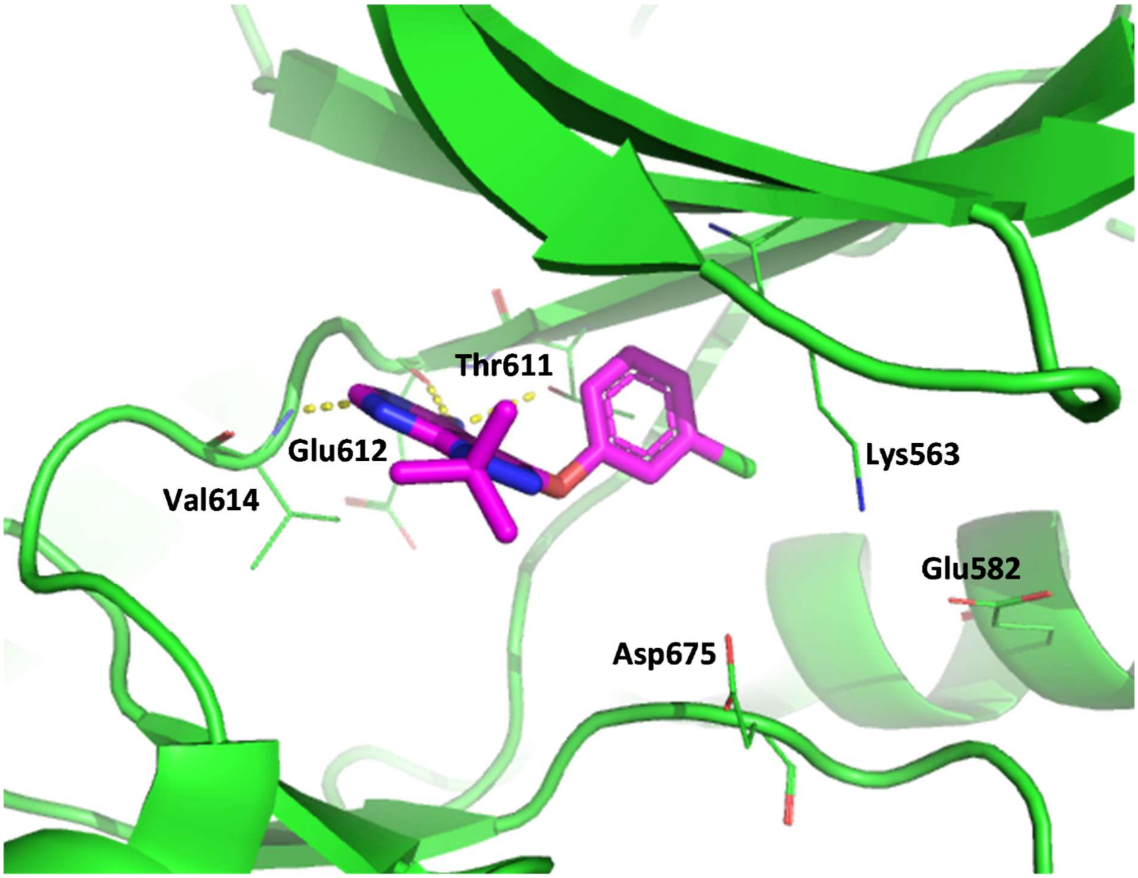

Figure 1.4: Crystal structure of *Plasmodium vivax* cGMP-dependent protein kinase (PDB code: **5F0A**)

The hinge region connects the N- and C-terminal lobes and forms part of the ATP binding site. The characteristic valine at the hinge region (**Val614**) usually forms the most influential hydrogen-binding interaction in a “donor-acceptor-donor” manner. Just before the hinge region and at the end of β-sheet β5 is the *P. vivax* (*Pv*)PKG gatekeeper residue (**Thr611**). This is relatively small compared to the human PKG gatekeeper residue (6C0T: HuPKG Met114), thus increasing target selectivity.[78] This is considered an advantage as the back pocket is now easily accessible, which increases selectivity over human kinases as demonstrated by various *Plasmodium* PKG inhibitors.

The phosphate binding loop (P-loop) secures the ATP in place, specifically the phosphate channel, by acting as a lid. The glycine-rich sequence ^{541}GRGTFG^{546} is conserved in *Pv*PKG and the signature sequence ^{561}ALK^{563} (Ala561-Leu562-Lys563) is also identified on β3. In the active αC_{in} conformation (alpha carbon terminal in the inward conformation), the catalytic glutamate (**Glu582**) in the αC-helix forms a salt bridge with the conserved catalytic lysine (**Lys563**). As the catalytic lysine is involved in the transfer of the phosphate group, interaction with this conserved residue contributes to enzyme inhibition.[79]

The C-terminal lobe forms the base of the catalytic pocket and plays a crucial role in catalytic and substrate binding. The catalytic loop and the activation segment are located there. In the active DFG_{in} conformation (Asp-Phe-Gly amino acid sequence in the inward conformation), the catalytic aspartate **Asp675**, which is the starting point of the activation segment, points towards the binding pocket. The conserved APE (Ala-Pro-Glu) motif (^{697}APE^{699}) is located at the end of the activation segment in *Pv*PKG.

The discovery of small molecule ATP-competitive *Plasmodium* PKG inhibitors has revealed the significance of PKG inhibition in the malaria life cycle.[54] Various approaches have been used to study the function of PKG in *Plasmodium,* including chemogenetics, chemoproteomics, and PKG conditional knockout (cKO) and knock-down (cKD) parasite lines.[65] Although *Plasmodium* PKG inhibitors are slow acting, they are highly efficacious *in vitro*.[69, 80] Various *P. falciparum* PKG inhibitors are described below.

The lead compound ML10 (*Pf*PKG IC_{50} = 0.16 nM) was discovered by Baker et al. from an imidazopyridine series (**Figure 1.5**). *Plasmodium* PKG was confirmed to be the target via screening against the gatekeeper mutant line (*Pf*PKG T618Q). [81]

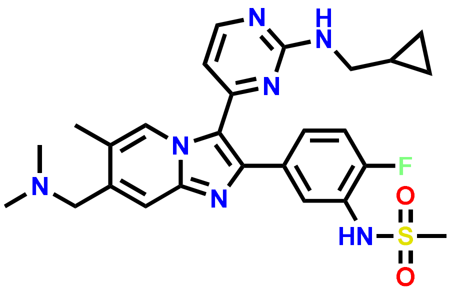

Figure 1.5: ML10, a *Pf*PKG inhibitor with *Pf*PKG IC_{50} = 0.16 nM and *Pf* EC_{50} = 2.1 nM

The crystal structure of *Pv*PKG in complex with ML10 revealed structural insights related to its efficacy (**Figure 1.6**). Firstly, the crucial hinge interaction is formed between the amine of the amino-pyrimidine moiety and the backbone of valine **Val614**. Secondly, **Thr611**, the gatekeeper, is relatively small when compared to most human serine/threonine kinases. This exposes the back pocket, which is occupied by the fluorophenyl of the ligand. This contributes to the selectivity observed over the *Pf*PKG T618Q mutant (*Pf*PKG T618Q IC_{50} = 29.5 µM). Interactions with **Asp675** and **Phe676** of the DFG chain and additional hydrophobic interactions introduced between the cyclopropylmethyl and methyl on the imidazopyridazine core and the kinase domain contribute to enzyme inhibition. Oral administration of this lead compound in a humanized mouse model of *P. falciparum* infection, provided an *in vivo* proof-of-concept of the ability to clear parasites from the blood and block transmission to mosquitos.

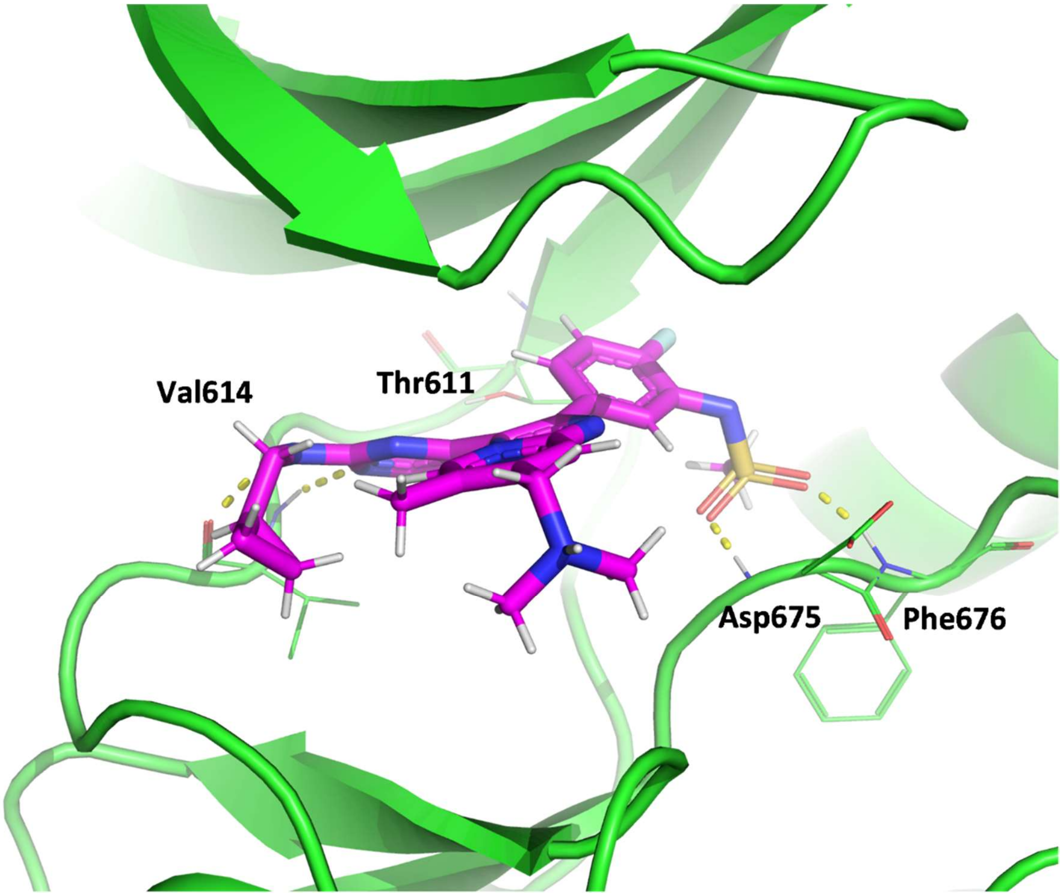

Figure 1.6: *Pv*PKG-ML10 crystal structure complex (PDB ID: **5EZR**) with interacting residues shown.

The efficacy demonstrated by ML10 encouraged Penzo et al. to search for novel classes of PKG inhibitors via high-throughput screening (HTS) of GSK's full diversity collections against recombinant *Pf*PKG.[80] Together with a number of other scaffolds, the trisubstituted thiazole scaffold was identified as a PKG inhibitor chemotype (**Figure 1.7**). Development of the trisubstituted thiazoles yielded analogues with improved kinase selectivity, potency, and ADME (Absorption, Distribution, Metabolism, Excretion) properties.[82]

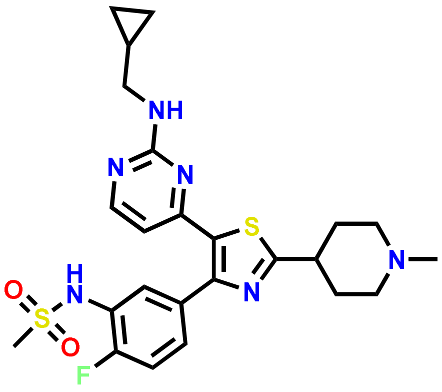

Figure 1.7: Trisubstituted thiazole *Pf*PKG inhibitor with *Pf*PKG IC_{50} = 2 nM and *Pf* EC_{50} = 113 nM

*Pf*PKG was recently identified and validated as the target of MMV030084 (**Figure 1.8**) using chemoproteomic and genetic tools.[70] Similar to ML10, this trisubstituted imidazole demonstrated inhibition of merozoite egress from asexual blood-stage schizonts, hepatocyte invasion by *Plasmodium* sporozoites, and male gamete exflagellation.

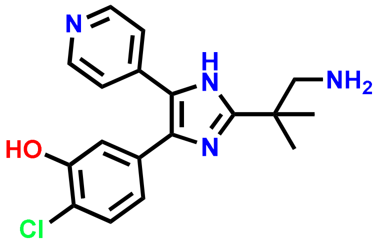

Figure 1.8: MMV030084, a *Pf*PKG inhibitor with *Pf*PKG IC_{50} = 0.4 nM and *Pf* EC_{50} = 120 nM

Resistant selection studies on both ML10 and MMV030084 did not lead to any mutations in PKG. It is nevertheless noteworthy that continuous exposure to MMV030084 yielded a T1268R mutation in tyrosine kinase-like protein 3 (TKL3; PF3D7_1349300), leading to low levels of resistance. In addition to its role in the parasite's survival, *Plasmodium* PKG is a favorable target as its inhibitors demonstrate multistage activity and low propensity to develop resistance.

1.5.2. Phosphatidylinositol-4-kinase (PI4K)

Most aspects of cellular function involve lipid phosphoinositide kinases (PIKs). These play fundamental roles in organelle identity, growth, membrane trafficking, and cell division.[83] The name of lipid PIKs is related to their phosphoinositide product.[84] In 2013, McNamara et al. identified *Plasmodium* PI4KIIIβ as a promising drug target of imidazopyrazine/pyridine analogues.[85] These compounds were of interest due to the transmission-blocking, liver-stage, and asexual blood-stage activities they exhibited in various mouse models. This demonstrates that *Plasmodium* PI4KIIIβ plays an essential role in multiple stages of the parasite's life-cycle, satisfying most TCPs set by MMV. *In vitro* resistant selections were involved in the target identification process. This resulted in mutations in RabIIa and the kinase domain of PI4KIIIβ in drug-resistant *P. falciparum* lines. The small GTPase, RabIIa, has been shown to interact with HuPI4KIIIβ.[86] As part of target confirmation studies, compounds were screened in a biochemical assay against the wild-type *P. vivax* PI4KIIIβ, which identified them as potent ATP-competitive PI4KIIIβ inhibitors. MMV390048 (**Figure 1.9**), the most advanced *Plasmodium* PI4K inhibitor, reached phase II clinical trials[87]. *Plasmodium* PI4KIIIβ has therefore been clinically validated as an antimalarial target.[87, 88] Target identification studies using a combination of resistance selection, chemoproteomic and biochemical assay approaches identified *Plasmodium* PI4K as the primary target of MMV390048. Notably, this enzyme demonstrated a moderate propensity for resistance.[89]

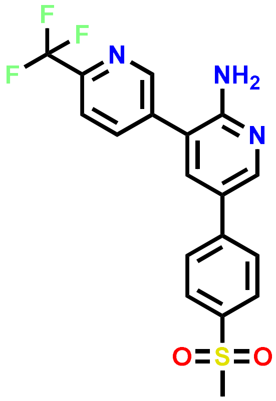

Figure 1.9: MMV390048, a *Plasmodium* PI4K inhibitor with *Pv*PI4K IC_{50} = 3.4 nM and *Pf* EC_{50} = 28 nM

To date, no *Plasmodium* PI4K structure has been elucidated. In this case, a homology model which uses an experimentally validated related structure as a template to build a three-dimensional protein structure, is used.[90] A published *Pf*PI4K homology model developed by Fienberg et al. in 2020, using the Schrodinger software[91], was used to give structural insight into *Plasmodium* PI4K (**Figure 1.10**).[92]

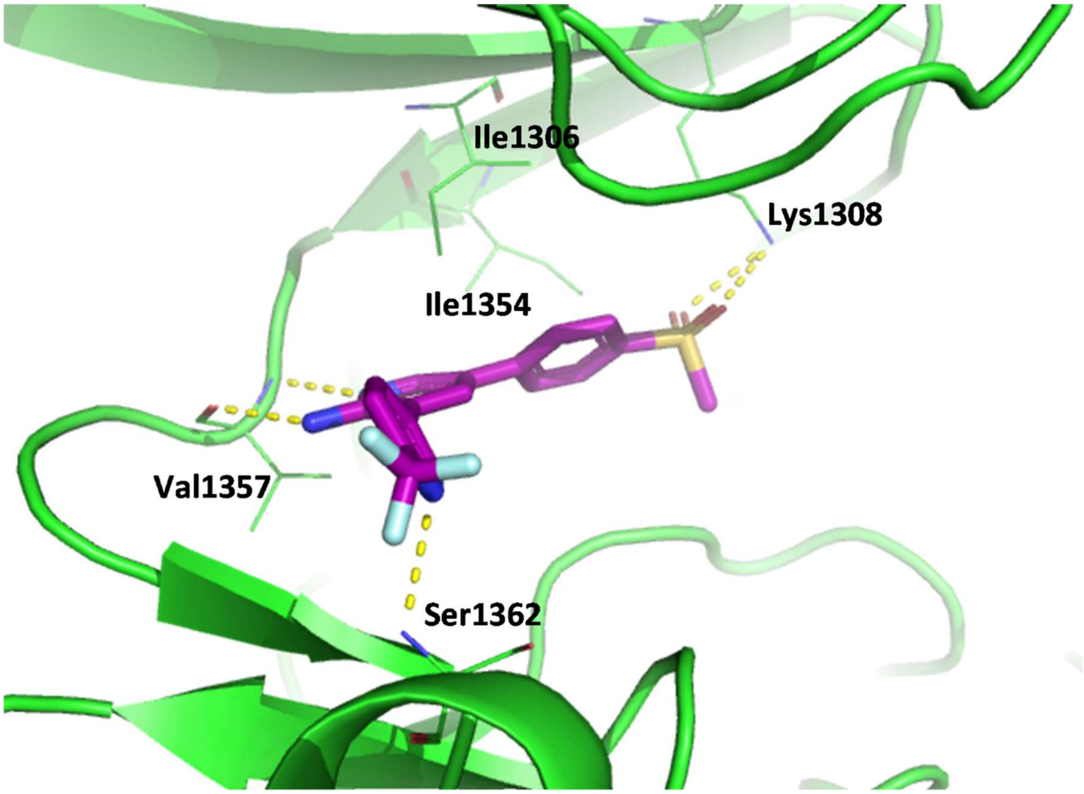

Figure 1.10: Homology model of *Plasmodium falciparum* phosphatidylinositol-4 kinase (*Pf*PI4K) with **MMV390048** bound into the active site. Hinge residue: **Val1357**, gatekeeper residue: **Ile1354** and catalytic lysine: **Lys1308**.

In contrast to the five-stranded β-sheets observed in *Plasmodium* PKG, the N-terminal lobe of *Plasmodium* PI4K is made up of four-stranded β-sheets (β1-β4), due to the lack of stability of one of the β-sheets. Similar to *Plasmodium* PKG and other kinases, the cleft between the C- and N-terminal lobes forms the ATP binding pocket. The conserved valine (**Val1357**) on the hinge loop forms the crucial "donor-acceptor-donor" H-bond interaction with the *Plasmodium* PI4K inhibitor **MMV390048**. In contrast to the small gatekeeper in *Pv*PKG, *Pf*PI4K has a relatively large gatekeeper residue (**Ile1354**). However, the affinity pocket is still accessible to PIKs despite the large gatekeeper residue.[93] The sequence motif of the P-loop in *Pf*PI4K is not conserved in PIKs. The conserved salt bridge interaction with the catalytic lysine (**Lys1308**) is due to the active αC_{in} conformation of the αC-helix.

The alanine residue in the AxK signature sequence is replaced with the larger hydrophobic residue **Ile1306**, which is characteristic of PIKs. The active $\mathrm{DFG_{in}}$ conformation, specifically $^{1430}\mathrm{DYG}^{1432}$ in *Pf*PI4K, is conserved as in PIKs. In place of the APE motif, *Pf*PI4K displays the $^{1432}\mathrm{GFMLT}^{1436}$ motif at the end of the activation segment, which is conserved in PIKs.[94]

1.6. Application of polypharmacology

As *Plasmodium* PI4K and PKG are essential to the parasite's lifecycle and are involved in several pathways, they are good candidates for polypharmacology. Polypharmacology may be defined as the use of one drug effectively inhibiting several targets.[95] The advantages of polypharmacology have been demonstrated by the marketed anticancer drug imatinib, which inhibits several kinases including Brc-Abl tyrosine kinase, the stem cell factor c-kit, and platelet-derived growth factor (PDGF). It is thus used in the treatment of various malignancies.[96]

Polypharmacology also makes use of synergistic effects as a drug may inhibit targets involved in the same signaling pathway. Another advantage of polypharmacology that is relevant to antimalarials is the low probability of resistance development. As seen in the previous section, current marketed antimalarials are plagued by resistance. This is because the probability of two independent targets spontaneously generating resistance mutations is quite low.[97]

As malaria primarily affects poverty-stricken parts of the world, the use of polypharmacology may reduce the cost and pill burden. Usually, the inhibition of several targets requires the administration of several pills, which is associated with high production costs. However, when one compound is used to inhibit several targets, only one pill is needed, thus greatly reducing production costs.

1.7. Computer-aided drug design (CADD)

Historically, phenotypic screening was the major approach used in antimalarial drug discovery.[98, 99] One of the challenges of this approach is the lack of information about the compound's mechanism of action (MoA), which may lead to selectivity issues. In an effort to circumnavigate these issues, knowledge of the compound's biological target can be exploited during the optimization process to reduce off-target effects. In target-based drug discovery, the hit identification process is often triggered after validation of the target (**Figure 1.11**).

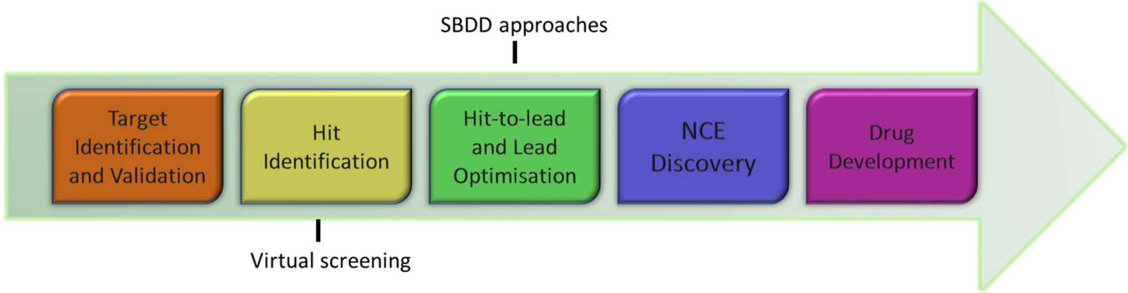

Figure 1.11: Drug discovery process. SBDD, structure-based drug discovery; NCE, new chemical entity

At the hit identification stage, drug discovery programs rely heavily on *in vitro* assay technologies, such as DNA-encoded libraries (DEL), fragment-based screening (FBS), and HTS. Historically, most drug candidates were identified via HTS.[100]

The major limitation of HTS is that it can only be carried out on compounds that exist in a particular collection. Additionally, hits produced after an HTS campaign always require exhaustive counter-screening to sieve out non-specific binders and false positives.[101-104] It is therefore becoming increasingly popular to reinforce traditional hit identification methods with virtual screening techniques. One can search enormous compound databases computationally to prioritize a subgroup of compounds for *in vitro* screening assays based on structural complementarity to the target active site, or on biological and chemical similarities with known active compounds.[105, 106] With pharmacophore-based searching algorithms and high-throughput Docking (HTD) gaining traction, these are now the main source of hit molecules.[107]

HTD is a structure-based method used to virtually screen a large dataset of compounds against a certain target. The credibility of this method has increased thanks to the volume of structural information provided by the PDB, and it is now one of the main sources of drug discovery starting points.[108-110] A complementary approach to HTD is the use of pharmacophore search algorithms. This computationally efficient method is used when there is no 3D structural information available for the target. A ligand with known activity is used to create a pharmacophore, whose favorable chemical features are then used to screen the dataset.

Due to the increased time and cost associated with HTS, virtual screening is used to reduce budget and time constraints. One of the advantages of incorporating virtual screening in the hit identification process is that a relatively small number of compounds is taken forward for experimental testing (medium- or low-throughput screening, rather than HTS). Another advantage is the possibility of performing proteomic and/or genetic studies, which can be used to elucidate a growing number of drug targets used in assays.[111, 112]

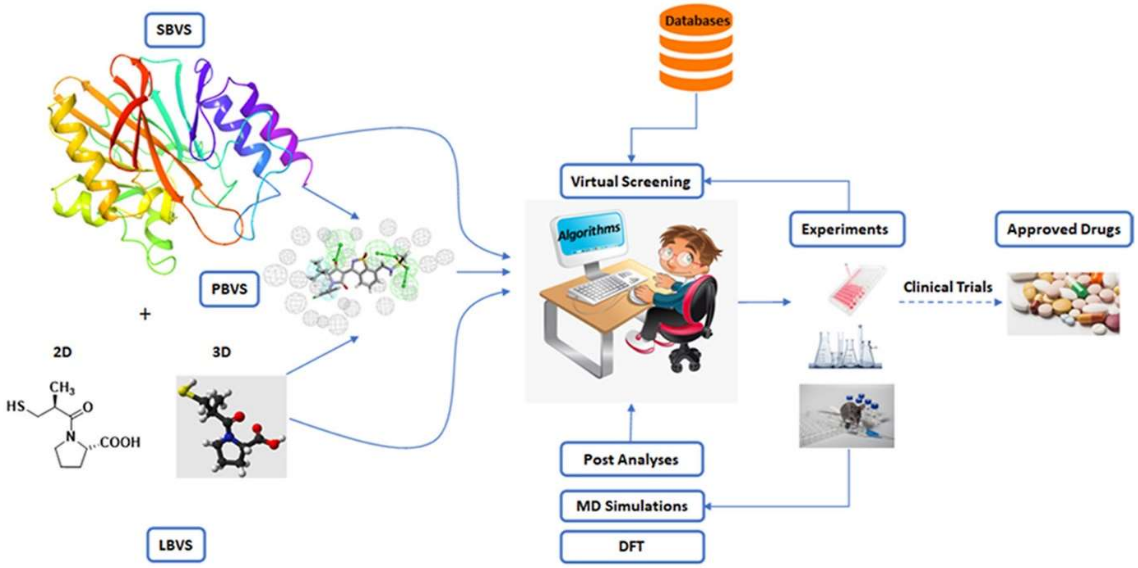

Figure 1.12: Illustration of Computer-Aided Drug Discover (CADD).[113] **SBVS**: Structure-based virtual screening; **PBVS**: Pharmacophore-based virtual screening; **LBVS**: Ligand-based virtual screening.

Using the structure of the known target, an active ligand or pharmacophore mapping as a starting point; molecules are designed or filtered *in silico* reducing the burden of time. This is then followed by various *in vitro* and *in vivo* experiments that bring the molecule closer to the market (**Figure 1.12**).[113]

Therefore, rational drug discovery approaches can be used to computationally visualize the target-compound interaction and optimize target inhibition. Much of the success of anticancer kinase inhibitors is attributed to the use of CADD.[114]

CADD can be carried out in two ways: ligand-based drug design (LBDD) or structural-based drug design (SBDD). The SBDD approach is based on structural information gathered about the biological target. This includes methods such as structure-based virtual screening (SBVS), molecular docking, and molecular dynamics. Contrastingly, the LBDD approach is carried out in the absence of structural information relating to the biological target and involves methods such as quantitative structure-activity relationship (QSAR) modeling, ligand-based virtual screening (LBVS), pharmacophore generation, and similarity searching.[115] The SBDD approach was used in this project because of the availability of structural information for the kinases of interest.

A ligand's most probable orientation towards a macromolecule can be predicted using molecular docking.[116] Ligand-protein docking involves the use of scoring functions to calculate which conformation is best placed into the target's binding site, from a sample of conformations.[117, 118] A scoring function preceded by a search algorithm is included in a typical molecular docking protocol.[119] There are deterministic, stochastic, and systematic search algorithms.[120] In stochastic search algorithms, random changes are made in the search space and the user defines the criteria for the termination of changes. In systematic search algorithms, the search space is sampled at different intervals[121] while deterministic search algorithms depend on parameter values.[122]

The scoring function that follows assesses the interactions formed to eventually estimate the affinity of the small molecule to the biological target.[109] Scoring functions may be empirical, machine-learning based, physics-based, or knowledge-based.[123, 124] By accumulating energetic factors for protein-ligand binding (hydrophobic effects, hydrogen bonds, etc.), the complex's binding affinity is estimated by the empirical scoring function.[125] Use of the machine learning-based scoring function is gaining traction as it combines the evaluation of protein-ligand interaction and QSAR analysis. Here, certain descriptors (hydrogen bonds, molecular weight, surface properties, etc.) are used to encode structural protein-ligand interaction fingerprints with machine-learning algorithms ran for selection.[126, 127] In addition to the enthalpy and torsion entropy of the ligand, explicit and implicit solvent models describe the solvation/desolvation effect, which are computed to calculate the free energy of binding done by the physics-based scoring function.[128] The effects and movements of the solute molecules are considered within a given region around the solute molecules for an explicit solvent model whereas solvents are treated as a continuous medium surrounding the solutes for implicit solvent models.[129, 130] Entropic and solvent effects may be treated implicitly using Helmholtz free energies.[124, 131]

To investigate the time-dependent evolution of a molecular system, a molecular dynamic simulation is carried out. These simulations rely on classical mechanics where Newtonian laws of motion are used to compute the velocities and positions of atoms.[132] Using the potential energy functions, force fields represent the computed forces acting on the atoms. Non-bonded terms (Coulomb electrostatics and Lennard-Jones repulsion and dispersion) and bonded terms (torsion potential, covalent bond-stretching, improper torsions, and angle-bending) are expressed in common force fields.[133] There are various force fields used, including AMBER,[134, 135] COMPASS,[136] GROMOS,[137] CHARMM,[138] and OPLS.[139] In recent years, GROMOS, OPLS and AMBER account for relatively 90% of published articles.[113, 140]The variation between these force fields are in the treatment of solvent models.[141] The most preferred to use when comparing with NMR data are GROMOS, CHARMM and OPLS as they do not exaggerate the helical region.[142] One of the cons of these force fields is that for prolonged simulations (for example >100 ns), they risk non-native conformational states.[143]

Recent methodological advances in high-throughput nuclear magnetic resonance (NMR) spectroscopy and X-ray crystallographic approaches have been leveraged by several structural genomic initiatives, causing an explosion of structural information.[144, 145] Provided structural information of the therapeutic target is available, phenotypic HTS may be complemented by SBDD approaches.[146] Furthermore, subtle alterations within the functional group of the drug-like ligand may be accompanied by complex structure-function consequences. The ligand can be modified *in silico* to achieve an enhanced theoretical fit between the complementary molecular volumes and defined binding sites, using sophisticated molecular modeling software.[147]

Notably, SBDD is an iterative approach that involves cycles of optimization and subsequent design with the goal of identifying a modulator of the therapeutic target. Structure-based virtual screening asses a library of compounds against a known target and thereafter molecules can be designed and evaluated through further docking, scoring, and ranking initial hits based on their electrostatic and static interactions with the target site.[122, 148] Optimization of lead molecules is then carried out to improve potency and reduce toxicity. Although this is a highly iterative approach, *in silico* design and optimization cycles significantly reduce the time required for lead optimization meriting pre-clinical evaluation.[149]

SBDD has played major roles in the discovery of several marketed drugs. However, the anticancer drug pazopanib is used here as an example to briefly describe the role of SBDD. Harris et al. combined homology modeling and various SBDD methods to develop this drug.[150, 151] The binding modes of dimethoxyquinazoline analogues were predicted using the Vascular Endothelial Growth Factor Receptor 2 (VEGFR2) homology model. The *in silico* results were later confirmed through crystallization of the complexes. This resulted in further optimization and eventually led to the marketing of this drug.

The SBDD technique was also used to stifle the progress of human immunodeficiency virus (HIV)/acquired immunodeficiency syndrome (AIDS), another major epidemic, with over 30 anti-HIV compounds developed within 30 years of discovering the disease, as described in the next section.[152-164]

1.8. Role of CADD in AIDS Drug Discovery

Shifting the focus to another major epidemic wreaking havoc in the WHO African region, with over 460,000 deaths in 2020, the treatment of AIDS has greatly evolved.[165] There have been just over 30 anti-HIV compounds within the over 30 years of the discovery of the disease.[166]

Some of these compounds were discovered through the integration of a SBDD approach.[167] The two variants of the Human Immunodeficiency Virus (HIV) that cause this disease are HIV-1 and HIV-2.

The HIV-1 complete nucleotide sequence shows a relatively simple retrovirus. This genome consists of *pol*, *gag* and *env* as three Open Reading Frames (ORF).[152] The *pol* ORF contains the only unique enzymes: protease (PR), integrase and reverse transcriptase (RT). The mentioned enzymes have all become therapeutic targets for the HIV drug discovery. Specifically, the retroviral protease was earlier discovered as a potential target and its respective inhibitors were then designed and developed.[153, 168] This exemplified the relevance of SBDD.

There is significant similarity between the aspartic proteases and HIV-1 PR.[154] Through either chemical inhibition or mutation, inactivation of HIV-1 PR leads to the production of non-infectious and immature viral particles.[168, 169] This eventually led to the validation of the target as it is essential for proper maturation and virion assembly. The crystal structures of HIV-1 PR were readily available playing a crucial role in the rapid progress in the drug development where six inhibitors of this enzyme were approved between 1995 and 2001.[155, 156, 170]

1.8.1. Saquinavir

Initiated by the transition-state mimics with peptide derivatives, Hoffmann-La Roche designed Saquinavir using a rational drug design approach.[158] The observation that the HIV-1 PR cleaves sequences with dipeptides Phe-Pro or Typ-Pro was the criterion used. This enzyme suggested high selectivity as mammalian proteases do not cleave peptide sequences followed by a Proline. Crystallographic studies of the HIV-1 PR in complex with a peptidic inhibitor, Ro 31-8558 revealed the binding mode and future modification suggestions. (**Figure 1.13**)

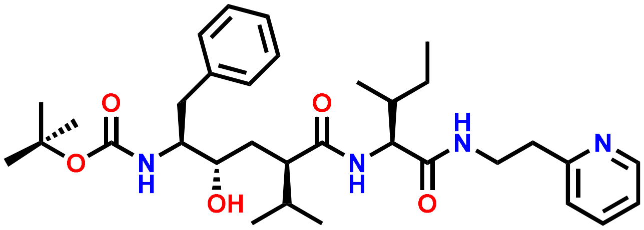

Figure 1.13: Structure of HIV-1 PR peptidic inhibitor, Ro 31-8588

Suitable structure-based optimisation by using (S,S,S)-decahydro-isoquinoline-3-carbonyl (DIQ) as a replacement led to the discovery of Ro 31-8959 (Saquinavir). (**Figure 1.14**)

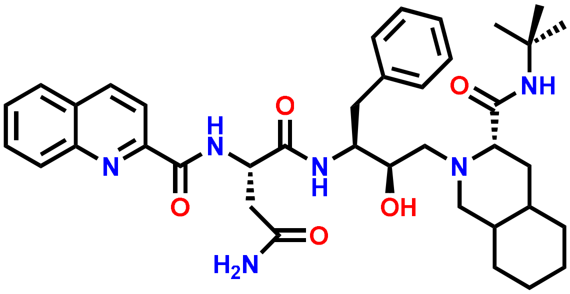

Figure 1.14: Structure of FDA-approved anti-HIV drug, Saquinavir (Ro 31-8959)

With a $K_i < 0.1$ nM against HIV-2 PR and a corresponding K_i of 0.12 nM against HIV-1 PR, crystallographic studies were conducted in Saquinavir complexes.[158] A water molecule (Wat301) connects the ligand with the flap regions through maintaining a hydrogen bond with the carbonyl of the DIQ moiety (**Figure 1.15**).[159]

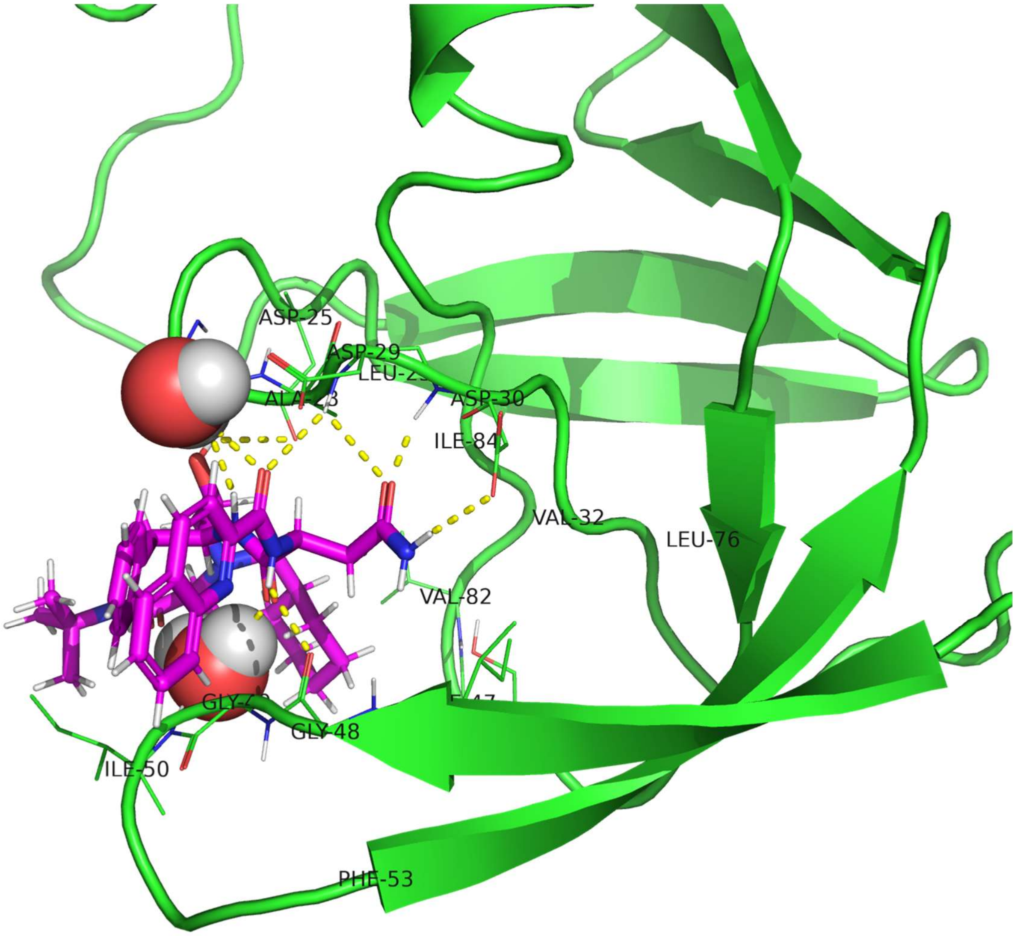

Figure 1.15: Crystal structure of wild-type HIV-1 Protease in complex with the antiviral drug, Saquinavir. (PDB Code: **3OXC**)[171]

Saquinavir also exhibited high selectivity with only minor human aspartic proteases inhibition. Therefore, Saquinavir was approved by the FDA in 1995 as the first protease inhibitor.

1.8.2. Nelfinavir

Currently part of the Pfizer, Agouron was established to specifically discover drugs using a rational design approach. Instead of normal peptide bonds, statine isosteres were the central parts of two Agouron hit compounds, AG-1002 and AG-1004 (**Figure 1.16**).[160, 172]

A

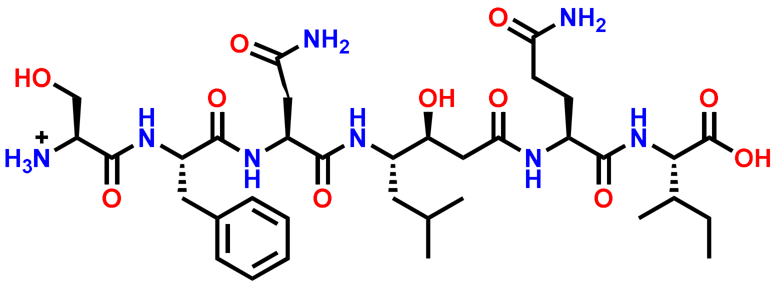

B

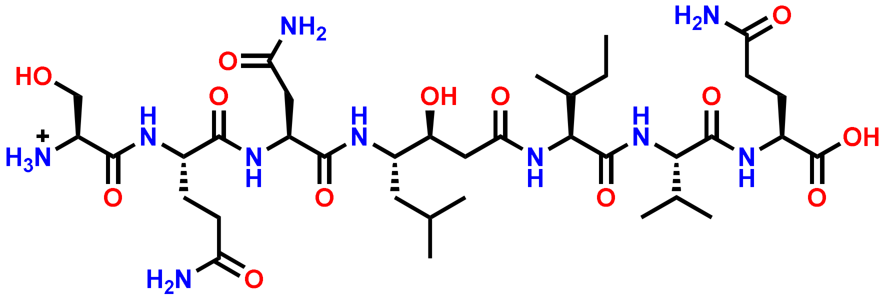

Figure 1.16: Structure of Agouron hit compounds, AG-1002 (**A**) and AG-1004 (**B**)

Iterative analysis of protein complexes with peptidic inhibitors and consequent replacement of some parts with nonpeptidic substituents, played an invaluable role in the design of nonpeptidic inhibitors.[161] Similar to Saquinavir, Nelfinavir contains the same DIQ in its carbonyl terminus, in addition to the novel 2-methyl-3hydroxybenzamide group (**Figure 1.17**). The co-crystal structure of HIV-1 PR and Nelfinavir revealed the binding mode (**Figure 1.18**).[162]

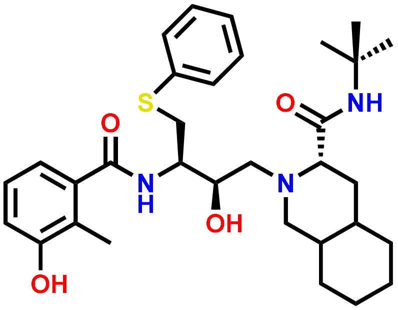

Figure 1.17: Structure of FDA-approved anti-HIV drug, Nelfinavir (Viracept, Ag-1343)

The increase of potency by an order of magnitude is attributed to the S-phenyl group in the P1 subsite.

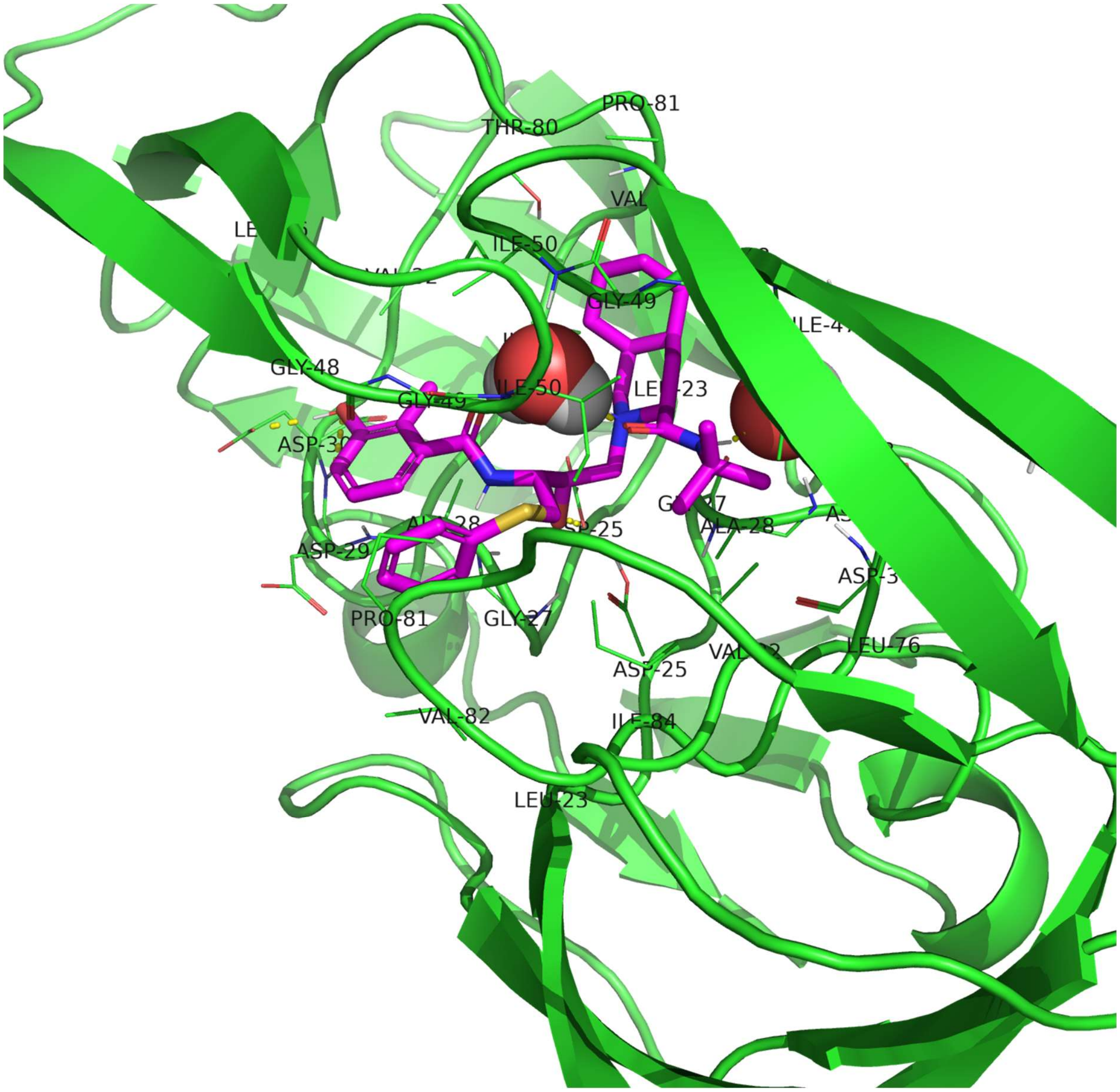

Figure 1.18: Crystal structure of wild-type HIV-1 Protease in complex with the antiviral drug, Nelfinavir. (PDB Code: **3EKX**)[173]

In 1997, Nelfinavir received FDA-approval and became the first inhibitor to be indicated for paediatric AIDS.

1.8.3. Kaletra

Developed at Abbott in the late 2000s, Kaletra became the first second-generation protease inhibitor to be FDA-approved. Kaletra consists of two protease inhibitors: novel protease inhibitor lopinavir (ABT-378) (133mg) and ritonavir (33mg). (**Figure 1.19**)

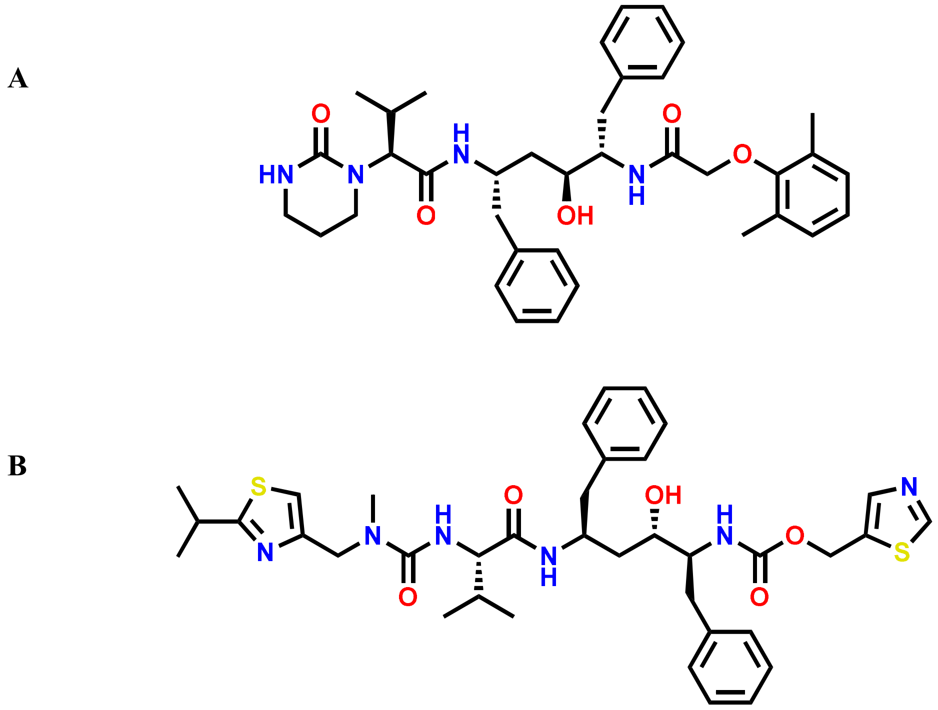

Figure 1.19: Structure of the components of the FDA-approved anti-HIV drug, Kaletra: Lopinavir (**A**) and Ritonavir (**B**)

In the drug-resistant strains of the virus, the Val82 residue is often mutated. Hence, lopinavir was designed to reduce interactions with the mentioned residue (**Figure 1.20**).[163]

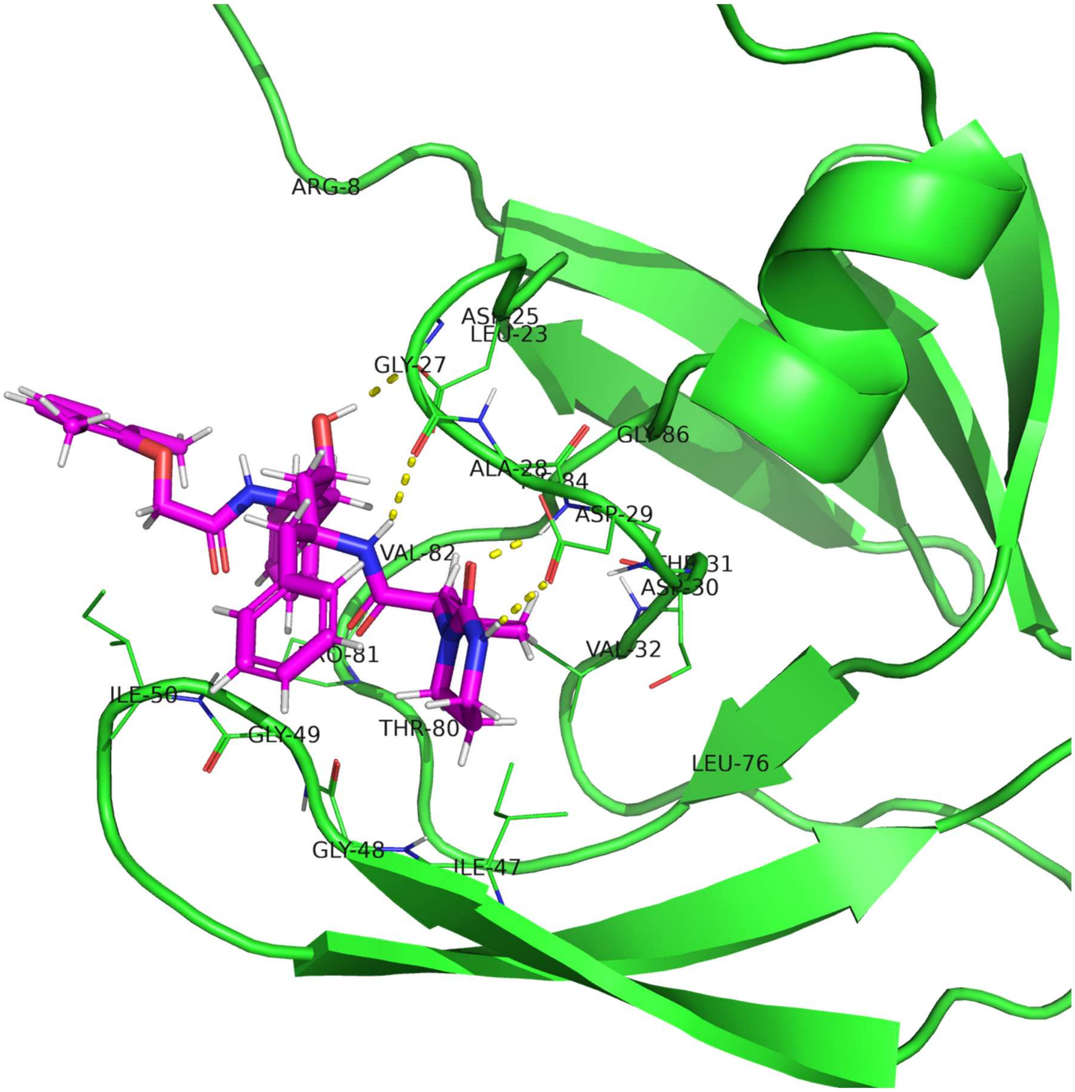

Figure 1.20: Crystal structure of wild-type HIV-1 Protease in complex with the antiviral drug, Nelfinavir. (PDB Code: **1MUI**)[174]

Lopinavir and Ritonavir have a similar core. However, the phenoxyacetyl group in Lopinavir replaced the 5-thiazolyl end group in Ritonavir. Additionally, a modified valine with a six-membered cyclic urea attached to the amino terminus in Lopinavir replaced the 2-isopropylthiazolyl group in Ritonavir. The therapeutic and chemical properties were then investigated.[175, 176]

Relatively high potency ($K_i = 1.3$ pM) was exhibited by Lopinavir against both wild-type and mutant strains of HIV-1 PR. Administered alone, the concentration of Lopinavir in plasma decreased at a rapid rate and even faster in humans. Administering Lopinavir together with Ritonavir in subclinical amounts was investigated. It was discovered that after a single 400mg dose, the concentration of Lopinavir exceeding its EC_{50} was maintained for over 24 hours. Currently, Kaletra is only administered after the failure of the primary therapy of protease inhibitors.

1.9. Libraries available for Kinase Drug Discovery

As shown in **Figure 1.12**, databases are also involved in the virtual screening campaign. Due to the conserved nature of the ATP binding site, a library of kinase inhibitors is an appropriate starting point in the design of novel *Plasmodium* kinase inhibitors.[177] An example of a set of kinase inhibitors is the GSK Published Kinase Inhibitor Set (PKIS) which is a library of 367 compounds that have displayed activity against the protein kinase family.[178, 179] This library is an open source tool and hence widely distributed across various academic research groups.

Another example of a target-focused library of compounds is the Soft-Focus Kinase (SFK) library. This project, initiated by the BioFocus group in 1999, involved the design and commercial production of kinase inhibitors.[180] Notably, through the exploitation of this set was the first clinically-validated *Pf*PI4K inhibitor (MMV390048) discovered.[181]

The Medicine for Malaria Venture (MMV) have also developed four compound libraries that may be used for virtual screening. Unlike the previously mentioned libraries, these sets of compounds are not target-focused.[182] The launched boxes include the Malaria Box[183, 184], the Pathogen Box[185], the Pandemic Response Box (PRB)[186] and the most recent, the COVID box[187]. Apart from the COVID box which has 160 compounds, the remaining compound libraries each have 400 compounds. The PRB was used in this project for hit identification studies using virtual screening techniques. The PRB is a set of 400 structurally diverse compounds and comprises 201 antibacterial, 153 antiviral, and 46 antifungal compounds. There are also a number of kinase inhibitors in the PRB.

1.10. Research question, aims, and objectives

1.10.1. Research question

The aim of this research project was to determine whether computer-aided drug design (CADD) could constructively inform the design and accelerate the identification of selective inhibitors of *Pf*PI4K and *Pf*PKG.

1.10.2. Objective

The main objective of this project was to design and identify *P. falciparum* kinase inhibitors using CADD with supportive *in vitro* experimental validation. It was also aimed at identifying design strategies to reduce human kinase inhibition.

1.10.3. Specific aims

- To design and synthesize novel pyrazolo[3,4-d]pyrimidine (MLN0128) analogues, which are potent dual *Pf*PI4K/*Pf*PKG inhibitors and show reduced activity against human kinases (**Chapter II**)
- To accelerate the identification of potent imidazopyridazine (SFK52)-based *Pf*PKG inhibitors, which also retain*Pf*PI4K inhibition (**Chapter III**)
- To virtually screen the pandemic response box (PRB) to identify chemotypes with dual *Pf*PI4K/*Pf*PKG inhibition (**Chapter IV**).

1.11 References

1. Organization, W. H. *World Malaria Report 2019*; Geneva, 2019; p 232.

2. Kimura, M.; Kaneko, O.; Liu, Q.; Zhou, M.; Kawamoto, F.; Wataya, Y.; Otani, S.; Yamaguchi, Y.; Tanabe, K., Identification of the four species of human malaria parasites by nested PCR that targets variant sequences in the small subunit rRNA gene. *Parasitol. Int.* **1997,** *46* (2), 91-95.

3. White, N. J., Determinants of relapse periodicity in Plasmodium vivax malaria. *Malar. J.* **2011,** *10* (1), 1-36.

4. Hall, N.; Karras, M.; Raine, J. D.; Carlton, J. M.; Kooij, T. W.; Berriman, M.; Florens, L.; Janssen, C. S.; Pain, A.; Christophides, G. K., A comprehensive survey of the Plasmodium life cycle by genomic, transcriptomic, and proteomic analyses. *Science* **2005,** *307* (5706), 82-86.

5. Hill, A. V., Vaccines against malaria. *Philos. Trans. R. Soc., B* **2011,** *366* (1579), 2806-2814.

6. Woodland, J. G.; Chibale, K., Quinine fever. *Nat. Chem.* **2022,** *14* (1), 112-112.

7. Dziekan, J. M.; Yu, H.; Chen, D.; Dai, L.; Wirjanata, G.; Larsson, A.; Prabhu, N.; Sobota, R. M.; Bozdech, Z.; Nordlund, P., Identifying purine nucleoside phosphorylase as the target of quinine using cellular thermal shift assay. *Sci. Transl. Med.* **2019,** *11* (473), eaau3174.

8. Achan, J.; Talisuna, A. O.; Erhart, A.; Yeka, A.; Tibenderana, J. K.; Baliraine, F. N.; Rosenthal, P. J.; D'Alessandro, U., Quinine, an old anti-malarial drug in a modern world: role in the treatment of malaria. *Malar. J.* **2011,** *10* (1), 1-12.

9. Coatney, G. R., Pitfalls in a discovery: the chronicle of chloroquine. *Am J Trop Med Hyg* **1963,** *12* (2), 121-128.

10. Hahn, F. E., Chloroquine (resochin). In *Mechanism of Action of Antimicrobial and Antitumor Agents*, Springer: 1975; pp 58-78.

11. Slater, A.; Cerami, A., Inhibition by chloroquine of a novel haem polymerase enzyme activity in malaria trophozoites. *Nature* **1992,** *355* (6356), 167-169.

12. Chou, A. C.; Fitch, C. D., Heme polymerase: modulation by chloroquine treatment of a rodent malaria. *Life Sci.* **1992,** *51* (26), 2073-2078.

13. Fogh, S.; Jepsen, S.; Effersøe, P., Chloroquine-resistant Plasmodium falciparum malaria in Kenya. *Trans. R. Soc. Trop. Med. Hyg.* **1979,** *73* (2), 228-229.

14. Harinasuta, T.; Suntharasamai, P.; Viravan, C., Chloroquine-resistant falciparum malaria in Thailand. *Lancet* **1965**, 657-60.

15. Schuurkamp, G. J.; Spicer, P. E.; Kereu, R. K.; Bulungol, P. K.; Rieckmann, K. H., Chloroquine-resistant Plasmodium vivax in Papua New Guinea. *Trans. R. Soc. Trop. Med. Hyg.* **1992,** *86* (2), 121-122.

16. Comer, R. D.; Young, M. D.; Porter Jr, J. A.; Gauld, J. R.; Merritt, W., Chloroquine resistance in Plasmodium falciparum malaria on the Pacific coast of Colombia. *Am J Trop Med Hyg* **1968,** *17* (6), 795-799.

17. Trape, J.-F., The public health impact of chloroquine resistance in Africa. *Am J Trop Med Hyg* **2001,** *64* (1_suppl), 12-17.

18. Ecker, A.; Lehane, A. M.; Clain, J.; Fidock, D. A., PfCRT and its role in antimalarial drug resistance. *Trends Parasitol.* **2012,** *28* (11), 504-514.

19. Crowther, A.; Levi, A., Proguanil—the isolation of a metabolite with high antimalarial activity. *Br. J. Pharmacol. Chemother.* **1953,** *8* (1), 93.

20. Srivastava, I. K.; Vaidya, A. B., A mechanism for the synergistic antimalarial action of atovaquone and proguanil. *Antimicrob. Agents Chemother.* **1999,** *43* (6), 1334-1339.

21. McKeage, K.; Scott, L. J., Atovaquone/proguanil. *Drugs* **2003,** *63* (6), 597-623.

22. Cowman, A. F.; Morry, M. J.; Biggs, B. A.; Cross, G.; Foote, S. J., Amino acid changes linked to pyrimethamine resistance in the dihydrofolate reductase-thymidylate synthase gene of Plasmodium falciparum. *Proc. Natl. Acad. Sci.* **1988,** *85* (23), 9109-9113.

23. Young, M. D.; Burgess, R. W., Pyrimethamine resistance in Plasmodium vivax malaria. *Bull. W. H. O.* **1959,** *20* (1), 27.

24. Matondo, S. I.; Temba, G. S.; Kavishe, A. A.; Kauki, J. S.; Kalinga, A.; van Zwetselaar, M.; Reyburn, H.; Kavishe, R. A., High levels of sulphadoxine-pyrimethamine resistance Pfdhfr-Pfdhps quintuple mutations: a cross sectional survey of six regions in Tanzania. *Malar. J.* **2014,** *13* (1), 1-7.

25. Koukouikila-Koussounda, F.; Bakoua, D.; Fesser, A.; Nkombo, M.; Vouvoungui, C.; Ntoumi, F., High prevalence of sulphadoxine–pyrimethamine resistance-associated mutations in Plasmodium falciparum field isolates from pregnant women in Brazzaville, Republic of Congo. *Infect., Genet. Evol.* **2015,** *33*, 32-36.

26. Wong, W.; Bai, X.-C.; Sleebs, B. E.; Triglia, T.; Brown, A.; Thompson, J. K.; Jackson, K. E.; Hanssen, E.; Marapana, D. S.; Fernandez, I. S., Mefloquine targets the Plasmodium falciparum 80S ribosome to inhibit protein synthesis. *Nat. Microbiol.* **2017,** *2* (6), 1-9.

27. Palmer, K. J.; Holliday, S. M.; Brogden, R. N., Mefloquine. *Drugs* **1993,** *45* (3), 430-475.

28. Karbwang, J.; White, N. J., Clinical pharmacokinetics of mefloquine. *Clin. Pharmacokinet.* **1990,** *19* (4), 264-279.

29. Mockenhaupt, F., Mefloquine resistance in Plasmodium falciparum. *Parasitol. Today* **1995,** *11* (7), 248-253.

30. Miller, L. H.; Su, X., Artemisinin: discovery from the Chinese herbal garden. *Cell* **2011,** *146* (6), 855-858.

31. White, N. J.; Hien, T. T.; Nosten, F. H., A brief history of Qinghaosu. *Trends Parasitol.* **2015,** *31* (12), 607-610.

32. Chotivanich, K.; Udomsangpetch, R.; Dondorp, A.; Williams, T.; Angus, B.; Simpson, J.; Pukrittayakamee, S.; Looareesuwan, S.; Newbold, C.; White, N., The mechanisms of parasite clearance after antimalarial treatment of Plasmodium falciparum malaria. *J. Infect. Dis.* **2000,** *182* (2), 629-633.

33. Terkuile, F.; White, N.; Holloway, P.; Pasvol, G.; Krishna, S., Plasmodium falciparum: in vitro studies of the pharmacodynamic properties of drugs used for the treatment of severe malaria. *Exp. Parasitol.* **1993,** *76* (1), 85-95.

34. Skinner, T. S.; Manning, L. S.; Johnston, W. A.; Davis, T. M., In vitro stage-specific sensitivity of Plasmodium falciparum to quinine and artemisinin drugs. *Int. J. Parasitol.* **1996,** *26* (5), 519-525.

35. Bridgford, J. L.; Xie, S. C.; Cobbold, S. A.; Pasaje, C. F. A.; Herrmann, S.; Yang, T.; Gillett, D. L.; Dick, L. R.; Ralph, S. A.; Dogovski, C., Artemisinin kills malaria parasites by damaging proteins and inhibiting the proteasome. *Nat. Commun.* **2018,** *9* (1), 1-9.

36. Price, R. N., Artemisinin drugs: novel antimalarial agents. *Expert Opin. Invest. Drugs* **2000,** *9* (8), 1815-1827.

37. Olliaro, P.; Taylor, W., Developing artemisinin based drug combinations for the treatment of drug resistant falciparum malaria: A review. *J. Postgrad. Med.* **2004,** *50* (1), 40.

38. Sinclair, D.; Zani, B.; Donegan, S.; Olliaro, P.; Garner, P., Artemisinin-based combination therapy for treating uncomplicated malaria. *Cochrane Database Syst. Rev.* **2009,** (3).

39. White, N. J., Antimalarial drug resistance. *J. Clin. Investig.* **2004,** *113* (8), 1084-1092.

40. Ouji, M.; Augereau, J.-M.; Paloque, L.; Benoit-Vical, F., Plasmodium falciparum resistance to artemisinin-based combination therapies: A sword of Damocles in the path toward malaria elimination. *Parasite* **2018,** *25*.

41. Uwimana, A.; Legrand, E.; Stokes, B. H.; Ndikumana, J.-L. M.; Warsame, M.; Umulisa, N.; Ngamije, D.; Munyaneza, T.; Mazarati, J.-B.; Munguti, K., Emergence and clonal expansion of in vitro artemisinin-resistant Plasmodium falciparum kelch13 R561H mutant parasites in Rwanda. *Nat. Med.* **2020,** *26* (10), 1602-1608.

42. Burrows, J. N.; Duparc, S.; Gutteridge, W. E.; van Huijsduijnen, R. H.; Kaszubska, W.; Macintyre, F.; Mazzuri, S.; Möhrle, J. J.; Wells, T. N., New developments in anti-malarial target candidate and product profiles. *Malar. J.* **2017,** *16* (1), 26.

43. Moehrle, J. J., Development of New Strategies for Malaria Chemoprophylaxis: From Monoclonal Antibodies to Long-Acting Injectable Drugs. *Trop Med Infect Dis* **2022,** *7* (4), 58.

44. Bakheet, T. M.; Doig, A. J., Properties and identification of human protein drug targets. *Bioinformatics* **2009,** *25* (4), 451-457.

45. Duong-Ly, K. C.; Peterson, J. R., The human kinome and kinase inhibition. *Curr. Protoc. Pharmacol.* **2013,** *60* (1), 2.9. 1-2.9. 14.

46. Cohen, P., The origins of protein phosphorylation. *Nat. Cell Biol.* **2002,** *4* (5), E127-E130.

47. Sridhar, R.; Hanson-Painton, O.; Cooper, D. R., Protein kinases as therapeutic targets. *Pharm. Res.* **2000,** *17* (11), 1345-1353.

48. Cohen, P.; Cross, D.; Jänne, P. A., Kinase drug discovery 20 years after imatinib: progress and future directions. *Nat. Rev. Drug Discovery* **2021**, 1-19.

49. Bournez, C.; Carles, F.; Peyrat, G.; Aci-Sèche, S.; Bourg, S.; Meyer, C.; Bonnet, P., Comparative assessment of protein kinase inhibitors in public databases and in PKIDB. *Mol.* **2020,** *25* (14), 3226.

50. Doerig, C.; Billker, O.; Haystead, T.; Sharma, P.; Tobin, A. B.; Waters, N. C., Protein kinases of malaria parasites: an update. *Trends Parasitol.* **2008,** *24* (12), 570-577.

51. Leroy, D.; Doerig, C., Drugging the Plasmodium kinome: The benefits of academia–industry synergy. *Trends Pharmacol. Sci.* **2008,** *29* (5), 241-249.

52. Solyakov, L.; Halbert, J.; Alam, M. M.; Semblat, J.-P.; Dorin-Semblat, D.; Reininger, L.; Bottrill, A. R.; Mistry, S.; Abdi, A.; Fennell, C., Global kinomic and phospho-proteomic analyses of the human malaria parasite Plasmodium falciparum. *Nat. Commun.* **2011,** *2* (1), 1-12.

53. Tewari, R.; Straschil, U.; Bateman, A.; Böhme, U.; Cherevach, I.; Gong, P.; Pain, A.; Billker, O., The systematic functional analysis of Plasmodium protein kinases identifies essential regulators of mosquito transmission. *Cell host & microbe* **2010,** *8* (4), 377-387.

54. Baker, D. A.; Matralis, A. N.; Osborne, S. A.; Large, J. M.; Penzo, M., Targeting the malaria parasite cGMP-dependent protein kinase to develop new drugs. *Front. Microbiol.* **2020,** *11*, 602803.

55. Gardner, M. J.; Hall, N.; Fung, E.; White, O.; Berriman, M.; Hyman, R. W.; Carlton, J. M.; Pain, A.; Nelson, K. E.; Bowman, S., Genome sequence of the human malaria parasite Plasmodium falciparum. *Nature* **2002,** *419* (6906), 498-511.

56. Aurrecoechea, C.; Brestelli, J.; Brunk, B. P.; Dommer, J.; Fischer, S.; Gajria, B.; Gao, X.; Gingle, A.; Grant, G.; Harb, O. S., PlasmoDB: a functional genomic database for malaria parasites. *Nucleic Acids Res.* **2009,** *37* (suppl_1), D539-D543.

57. Srinivasan, N.; Krupa, A., A genomic perspective of protein kinases in Plasmodium falciparum. *Proteins: Struct., Funct., Bioinf.* **2005,** *58* (1), 180-189.

58. Ward, P.; Equinet, L.; Packer, J.; Doerig, C., Protein kinases of the human malaria parasite Plasmodium falciparum: the kinome of a divergent eukaryote. *BMC genomics* **2004,** *5* (1), 1-19.

59. Lucet, I. S.; Tobin, A.; Drewry, D.; Wilks, A. F.; Doerig, C., Plasmodium kinases as targets for new-generation antimalarials. *Future Med. Chem.* **2012,** *4* (18), 2295-2310.

60. Urich, R.; Wishart, G.; Kiczun, M.; Richters, A.; Tidten-Luksch, N.; Rauh, D.; Sherborne, B.; Wyatt, P. G.; Brenk, R., De novo design of protein kinase inhibitors by in silico identification of hinge region-binding fragments. *ACS Chem. Biol.* **2013,** *8* (5), 1044-1052.

61. Govindasamy, K.; Jebiwott, S.; Jaijyan, D.; Davidow, A.; Ojo, K.; Van Voorhis, W.; Brochet, M.; Billker, O.; Bhanot, P., Invasion of hepatocytes by Plasmodium sporozoites requires cGMP-dependent protein kinase and calcium dependent protein kinase 4. *Mol. Microbiol.* **2016,** *102* (2), 349-363.

62. Brochet, M.; Collins, M. O.; Smith, T. K.; Thompson, E.; Sebastian, S.; Volkmann, K.; Schwach, F.; Chappell, L.; Gomes, A. R.; Berriman, M., Phosphoinositide metabolism links cGMP-dependent protein kinase G to essential Ca2+ signals at key decision points in the life cycle of malaria parasites. *PLoS Biol.* **2014,** *12* (3), e1001806.

63. Falae, A.; Combe, A.; Amaladoss, A.; Carvalho, T.; Menard, R.; Bhanot, P., Role of Plasmodium berghei cGMP-dependent protein kinase in late liver stage development. *J. Biol. Chem.* **2010,** *285* (5), 3282-3288.

64. Koussis, K.; Withers-Martinez, C.; Baker, D. A.; Blackman, M. J., Simultaneous multiple allelic replacement in the malaria parasite enables dissection of PKG function. *Life Sci. Alliance* **2020,** *3* (4).

65. Taylor, H. M.; McRobert, L.; Grainger, M.; Sicard, A.; Dluzewski, A. R.; Hopp, C. S.; Holder, A. A.; Baker, D. A., The malaria parasite cyclic GMP-dependent protein kinase plays a central role in blood-stage schizogony. *Eukaryot. Cell* **2010,** *9* (1), 37-45.

66. McRobert, L.; Taylor, C. J.; Deng, W.; Fivelman, Q. L.; Cummings, R. M.; Polley, S. D.; Billker, O.; Baker, D. A., Gametogenesis in malaria parasites is mediated by the cGMP-dependent protein kinase. *PLoS Biol.* **2008,** *6* (6), e139.

67. Deng, W.; Baker, D. A., A novel cyclic GMP-dependent protein kinase is expressed in the ring stage of the Plasmodium falciparum life cycle. *Mol. Microbiol.* **2002,** *44* (5), 1141-1151.

68. Alam, M. M.; Solyakov, L.; Bottrill, A. R.; Flueck, C.; Siddiqui, F. A.; Singh, S.; Mistry, S.; Viskaduraki, M.; Lee, K.; Hopp, C. S., Phosphoproteomics reveals malaria parasite Protein Kinase G as a signalling hub regulating egress and invasion. *Nat. Commun.* **2015,** *6* (1), 1-15.

69. Collins, C. R.; Hackett, F.; Strath, M.; Penzo, M.; Withers-Martinez, C.; Baker, D. A.; Blackman, M. J., Malaria parasite cGMP-dependent protein kinase regulates blood stage merozoite secretory organelle discharge and egress. *PLoS Pathog.* **2013,** *9* (5), e1003344.

70. Vanaerschot, M.; Murithi, J. M.; Pasaje, C. F. A.; Ghidelli-Disse, S.; Dwomoh, L.; Bird, M.; Spottiswoode, N.; Mittal, N.; Arendse, L. B.; Owen, E. S., Inhibition of resistance-refractory P. falciparum kinase PKG delivers prophylactic, blood stage, and transmission-blocking antiplasmodial activity. *Cell Chem. Biol.* **2020,** *27* (7), 806-816. e8.

71. Knighton, D. R.; Zheng, J. H.; Ten Eyck, L. F.; Ashford, V. A.; Xuong, N.-H.; Taylor, S. S.; Sowadski, J. M., Crystal structure of the catalytic subunit of cyclic adenosine monophosphate-dependent protein kinase. *Science* **1991,** *253* (5018), 407-414.

72. Baker, D. A.; Deng, W., Cyclic GMP-dependent protein kinases in protozoa. *Front Biosci* **2005,** *10*, 1229-1238.

73. Franz, E.; Knape, M. J.; Herberg, F. W., cGMP binding domain D mediates a unique activation mechanism in Plasmodium falciparum PKG. *ACS Infect. Dis.* **2017,** *4* (3), 415-423.

74. Byun, J. A.; Van, K.; Huang, J.; Henning, P.; Franz, E.; Akimoto, M.; Herberg, F. W.; Kim, C.; Melacini, G., Mechanism of allosteric inhibition in the Plasmodium falciparum cGMP-dependent protein kinase. *J. Biol. Chem.* **2020,** *295* (25), 8480-8491.

75. Kim, J. J.; Flueck, C.; Franz, E.; Sanabria-Figueroa, E.; Thompson, E.; Lorenz, R.; Bertinetti, D.; Baker, D. A.; Herberg, F. W.; Kim, C., Crystal structures of the carboxyl cGMP binding domain of the Plasmodium falciparum cGMP-dependent protein kinase reveal a novel capping triad crucial for merozoite egress. *PLoS Pathog.* **2015,** *11* (2), e1004639.

76. Deng, W.; Parbhu-Patel, A.; Meyer, D. J.; Baker, D. A., The role of two novel regulatory sites in the activation of the cGMP-dependent protein kinase from Plasmodium falciparum. *Biochem. J.* **2003,** *374* (2), 559-565.

77. Huang, J.; Byun, J. A.; VanSchouwen, B.; Henning, P.; Herberg, F. W.; Kim, C.; Melacini, G., Dynamical Basis of Allosteric Activation for the Plasmodium falciparum Protein Kinase G. *J. Phys. Chem. B* **2021**.

78. Qin, L.; Sankaran, B.; Aminzai, S.; Casteel, D. E.; Kim, C., Structural basis for selective inhibition of human PKG Iα by the balanol-like compound N46. *J. Biol. Chem.* **2018,** *293* (28), 10985-10992.

79. Carrera, A. C.; Alexandrov, K.; Roberts, T. M., The conserved lysine of the catalytic domain of protein kinases is actively involved in the phosphotransfer reaction and not required for anchoring ATP. *Proc. Natl. Acad. Sci.* **1993,** *90* (2), 442-446.

80. Penzo, M.; de Las Heras-Dueña, L.; Mata-Cantero, L.; Diaz-Hernandez, B.; Vazquez-Muñiz, M.-J.; Ghidelli-Disse, S.; Drewes, G.; Fernandez-Alvaro, E.; Baker, D. A., High-throughput screening of the Plasmodium falciparum cGMP-dependent protein kinase identified a thiazole scaffold which kills erythrocytic and sexual stage parasites. *Sci. Rep.* **2019,** *9* (1), 1-13.

81. Baker, D. A.; Stewart, L. B.; Large, J. M.; Bowyer, P. W.; Ansell, K. H.; Jiménez-Díaz, M. B.; El Bakkouri, M.; Birchall, K.; Dechering, K. J.; Bouloc, N. S., A potent series targeting the malarial cGMP-dependent protein kinase clears infection and blocks transmission. *Nat. Commun.* **2017,** *8* (1), 1-9.

82. Tsagris, D. J.; Birchall, K.; Bouloc, N.; Large, J. M.; Merritt, A.; Smiljanic-Hurley, E.; Wheldon, M.; Ansell, K. H.; Kettleborough, C.; Whalley, D., Trisubstituted thiazoles as potent and selective inhibitors of Plasmodium falciparum protein kinase G (PfPKG). *Bioorg. Med. Chem. Lett.* **2018,** *28* (19), 3168-3173.

83. Balla, T., Phosphoinositides: tiny lipids with giant impact on cell regulation. *Physiol. Rev.* **2013,** *93* (3), 1019-1137.

84. Burke, J. E., Structural basis for regulation of phosphoinositide kinases and their involvement in human disease. *Mol. Cell* **2018,** *71* (5), 653-673.

85. McNamara, C. W.; Lee, M. C.; Lim, C. S.; Lim, S. H.; Roland, J.; Nagle, A.; Simon, O.; Yeung, B. K.; Chatterjee, A. K.; McCormack, S. L., Targeting Plasmodium PI (4) K to eliminate malaria. *Nature* **2013,** *504* (7479), 248-253.

86. Burke, J. E.; Inglis, A. J.; Perisic, O.; Masson, G. R.; McLaughlin, S. H.; Rutaganira, F.; Shokat, K. M.; Williams, R. L., Structures of PI4KIIIβ complexes show simultaneous recruitment of Rab11 and its effectors. *Science* **2014,** *344* (6187), 1035-1038.

87. Paquet, T.; Le Manach, C.; Cabrera, D. G.; Younis, Y.; Henrich, P. P.; Abraham, T. S.; Lee, M. C.; Basak, R.; Ghidelli-Disse, S.; Lafuente-Monasterio, M. J., Antimalarial efficacy of MMV390048, an inhibitor of Plasmodium phosphatidylinositol 4-kinase. *Sci. Transl. Med.* **2017,** *9* (387).

88. Sinxadi, P.; Donini, C.; Johnstone, H.; Langdon, G.; Wiesner, L.; Allen, E.; Duparc, S.; Chalon, S.; McCarthy, J. S.; Lorch, U., Safety, tolerability, pharmacokinetics, and antimalarial activity of the novel Plasmodium phosphatidylinositol 4-kinase inhibitor MMV390048 in healthy volunteers. *Antimicrob. Agents Chemother.* **2020,** *64* (4), e01896-19.

89. Brunschwig, C.; Lawrence, N.; Taylor, D.; Abay, E.; Njoroge, M.; Basarab, G. S.; Le Manach, C.; Paquet, T.; Cabrera, D. G.; Nchinda, A. T., UCT943, a next-generation

Plasmodium falciparum PI4K inhibitor preclinical candidate for the treatment of malaria. *Antimicrob. Agents Chemother.* **2018,** *62* (9), e00012-18.

90. Bordoli, L.; Kiefer, F.; Arnold, K.; Benkert, P.; Battey, J.; Schwede, T., Protein structure homology modeling using SWISS-MODEL workspace. *Nat. Protoc.* **2009,** *4* (1), 1-13.

91. Bell, J.; Cao, Y.; Gunn, J.; Day, T.; Gallicchio, E.; Zhou, Z.; Levy, R.; Farid, R., PrimeX and the Schrödinger computational chemistry suite of programs. **2012**.

92. Fienberg, S.; Eyermann, C. J.; Arendse, L. B.; Basarab, G. S.; McPhail, J. A.; Burke, J. E.; Chibale, K., Structural Basis for Inhibitor Potency and Selectivity of Plasmodium falciparum Phosphatidylinositol 4-Kinase Inhibitors. *ACS Infect. Dis.* **2020,** *6* (11), 3048-3063.

93. Berndt, A.; Miller, S.; Williams, O.; Le, D. D.; Houseman, B. T.; Pacold, J. I.; Gorrec, F.; Hon, W.-C.; Ren, P.; Liu, Y., The p110δ structure: mechanisms for selectivity and potency of new PI (3) K inhibitors. *Nat. Chem. Biol.* **2010,** *6* (2), 117-124.

94. Kanev, G. K.; de Graaf, C.; de Esch, I. J.; Leurs, R.; Würdinger, T.; Westerman, B. A.; Kooistra, A. J., The landscape of atypical and eukaryotic protein kinases. *Trends Pharmacol. Sci.* **2019,** *40* (11), 818-832.

95. Boran, A. D.; Iyengar, R., Systems approaches to polypharmacology and drug discovery. *Curr. Opin. Drug Discovery Dev.* **2010,** *13* (3), 297.

96. Druker, B. J., Translation of the Philadelphia chromosome into therapy for CML. *Am. J. Hematol* **2008,** *112* (13), 4808-4817.

97. Silver, L. L., Appropriate targets for antibacterial drugs. *Cold Spring Harbor Perspect. Med.* **2016,** *6* (12), a030239.

98. Gamo, F.-J.; Sanz, L. M.; Vidal, J.; De Cozar, C.; Alvarez, E.; Lavandera, J.-L.; Vanderwall, D. E.; Green, D. V.; Kumar, V.; Hasan, S., Thousands of chemical starting points for antimalarial lead identification. *Nature* **2010,** *465* (7296), 305-310.

99. Guiguemde, W. A.; Shelat, A. A.; Bouck, D.; Duffy, S.; Crowther, G. J.; Davis, P. H.; Smithson, D. C.; Connelly, M.; Clark, J.; Zhu, F., Chemical genetics of Plasmodium falciparum. *Nature* **2010,** *465* (7296), 311-315.

100. Mayr, L. M.; Bojanic, D., Novel trends in high-throughput screening. *Curr. Opin. Pharmacol.* **2009,** *9* (5), 580-588.

101. Fox, S.; Farr-Jones, S.; Sopchak, L.; Boggs, A.; Nicely, H. W.; Khoury, R.; Biros, M., High-throughput screening: update on practices and success. *J. Biomol. Screening* **2006,** *11* (7), 864-869.

102. Shoichet, B. K., Screening in a spirit haunted world. *Drug discovery today* **2006,** *11* (13-14), 607-615.

103. Coma, I.; Clark, L.; Diez, E.; Harper, G.; Herranz, J.; Hofmann, G.; Lennon, M.; Richmond, N.; Valmaseda, M.; Macarron, R., Process validation and screen reproducibility in high-throughput screening. *J. Biomol. Screening* **2009,** *14* (1), 66-76.

104. Holenz, J.; Stoy, P., Advances in lead generation. *Bioorg. Med. Chem. Lett.* **2019,** *29* (4), 517-524.

105. Alvarez, J. C., High-throughput docking as a source of novel drug leads. *Curr. Opin. Chem. Biol.* **2004,** *8* (4), 365-370.

106. Klebe, G., Virtual ligand screening: strategies, perspectives and limitations. *Drug discovery today* **2006,** *11* (13-14), 580-594.

107. McInnes, C., Virtual screening strategies in drug discovery. *Curr. Opin. Chem. Biol.* **2007,** *11* (5), 494-502.

108. Halperin, I.; Ma, B.; Wolfson, H.; Nussinov, R., Principles of docking: An overview of search algorithms and a guide to scoring functions. *Proteins: Struct., Funct., Bioinf.* **2002,** *47* (4), 409-443.

109. Kitchen, D. B.; Decornez, H.; Furr, J. R.; Bajorath, J., Docking and scoring in virtual screening for drug discovery: methods and applications. *Nat. Rev. Drug Discovery* **2004,** *3* (11), 935-949.

110. Abagyan, R.; Totrov, M., High-throughput docking for lead generation. *Curr. Opin. Chem. Biol.* **2001,** *5* (4), 375-382.

111. Lenz, G. R.; Nash, H. M.; Jindal, S., Chemical ligands, genomics and drug discovery. *Drug Discovery Today* **2000,** *5* (4), 145-156.

112. Bajorath, J., Integration of virtual and high-throughput screening. *Nat. Rev. Drug Discovery* **2002,** *1* (11), 882-894.

113. Sabe, V. T.; Ntombela, T.; Jhamba, L. A.; Maguire, G. E.; Govender, T.; Naicker, T.; Kruger, H. G., Current trends in computer aided drug design and a highlight of drugs discovered via computational techniques: A review. *Eur. J. Med. Chem.* **2021,** *224*, 113705.

114. Agafonov, R. V.; Wilson, C.; Kern, D., Evolution and intelligent design in drug development. *Front. Mol. Biosci.* **2015,** *2*, 27.

115. Ferreira, L. G.; Dos Santos, R. N.; Oliva, G.; Andricopulo, A. D., Molecular docking and structure-based drug design strategies. *Mol.* **2015,** *20* (7), 13384-13421.

116. Lengauer, T.; Rarey, M., Computational methods for biomolecular docking. *Curr. Opin. Struct. Biol.* **1996,** *6* (3), 402-406.

117. Warren, G. L.; Andrews, C. W.; Capelli, A.-M.; Clarke, B.; LaLonde, J.; Lambert, M. H.; Lindvall, M.; Nevins, N.; Semus, S. F.; Senger, S., A critical assessment of docking programs and scoring functions. *J. Med. Chem.* **2006,** *49* (20), 5912-5931.

118. Sousa, S. F.; Fernandes, P. A.; Ramos, M. J., Protein–ligand docking: current status and future challenges. *Proteins: Struct., Funct., Bioinf.* **2006,** *65* (1), 15-26.

119. Taylor, R. D.; Jewsbury, P. J.; Essex, J. W., A review of protein-small molecule docking methods. *J. Comput.-Aided Mol. Des.* **2002,** *16* (3), 151-166.

120. Novič, M.; Tibaut, T.; Anderluh, M.; Borišek, J.; Tomašič, T., The Comparison of Docking Search Algorithms and Scoring Functions: An Overview and Case Studies. *Methods and Algorithms for Molecular Docking-Based Drug Design and Discovery* **2016**, 99-127.

121. Morris, G. M.; Lim-Wilby, M., Molecular docking. In *J Mol Model*, Springer: 2008; pp 365-382.

122. Barril, X.; Hubbard, R.; Morley, S., Virtual screening in structure-based drug discovery. *Mini-Rev. Med. Chem.* **2004,** *4* (7), 779-791.

123. Liu, J.; Wang, R., Classification of current scoring functions. *J. Chem. Inf. Model.* **2015,** *55* (3), 475-482.

124. Li, J.; Fu, A.; Zhang, L., An overview of scoring functions used for protein–ligand interactions in molecular docking. *Interdiscip. Sci.: Comput. Life Sci.* **2019,** *11* (2), 320-328.

125. Eldridge, M. D.; Murray, C. W.; Auton, T. R.; Paolini, G. V.; Mee, R. P., Empirical scoring functions: I. The development of a fast empirical scoring function to estimate the binding affinity of ligands in receptor complexes. *J. Comput.-Aided Mol. Des.* **1997,** *11* (5), 425-445.

126. Zhang, S.; Golbraikh, A.; Tropsha, A., Development of Quantitative Structure− Binding Affinity Relationship Models Based on Novel Geometrical Chemical Descriptors of the Protein− Ligand Interfaces. *J. Med. Chem.* **2006,** *49* (9), 2713-2724.

127. Deng, W.; Breneman, C.; Embrechts, M. J., Predicting protein− ligand binding affinities using novel geometrical descriptors and machine-learning methods. *J Chem Inf Comput Sci* **2004,** *44* (2), 699-703.

128. Huang, N.; Kalyanaraman, C.; Irwin, J. J.; Jacobson, M. P., Physics-based scoring of protein− ligand complexes: Enrichment of known inhibitors in large-scale virtual screening. *J. Chem. Inf. Model.* **2006,** *46* (1), 243-253.

129. Fehér, P. P.; Stirling, A., Assessment of reactivities with explicit and implicit solvent models: QM/MM and gas-phase evaluation of three different Ag-catalysed furan ring formation routes. *New J. Chem.* **2019,** *43* (39), 15706-15713.

130. Tomasi, J.; Mennucci, B.; Cammi, R., Quantum mechanical continuum solvation models. *Chem. Rev.* **2005,** *105* (8), 2999-3094.

131. Muegge, I.; Martin, Y. C., A general and fast scoring function for protein− ligand interactions: a simplified potential approach. *J. Med. Chem.* **1999,** *42* (5), 791-804.

132. Klepeis, J. L.; Lindorff-Larsen, K.; Dror, R. O.; Shaw, D. E., Long-timescale molecular dynamics simulations of protein structure and function. *Curr. Opin. Struct. Biol.* **2009,** *19* (2), 120-127.

133. Vanommeslaeghe, K.; Guvench, O., Molecular mechanics. *Curr. Pharm. Des.* **2014,** *20* (20), 3281-3292.

134. Cornell, W. D.; Cieplak, P.; Bayly, C. I.; Gould, I. R.; Merz, K. M.; Ferguson, D. M.; Spellmeyer, D. C.; Fox, T.; Caldwell, J. W.; Kollman, P. A., A second generation force field for the simulation of proteins, nucleic acids, and organic molecules. *J. Am. Chem. Soc.* **1995,** *117* (19), 5179-5197.

135. Weiner, S. J.; Kollman, P. A.; Case, D. A.; Singh, U. C.; Ghio, C.; Alagona, G.; Profeta, S.; Weiner, P., A new force field for molecular mechanical simulation of nucleic acids and proteins. *J. Am. Chem. Soc.* **1984,** *106* (3), 765-784.

136. Sun, H., COMPASS: an ab initio force-field optimized for condensed-phase applications overview with details on alkane and benzene compounds. *J. Phys. Chem. B* **1998,** *102* (38), 7338-7364.

137. Oostenbrink, C.; Villa, A.; Mark, A. E.; Van Gunsteren, W. F., A biomolecular force field based on the free enthalpy of hydration and solvation: the GROMOS force-field parameter sets 53A5 and 53A6. *J. Comput. Chem.* **2004,** *25* (13), 1656-1676.

138. Yin, D.; MacKerell Jr, A. D., Combined ab initio/empirical approach for optimization of Lennard–Jones parameters. *J. Comput. Chem.* **1998,** *19* (3), 334-348.

139. Jorgensen, W. L.; Maxwell, D. S.; Tirado-Rives, J., Development and testing of the OPLS all-atom force field on conformational energetics and properties of organic liquids. *J. Am. Chem. Soc.* **1996,** *118* (45), 11225-11236.

140. Guvench, O.; MacKerell, A. D., Comparison of protein force fields for molecular dynamics simulations. *J Mol Model* **2008**, 63-88.

141. Beauchamp, K. A.; Lin, Y.-S.; Das, R.; Pande, V. S., Are protein force fields getting better? A systematic benchmark on 524 diverse NMR measurements. *J. Chem. Theory Comput.* **2012,** *8* (4), 1409-1414.

142. Best, R. B.; Buchete, N.-V.; Hummer, G., Are current molecular dynamics force fields too helical? *Biophys. J.* **2008,** *95* (1), L07-L09.

143. Lange, O. F.; Van der Spoel, D.; De Groot, B. L., Scrutinizing molecular mechanics force fields on the submicrosecond timescale with NMR data. *Biophys. J.* **2010,** *99* (2), 647-655.

144. Burley, S. K.; Berman, H. M.; Bhikadiya, C.; Bi, C.; Chen, L.; Di Costanzo, L.; Christie, C.; Dalenberg, K.; Duarte, J. M.; Dutta, S., RCSB Protein Data Bank: biological macromolecular structures enabling research and education in fundamental biology, biomedicine, biotechnology and energy. *Nucleic Acids Res.* **2019,** *47* (D1), D464-D474.

145. Rose, P. W.; Prlić, A.; Altunkaya, A.; Bi, C.; Bradley, A. R.; Christie, C. H.; Costanzo, L. D.; Duarte, J. M.; Dutta, S.; Feng, Z., The RCSB protein data bank: integrative view of protein, gene and 3D structural information. *Nucleic Acids Res.* **2016**, gkw1000.

146. Kalyaanamoorthy, S.; Chen, Y.-P. P., Structure-based drug design to augment hit discovery. *Drug discovery today* **2011,** *16* (17-18), 831-839.

147. Batool, M.; Ahmad, B.; Choi, S., A structure-based drug discovery paradigm. *Int. J. Mol. Sci.* **2019,** *20* (11), 2783.

148. Meng, X.-Y.; Zhang, H.-X.; Mezei, M.; Cui, M., Molecular docking: a powerful approach for structure-based drug discovery. *Curr. Comput.-Aided Drug Des.* **2011,** *7* (2), 146-157.

149. Lionta, E.; Spyrou, G.; K Vassilatis, D.; Cournia, Z., Structure-based virtual screening for drug discovery: principles, applications and recent advances. *Curr. Top. Med. Chem.* **2014,** *14* (16), 1923-1938.

150. Harris, P. A.; Boloor, A.; Cheung, M.; Kumar, R.; Crosby, R. M.; Davis-Ward, R. G.; Epperly, A. H.; Hinkle, K. W.; Hunter III, R. N.; Johnson, J. H., Discovery of 5-[[4-[(2, 3-dimethyl-2 H-indazol-6-yl) methylamino]-2-pyrimidinyl] amino]-2-methyl-benzenesulfonamide (Pazopanib), a novel and potent vascular endothelial growth factor receptor inhibitor. *J. Med. Chem.* **2008,** *51* (15), 4632-4640.

151. Harris, P. A.; Cheung, M.; Hunter, R. N.; Brown, M. L.; Veal, J. M.; Nolte, R. T.; Wang, L.; Liu, W.; Crosby, R. M.; Johnson, J. H., Discovery and evaluation of 2-anilino-5-aryloxazoles as a novel class of VEGFR2 kinase inhibitors. *J. Med. Chem.* **2005,** *48* (5), 1610-1619.

152. Ratner, L.; Haseltine, W.; Patarca, R.; Livak, K. J.; Starcich, B.; Josephs, S. F.; Doran, E. R.; Rafalski, J. A.; Whitehorn, E. A.; Baumeister, K., Complete nucleotide sequence of the AIDS virus, HTLV-III. *Nature* **1985,** *313* (6000), 277-284.

153. Katoh, I.; Yasunaga, T.; Ikawa, Y.; Yoshinaka, Y., Inhibition of retroviral protease activity by an aspartyl proteinase inhibitor. *Nature* **1987,** *329* (6140), 654-656.

154. Toh, H.; Ono, M.; Saigo, K.; Miyata, T., Retroviral protease-like sequence in the yeast transposon Ty 1. *Nature* **1985,** *315* (6021), 691-691.

155. Navia, M. A.; Fitzgerald, P. M.; McKeever, B. M.; Leu, C.-T.; Heimbach, J. C.; Herber, W. K.; Sigal, I. S.; Darke, P. L.; Springer, J. P., Three-dimensional structure of aspartyl protease from human immunodeficiency virus HIV-1. *Nature* **1989,** *337* (6208), 615-620.

156. Lapatto, R.; Blundell, T.; Hemmings, A.; Overington, J.; Wilderspin, A.; Wood, S.; Merson, J. R.; Whittle, P. J.; Danley, D. E.; Geoghegan, K. F., X-ray analysis of HIV-1 proteinase at 2.7 Å resolution confirms structural homology among retroviral enzymes. *Nature* **1989,** *342* (6247), 299-302.

157. Wlodawer, A.; Vondrasek, J., Inhibitors of HIV-1 protease: a major success of structure-assisted drug design. *Annu. Rev. Biophys. Biomol. Struct.* **1998,** *27* (1), 249-284.

158. Roberts, N. A.; Martin, J. A.; Kinchington, D.; Broadhurst, A. V.; Craig, J. C.; Duncan, I. B.; Galpin, S. A.; Handa, B. K.; Kay, J.; Kröhn, A., Rational design of peptide-based HIV proteinase inhibitors. *Science* **1990**, 358-361.

159. Krohn, A.; Redshaw, S.; Ritchie, J. C.; Graves, B. J.; Hatada, M. H., Novel binding mode of highly potent HIV-proteinase inhibitors incorporating the (R)-hydroxyethylamine isostere. *J. Med. Chem.* **1991,** *34* (11), 3340-3342.

160. Varney, M. D.; Appelt, K.; Kalish, V.; Reddy, M. R.; Tatlock, J.; Palmer, C. L.; Romines, W. H.; Wu, B.-W.; Musick, L., Crystal-structure-based design and synthesis of novel C-terminal inhibitors of HIV protease. *J. Med. Chem.* **1994,** *37* (15), 2274-2284.

161. Reich, S. H.; Melnick, M.; Davies, J. F.; Appelt, K.; Lewis, K. K.; Fuhry, M. A.; Pino, M.; Trippe, A. J.; Nguyen, D.; Dawson, H., Protein structure-based design of potent orally bioavailable, nonpeptide inhibitors of human immunodeficiency virus protease. *Proc. Natl. Acad. Sci.* **1995,** *92* (8), 3298-3302.

162. Kaldor, S. W.; Kalish, V. J.; Davies, J. F.; Shetty, B. V.; Fritz, J. E.; Appelt, K.; Burgess, J. A.; Campanale, K. M.; Chirgadze, N. Y.; Clawson, D. K., Viracept (nelfinavir

mesylate, AG1343): a potent, orally bioavailable inhibitor of HIV-1 protease. *J. Med. Chem.* **1997,** *40* (24), 3979-3985.

163. Sham, H. L.; Kempf, D. J.; Molla, A.; Marsh, K. C.; Kumar, G. N.; Chen, C.-M.; Kati, W.; Stewart, K.; Lal, R.; Hsu, A., ABT-378, a highly potent inhibitor of the human immunodeficiency virus protease. *Antimicrob. Agents Chemother.* **1998,** *42* (12), 3218-3224.

164. Van Montfort, R. L.; Workman, P., Structure-based drug design: aiming for a perfect fit. *Essays Biochem.* **2017,** *61* (5), 431-437.

165. Organization, W. H., HIV data and statistics. *Key facts and latest estimates on the global HIV epidemic - 2020* **2021**.

166. FDA-Approved HIV Medicines. https://hivinfo.nih.gov/understanding-hiv/fact-sheets/fda-approved-hiv-medicines (accessed 09/09/2021).

167. De Clercq, E., Anti-HIV drugs: 25 compounds approved within 25 years after the discovery of HIV. *Int. J. Antimicrob. Agents* **2009,** *33* (4), 307-320.

168. Kohl, N. E.; Emini, E. A.; Schleif, W. A.; Davis, L. J.; Heimbach, J. C.; Dixon, R.; Scolnick, E. M.; Sigal, I. S., Active human immunodeficiency virus protease is required for viral infectivity. *Proc. Natl. Acad. Sci.* **1988,** *85* (13), 4686-4690.

169. Seelmeier, S.; Schmidt, H.; Turk, V.; Von Der Helm, K., Human immunodeficiency virus has an aspartic-type protease that can be inhibited by pepstatin A. *Proc. Natl. Acad. Sci.* **1988,** *85* (18), 6612-6616.

170. Wlodawer, A.; Miller, M.; Jaskólski, M.; Sathyanarayana, B. K.; Baldwin, E.; Weber, I. T.; Selk, L. M.; Clawson, L.; Schneider, J.; Kent, S. B., Conserved folding in retroviral proteases: crystal structure of a synthetic HIV-1 protease. *Science* **1989**, 616-621.

171. Tie, Y.; Kovalevsky, A. Y.; Boross, P.; Wang, Y. F.; Ghosh, A. K.; Tozser, J.; Harrison, R. W.; Weber, I. T., Atomic resolution crystal structures of HIV-1 protease and

mutants V82A and I84V with saquinavir. *Proteins: Struct., Funct., Bioinf.* **2007,** *67* (1), 232-242.

172. Appelt, K., Crystal structures of HIV-1 protease-inhibitor complexes. *Perspect. Drug Discovery Des.* **1993,** *1* (1), 23-48.

173. King, N. M.; Prabu-Jeyabalan, M.; Bandaranayake, R. M.; Nalam, M. N.; Nalivaika, E. A.; Ozen, A.; Haliloglu, T.; Yılmaz, N. e. K.; Schiffer, C. A., Extreme entropy–enthalpy compensation in a drug-resistant variant of HIV-1 protease. *ACS Chem. Biol.* **2012,** *7* (9), 1536-1546.

174. Stoll, V.; Qin, W.; Stewart, K. D.; Jakob, C.; Park, C.; Walter, K.; Simmer, R.; Helfrich, R.; Bussiere, D.; Kao, J., X-ray crystallographic structure of ABT-378 (lopinavir) bound to HIV-1 protease. *Bioorg. Med. Chem.* **2002,** *10* (8), 2803-2806.

175. Hurst, M.; Faulds, D., Lopinavir. *Drugs* **2000,** *60* (6), 1371-1379.

176. Wlodawer, A., ABT-378 Abbott Laboratories. *Curr. Opin. Anti-Infect. Investig. Drugs* **1999,** *1*, 246-50.

177. Bajusz, D.; G Ferenczy, G.; M Keseru, G., Structure-based virtual screening approaches in kinase-directed drug discovery. *Curr. Top. Med. Chem.* **2017,** *17* (20), 2235-2259.

178. H Drewry, D.; M Willson, T.; J Zuercher, W., Seeding collaborations to advance kinase science with the GSK Published Kinase Inhibitor Set (PKIS). *Curr. Top. Med. Chem.* **2014,** *14* (3), 340-342.

179. Tamir, T. Y.; Drewry, D. H.; Wells, C.; Major, M. B.; Axtman, A. D., PKIS deep dive yields a chemical starting point for dark kinases and a cell active BRSK2 inhibitor. *Sci. Rep.* **2020,** *10* (1), 1-12.

180. John Harris, C.; D Hill, R.; W Sheppard, D.; J Slater, M.; FW Stouten, P., The design and application of target-focused compound libraries. *Comb. Chem. High Throughput Screening* **2011,** *14* (6), 521-531.

181. Paquet, T.; Le Manach, C.; Cabrera, D. G.; Younis, Y.; Henrich, P. P.; Abraham, T. S.; Lee, M. C.; Basak, R.; Ghidelli-Disse, S.; Lafuente-Monasterio, M. J., Antimalarial efficacy of MMV390048, an inhibitor of Plasmodium phosphatidylinositol 4-kinase. *Science translational medicine* **2017,** *9* (387), eaad9735.

182. Samby, K.; Willis, P. A.; Burrows, J. N.; Laleu, B.; Webborn, P. J., Actives from MMV Open Access Boxes? A suggested way forward. *PLoS Pathog.* **2021,** *17* (4), e1009384.

183. Spangenberg, T.; Burrows, J. N.; Kowalczyk, P.; McDonald, S.; Wells, T. N.; Willis, P., The open access malaria box: a drug discovery catalyst for neglected diseases. *PloS one* **2013,** *8* (6), e62906.

184. Van Voorhis, W. C.; Adams, J. H.; Adelfio, R.; Ahyong, V.; Akabas, M. H.; Alano, P.; Alday, A.; Alemán Resto, Y.; Alsibaee, A.; Alzualde, A., Open source drug discovery with the malaria box compound collection for neglected diseases and beyond. *PLoS Pathog.* **2016,** *12* (7), e1005763.

185. Preston, S.; Jiao, Y.; Jabbar, A.; McGee, S. L.; Laleu, B.; Willis, P.; Wells, T. N.; Gasser, R. B., Screening of the 'Pathogen Box'identifies an approved pesticide with major anthelmintic activity against the barber's pole worm. *Int J Parasitol Drugs Drug Resist* **2016,** *6* (3), 329-334.

186. Reader, J.; van der Watt, M. E.; Taylor, D.; Le Manach, C.; Mittal, N.; Ottilie, S.; Theron, A.; Moyo, P.; Erlank, E.; Nardini, L., Multistage and transmission-blocking targeted antimalarials discovered from the open-source MMV Pandemic Response Box. *Nat. Commun.* **2021,** *12* (1), 1-15.

187. Almeida-Paes, R.; de Andrade, I. B.; Ramos, M. L. M.; Rodrigues, M. V. d. A.; do Nascimento, V. A.; Bernardes-Engemann, A. R.; Frases, S., Medicines for Malaria Venture COVID Box: a source for repurposing drugs with antifungal activity against human pathogenic fungi. *Mem. Inst. Oswaldo Cruz* **2021,** *116*.

CHAPTER TWO: Pyrazolo[3,4-d]pyrimidines (MLN0128 Series)

2.1. Introduction

Compounds incorporating the pyrazolo[3,4-d]pyrimidine core have demonstrated various pharmacological properties, including antimalarial,[1-3] anticancer,[4-12] antimicrobial,[13, 14] and anti-inflammatory activities.[15] Within the context of this thesis work, researchers at the GlaxoSmithKline (GSK) Cellzome facility identified the pyrazolo[3,4-d]pyrimidine mammalian target of rapamycin (mTOR) inhibitor MLN0128 (**Figure 2.1**) from a Kinobead-based[16] screening of 84 clinically validated human kinase inhibitors against 89 *P. falciparum* kinases obtained from a blood-stage extract. MLN0128 was revealed to be a dual inhibitor of *Pf*PI4K and *Pf*PKG with IC_{50} values of 0.02 µM and 0.035 µM, respectively. Additionally, this compound demonstrated whole cell antiparasitic activity by inhibiting the growth of the *P. falciparum* 3D7 strain in the 48- and 72-h assays with IC_{50} values of 0.2 µM and 0.078 µM, respectively. It is noteworthy that, as shown in **Figure 2.1**, MLN0128 also inhibited other *Plasmodium* kinases including *P. falciparum* phosphatidylinositol-3 kinase (*Pf*PI3K), *P. falciparum* cyclin-dependent protein kinase 5 (*Pf*CRK5), *P. falciparum* casein kinase 1 (*Pf*CK1) and *P. falciparum* calcium-dependent protein kinases (*Pf*CDPKs).

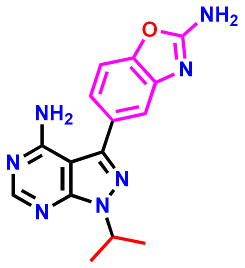

MLN0128
mTOR: 1nM
***P. falciparum* IC_{50}: 0.2 µM**
***Pf*PKG: 0.02 µM** **PfCK1: 0.63 µM**
***Pf*PI4K: 0.035 µM** ***Pf*PK2: 2.4 µM**
***Pf*PI3K: 0.1 µM** ***Pf*CDPK4: 6.5 µM**
***Pf*CRK5: 0.2 µM** ***Pf*CDPK: 12 µM**
***Pf*PK5: 0.21 µM**

Figure 2.1: Structure and enzymatic activities of **MLN0128** determined via kinobead binding studies.

mTOR, mammalian target of rapamycin; IC_{50}, 50% inhibitory concentration; *P. falciparum*, *Plasmodium falciparum*; *Pf*PKG, *P. falciparum* cyclic guanosine monophosphate (cGMP)-dependent protein kinase; *Pf*PI4K, *P. falciparum* phosphatidylinositol-4 kinase; *Pf*PI3K, *P. falciparum* phosphatidylinositol-3 kinase; *Pf*CRK5, *P. falciparum* cyclin-dependent protein kinase 5; *Pf*PK5, *P. falciparum* protein kinase 5; *Pf*CRK5, *P. falciparum* cyclin-dependent protein kinase 5; *Pf*CK1, *P. falciparum* casein kinase 1; *Pf*PK2, *P. falciparum* protein kinase 2; *Pf*CDPK4, *P. falciparum* calcium-dependent protein kinase-4; *Pf*CDPK, *P. falciparum* calcium-dependent protein kinase.

The serine/threonine protein kinase mTOR is part of the phosphoinositide-3-kinase-related (PIKK) family.[17] This kinase is involved in various pathways that control lipid and protein synthesis, autophagy, and cell survival.[18] Dysregulation of this signaling pathway has been linked to tumorigenesis, making it a desirable target when designing anticancer compounds.[19] With regard to the sensitivity of the protein to rapamycin, a classical mTOR inhibitor, complexes are classified as $mTORC_1$ (rapamycin-sensitive complex) or $mTORC_2$ (rapamycin-insensitive complex).[20] Although MLN0128 is an ATP-competitive mTOR inhibitor, other mTOR inhibitors bind to allosteric sites of the kinase.[21] With an enzymatic IC_{50} of 1 nM, MLN0128 is a dual inhibitor of both mTOR complexes ($mTORC_1$ and $mTORC_2$). It has been shown to induce apoptosis and inhibit proliferation more effectively than rapamycin.[21-25] It is currently in phase II clinical trials against various cancers in monotherapy and in combination with other anticancer drugs.[26, 27]

Concerning malaria, Krishnan et al. identified NCATS-SM3710, a derivative of the mTOR inhibitor Torin 2, which showed potent *in vivo* activity against multiple stages of the *P. berghei* life-cycle (**Figure 2.2**).[28] *Pf*PI4K was identified as the target for NCATS-SM3710 through resistance selection studies.

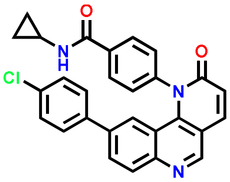

Gametocyte EC_{50}: 0.108 µM
*Pf*NF54 EC_{50}: 0.024 µM
mTOR IC_{50}: 0.795 µM
*Pf*PI4K IC_{50}: 0.002 µM

Figure 2.2: Structure of NCATS-SM3710, a *Pf*PI4K inhibitor. This compound also exhibited activity against multiple stages of the *P. berghei* life cycle.

2.2. Aims and specific objectives

2.2.1. Aims

The aim of the work described in this chapter was to develop a structure-activity relationship (SAR) of the MLN0128 series to enhance dual inhibition of *Plasmodium* PI4K and PKG. Using CADD methods, MLN0128 analogues were designed and synthesized with the aim of improving selectivity towards *Plasmodium* PI4K and PKG over human kinases, while maintaining whole-cell activity.

2.2.2. Specific objectives

1. Build a *Pf*PI4K homology model and identify appropriate *Plasmodium* PKG and mTOR crystal structures for molecular docking studies.
2. Design a library of MLN0128 analogues for virtual screening against on-targets (*Plasmodium* PI4K and PKG) and off-target (mTOR).
3. Synthesize the prioritized MLN0128 analogues based on molecular docking studies.
4. Screen the synthesized MLN0128 analogues for whole cell antiparasitic activity, *Plasmodium* PI4K and PKG, and human PI4K and mTOR enzymes.
5. Perform solubility studies.

The cascade followed in the design of MLN0128 analogues is illustrated in **Figure 2.3**.

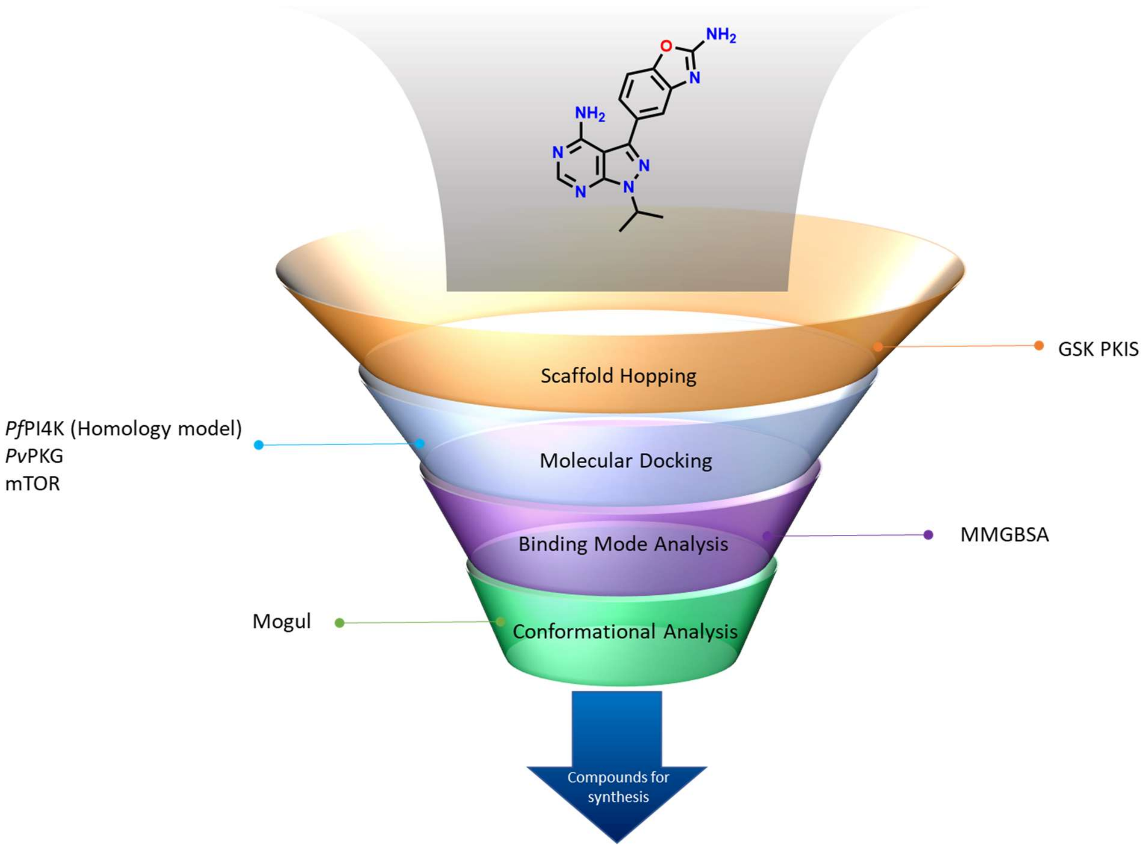

Figure 2.3: Cascade followed for the design of MLN0128 analogues. Using the GSK published kinase inhibitor set (PKIS)[29], scaffold-hopping was used to design MLN0128 analogues. These were then docked into the targets of interest: *Pf*PI4K, *Pv*PKG, and the off target mTOR. The binding poses and conformation of the ligand were then analyzed to select a final list of compounds for synthesis.

2.3. *Pf*PI4K homology modeling

2.3.1. Introduction

Since a structure-based approach was envisaged for the design of MLN0128 analogues, it was crucial that structural information of the targets is available. Currently, the crystal structure of *Plasmodium* PI4K remains to be elucidated. In literature, when using structure-based methods, it is common practice to build a homology model to inform molecular design.[30-34] Similarly, homology modeling was used here as an alternative method to obtain the structure of *Plasmodium* PI4K. In homology modeling, a similar protein with a known structure (referred to as the template) is aligned to the query protein sequence (*Pf*PI4K). This is used as a foundation in the prediction of the *Pf*PI4K structure. The model is then optimized and validated using known *Pf*PI4K inhibitors.

2.3.2. Identification and selection of templates

In a genome-wide or gene-by-gene scale, PlasmoDB (http://PlasmoDB.org) is a functional genomic database providing a vital resource for visualization and data analysis of *Plasmodium* species.[35] The target sequence of *Pf*PI4K was obtained from this database (PlasmoDB ID: PF3D7_0509800).

The National Centre for Biotechnology Information Basic Local Alignment Search Tool (NCBI-BLAST) can be used to search for local similarity between protein sequences.[36] It compares sequences using an algorithm, optimized for speed, to search for optimal local alignments in sequence databases to match the query sequence of *Pf*PI4K. A BLAST similarity score (S) is calculated to rank alignments. This is the sum of gap and substitution scores. The gap score is the sum of L and G, where L is the gap extension penalty and G is the gap opening penalty. The mathematical definition of the BLAST score and its parameters are shown in **Figure 2.4**.

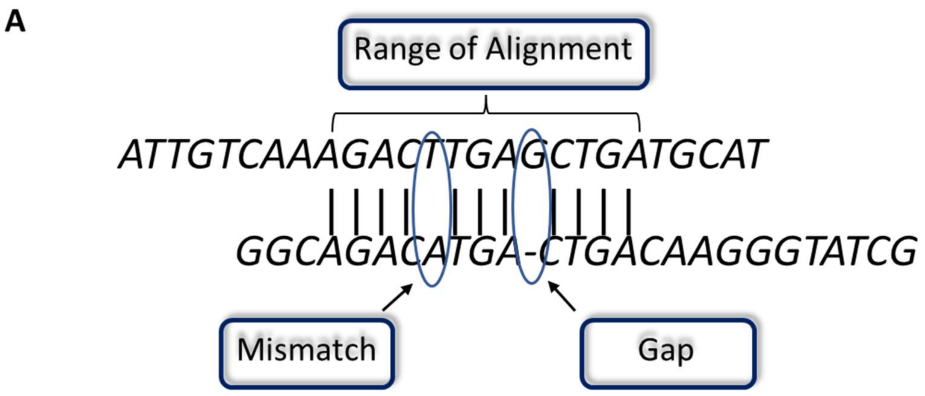

B

$$S = \Sigma(\text{identities, mismatches}) - \Sigma(\text{gap penalties})$$

$$\text{Score} = \text{Max}(S)$$

Figure 2.4: (**A**) Parameters used to calculate the BLAST score, (**B**) mathematical equation used to calculate the BLAST score

A sequence similarity search was conducted using the BLAST similarity search algorithm to screen the *Pf*PI4K target sequence against database entries with deposited structures in the Protein Data Bank (PDB). This database stores structural data for large biological molecules, such as proteins and nucleic acid found in all organisms, in a three-dimensional (3D) format.[37]

According to results from the similarity search of the whole structure and consistent with published articles[31-34], the human PI4KIIIβ enzyme crystallized in a complex with the human PI4K inhibitor PIK93 (PDB Code: 4D0L) was the closest structural homologue (BLAST similarity score with *Pf*PI4K = 42%).[38] It was therefore selected as the most suitable template for the homology model. Other proteins identified (e.g., PDB ID: 6GL3[39]) all shared the same construct as PI4KIIIβ.

The crystal structure of human PI4KIIIβ comprises two domains: a PI3K-related kinase domain (residues 306–801) and the right-handed helical solenoid (residues 128–243). The PI4KIIIβ kinase domain consists of two lobes: the largely helical C-terminal lobe and the N-terminal containing an antiparallel five-stranded β sheet. Located in a cleft between the two kinase domain lobes is the ATP binding site. PIK93 is bound into the ATP binding pocket and forms hydrogen bonds with the hinge (**Figure 2.5**).

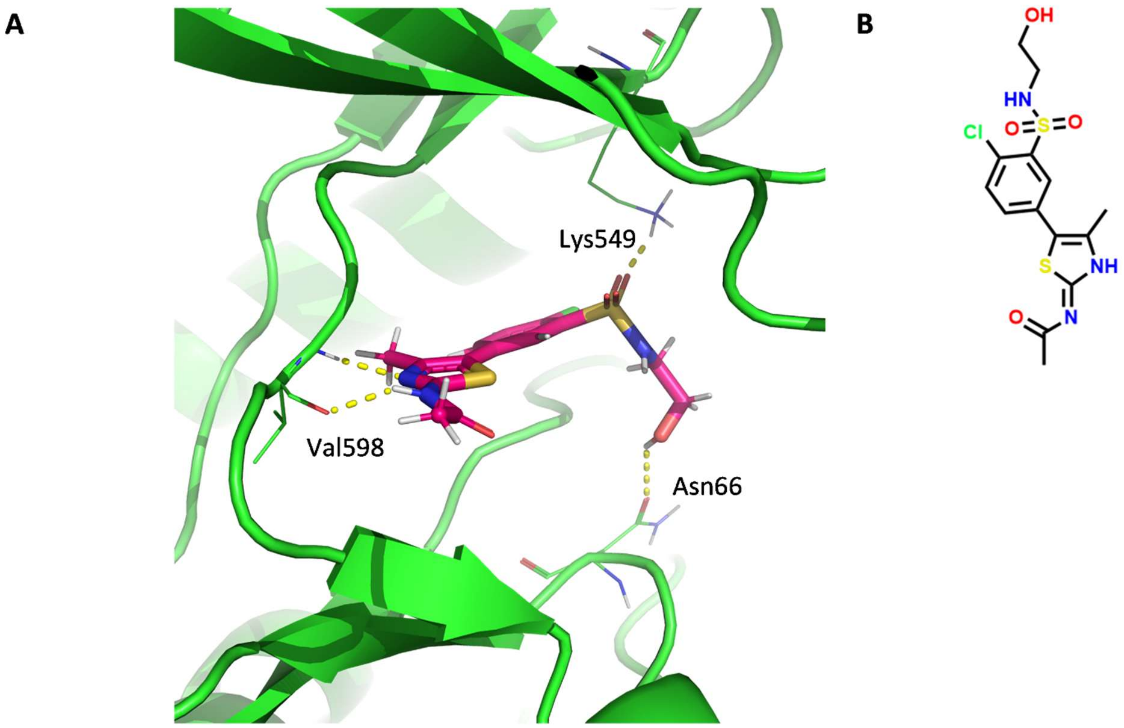

Figure 2.5: (**A**) The ATP-binding site of HuPI4KIIIβ (PDB ID: 4D0L) with the co-crystallized ligand PIK93. The interacting residues are labelled and shown. (**B**) The 2D structure of PIK93.

2.3.3. Sequence alignment

The *Pf*PI4K sequence (1021–1524) was aligned to the template sequence (HuPI4KIIIβ) using the alignment method in the structure prediction protocol in the Prime[40] Module within Maestro v.11.5.011 software GUI.[41] The alignment was performed using the ClustalW method which generates a hierarchy for alignment by performing pairwise cluster analysis on the data.[42] The sequence alignment was also screened against the Pfam database to identify the globally conserved residues belonging to the phosphatidylinositol-3 and 4-kinase family.[43] Based on this analysis, seven of a possible eight conserved residues identified by the algorithm were present and aligned with the only non-matched residue (*Pf*PI4K P1448) falling outside of the ATP binding site. Alignments of conserved residues are shown in **Figure 2.6**. Apart from the Phe638/Phe1394 alignment, the aligned residues belong to the ATP binding site.

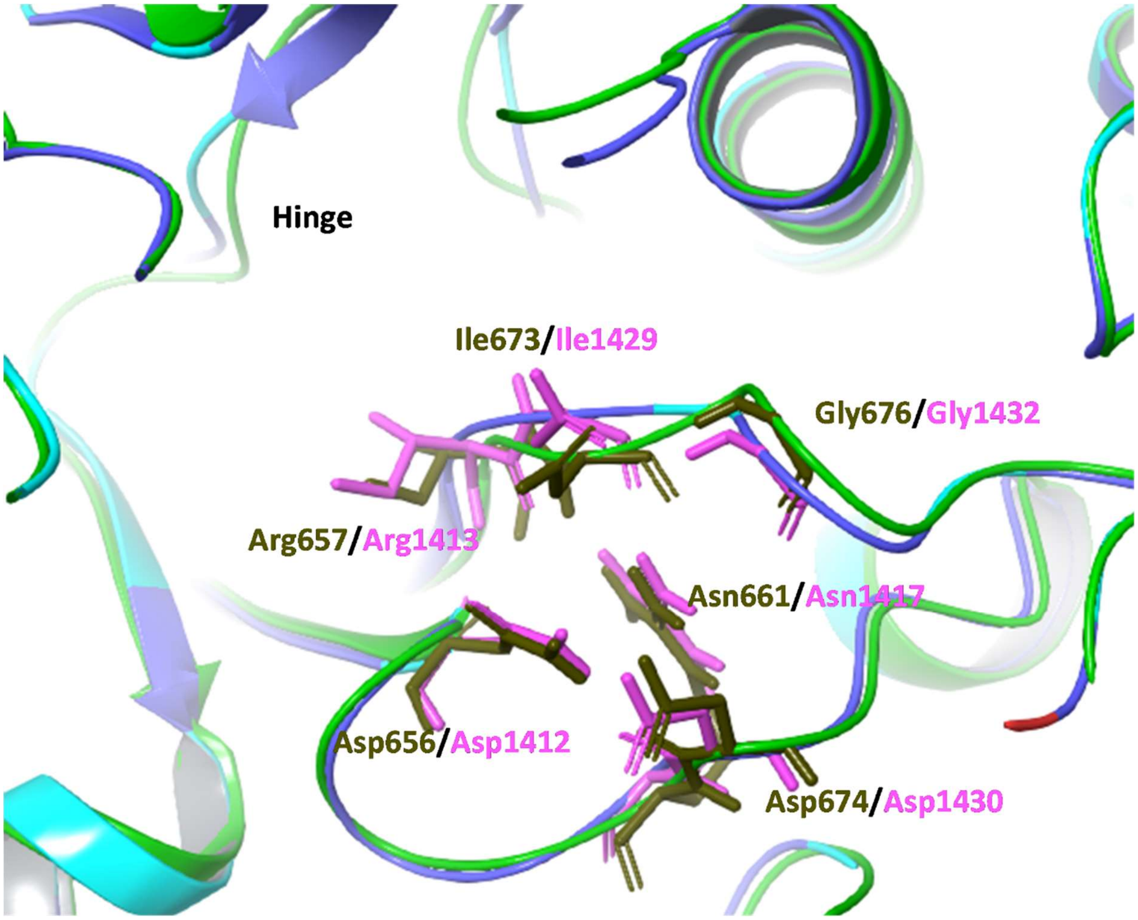

Figure 2.6: Alignment of globally conserved residues in the ATP binding site. HuPI4KIIIβ is shown in green (PDB ID: 4D0L) while the cyan and purple ribbons are part of the *Pf*PI4K homology model. Pink and brown residues belong to HuPI4KIIIβ and *Pf*PI4K, respectively.

However, the mismatch of the HuPI4KIIIβ Ala692 and *Pf*PI4K Pro1448 residues is far from the active site of the kinase, as shown in **Figure 2.7**.

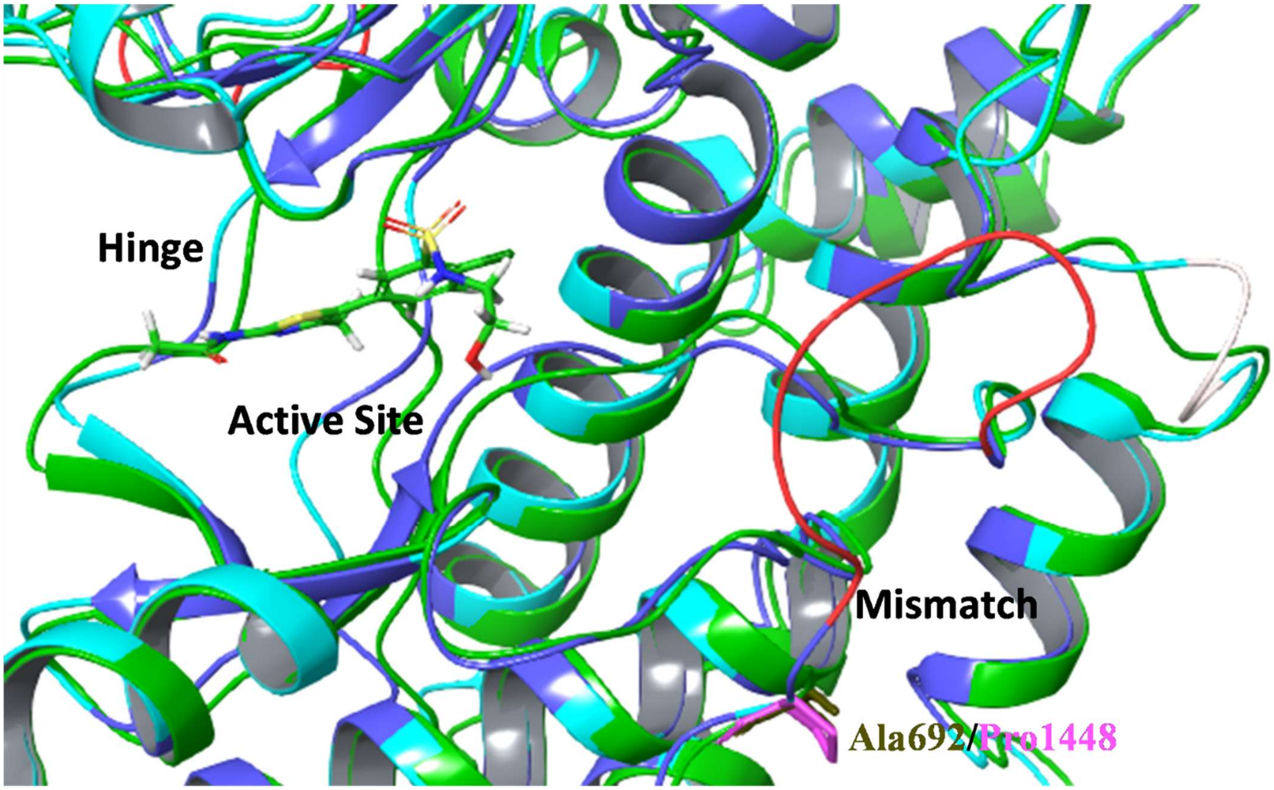

Figure 2.7: Illustration showing that the mismatch of the Ala692/Pro1448 is far from the active site

The expectation value (E-value) is a statistical parameter that provides insight into whether a similarity would occur by chance. If the E-value is $<10^{-5}$, the probability that a sequence belongs to the same family is 79.5%. Therefore, an E-value is deemed acceptable when it is $\leq 10^{-5}$. The calculated E-value for this sequence alignment was $5.9e^{-29}$. The mathematical representation of the E-value is shown in **Equation 2.1**, where m and n are the length of the database and query sequence, respectively. K is the constant associated with the scoring matrix while lambda (λ) is the Gumble distribution constant. They are referred to as the natural scales for the scoring system and search space size respectively.[44]

$$\text{E-value} = K*m*n*e^{-\lambda s}$$

Equation 2.1: Mathematical representation of the expected value calculated during sequence alignment.

2.3.4. Model building and loop modelling

To close gaps and construct insertions, the *Pf*PI4K homology model was built using the knowledge-based method in the Prime Module and was then followed by loop refinement. Compared to α-helices and β-strands, loops exhibit higher structural variability, making them more difficult to model.[45]

The alignment of Tyr1356 in *Pf*PI4K onto the Pro597 in HuPI4KIIIβ on the hinge loop created a difference in the conformation of the hinge loop because of the distortion observed in the HuPI4KIIIβ structure. The hinge loop was therefore refined to establish a proper hinge conformation, which was then validated in the next section using known *Pf*PI4K inhibitors. The loops involved in the ATP binding site were then refined using the implicit solvent model (VSGB[46]) and the OPLS3e forcefield.[47]

2.3.5. Model optimization and validation

Once prepared, optimization and validation of the homology model commenced. The MLN018 ligand was prepared and docked into the ATP-binding site of the homology model to get a global minimum established. Residues within a 10-Å radius of the ligand were minimized using the VSGB solvation model and the OPLS3e forcefield. The Ramachandran plot was used to determine the quality of the model. This is a plot of the torsional angles (phi and psi) of amino acids contained within a protein structure that is used for comparison with the heatmap of all proteins in the PDB. The amino acid residues that fall out of the acceptable region of the Ramachandran plot have conformations that are not possible due to steric hindrance. In the homology model, 98.8% of residues were properly aligned and in favored regions when compared to structures in the PDB (**Figure 2.8**). The remaining residues were in the disallowed regions, although this did not include any of the amino acids in the ATP binding site.

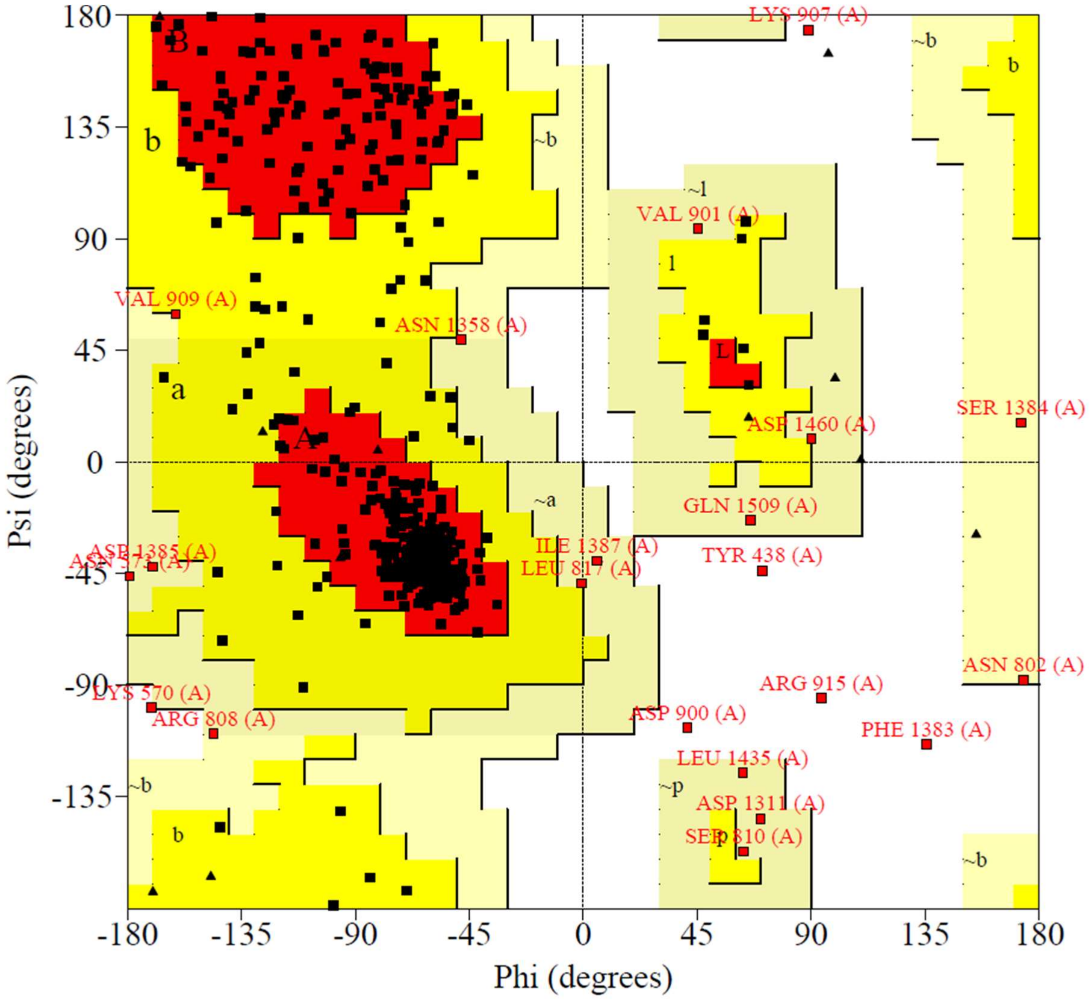

Figure 2.8: Ramachandran plot of the *Pf*PI4K homology model

Of the modelled residues, 84.1% occupy the most favored regions (red); 11.5% occupy allowed regions (yellow); 3.2% occupy generously allowed regions (light yellow); and 1.3% occupy disallowed regions (white). This is unlike the values reported for a recently published Ramachandran plot of a *Pf*PI4K homology model which had 77 % in the most favored regions, 19.7% in the allowed regions, 2.6% in the generously allowed regions and 0.7% in the disallowed regions.[48]

The model was then validated against five known kinase inhibitors (**Table 2.1**) using the docking protocol shown in **section 6.1.2**.

Table 2.1: Ligands used to validate the *Plasmodium falciparum* phosphatidylinositol-4 kinase (*Pf*PI4K) homology model

Compound	**Structure**	**Target**	**IC_{50} (nM)**
MMV390048[49]	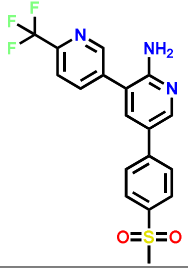	*Pv*PI4K	3.4
KDU691[50]	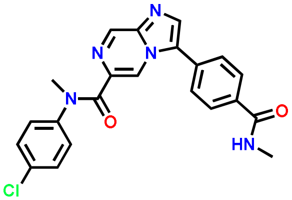	*Pv*PI4K	1.5
BQR695[51]	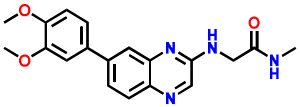	*Pv*PI4K	3.5
KAI407[52]	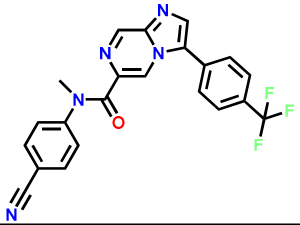	*Pf*PI4K	50 ± 16
KAI715[33]	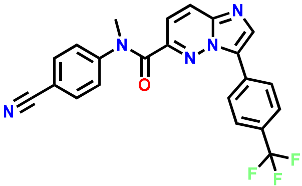	*Pf*PI4K	11

The *Pf*PI4K inhibitors KAI715 and KDU691 were used as examples to demonstrate the favorable poses used to validate the *Pf*PI4K homology model (**Figure 2.9**). Favorable poses depend on the hinge binding moiety. In KAI715, the imidazole of the imidazopyridazine core forms the hinge interaction, while the imidazole of the imidazopyrazine core of KDU691 forms the same interaction. The success of this orientation is confirmed by comparing the orientation of similar co-crystallized ligands, such as the imidazopyridazine inhibitor in the human Pim-1 kinase (PDB ID: 5KZI).[53] An unfavorable pose would be the flip of this orientation in which the pyridazine or pyrazine core would interact with the hinge region.

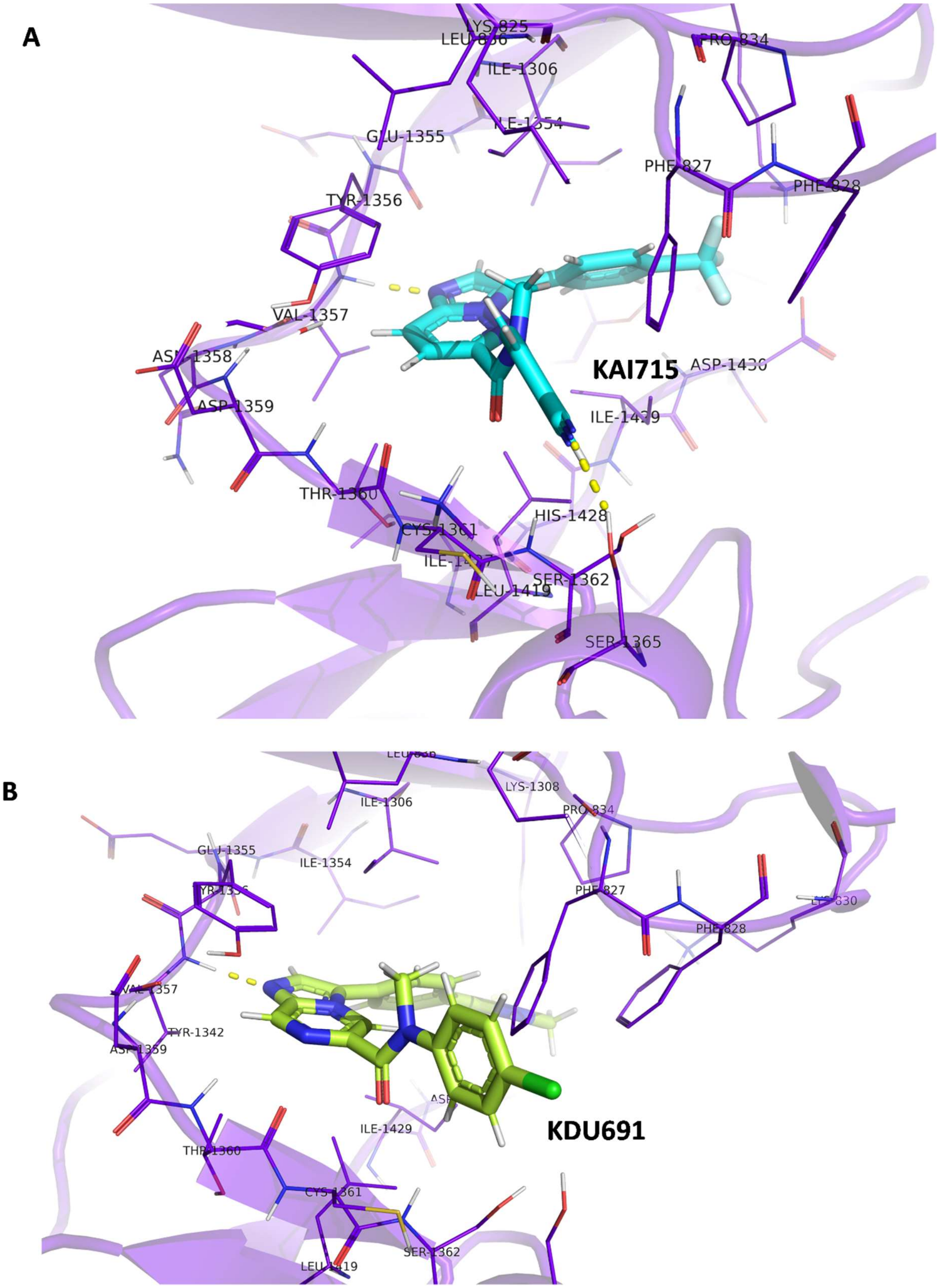

Figure 2.9: KAI715 (**A**) and KDU691 (**B**) docked into *Pf*PI4K (purple) to validate the homology model.

2.4 Design of MLN0128 analogues

As a target-based approach was employed in this project, molecular docking studies were carried out to design MLN0128 analogues. In molecular docking studies, the primary objective is to score the ligand library and preferentially rank active compounds ahead of inactive compounds.[54] This allows the maximum number of active ligands to be identified as early as possible. For successful molecular docking studies, target structures must be determined. The same kinase can be crystallized in multiple conformations depending on the bound ligand and other experimental factors. Therefore, if possible, it is paramount to select a crystal structure with which a ligand analogous to the compound of interest is co-crystallized because similar binding pocket conformations are induced by similarly shaped ligands.

Therefore, *Pv*PKG co-crystallized with a pyrazolo[3,4-d]pyrimidine analogue (PDB ID: 5F0A), the ligand most similar to MLN0128, was selected.[55] The mTOR structure co-crystallized with 2-[4-amino-1-(propan-2-yl)-1H-pyrazolo[3,4-d]pyrimidin-3-yl]-1H-indol-5-ol (PDB ID: 4JT5), another pyrazolo[3,4-d]pyrimidine analogue, was used for docking experiments.[18] Both co-crystallized ligands have pyrazolo[3,4-d]pyrimidine cores as shown in **Figure 2.10**.

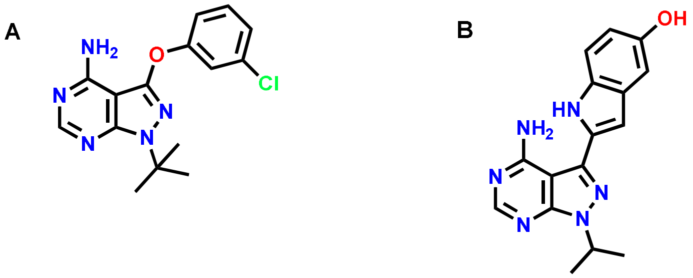

Figure 2.10: Co-crystallized ligands of *Pv*PKG (**A**: PDB ID: 5F0A) and mTOR (**B**: PDB ID: 4JT5). These are both pyrazolo[3,4-d]pyrimidine analogues.

2.4.1. Molecular docking of MLN0128

Before designing analogues, MLN0128 was docked into the targets to identify strategies to improve inhibition and selectivity. To rationalize MLN0128 inhibition *in silico*, the plausible docking poses of MLN0128 bound to the targets needed to be demonstrated. Following the docking protocol in the experimental section (**section 6.1.2**), MLN0128 was docked into its original target mTOR (PDB ID: 4JT5), followed by docking in the homology model, *Pf*PI4K, and the *Pv*PKG crystal structure (PDB ID: 5F0A). The accuracy of the docking protocol described in **section 6.1** was successfully shown by reproducing the binding pose of co-crystallized ligands in their respective crystal structures. The root mean square deviation (RMSD) of the crystallographic pose of the ligand compared with the generated docked pose was 0.23 for *Pv*PKG and 0.023 and mTOR, a value of less than one is preferred. This revealed that interactions were formed between the ligand and target.

Docked pose of MLN0128 in human mTOR

Mimicking the adenine ring of ATP, the 4-amino group on the pyrazolopyrimidine core forms hinge interactions, particularly a hydrogen bond, with the backbone carbonyl of Gly2238. The N-3 nitrogen participates in a hydrogen bond with the amide group of Val2240. Extending into the back pocket, the benzene ring of the benzo[d]oxazole forms a π-stacking interaction with Tyr2225, while the 2-amino group forms a hydrogen bond with Asp2357, a conserved residue within the catalytic αC-helix (**Figure 2.11**). The oxygen atom on the benzo[d]oxazole moiety is involved in hydrogen bonding with Asp2195. No interactions take place in the front pocket.

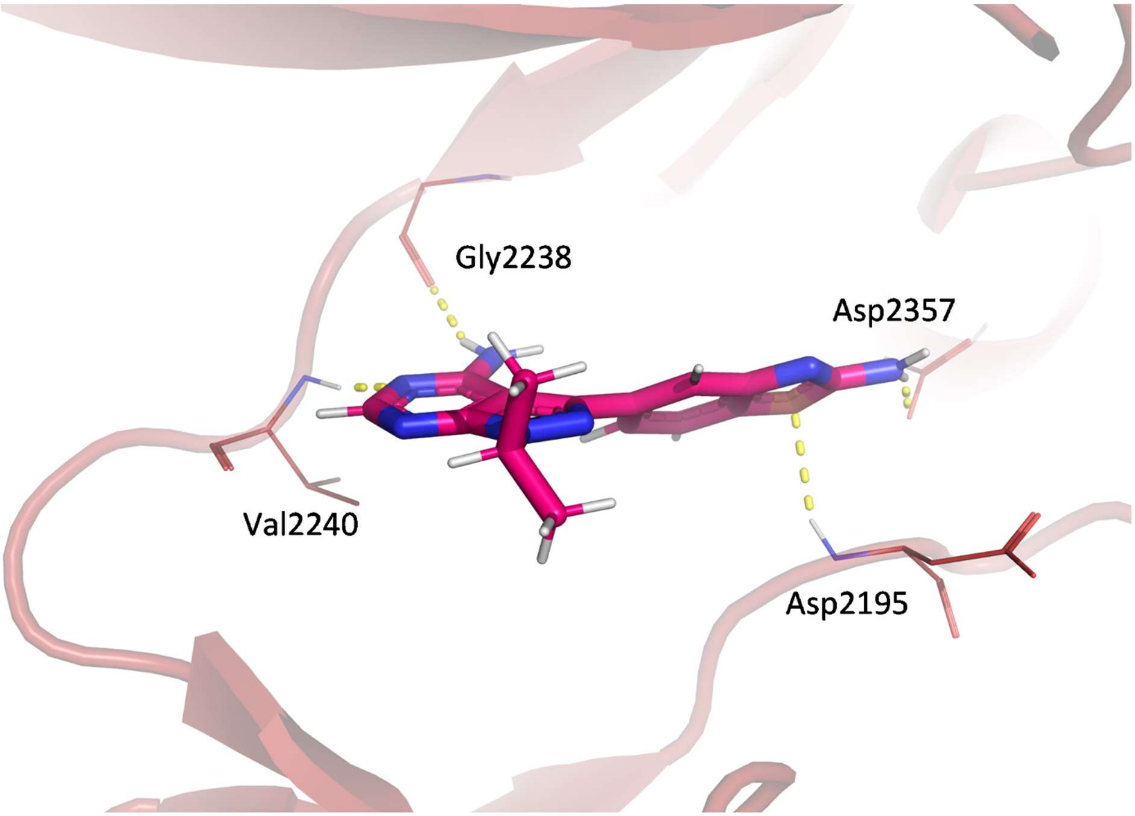

Figure 2.11: Mammalian target of rapamycin (mTOR; red) binding with MLN0128 (magenta). mTOR, red; MLN0128, magenta. Interacting residues and hydrogen bonds are shown.

Docking pose of MLN0128 into PfPI4K

Similar to the mTOR-MLN0128 docked complex, the pyrazolo[3,4-d]pyrimidine core forms hinge interactions. The 4-amino group forms a hydrogen bond with the backbone carbonyl of Glu1355 (Gly2238 in mTOR) and the N-3 nitrogen participates in a hydrogen bond with the amide of Val1357 (Val2240 in mTOR). The pyrazole moiety forms a face-to-edge π-stacking interaction with Phe827. With the 2-amino substituent of the benzo[d]oxazole in the back pocket, a hydrogen bond is formed with both Asp1430 (Asp2195 in mTOR) and Glu1316 (Asp2357 in mTOR; **Figure 2.12**). Similar to MLN0128 in mTOR, no interactions take place in the front pocket.

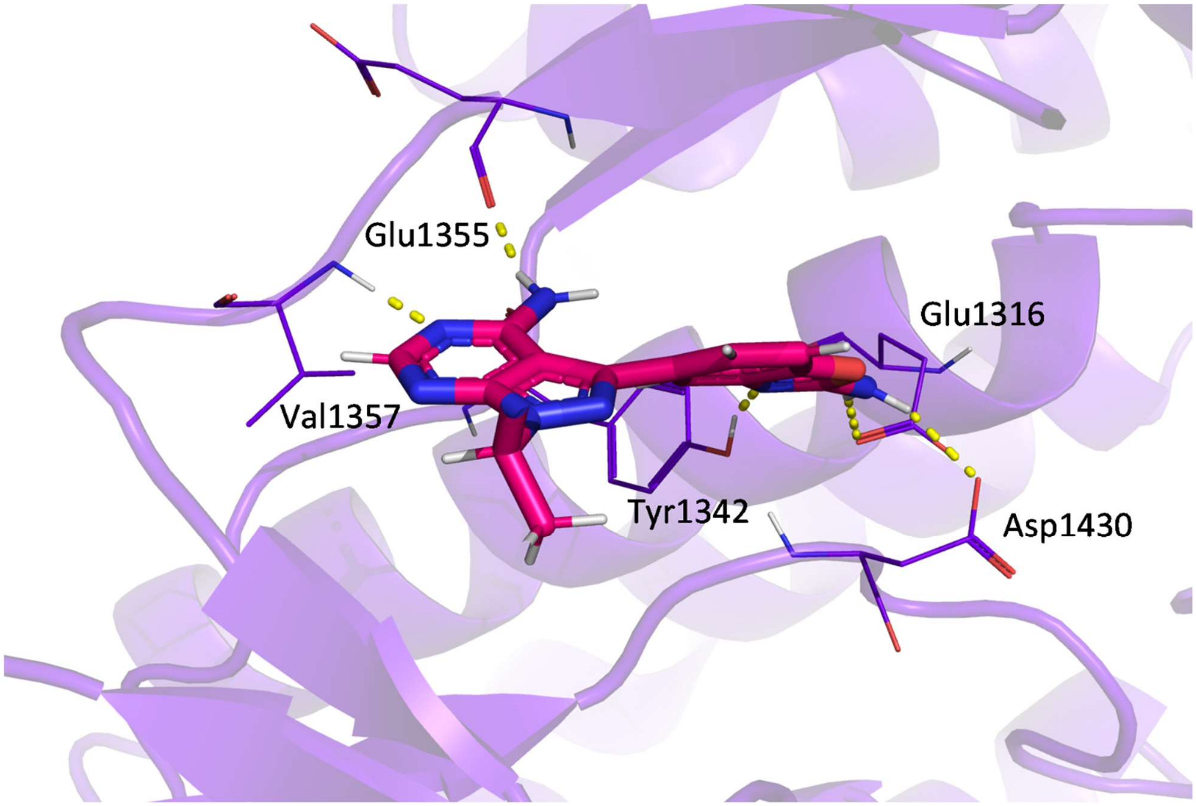

Figure 2.12: Phosphatidylinositol-4 kinase **(**PI4K; purple) binding with MLN0128. PI4K, purple; MLN0128, magenta. Interacting residues and hydrogen bonds are shown.

Docking pose of MLN0128 into PvPKG

As expected, the pyrazolo[3,4-d]pyrimidine core also forms hinge interactions. The 4-amino substituent forms a hydrogen bond with the backbone carbonyl of Glu612 (Gly2238 in mTOR; Glu1355 in *Pf*PI4K) and the N-3 nitrogen participates in a hydrogen bond with the amide of Val614 (Val2240 in mTOR; Val1357 in *Pf*PI4K). Similarly, in the back pocket, there is a π-cation interaction between the benzo[d]oxazole group and the catalytic lysine, and the N-3 also forms a hydrogen bond with Asp675 (Asp2195 in mTOR; Asp1430 in *Pf*PI4K; **Figure 2.13**). The amino group on the aforementioned moiety forms an H-bond with Glu582 in the back pocket. The corresponding residues in *Pf*PI4K and mTOR are Glu1316 and Asp2357, respectively. There are also no interactions in the front pocket.

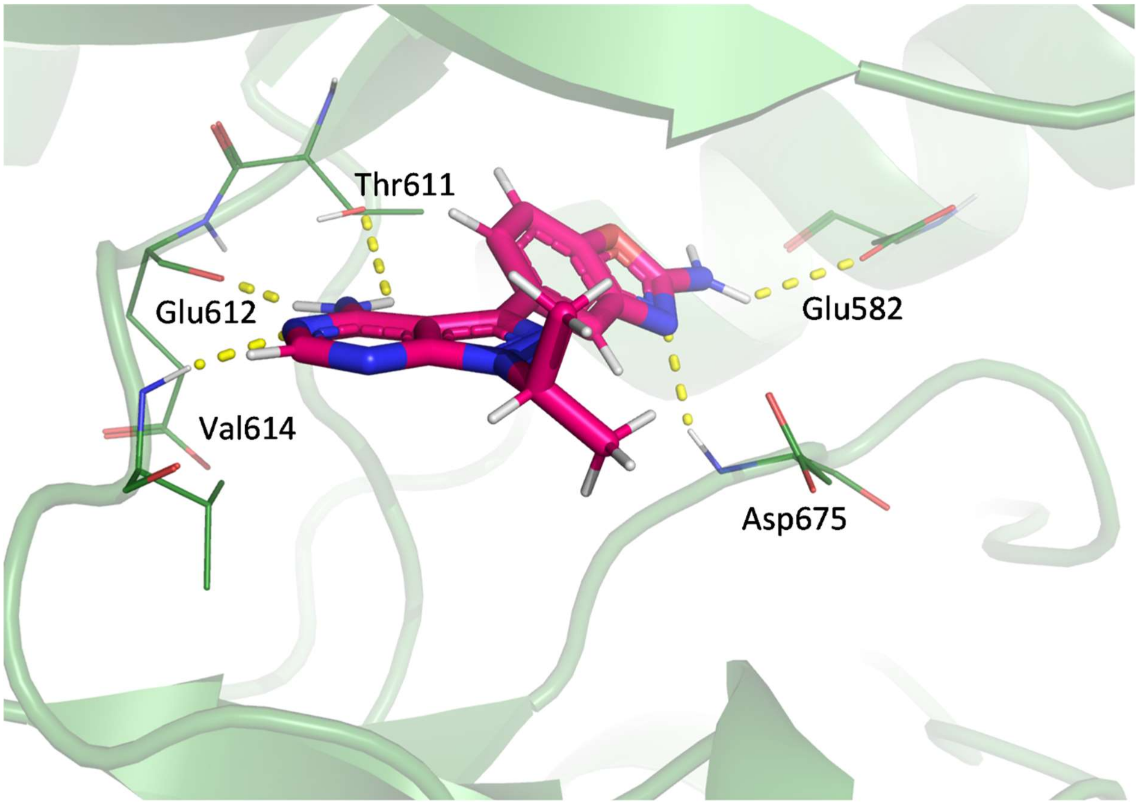

Figure 2.13: cGMP-dependent protein kinase (PKG) binding with MLN0128. PKG, green; MLN0128, magenta. Interacting residues and hydrogen bonds are shown.

Having predicted the orientation of MLN0128 in the binding sites, the next step was to identify strategies to improve the potency and selectivity of MLN0128.

2.4.2. Design of MLN0128 analogues

The binding sites of the *Plasmodium* targets *Pv*PKG and *Pf*PI4K were each aligned to the binding site of the off-target human kinase mTOR (**Figure 2.14**). This was done to identify aligned residues that may be exploited to improve selectivity of the *Plasmodium* kinases over the human kinase.

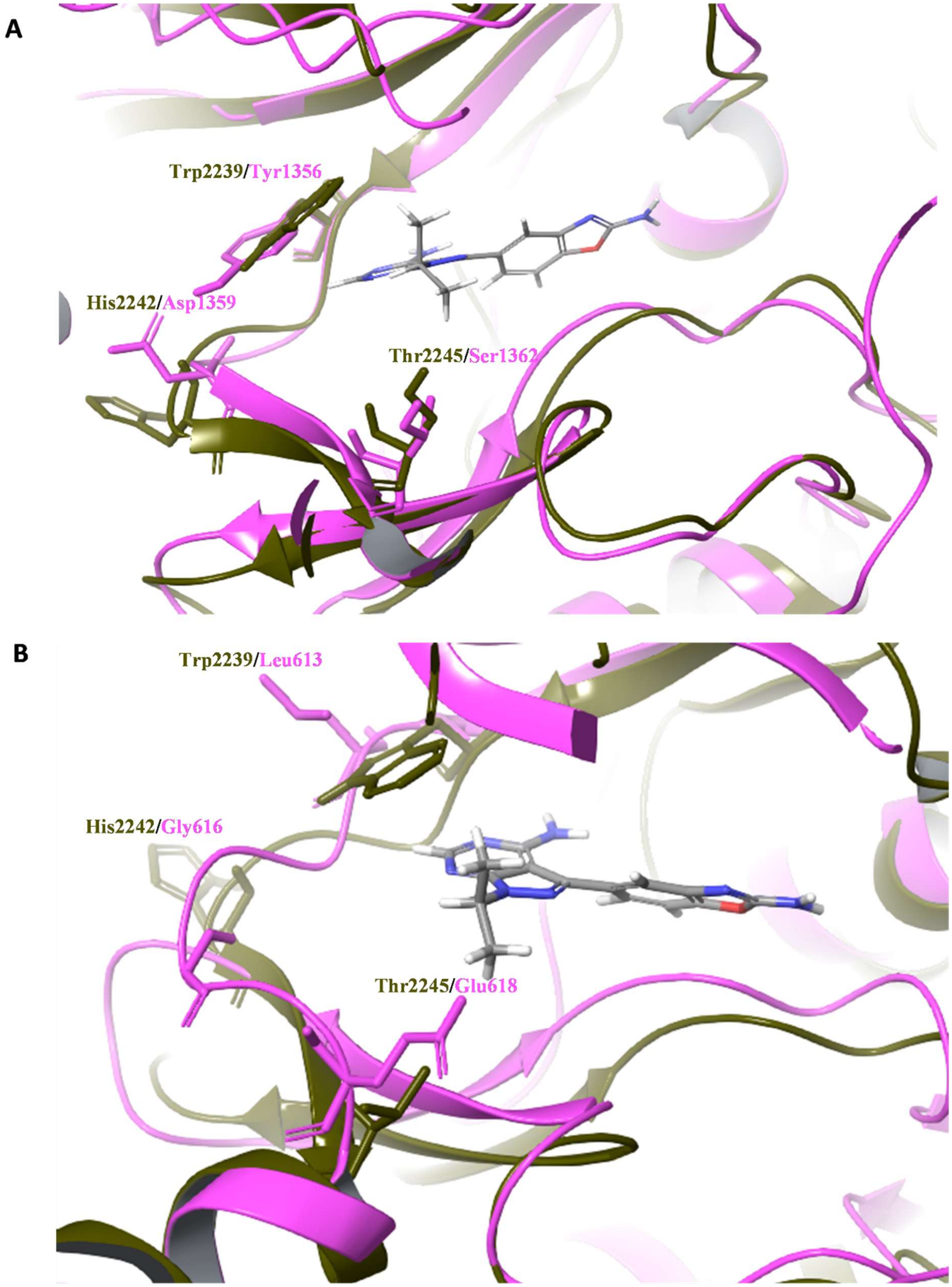

Figure 2.14: **(A)** *Pf*PI4K homology model (pink) and (**B**) *Pv*PKG crystal structure (pink) aligned to mTOR (brown).

The tyrosine (**Tyr1356**) and charged aspartic acid (**Asp1359**) residues found at the hinge loop of *Pf*PI4K were replaced with the bulky tryptophan (**Trp2239**) and histidine (**His2242**) at the respective positions on the human mTOR target. The amino acid residues at the same position in *Pv*PKG are **Leu613** and **Gly616**. The human kinase mTOR contains a threonine (**Thr2245**) at the front pocket while *Pv*PKG contains a glutamic acid (**Glu618**) residue at the same position. The front pocket in *Pf*PI4K has a serine residue. Because of the observed difference in aligned residues in the front pocket, MLN0128 analogues should be designed to interact with those residues by replacing the isopropyl in MLN0128.

Using the GSK published kinase inhibitor set (PKIS), a library of MLN0128 analogues was designed, retaining the hinge and back pocket interactions by fixing the 4-amino pyrazolo[3,4-d]pyrimidine core and the benzoxazole moiety. The PKIS, which comprised 367 compounds, was obtained from the ChEMBL database and imported into the scaffold decomposition module of the Canvas software.[29, 56] This scaffold decomposition method exhaustively decomposed the structures, by removing monovalent atoms until only linker and ring atoms remained, subsequently forming Bemis-Murcko scaffolds.[57]

For example, as illustrated in **Figure 2.15**, one of the Bemis-Murcko scaffolds of GSK-571989A is attached to the MLN0128 core using various linkers forming a library of several hundred MLN0128 analogues.

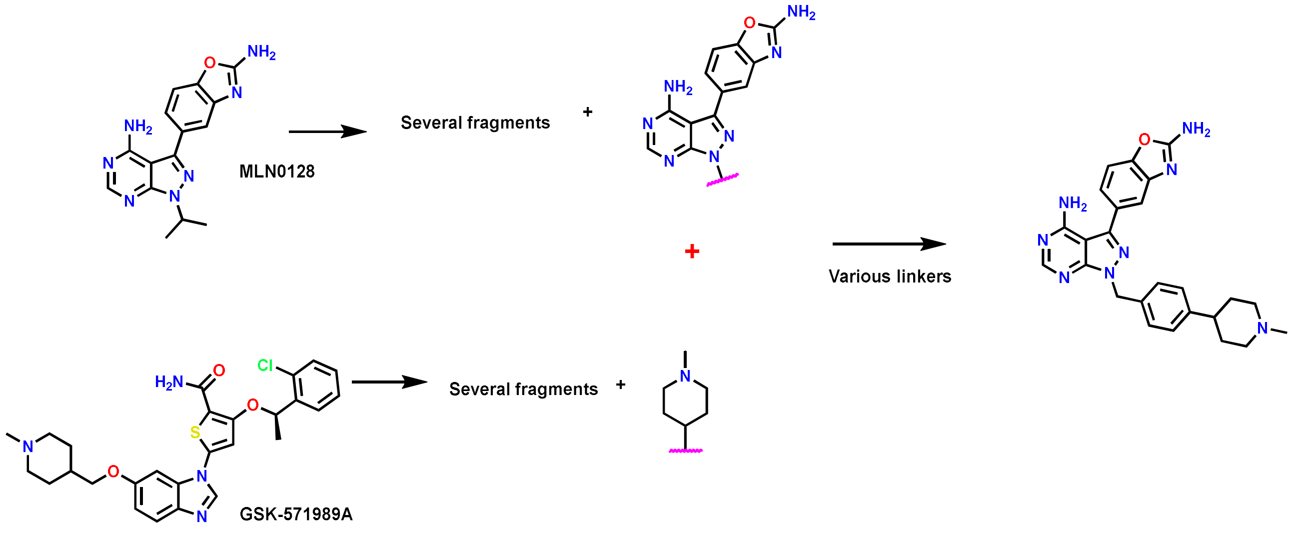

Figure 2.15: Illustration of the scaffold decomposition process involved in the design of MLN0128 analogues.

The library of MLN0128 analogues, built using the scaffold decomposition method, was docked into the targets of interest (*Pf*PI4K, *Pv*PKG, and mTOR) following the docking protocol in **section 6.1.2**. The designed MLN0128 analogues are listed in **Tables 2.2** and **Table 2.3** in addition to their calculated binding energies. These analogues comprised of hydrogen-bond donor moieties, varying in position, to interact with the residues in the front pocket. These moieties gave rise to favorable interactions, namely Asp675 in *Pv*PKG and Tyr1356 in *Pf*PI4K. The methyl linker was also hypothesized to impart high selectivity. The selected analogues showed favorable poses in *Plasmodium* targets and unfavorable poses in the human target (**Figure 2.16**). This was predicted to improve selectivity for the *Plasmodium* targets over the human target(s). The unfavorable poses show the analogue folding into itself, while the favorable poses had the added R-groups stretching into the front pocket of *Pv*PKG and the hinge of *Pf*PI4K.

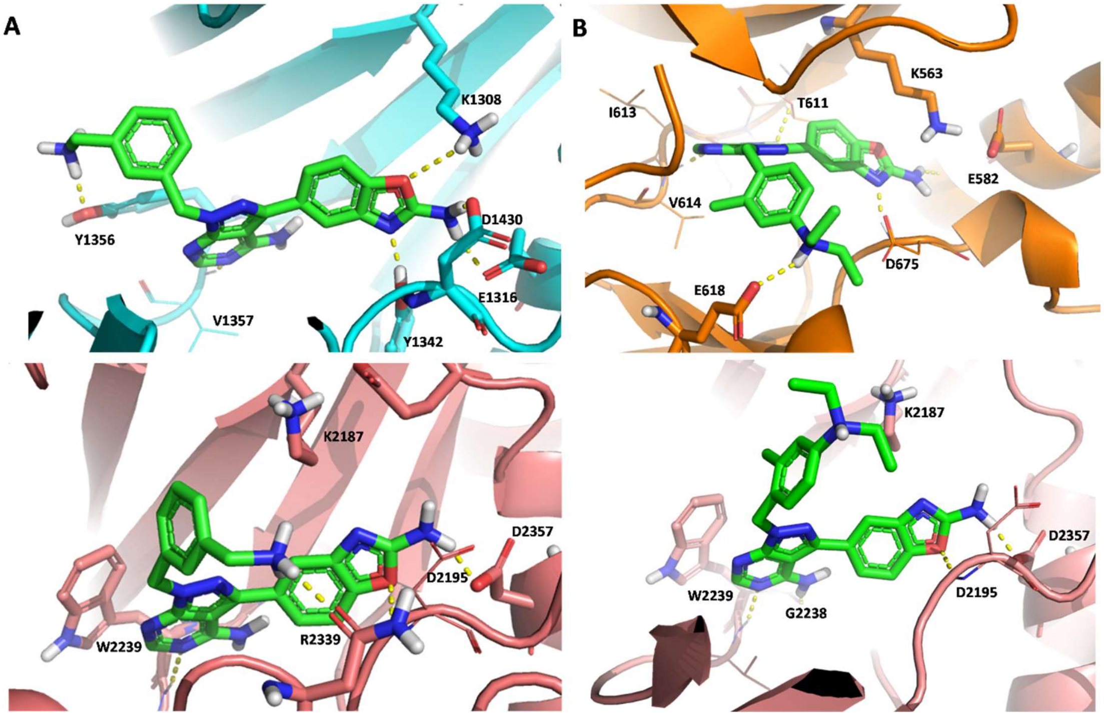

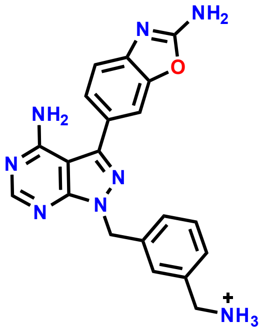

20

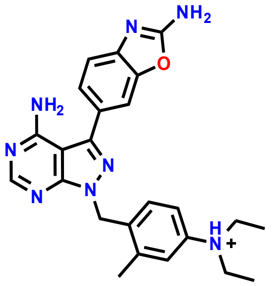

8

Figure 2.16: MLN0128 analogues docked into (**A**) *Pf*PI4K (cyan) and (**B**) *Pv*PKG (orange) with the respective analogues also docked into mTOR to demonstrate favorable and unfavorable poses

Table 2.2: Selected ligands with favorable poses in *P. vivax* cGMP-dependent protein kinase (*Pv*PKG)

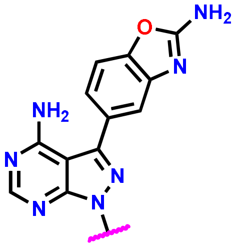

Compound structure	Compound code	PKG pose	mTOR pose
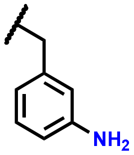	1	Favorable	Unfavorable
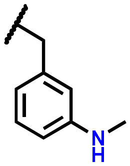	2	Favorable	Unfavorable
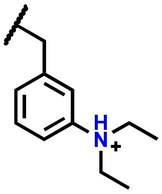	3	Favorable	Unfavorable
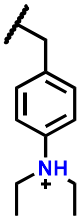	4	Favorable	Unfavorable
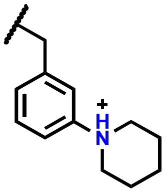	5	Favorable	Unfavorable

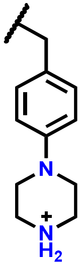	6	Favorable	Unfavorable
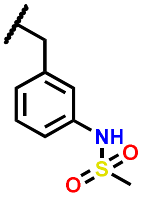	7	Favorable	Unfavorable
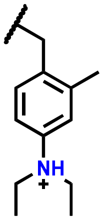	8	Favorable	Unfavorable
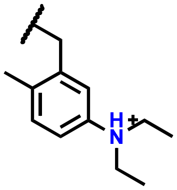	9	Favorable	Unfavorable
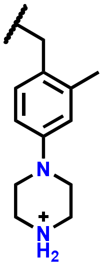	10	Favorable	Unfavorable
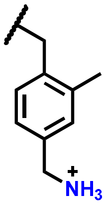	11	Favorable	Unfavorable

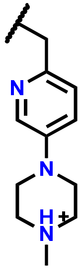	12	Favorable	Unfavorable
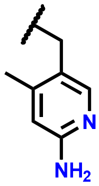	13	Favorable	Unfavorable
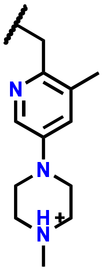	14	Favorable	Unfavorable
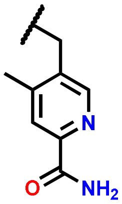	15	Favorable	Unfavorable
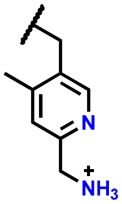	16	Favorable	Unfavorable
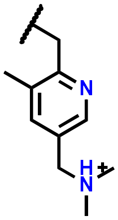	17	Favorable	Unfavorable
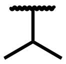	**MLN0128**	**Favorable**	**Favorable**

Table 2.3: Selected ligands with favorable poses in *P. falciparum* phosphatidylinositol 4-kinase (*Pf*PI4K)

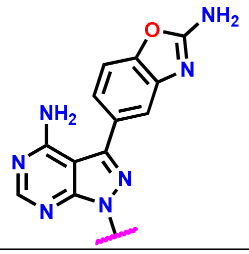

Compound structure	**Compound code**	**PI4K pose**	**mTOR pose**
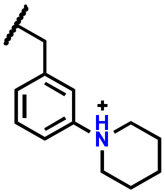	5	Favorable	Unfavorable
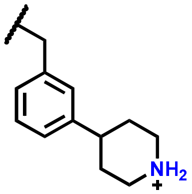	18	Favorable	Unfavorable
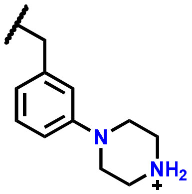	19	Favorable	Favorable
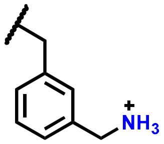	20	Favorable	Unfavorable
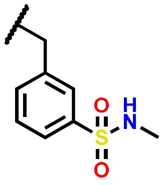	21	Favorable	Unfavorable

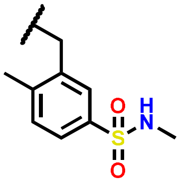	22	Favorable	Unfavorable
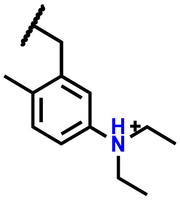	9	Favorable	Unfavorable
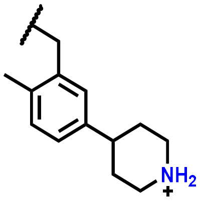	23	Favorable	Unfavorable
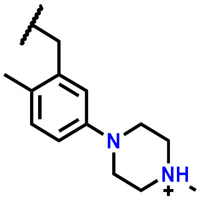	24	Favorable	Unfavorable
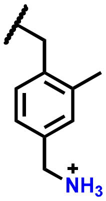	11	Favorable	Unfavorable
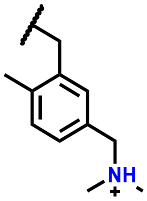	25	Favorable	Unfavorable

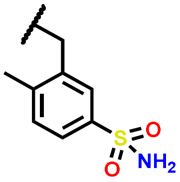	26	Favorable	Unfavorable
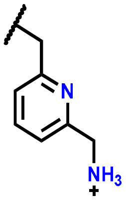	27	Favorable	Favorable
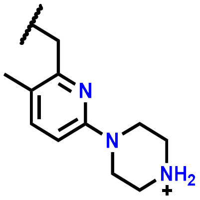	28	Favorable	Unfavorable
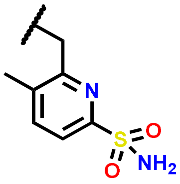	29	Favorable	Unfavorable
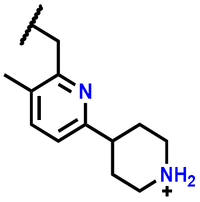	30	Favorable	Unfavorable
	**MLN0128**	**Favorable**	**Favorable**

Combining the compounds in **Table 2.2** and **Table 2.3**, a total of 30 compounds were considered for synthesis. However, taking into account the ease of synthesis, MLN0128 analogues with amide and sulphonamide derivatives at various positions were prioritized for synthesis and proof-of-concept (**Figure 2.17**). The *para* and *meta* positions are predicted to be preferable, although a few *ortho*-MLN0128 analogues were also prioritized for synthesis. The methyl linker was paramount as it was predicted to improve selectivity of *Plasmodium* kinases over human kinases.

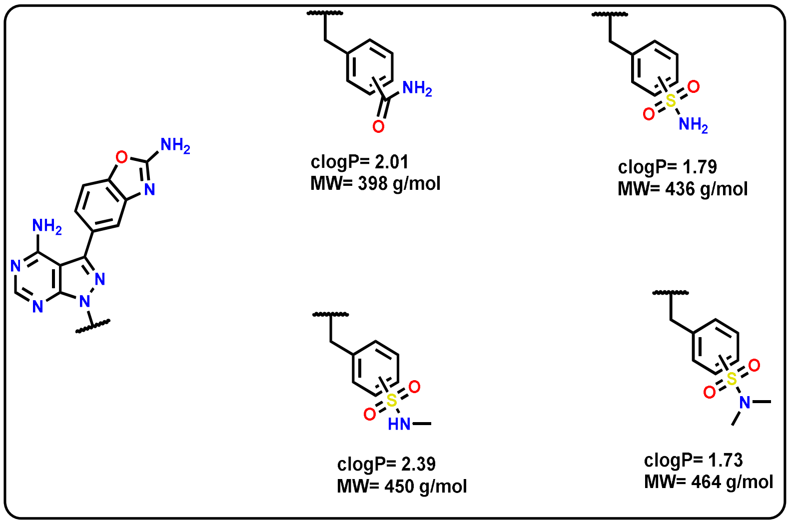

Figure 2.17: MLN0128 analogues selected for synthesis. cLogP, calculated partition coefficient; MW, molecular weight

2.5. Synthesis of MLN0128 analogues

Target compounds were obtained as previously described by Fraser et al (**Scheme 2.1**).[58] The synthetic scheme was not the usual linear scheme, therefore, different sections show how the various intermediates were synthesized.

In summary, condensation of the commercially available 5-amino-1H-pyrazolo-4-carbonitrile with formamide afforded the pyrazolopyrimidine core (**36**). Iodination of this core to form intermediate **37** was achieved using N-iodosuccinimide. The synthesis of the *para*- and *meta*-

amide intermediates (**38a, b**) was done through acid-catalyzed hydrolysis of the appropriate bromomethyl benzonitrile (shown in section A of **Scheme 2.1**). For the *ortho* amide, the 2-(bromomethyl)benzonitrile was attached to 3-iodo-1H-pyrazolo[3,4-d]pyrimidin-4-amine through N-alkylation to form **39**, which was followed by base-catalyzed hydrolysis to afford intermediate **40** (Section B). As illustrated in Section C, the *para*-sulfonamide intermediates (**41a-c**) were synthesized from the commercially available 4-(bromomethyl) benzene sulphonyl chloride where a coupling reaction occurs with the respective amine acting as the nucleophile and DIPEA as the base. To obtain the *meta*-sulphonamides (Section D), respective benzoic acids were first reduced to their corresponding alcohols in the presence of lithium aluminum hydride ($LiAlH_4$) (**42a, b**). Using thionyl chloride ($SOCl_2$), the reduced product was chlorinated to form the desired intermediates (**43a, b**).

The synthesized amides and sulphonamides were introduced to the core scaffold (**37**) via N-alkylation to provide intermediates **45a-h**. Subsequently, 2-amino-1,3-benzoxazole-5-boronic ester (**44**) was synthesized through Suzuki-Miyaura coupling of the commercially available 5-bromobenzo[d]oxazole-2-amine with bis(pinacolato)diborate as shown in Section E. The target compounds (**46a-h**) were obtained via Suzuki-Miyaura coupling of the synthesized boronic ester **44** and intermediates **45a-h**. The palladium catalyst used for the synthesis of the organoborane benzoxazole moiety was 1,1'-bis(diphenylphosphino)ferrocene dichloropalladium (II) in complex with dichloromethane (PdCl2(dppf)·DCM), while tetrakis(triphenylphosphine)palladium was used in the final step to yield the final products. Potassium acetate and sodium carbonate, respectively, were employed to create the basic environment needed.

The yields of the final products synthesized using this synthetic scheme ranged between 4 – 47% are listed in **Table 2.4**. In the presence of compounds with free amino groups, palladiumcatalyzed cross-coupling reactions generally proceed with difficulty. This could, therefore, explain the low yields of **46d** and **46h**.[59, 60]

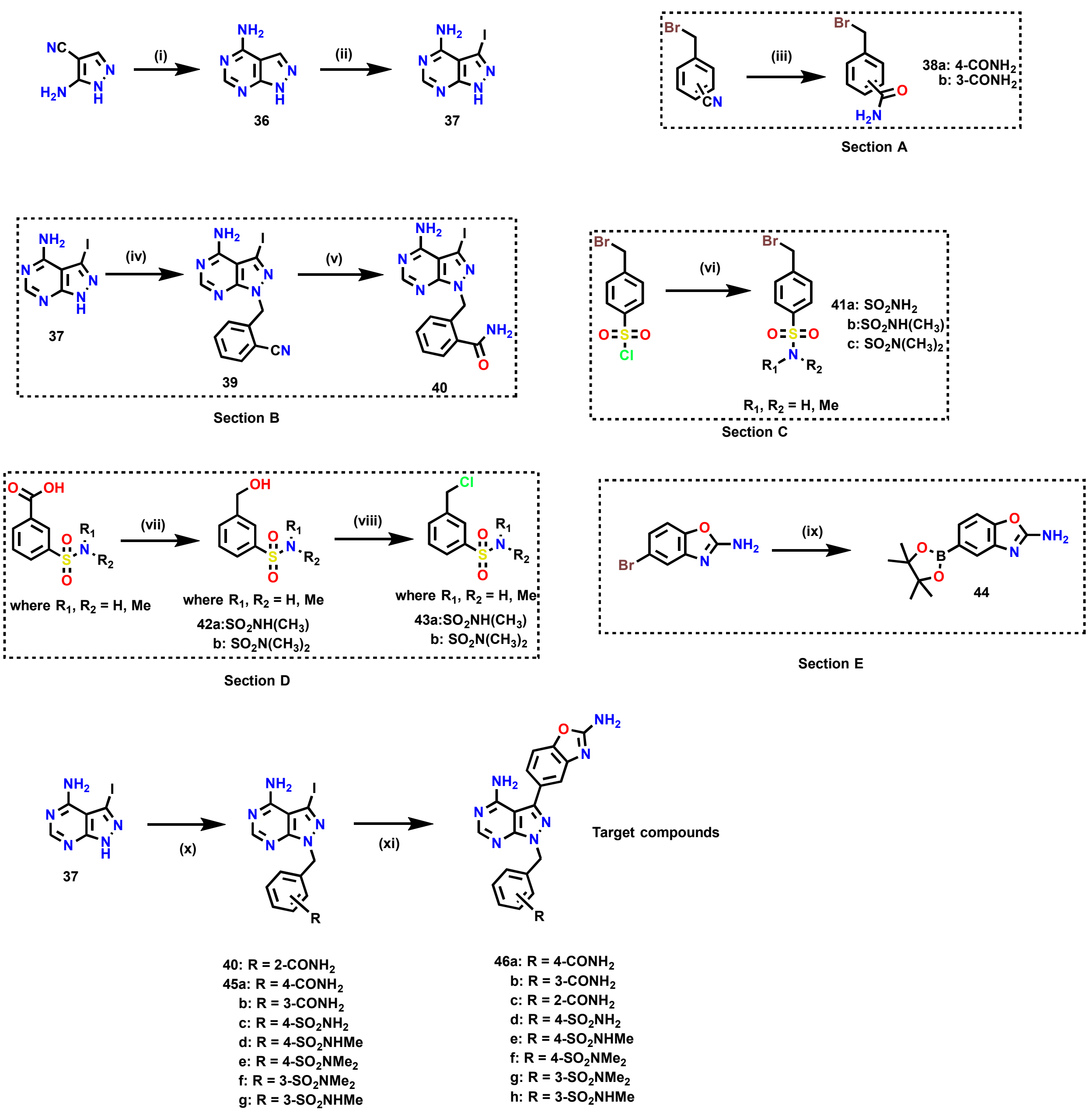

Scheme 2.1: Synthetic scheme for target compounds. *Reagents and conditions*: (i) Formamide, 180 °C, 8 h; (ii) N-iodosuccinimide (NIS), dimethylformamide (DMF), 80 °C, 8 h; (iii) sulfuric acid, 50 °C, 1 h; (iv) 2-(bromomethyl) benzonitrile, K_2CO_3, DMF, 30 °C, 2 h; (v) potassium hydroxide, ethanol/Water (1:1), 80 °C, 2 h; (vi) relevant amine, N,N-diisopropylethylamine (DIPEA), tetrahydrofuran (THF), 0 °C, 2 h; (vii) lithium aluminum hydride ($LiAlH_4$), THF, 0 °C, 2 h; (viii) thionyl chloride ($SOCl_2$), dichloromethane (DCM), 25 °C, 8 h; (ix) bis(pinacolato)diborate, $PdCl_2$(dppf)-dichloromethane (DCM), $C_2H_3O_2K$, 100 °C, 8 h; (x) K_2CO_3, DMF, 30 °C, 2 h; (xi) tetrakis(triphenylphosphine)palladium, Na_2CO_3, 100 °C, 8 h.

Table 2.4: Isolated yields for target compounds synthesized according to **Scheme 2.1**

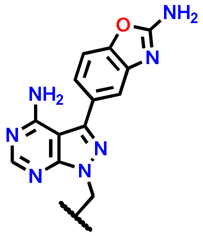

Compound	R	% Yield
46a	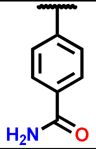	36
46b	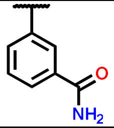	12
46c	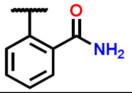	16
46d	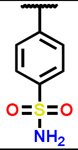	4
46e	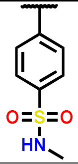	26
46f	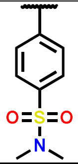	47
46g	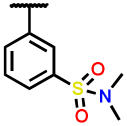	11
46h	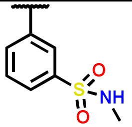	5

2.6. Characterization of key intermediates and target compounds

Proton nuclear magnetic resonance (^{1}H-NMR) and HPLC-mass spectrometry were used to characterize intermediate compounds. ^{13}C-NMR spectra were also analyzed for full characterization of target compounds.

The pyrazolo[3,4-d]pyrimidine core was iodinated using N-iodosuccinimide (NIS). The success of this reaction was confirmed via ^{1}H-NMR spectroscopy, shown in **Section 6.9**. The loss of the proton at the pyrazole moiety was confirmed by the loss of corresponding signal. The highly deshielded proton resonating downfield at δ = 13.78 ppm could still be observed (**Section 6.9**).

The amide and sulphonamide intermediates were then introduced to the iodinated pyrazolo[3,4-d]pyrimidine core through N-alkylation. Using 4-((4-amino-3-iodo-1H-pyrazolo[3,4-d]pyrimidin-1-yl)methyl)-N, N-dimethylbenzene sulphonamide (**45f**) as an example, the ^{1}H-NMR spectrum showed the characteristic aromatic singlet of the pyrazolo[3,4-d]pyrimidine core at δ = 8.21 ppm (**Figure 2.18**).

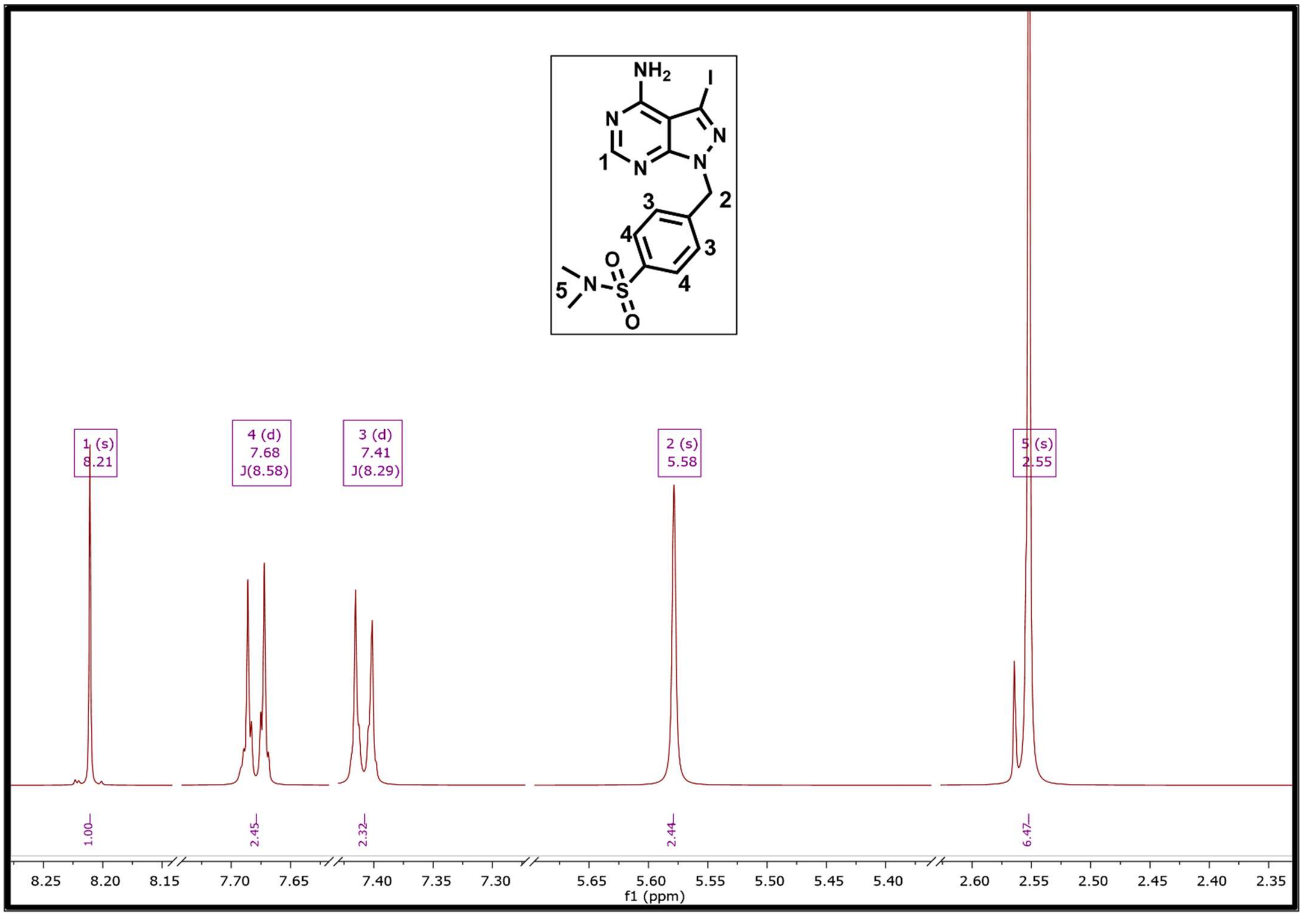

Figure 2.18: ^{1}H-NMR spectrum of 4-((4-amino-3-iodo-1H-pyrazolo[3,4-d]pyrimidin-1-yl)methyl)-N,N-dimethylbenzenesulfonamide (**45f**)

The desired target compounds were synthesized via Suzuki-Miyaura coupling between the appropriate **45f** and the previously synthesized 5-(4,4,5,5-tetramethyl-1,3,2-dioxaborolan-2-yl)benzo[d]oxazol-2-amine.

The ^{1}H-NMR spectrum of the target compound(s) revealed the additional proton signals of the aminobenzo[d]oxazole moiety, with the characteristic doublet of doublets of proton H7, with a J_{meta} and J_{ortho} coupling constants of 8.09 and 1.75, respectively (**Figure 2.19**). The ^{13}C-NMR spectrum also depicts the carbons of the sulphonamide final product (**Figure 2.20**). This spectrum shows the expected signals for the methyl linker (6) and the dimethyl carbons (11) with carbon attached to the amino of the benzoxazole moiety (18) showing a signal at 163.

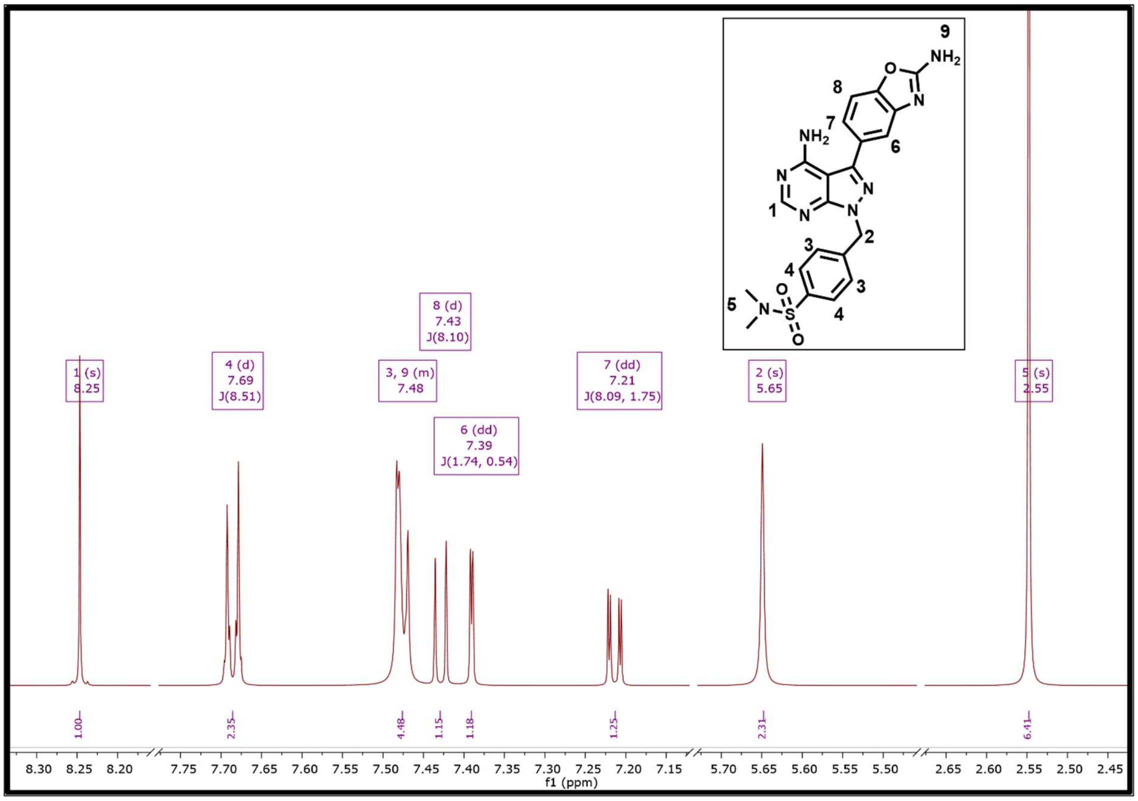

Figure 2.19: ^{1}H-NMR spectrum of a target compound, 4-((4-amino-3-(2-aminobenzo[d]oxazol-5-yl)-1H-pyrazolo[3,4-d]pyrimidin-1-yl)methyl)-N,N-dimethylbenzenesulfonamide (**46f**)

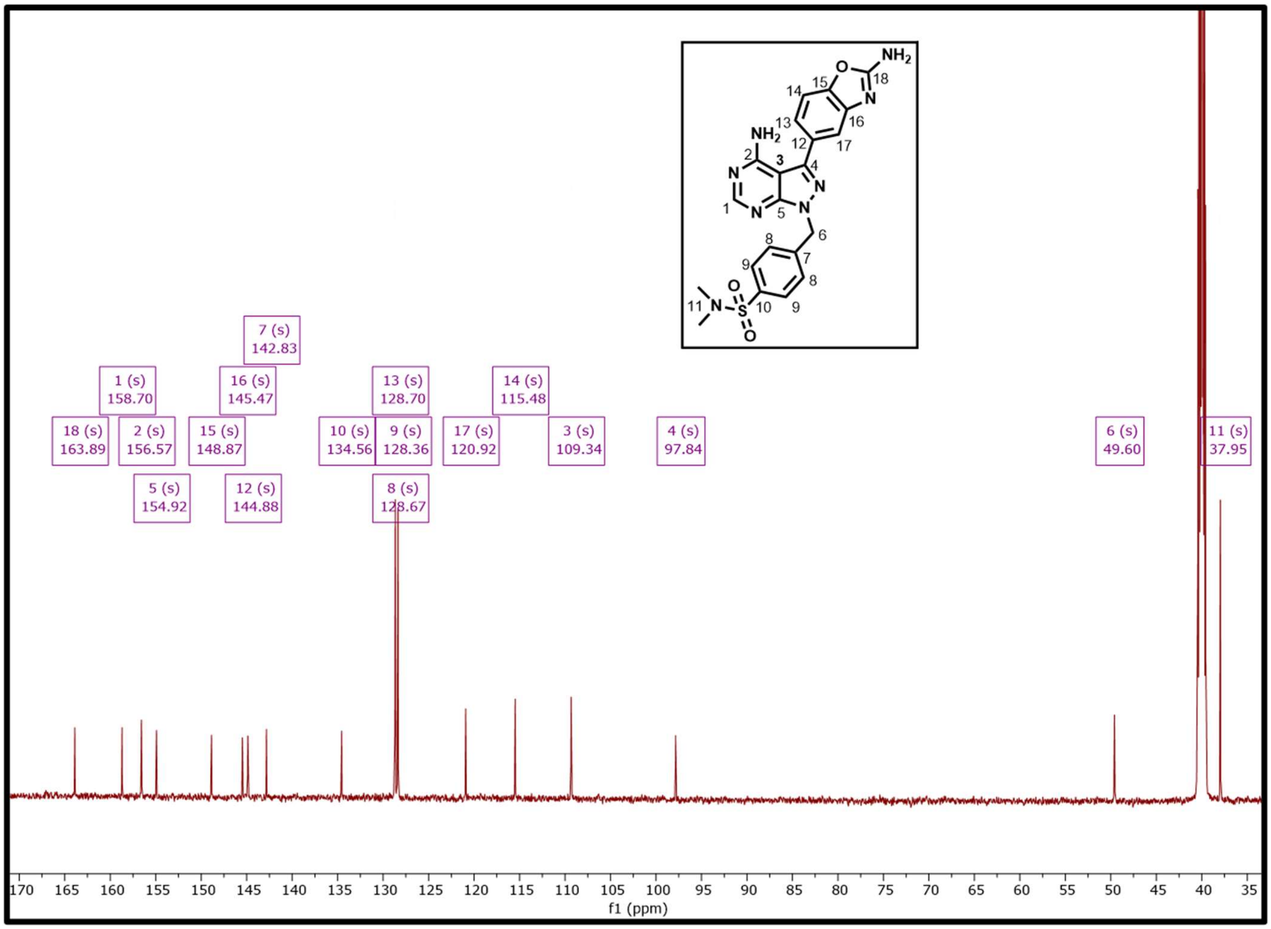

Figure 2.20: ^{13}C-NMR spectrum of 4-((4-amino-3-(2-aminobenzo[d]oxazol-5-yl)-1H-pyrazolo[3,4-d]pyrimidin-1-yl)methyl)-N,N-dimethylbenzenesulfonamide (**46f**)

2.7. Biological evaluation of MLN0128 analogues

2.7.1. Introduction

The inhibitory activities of MLN0128 analogues were investigated *in vitro* in *Plasmodium* PI4K and PKG kinase assays using purified recombinant proteins. Due to challenges in expressing and purifying *Pf*PI4K, *Pv*PI4K was used. Kinase activity was determined using the ADP-Glo kinase assay to measure ADP formation.[61] To evaluate selectivity, compounds were also screened against HuPI4KIIIβ and mTOR. Compounds were also tested to evaluate their asexual blood stage antiplasmodium activities against the drug-sensitive *Pf*NF54 strain and the multidrug-resistant *Pf*K1 strain (**Table 2.7**). The experimental results were then rationalized using molecular docking to gain further insights into inhibitor-protein interactions influencing target potency.

2.7.2. Rationalization of *Pv*PI4K inhibition

Kinase inhibition assays were performed using ADP formation to indicate kinase activity as described in **section 6.2.4**.[62, 63] The activity exhibited by the MLN0128 analogues against *Pv*PI4K is shown in **Table 2.5**. The calculated binding energies of the synthesized analogues were also included in the table. Inhibition data were then rationalized using molecular docking experiments.

Table 2.5: Results from *Pv*PI4K screening with respective calculated binding energy

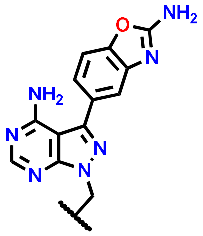

Compound	Structure	Binding energy (kcal/mol)	*Pv*PI4K IC$_{50}$, nM^{a} (SD)
46a	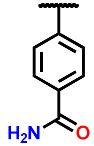	-61.74	12 (3)
46b	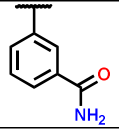	-67.20	4 (1)
46c	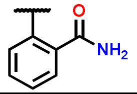	-64.56	4 (2)
46d	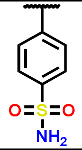	-65.85	12 (2)
46e	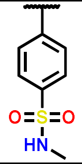	-57.78	13 (4)
46f	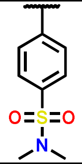	-63.49	10 (1)
46g	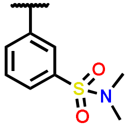	-66.95	4 (1)
46h	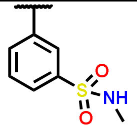	-66.23	2 (0.6)
MLN0128	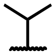	-50.15	5 (2)

^{a}*in vitro Pv*PI4K inhibition at 10 µM ATP. Results are from n = 2 independent experiments.

Generally, the *Pv*PI4K IC_{50} values of synthesized analogues were <0.02 µM. There was no drastic shift in potency between MLN0128 and its analogues. Interestingly, *meta*-substituted analogues were preferable to those with *para* substitutions. This is demonstrated by matched pairs **46b** (IC_{50} = 4 nM) and **46a** (12 nM), **46g** (4 nM) and **46f** (10 nM), and **46h** (2 nM) and **46e** (13 nM). The *ortho*-substituted compound **46c** (4 nM) showed comparable potency to its respective matched pair partner **46b** (4 nM). Additionally, *meta*-amides and *meta*-sulphonamides showed comparable potency. As shown in **Figure 2.21**, there was no correlation between calculated binding energies and *Pv*PI4K inhibition.

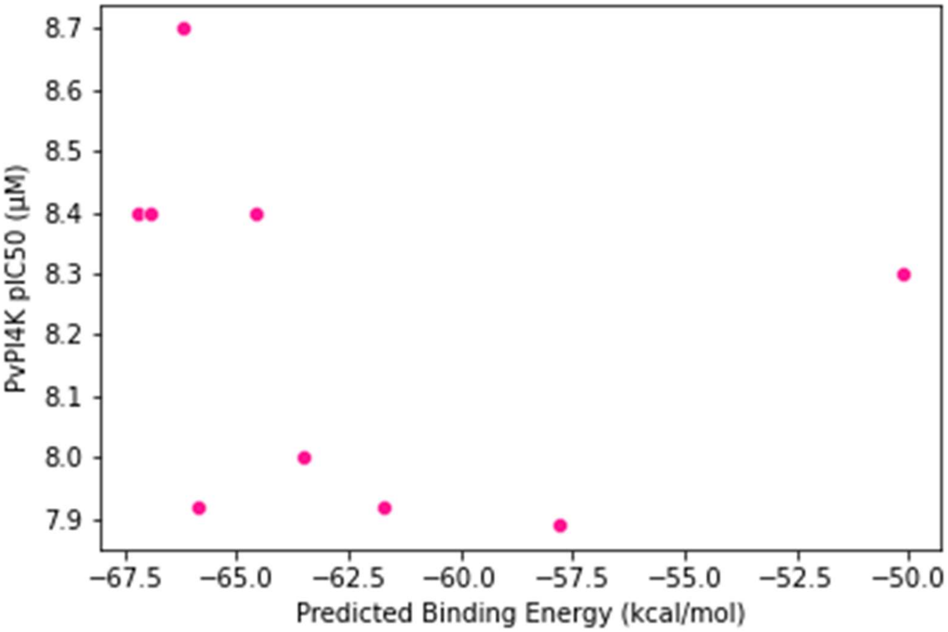

Figure 2.21: Scatter plot showing no correlation between *Plasmodium* PI4K docking score and enzymatic data

Notably, there was not a large enough range in *Pv*PI4K potency to identify correlations between the two parameters. Therefore, binding mode analysis was used to give further insight into *Pv*PI4K inhibition. The most and least potent compounds were **46h** (2 nM) and **46e** (13 nM), respectively. Interestingly, the compounds that exhibited this nearly 7-fold difference were matched pairs of N-methylamide. Their docking pose in the *Pf*PI4K homology model is shown in **Figure 2.22**.

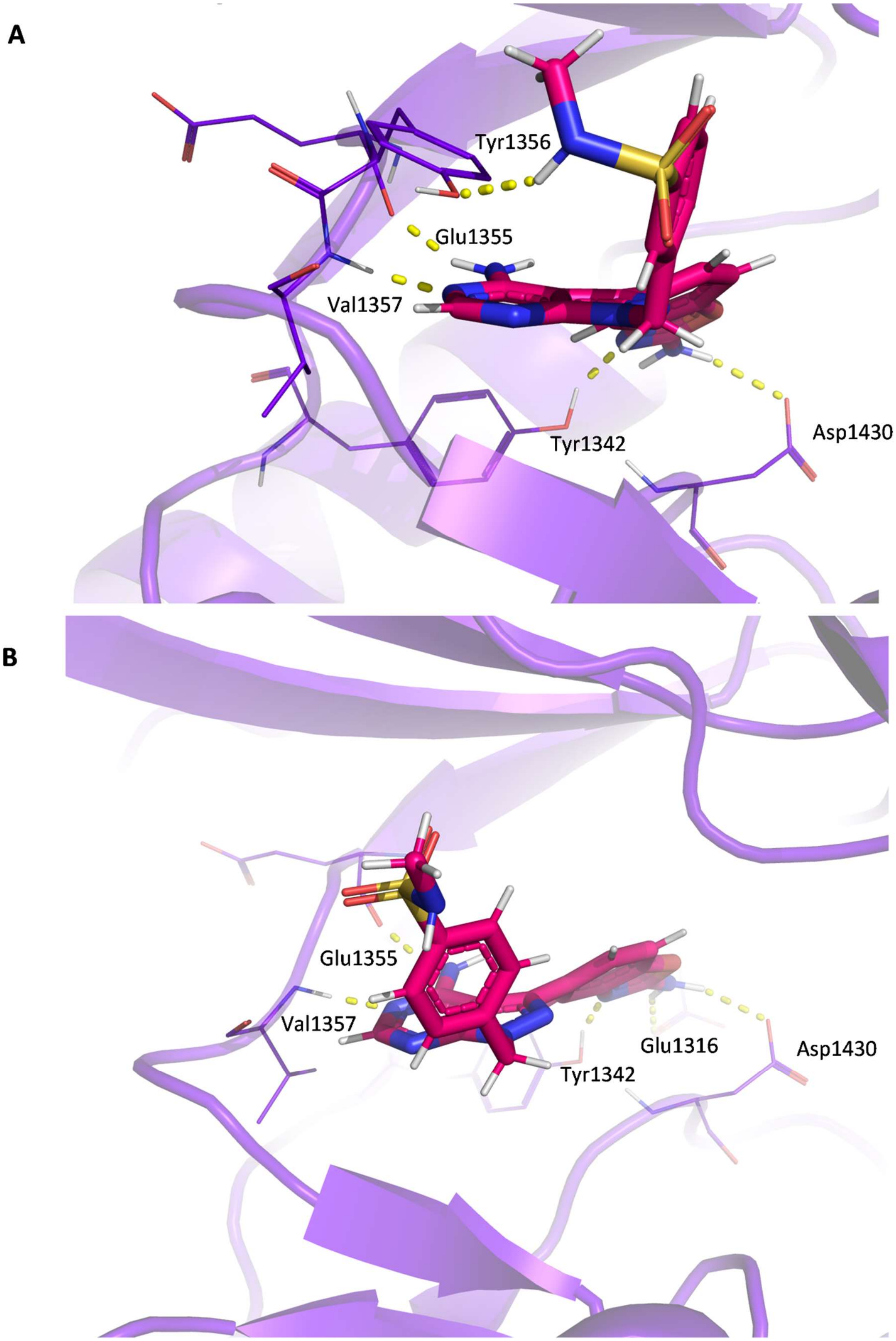

Figure 2.22: (**A) 46h** (0.002 µM) and **(B) 46e** (0.013 µM) docked into the *Pf*PI4K homology model (purple)

The major difference in the docking pose of the matched pairs was the methyl benzenesulphonamide moiety and was thus the focus of the binding mode analysis. **46h** (2 nM) forms a hydrogen-bond interaction with **Tyr1356**, a hinge residue. However, **46e** (13 nM) does not form this interaction. This interaction may play a significant role in increasing *Pv*PI4K potency as this was observed in other *meta*-analogues which in turn exhibited high enzymatic inhibition.

During the design of the next library of MLN0128 analogues, the focus may be placed on *meta* hydrogen bond-donating substituents as these analogues had the additional **Tyr1356** interaction. However, to further validate this interaction, the library should contain diverse analogues that may disrupt this interaction.

2.7.3. Rationalization of *Pf*PKG inhibition

Similarly, kinase inhibition assays were performed against the recombinantly expressed *Pf*PKG enzyme using an ADP-GLO kit as described in **section 6.2.4**.[62, 63] The results from the *Pf*PKG inhibition assays, together with the calculated binding energies and *Pf*PKG IC_{50} values, are shown in **Table 2.6**.

Table 2.6: Results from *Pf*PKG screening and calculated binding energy

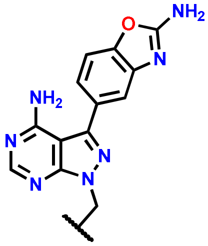

Compound	Structure	Binding energy (kcal/mol)	*Pf*PKG IC_{50}, µM (SD)[a]
46a	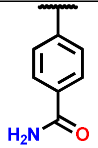	-62.26	0.8 (0.6)
46b	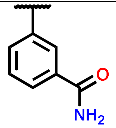	-65.47	0.12 (0.09)
46c	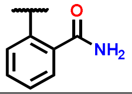	-72.39	0.3 (0.1)
46d	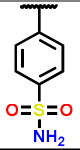	-66.00	0.35 (0.03)
46e	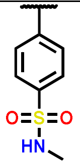	-55.77	0.25 (0.04)
46f	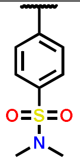	-59.92	0.8 (0.4)
46g	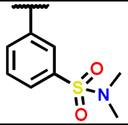	-66.32	0.18 (0.09)
46h	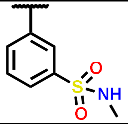	-48.94	0.22 (0.05)
MLN0128	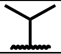	-57.84	0.02

[a] *in vitro Pf*PKG inhibition at 10 µM ATP. Results are from n = 2 independent experiments.

As observed in *Pv*PI4K inhibition, *meta* substitutions were seemingly preferred to *para* substitutions. This was evident as all compounds with *meta* substitutions had *Pf*PKG IC_{50} < 0.25 µM, and only one of the four *para*-substituted compounds showed an IC_{50} of 0.25 µM. There was about a >3-fold shift in *Pf*PKG potency observed in matched pairs: **46a** (0.8 µM) and **46b** (0.12 µM) and **46f** (0.8 µM) and **46g** (0.18 µM). The matched pairs of N-methylamide, **46e** and **46h**, had comparable potency with *Pf*PKG (IC_{50} = 0.25 µM and 0.22 µM, respectively). Similarly, the *meta*- (**46b**) and *ortho*- (**46c**) amides had comparable *Pf*PKG potency (0.12 µM and 0.3 µM, respectively). The *meta*- (**46b**, **46g**, and **46h**) and *ortho*- (**46c**) compounds exhibited dual potency against both *Pv*PI4K and *Pf*PKG. However, there was a loss of potency when compared to that of MLN0128.

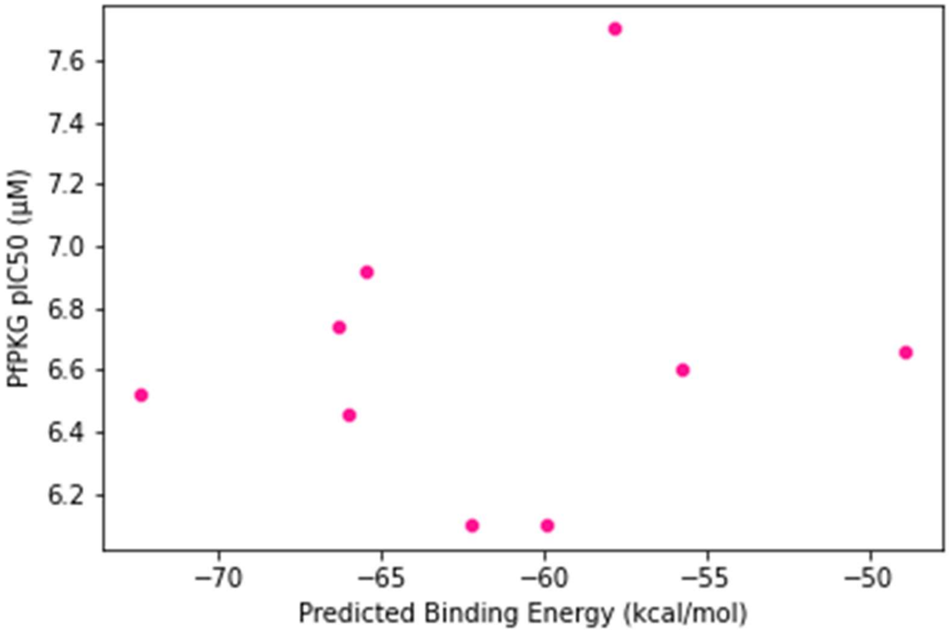

Figure 2.23: Scatter plot showing no correlation between *Plasmodium* PKG docking score and enzymatic data

There was no correlation between binding energies and *Pf*PKG potency in MLN0128 analogues as shown in **Figure 2.23**. However, this could be due to there being no significant difference in inhibition between the *para*-, *meta*- and *ortho*- derivatives. Therefore, a qualitative approach was used to analyze the structural properties affecting *Pf*PKG potency. Specifically, the binding mode of the respective ligands in the *Pf*PKG crystal structure was analyzed to provide insight into *Pf*PKG inhibition. The shift in *Pf*PKG potency exhibited between **46a** (0.8 µM) and **46b** (0.12 µM) may be due to the added interaction between **46b** and **Glu619**, as shown in **Figure 2.24**.

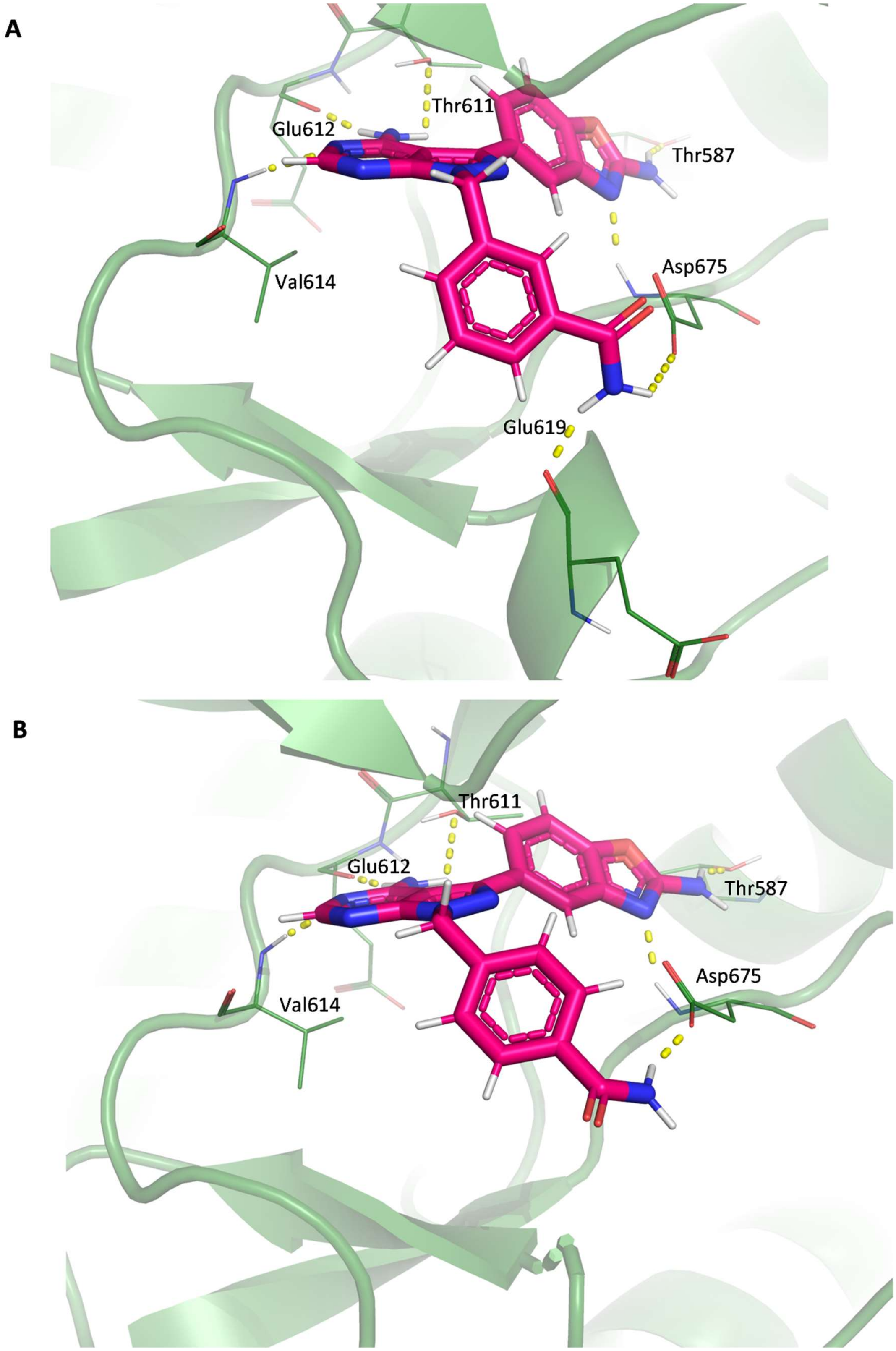

Figure 2.24: (**A**) **46b** (0.12 µM) and (**B**) **46a** (0.8 µM) docked into the *Pv*PKG (green) crystal structure (PDB ID: 5F0A)

The matched pair of N-methylsulphonamide **46h** and **46e** were almost equipotent (IC_{50} = 0.22 μM and 0.25 μM, respectively). This may be due to the same number of interactions maintained with the target (**Figure 2.25**). Interestingly, **46h** forms a hydrogen bond with **Glu662** while **46e** interacts with **Asp675**. This suggests that interactions with either of these residues have similar effects on *Pf*PKG potency.

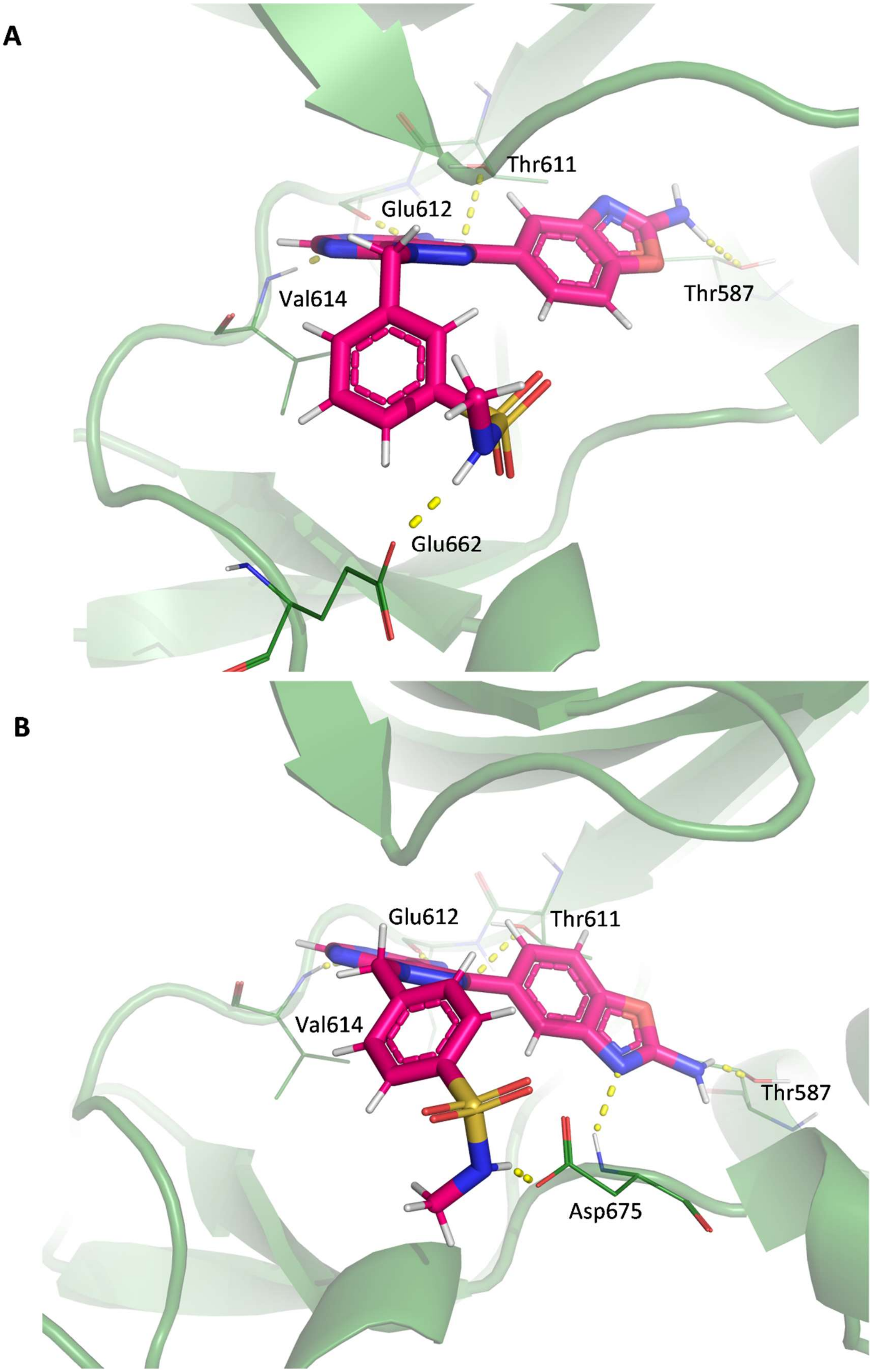

Figure 2.25: (**A**) **46h** (0.22 µM) and (**B**) **46e** (0.25 µM) docked into the *Pv*PKG (green) crystal structure (PDB ID: 5F0A)

A shift was also observed between the matched dimethylsulphonamide pair **46g** and **46f** (IC_{50} = 0.18 µM and 0.8 µM, respectively). The only difference in the binding mode of these analogues is the orientation of the dimethyl moieties (**Figure 2.26**). Compound **46g** has the previously mentioned moiety orientated toward the back pocket, which is highly hydrophobic, while **46f** has the moiety pointed away from the pocket. Therefore, there may be more hydrophobic contacts in **46g** than in **46e**. However, further computer-aided analysis, such as molecular dynamic simulations, is needed to investigate this hypothesis.

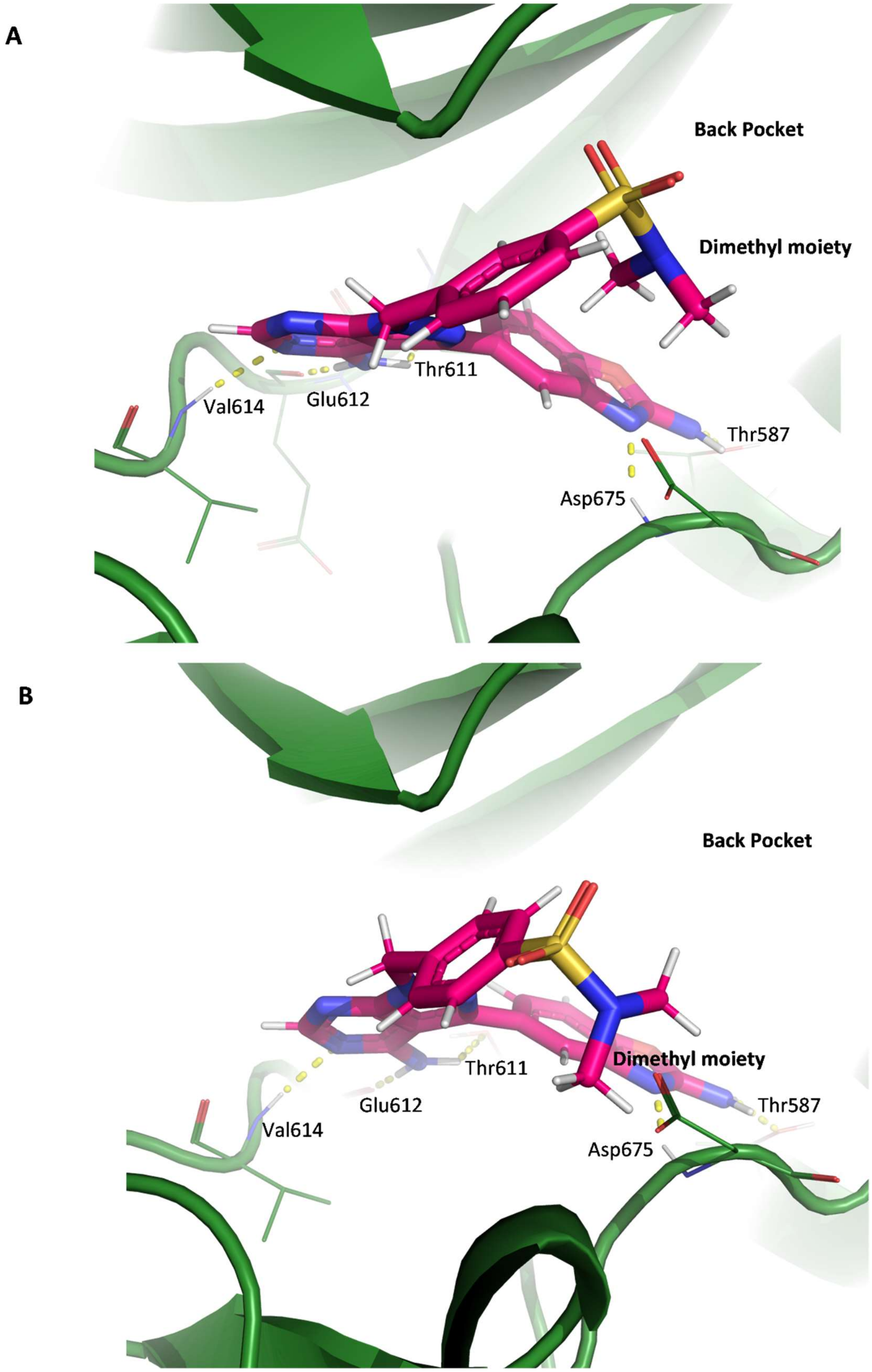

Figure 2.26: (**A**) **46g** (0.18 μM) and (**B**) **46f** (0.8 μM) docked into the *Pv*PKG (green) crystal structure (PDB ID: 5F0A)

In conclusion, the MLN0128 analogues were designed to improve selectivity of *Plasmodium* kinases over the human kinases while maintaining activity against *Plasmodium* PI4K and PKG. It was observed that, similar to *Pv*PI4K, *meta* and *ortho* MLN0128 analogues showed increased *Pf*PKG potency when compared to the *para* MLN0128 analogues. This demonstrates that, with further optimization using the important interactions observed, dual *Pv*PI4K/*Pf*PKG potency may be achieved. Changes in other parts of the molecule, including the benzo[d]oxazole appendage, may also deliver more potent compounds against *Pf*PKG. An example is the methylation of the amine to increase the hydrophobic interactions in the back pocket.

2.7.4. *In vitro* asexual blood-stage antiplasmodium activity and solubility profiling

Synthesized analogues were screened in an antiplasmodium asexual blood-stage activity assay against both drug-sensitive (*Pf*NF54) and multidrug-resistant strains (*Pf*K1; **Table 2.7).** These assays were carried out by H3D’s parasitology team at UCT. *Pv*PI4K and *Pf*PKG IC_{50} values are also included in this table for comparison purposes.

Table 2.7: *In vitro* activity against asexual blood-stage *P. falciparum* NF54 and K1 strains, *Pv*PI4K and *Pf*PKG IC$_{50}$ values, and solubility data

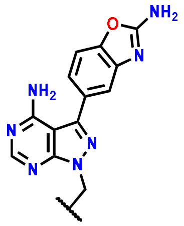

Compound	Structure	*Pv*PI4K IC$_{50}$, nM[a] (SD)	*Pf*PKG IC$_{50}$, µM (SD)[b]	*Pf*NF54 IC$_{50}$ (µM)	*Pf*K1 IC$_{50}$ (µM)	Solubility (µM)[c]
46a	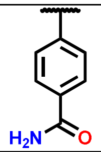	12 (3)	0.78 (0.6)	1.46	ND	20
46b	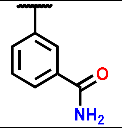	4 (1)	0.12 (0.09)	0.66	0.54	15
46c	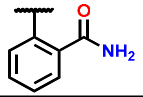	4 (2)	0.3 (0.1)	1.36	1.15	180
46d	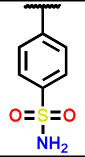	12 (2)	0.35 (0.03)	>6	ND	ND*
46e	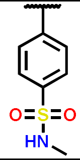	13 (4)	0.25 (0.04)	0.65	3.48	10
46f	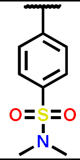	10 (1)	0.8 (0.4)	4.9	0.69	<5
46g	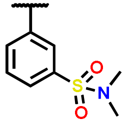	4 (1)	0.18 (0.09)	0.4	ND	<5
46h	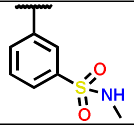	2 (0.6)	0.22 (0.05)	3.52	ND	5
MLN0128	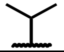	5(2)	0.02	0.1	0.47	115

[a] *in vitro Pv*PI4K inhibition at 10 µM ATP. [b] *in vitro Pf*PKG inhibition at 10 µM ATP. Results are from n = 2 independent experiments. [c] Determined at pH 6.5, using an HPLC-based miniaturized shake flask method. *Not determined.

The whole-cell activities of MLN0128 analogues were between 0.4 µM and >6 µM. Interestingly, compounds **46b** and **46g** both showed good whole-cell potency and were also the most potent compounds against both *Pv*PI4K and *Pf*PKG. There was lack of correlation between whole-cell and enzymatic potency. However, there were not enough data points to confirm this lack of correlation.

As shown in **Table 2.7**, both *meta*- and *para*-sulphonamide substituents generally showed poor solubility, as observed in compounds **46f** and **46g**. The *ortho*-amide analogue **46c** showed the highest solubility. Additionally, amide substituents such as **46b** showed moderate solubility, especially compared to the high solubility of the corresponding *ortho* substituent.

Meta-substituted compounds generally showed greater *Pf*NF54 activity, as observed in matched pairs **46b** (0.66 µM) and **46a** (1.46 µM), and **46g** (0.4 µM) and **46f** (4.9 µM). A 12-fold shift in *Pf*NF54 potency was observed in matched pair **46f** (4.9 µM) and **46g** (0.4 µM). Contrary to *Pf*PKG and *Pv*PI4K inhibition, **46h** (3.52 µM) was less active than **46e** (0.65 µM). This may be due to the poor solubility observed in **46h**. The potency of amide substituents was similar in both the chloroquine-sensitive and -resistant strains, as observed in **46b** (*Pf*NF54 IC_{50} = 0.66 µM; *Pf*K1 IC_{50} = 0.54 µM) and **46c** (*Pf*NF54 IC_{50} = 1.36 µM; *Pf*K1 IC_{50} = 1.15 µM). Surprisingly, **46f** was seven times more active against *Pf*K1 (0.69 µM) than *Pf*NF54 (4.9 µM).

In summary, compounds with *meta* substituents were generally more active *in vitro* activity against asexual blood-stage *Pf*NF54 and *Pf*K1. Similar observations were made with regard to *Pf*PKG/*Pv*PI4K inhibition.

2.7.5. Target selectivity with regards to mTOR and HuPI4KIIIβ

One of the aims of this project was to improve selectivity for *Plasmodium* kinases over human (off-target) kinases mTOR and PI4KIIIβ. This formed the basis of the design of MLN0128 analogues. MLN0128 is a potent mTOR inhibitor with IC_{50} = 1 nM. Therefore, analogues synthesized were screened against mTOR kinase by the Reaction Biology Corporation (Malvern, PA 19355; **Table 2.8**). The protocol used is described in **section 6.2.3**. MLN0128 analogues were also screened against human PI4KIIIβ (HuPI4KIIIβ) to confirm that selectivity was maintained. Molecular docking experiments were also carried out with MLN0128 analogues against mTOR (PDB ID: 4JT5) and HuPI4KIIIβ (PDB ID: 4D0L) to identify structural properties affecting kinase inhibition.

Table 2.8: Results from mTOR and HuPI4K screening and *Pv*PI4K inhibition data

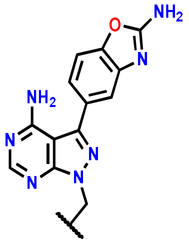

Compound	Structure	*Pv*PI4K IC50, µM^a (SD)	mTOR IC50 (µM)	HuPI4KIIIβ IC50 (µM)
46a	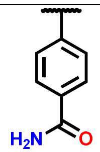	0.012 (0.003)	0.013	>10
46b	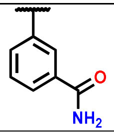	0.004 (0.001)	0.002	>10
46c	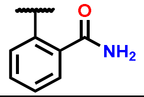	0.004 (0.002)	0.009	>10
46d	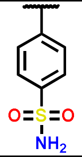	0.012 (0.002)	0.277	>10
46e	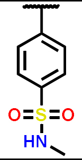	0.013 (0.004)	0.051	>10
46f	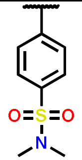	0.010 (0.001)	0.038	>10
46g	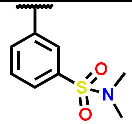	0.004 (0.001)	0.004	>10
46h	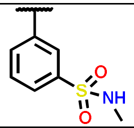	0.002 (0.0006)	0.008	>10
MLN0128	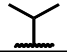	0.005(0.002)	0.001	>10

A substantial shift in mTOR inhibition (approximately 300-fold) was observed in the bulkier **46d** (0.277 µM). Similarly, there was a 40-fold shift in mTOR inhibition exhibited by the bulky **46f** (0.038 µM). Compounds **46b** (0.002 µM), **46c** (0.009 µM), **46g** (0.004 µM), and **46h** (0.008 µM) showed very little selectivity compared to MLN0128. These MLN0128 analogues were selective against HuPI4KIIIβ.

To translate the success of the HuPI4KIIIβ selectivity observed to mTOR selectivity, structure-based studies were carried out. The lack of HuPI4KIIIβ inhibition at the maximum concentration tested may be due to the incorrect binding pose when the analogues were docked in the HuPI4KIIIβ crystal structure (PDB ID: 4D0L). Molecular modeling techniques were then used to compare the binding site of both HuPI4KIIIβ and mTOR to give a structure-based rationale as to why good selectivity is shown over HuPI4KIIIβ. Therefore, this study may ascertain the structural differences between the kinases that may influence their respective selectivity with regards to MLN0128 analogues. The aligned crystal structures of mTOR (PDB ID: 4JT5) and HuPI4KIIIβ (PDB ID: 4D0L) are shown in **Figure 2.27**.

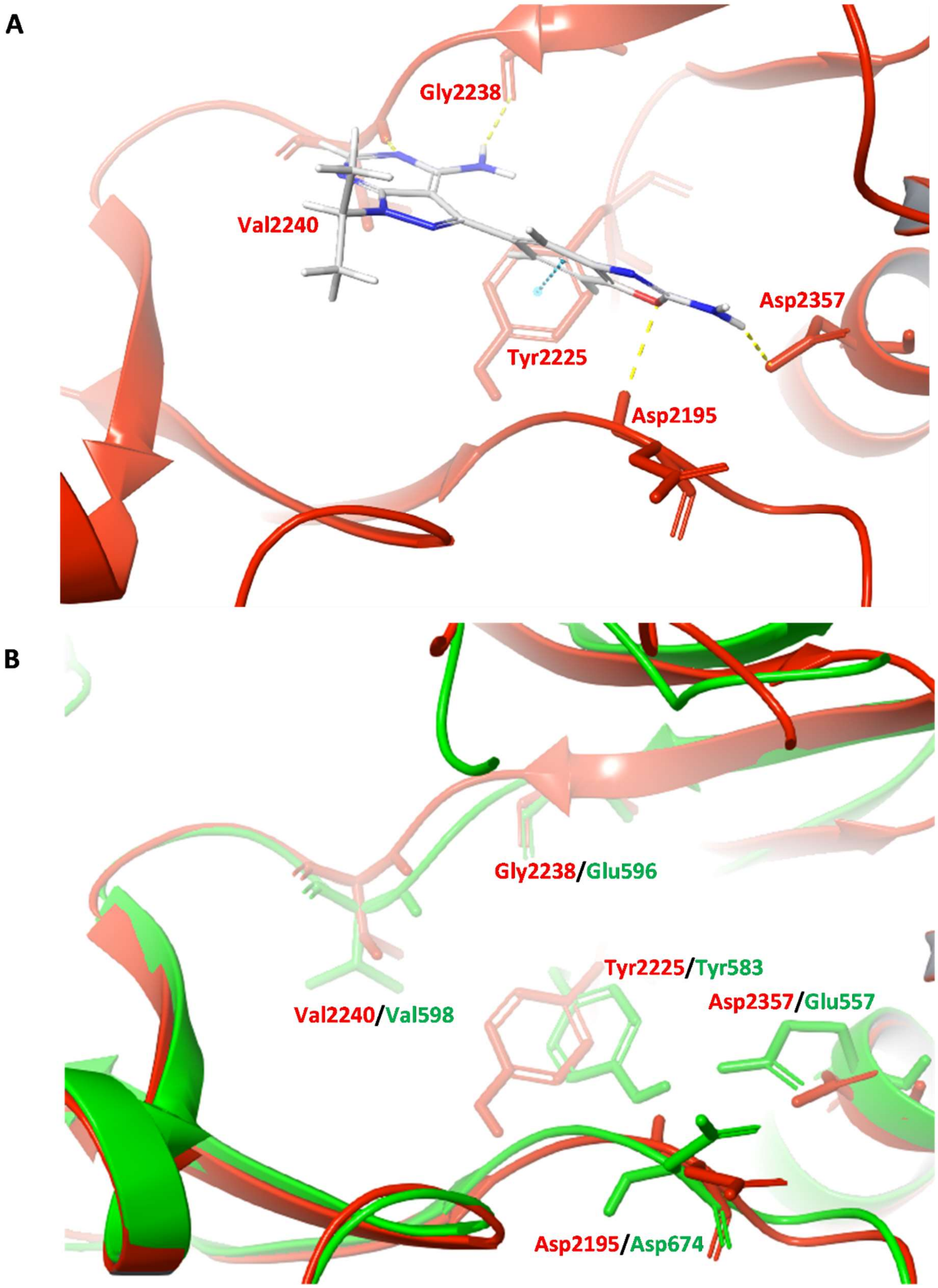

Figure 2.27: **(A)** MLN0128 docked into the mTOR (red) crystal structure (PDB ID: 4JT5), **(B)** HuPI4KIIIβ (PDB ID: 4D0L; green) aligned with mTOR (PDB ID: 4JT5; red)

As the same level of selectivity for mTOR over HuPI4KIIIβ was observed in MLN0128 and the analogues, MLN0128 was used for the binding mode analysis studies. The docked pose of MLN0128 in mTOR, with highlighted residues, gives an orientation in to the binding site (**Figure 2.27(A)**). Alignment of the interacting residues with the HuPI4KIIIβ binding site is shown in **Figure 2.25 (B).** The hinge residues **Val2240** and **Gly2238** in mTOR aligned with **Val598** and **Glu596**, respectively, in HuPI4KIIIβ. These interactions align well as only the backbone is used to form the hydrogen bond. This matching alignment is also observed in the DFG chain as **Asp2195** of mTOR aligned with **Asp674** of HuPI4KIIIβ. The mTOR residue, **Asp2195**, is reported to be an important contact residue.[64]

In the back pocket, structural differences were observed in **Asp2357** of mTOR aligned with the bulky **Glu557** in HuPI4KIIIβ. This turned the focus on the interactions formed by the benzoxazole moiety in the back pocket. The amine of the benzoxazole moiety interacts with **Asp2357**. Glutamic acid is larger than aspartic acid and significantly reduces the space in the back pocket. Moreover, there were notably different orientations in **Tyr2225** of mTOR which aligned with **Tyr583** in HuPI4KIIIβ. **Figure 2.28** shows that the HuPI4KIIIβ residues were orientated toward the inside of the back pocket, thus reducing the size of the pocket causing a flip in the docking pose. mTOR residues were smaller (e.g., **Asp2357**) and orientated away from the back pocket increasing the size of the pocket accommodating the benzo[d]oxazole moiety.

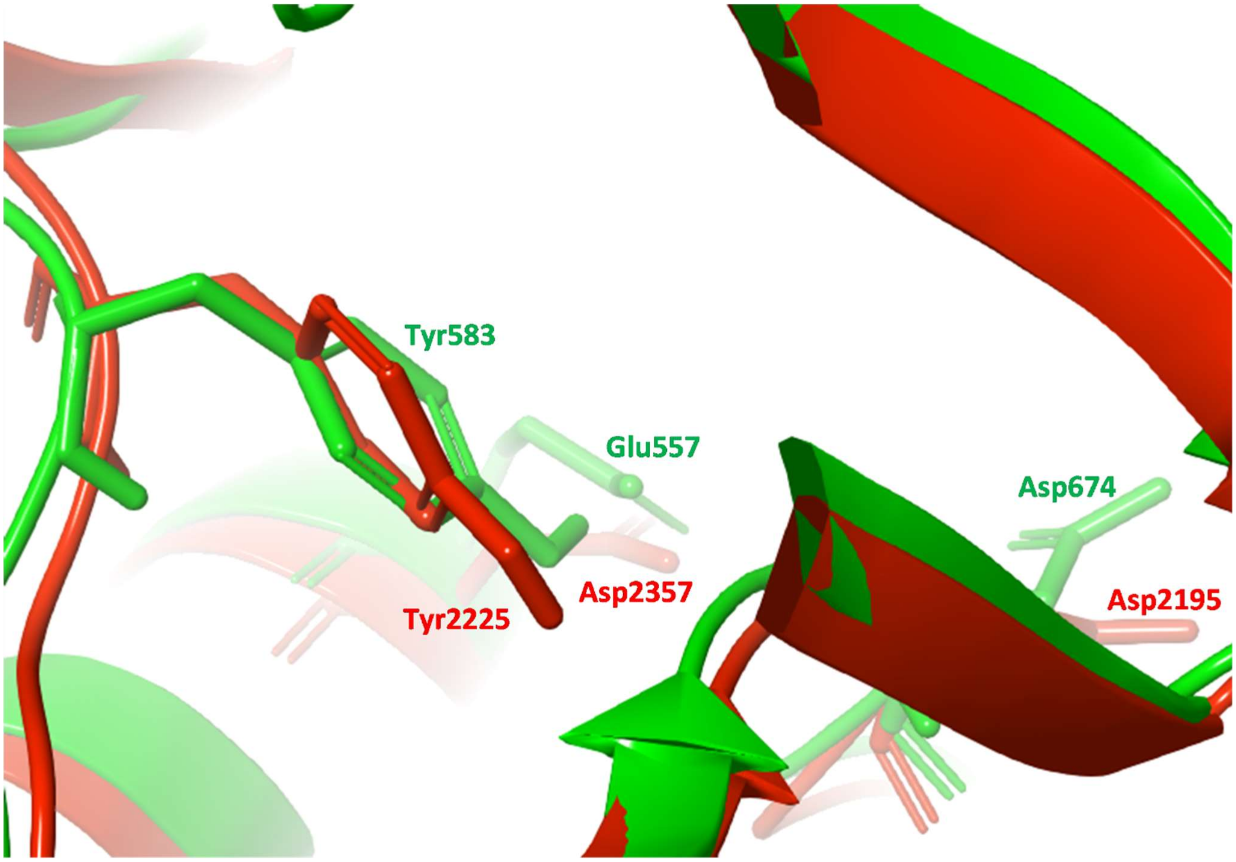

Figure 2.28: Aligned residues in the back pockets of mTOR (red) and residues in HuPI4K (green)

To further investigate the importance of these amino acids in the binding pose of MLN0128 in HuPI4KIIIβ and to translate the success of the corresponding selectivity, they were mutated computationally to form smaller residues (**Figure 2.29**). **Tyr583** was mutated to an alanine residue while **Glu557** was mutated to an aspartic acid. MLN0128 was then docked into the mutated crystal structure following the molecular docking protocol.

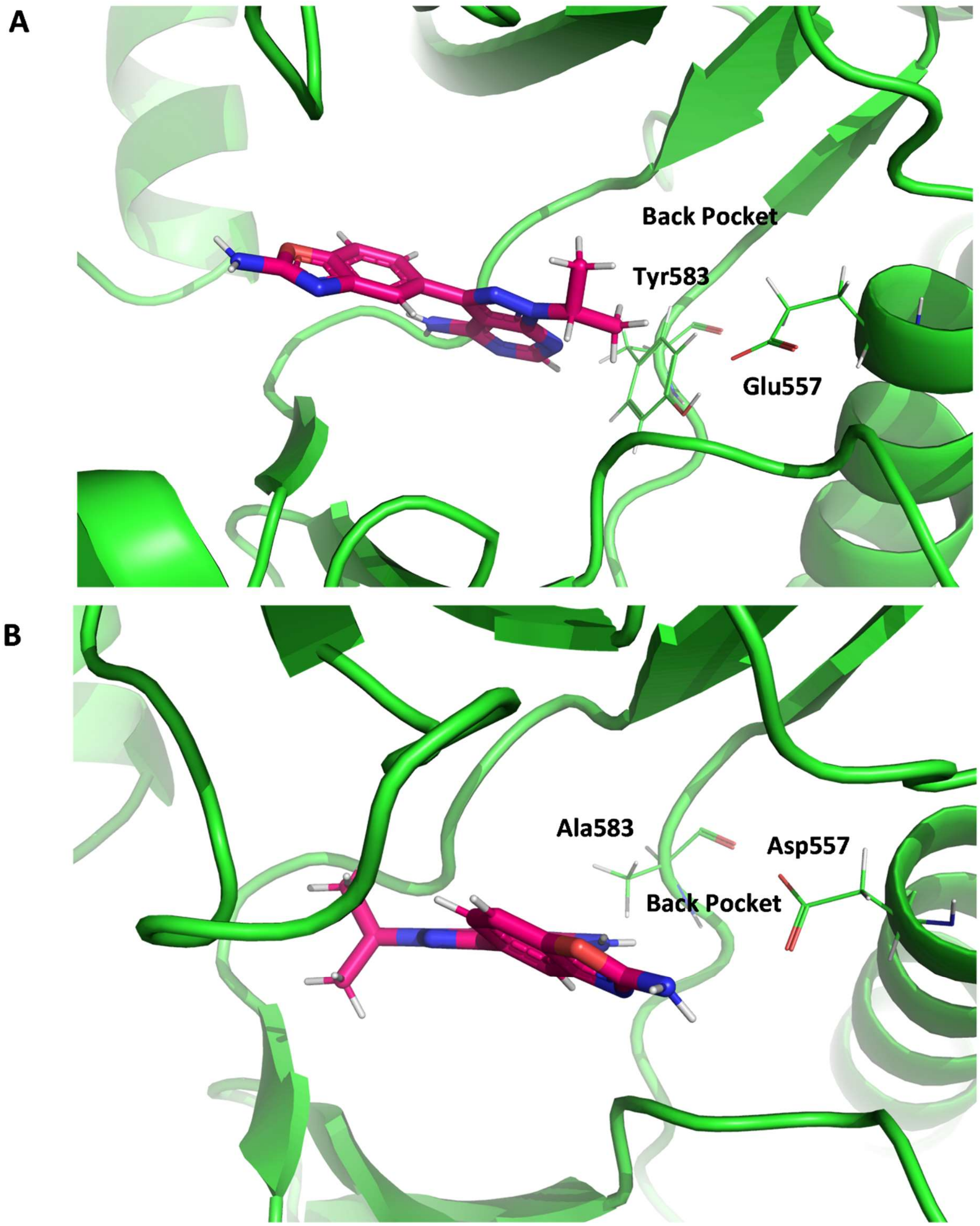

Figure 2.29: MLN0128 docked into wildtype (**A**) and computationally mutated HuPI4KIIIβ (**B**)

The predicted binding pose of MLN0128 in the mutated HuPI4KIIIβ revealed the pivotal role played by the already mentioned amino acid residues in selectivity in the back pocket (**Figure 2.29**). The structural differences mentioned in the back pocket may contribute to target selectivity exhibited over HuPI4KIIIβ implying that changes on the benzo[d]oxazole moiety could improve selectivity over mTOR. Hence could account for the loss in mTOR potency recorded in the MLN0128 patent literature which was achieved through changes on the benzo[d]oxazole moiety (**Figure 2.30**).[65]

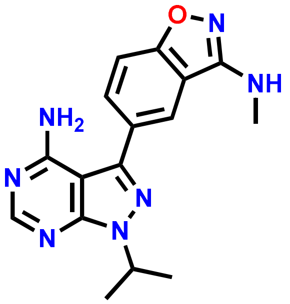

Figure 2.30: MLN0128 analogue with mTOR IC_{50} of >10 µM.

Notably, the residues corresponding to **Tyr583** and **Glu1316** in HuPI4KIIIβ are **Tyr1342** and **Glu1316,** respectively, in *Pf*PI4K. However, their respective orientations are not conclusive given that this is a homology model and not a crystal structure used here.

2.8. Conclusion and Future Work

Biological evaluation of MLN0128 analogues showed that *meta* substitutions were favorable for both enzymatic inhibition and antiplasmodium activity. Relatively, dual inhibition of *Pv*PI4K/*Pf*PKG was achieved by various MLN0128 analogues, including **46b**, **46c**, **46g**, and **46h**. However, only one analogue (**46d**) was selective, with an mTOR IC_{50} of 0.277 µM compared to MLN0128 mTOR inhibition of 0.001 µM.

As demonstrated computationally, exploiting the structural differences in the back pocket between HuPI4KIIIβ and mTOR, may improve selectivity. Therefore, conducting SAR studies on the benzo[d]oxazole moiety is paramount in the design of the next MLN0128 analogues.

However, reducing the size of the moiety in back pocket increases enzymatic inhibition. This is observed in the structure of the selective ML10 co-crystallised with *Pv*PKG where the fluorophenylmethanesulfonamide is the only moiety that occupies the back pocket (**Figure 2.31**).[66] This moiety occupies less space when compared to the benzo[d]oxazole of MLN0128.

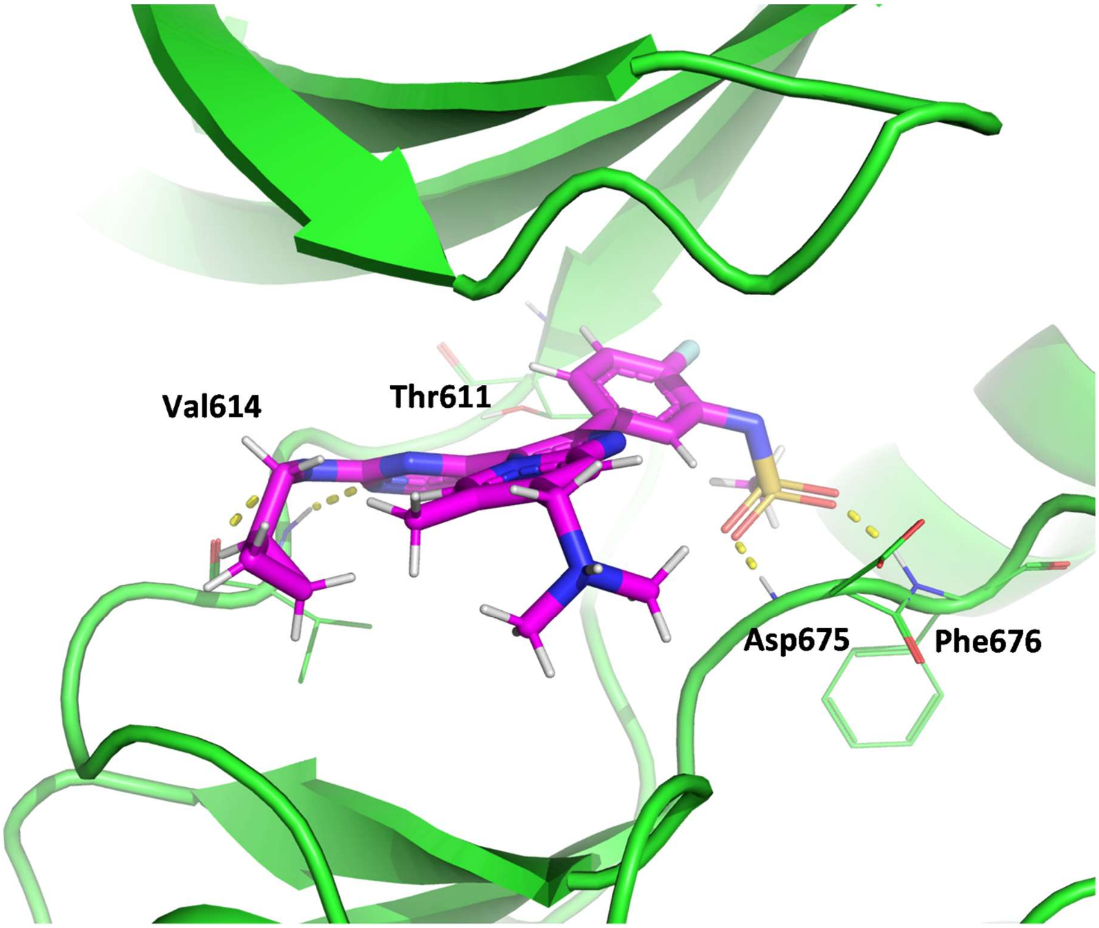

Figure 2.31: *Pv*PKG co-crystallised with potent and selective *Pf*PKG inhibitor, ML10.

Additionally, scaffold changes may bring about mTOR selectivity (**Figure 2.32**) where maintaining an amine at position 2 and introducing electron with drawing groups at position 4 (-CN, $-CH_2OH$, $-CF_3$) may result in loss of mTOR inhibition.[67]

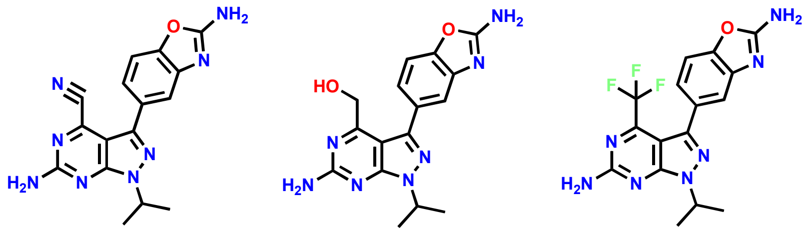

mTOR K_i (μM): 2.2

mTOR K_i (μM): 4

mTOR K_i (μM): 2.3

Figure 2.32: Examples of MLN0128 analogues with decreased mTOR inhibition.[67]

This investigative work may be used to structurally-inform findings the design the next library of MLN0128 analogues.

2.9. References

1. Ojo, K. K.; Eastman, R. T.; Vidadala, R.; Zhang, Z.; Rivas, K. L.; Choi, R.; Lutz, J. D.; Reid, M. C.; Fox, A. M.; Hulverson, M. A., A specific inhibitor of Pf CDPK4 blocks malaria transmission: chemical-genetic validation. *J. Infect. Dis.* **2014,** *209* (2), 275-284.

2. Ojo, K. K.; Pfander, C.; Mueller, N. R.; Burstroem, C.; Larson, E. T.; Bryan, C. M.; Fox, A. M.; Reid, M. C.; Johnson, S. M.; Murphy, R. C., Transmission of malaria to mosquitoes blocked by bumped kinase inhibitors. *J. Clin. Investig.* **2012,** *122* (6), 2301-2305.

3. Vidadala, R. S. R.; Ojo, K. K.; Johnson, S. M.; Zhang, Z.; Leonard, S. E.; Mitra, A.; Choi, R.; Reid, M. C.; Keyloun, K. R.; Fox, A. M., Development of potent and selective Plasmodium falciparum calcium-dependent protein kinase 4 (PfCDPK4) inhibitors that block the transmission of malaria to mosquitoes. *Eur. J. Med. Chem.* **2014,** *74*, 562-573.

4. Spreafico, A.; Schenone, S.; Serchi, T.; Orlandini, M.; Angelucci, A.; Magrini, D.; Bernardini, G.; Collodel, G.; Di Stefano, A.; Tintori, C., Antiproliferative and proapoptotic activities of new pyrazolo [3, 4-d] pyrimidine derivative Src kinase inhibitors in human osteosarcoma cells. *FASEB J* **2008,** *22* (5), 1560-1571.

5. Parsons, S. J.; Parsons, J. T., Src family kinases, key regulators of signal transduction. *Oncogene* **2004,** *23* (48), 7906-7909.

6. Radi, M.; Dreassi, E.; Brullo, C.; Crespan, E.; Tintori, C.; Bernardo, V.; Valoti, M.; Zamperini, C.; Daigl, H.; Musumeci, F., Design, synthesis, biological activity, and ADME properties of pyrazolo [3, 4-d] pyrimidines active in hypoxic human leukemia cells: a lead optimization study. *J. Med. Chem* **2011,** *54* (8), 2610-2626.

7. Deininger, M. W.; Vieira, S.; Mendiola, R.; Schultheis, B.; Goldman, J. M.; Melo, J. V., BCR-ABL tyrosine kinase activity regulates the expression of multiple genes implicated in the pathogenesis of chronic myeloid leukemia. *Cancer Res.* **2000,** *60* (7), 2049-2055.

8. Kopecky, D. J.; Hao, X.; Chen, Y.; Fu, J.; Jiao, X.; Jaen, J. C.; Cardozo, M. G.; Liu, J.; Wang, Z.; Walker, N. P., Identification and optimization of N3, N6-diaryl-1H-pyrazolo [3, 4-d] pyrimidine-3, 6-diamines as a novel class of ACK1 inhibitors. *Bioorg. Med. Chem. Lett.* **2008,** *18* (24), 6352-6356.

9. Lin, Q.; Wang, J.; Childress, C.; Yang, W., The activation mechanism of ACK1 (activated Cdc42-associated tyrosine kinase 1). *Biochem. J.* **2012,** *445* (2), 255-264.

10. Rashad, A. E.; Mahmoud, A. E.; Ali, M. M., Synthesis and anticancer effects of some novel pyrazolo [3, 4-d] pyrimidine derivatives by generating reactive oxygen species in human breast adenocarcinoma cells. *Eur. J. Med. Chem.* **2011,** *46* (4), 1019-1026.

11. Kaplan, J.; Verheijen, J. C.; Brooijmans, N.; Toral-Barza, L.; Hollander, I.; Yu, K.; Zask, A., Discovery of 3, 6-dihydro-2H-pyran as a morpholine replacement in 6-aryl-1H-pyrazolo [3, 4-d] pyrimidines and 2-arylthieno [3, 2-d] pyrimidines: ATP-competitive inhibitors of the mammalian target of rapamycin (mTOR). *Bioorg. Med. Chem. Lett.* **2010,** *20* (2), 640-643.

12. Ghorab, M. M.; Ragab, F. A.; Alqasoumi, S. I.; Alafeefy, A. M.; Aboulmagd, S. A., Synthesis of some new pyrazolo [3, 4-d] pyrimidine derivatives of expected anticancer and radioprotective activity. *Eur. J. Med. Chem.* **2010,** *45* (1), 171-178.

13. Bondock, S.; Rabie, R.; Etman, H. A.; Fadda, A. A., Synthesis and antimicrobial activity of some new heterocycles incorporating antipyrine moiety. *Eur. J. Med. Chem.* **2008,** *43* (10), 2122-2129.

14. Khobragade, C. N.; Bodade, R. G.; Konda, S. G.; Dawane, B. S.; Manwar, A. V., Synthesis and antimicrobial activity of novel pyrazolo [3, 4-d] pyrimidin derivatives. *Eur. J. Med. Chem.* **2010,** *45* (4), 1635-1638.

15. Yewale, S. B.; Ganorkar, S. B.; Baheti, K. G.; Shelke, R. U., Novel 3-substituted-1-aryl-5-phenyl-6-anilinopyrazolo [3, 4-d] pyrimidin-4-ones: Docking, synthesis and

pharmacological evaluation as a potential anti-inflammatory agents. *Bioorg. Med. Chem. Lett.* **2012,** *22* (21), 6616-6620.

16. Médard, G.; Pachl, F.; Ruprecht, B.; Klaeger, S.; Heinzlmeir, S.; Helm, D.; Qiao, H.; Ku, X.; Wilhelm, M.; Kuehne, T., Optimized chemical proteomics assay for kinase inhibitor profiling. *J. Proteome Res.* **2015,** *14* (3), 1574-1586.

17. Laplante, M.; Sabatini, D. M., mTOR signaling in growth control and disease. *Cell* **2012,** *149* (2), 274-293.

18. Yang, H.; Rudge, D. G.; Koos, J. D.; Vaidialingam, B.; Yang, H. J.; Pavletich, N. P., mTOR kinase structure, mechanism and regulation. *Nature* **2013,** *497* (7448), 217-223.

19. Hsieh, A. C.; Liu, Y.; Edlind, M. P.; Ingolia, N. T.; Janes, M. R.; Sher, A.; Shi, E. Y.; Stumpf, C. R.; Christensen, C.; Bonham, M. J., The translational landscape of mTOR signalling steers cancer initiation and metastasis. *Nature* **2012,** *485* (7396), 55-61.

20. Laplante, M.; Sabatini, D. M., mTOR signaling at a glance. *J. Cell Sci.* **2009,** *122* (20), 3589-3594.

21. Chen, Y.; Zhou, X., Research progress of mTOR inhibitors. *Eur. J. Med. Chem.* **2020,** 112820.

22. Burris, H. A.; Kurkjian, C.; Hart, L.; Pant, S.; Murphy, P.; Jones, S.; Neuwirth, R.; Patel, C.; Zohren, F.; Infante, J., TAK-228 (formerly MLN0128), an investigational dual TORC1/2 inhibitor plus paclitaxel, with/without trastuzumab, in patients with advanced solid malignancies. *Cancer Chemother. Pharmacol.* **2017,** *80* (2), 261-273.

23. Gökmen-Polar, Y.; Liu, Y.; Toroni, R. A.; Sanders, K. L.; Mehta, R.; Badve, S.; Rommel, C.; Sledge, G. W., Investigational drug MLN0128, a novel TORC1/2 inhibitor, demonstrates potent oral antitumor activity in human breast cancer xenograft models. *Breast Cancer Res. Treat.* **2012,** *136* (3), 673-682.

24. Slotkin, E. K.; Patwardhan, P. P.; Vasudeva, S. D.; de Stanchina, E.; Tap, W. D.; Schwartz, G. K., MLN0128, an ATP-competitive mTOR kinase inhibitor with potent in vitro and in vivo antitumor activity, as potential therapy for bone and soft-tissue sarcoma. *Mol. Cancer Ther.* **2015,** *14* (2), 395-406.

25. Liu, Q.; Thoreen, C.; Wang, J.; Sabatini, D.; Gray, N. S., mTOR mediated anti-cancer drug discovery. *Drug Discovery Today: Ther. Strategies* **2009,** *6* (2), 47-55.

26. Graham, L.; Banda, K.; Torres, A.; Carver, B. S.; Chen, Y.; Pisano, K.; Shelkey, G.; Curley, T.; Scher, H. I.; Lotan, T. L., A phase II study of the dual mTOR inhibitor MLN0128 in patients with metastatic castration resistant prostate cancer. *Invest. New Drugs* **2018,** *36* (3), 458-467.

27. Nayak, L.; Hays, J.; Do, K.; Muzikansky, A.; Gaffey, S.; Lee, E.; Rinne, M.; Norden, A.; Beroukhim, R.; Puduvalli, V., ACTR-93. A PHASE I STUDY OF MLN0128 (TAK-228) AND BEVACIZUMAB IN PATIENTS WITH ADVANCED SOLID TUMORS INCLUDING GLIOBLASTOMA. *Neuro-oncology* **2017,** *19* (suppl_6), vi20-vi21.

28. Krishnan, K.; Ziniel, P.; Li, H.; Huang, X.; Hupalo, D.; Gombakomba, N.; Guerrero, S. M.; Dotrang, T.; Lu, X.; Caridha, D., Torin 2 derivative, NCATS-SM3710, has potent multistage antimalarial activity through inhibition of P. falciparum phosphatidylinositol 4-kinase (Pf PI4KIIIβ). *ACS Pharmacol. Transl. Sci.* **2020,** *3* (5), 948-964.

29. H Drewry, D.; M Willson, T.; J Zuercher, W., Seeding collaborations to advance kinase science with the GSK Published Kinase Inhibitor Set (PKIS). *Curr. Top. Med. Chem.* **2014,** *14* (3), 340-342.

30. McNamara, C. W.; Lee, M.; Lim, C. S.; Lim, S. H.; Roland, J.; Nagle, A.; Simon, O.; Yeung, B. K.; Chatterjee, A. K.; McCormack, S. L., Targeting Plasmodium PI (4) K to eliminate malaria. *Nature* **2013,** *504* (7479), 248-253.

31. Fienberg, S.; Eyermann, C. J.; Arendse, L. B.; Basarab, G. S.; McPhail, J. A.; Burke, J. E.; Chibale, K., Structural Basis for Inhibitor Potency and Selectivity of Plasmodium falciparum Phosphatidylinositol 4-Kinase Inhibitors. *ACS Infect. Dis.* **2020,** *6* (11), 3048-3063.

32. Cheuka, P. M.; Centani, L.; Arendse, L. B.; Fienberg, S.; Wambua, L.; Renga, S. S.; Dziwornu, G. A.; Kumar, M.; Lawrence, N.; Taylor, D., New amidated 3, 6-diphenylated imidazopyridazines with potent antiplasmodium activity are dual inhibitors of Plasmodium phosphatidylinositol-4-kinase and cGMP-dependent protein kinase. *ACS Infect. Dis.* **2020,** *7* (1), 34-46.

33. Ren, J.-X.; Gao, N.-N.; Cao, X.-S.; Hu, Q.-A.; Xie, Y., Homology modeling and virtual screening for inhibitors of lipid kinase PI (4) K from Plasmodium. *Biomed. Pharmacother.* **2016,** *83*, 798-808.

34. Kandepedu, N.; Gonzàlez Cabrera, D.; Eedubilli, S.; Taylor, D.; Brunschwig, C.; Gibhard, L.; Njoroge, M.; Lawrence, N.; Paquet, T.; Eyermann, C. J., Identification, characterization, and optimization of 2, 8-disubstituted-1, 5-naphthyridines as novel Plasmodium falciparum phosphatidylinositol-4-kinase inhibitors with in vivo efficacy in a humanized mouse model of malaria. *J. Med. Chem* **2018,** *61* (13), 5692-5703.

35. Aurrecoechea, C.; Brestelli, J.; Brunk, B. P.; Dommer, J.; Fischer, S.; Gajria, B.; Gao, X.; Gingle, A.; Grant, G.; Harb, O. S., PlasmoDB: a functional genomic database for malaria parasites. *Nucleic Acids Res.* **2009,** *37* (suppl_1), D539-D543.

36. Johnson, M.; Zaretskaya, I.; Raytselis, Y.; Merezhuk, Y.; McGinnis, S.; Madden, T. L., NCBI BLAST: a better web interface. *Nucleic Acids Res.* **2008,** *36* (suppl_2), W5-W9.

37. Berman, H. M., The protein data bank: a historical perspective. *Acta Crystallogr., Sect. A: Found. Crystallogr.* **2008,** *64* (1), 88-95.

38. Burke, J. E.; Inglis, A. J.; Perisic, O.; Masson, G. R.; McLaughlin, S. H.; Rutaganira, F.; Shokat, K. M.; Williams, R. L., Structures of PI4KIIIβ complexes show simultaneous recruitment of Rab11 and its effectors. *Science* **2014,** *344* (6187), 1035-1038.

39. Reuberson, J.; Horsley, H.; Franklin, R. J.; Ford, D.; Neuss, J.; Brookings, D.; Huang, Q.; Vanderhoydonck, B.; Gao, L.-J.; Jang, M.-Y., Discovery of a potent, orally bioavailable PI4KIIIβ inhibitor (UCB9608) able to significantly prolong allogeneic organ engraftment in vivo. *J. Med. Chem* **2018,** *61* (15), 6705-6723.

40. Jacobson, M. P.; Pincus, D. L.; Rapp, C. S.; Day, T. J.; Honig, B.; Shaw, D. E.; Friesner, R. A., A hierarchical approach to all-atom protein loop prediction. *Proteins: Struct., Funct., Bioinf.* **2004,** *55* (2), 351-367.

41. Schrödinger Release 2020-2: Maestro, S., LLC, New York, NY, 2020.

42. Higgins, D. G.; Sharp, P. M., CLUSTAL: a package for performing multiple sequence alignment on a microcomputer. *Gene* **1988,** *73* (1), 237-244.

43. Xu, Q.; Dunbrack Jr, R. L., Assignment of protein sequences to existing domain and family classification systems: Pfam and the PDB. *Bioinformatics* **2012,** *28* (21), 2763-2772.

44. Altschul, S. F.; Madden, T. L.; Schäffer, A. A.; Zhang, J.; Zhang, Z.; Miller, W.; Lipman, D. J., Gapped BLAST and PSI-BLAST: a new generation of protein database search programs. *Nucleic Acids Res.* **1997,** *25* (17), 3389-3402.

45. Kmiecik, S.; Gront, D.; Kolinski, M.; Wieteska, L.; Dawid, A. E.; Kolinski, A., Coarse-grained protein models and their applications. *Chem. Rev.* **2016,** *116* (14), 7898-7936.

46. Li, J.; Abel, R.; Zhu, K.; Cao, Y.; Zhao, S.; Friesner, R. A., The VSGB 2.0 model: a next generation energy model for high resolution protein structure modeling. *Proteins: Struct., Funct., Bioinf.* **2011,** *79* (10), 2794-2812.

47. Harder, E.; Damm, W.; Maple, J.; Wu, C.; Reboul, M.; Xiang, J. Y.; Wang, L.; Lupyan, D.; Dahlgren, M. K.; Knight, J. L., OPLS3: a force field providing broad coverage of drug-like small molecules and proteins. *J. Chem. Theory Comput.* **2016,** *12* (1), 281-296.

48. Ibezim, A.; Madukaife, M. S.; Osigwe, S. C.; Engel, N.; Karuppasamy, R.; Ntie-Kang, F., Fragment-based virtual screening discovers potential new Plasmodium PI4KIIIβ ligands. *BMC Chem.* **2022,** *16* (1), 1-9.

49. Paquet, T.; Le Manach, C.; Cabrera, D. G.; Younis, Y.; Henrich, P. P.; Abraham, T. S.; Lee, M. C.; Basak, R.; Ghidelli-Disse, S.; Lafuente-Monasterio, M. J., Antimalarial efficacy of MMV390048, an inhibitor of Plasmodium phosphatidylinositol 4-kinase. *Sci. Transl. Med.* **2017,** *9* (387).

50. Dembele, L.; Ang, X.; Chavchich, M.; Bonamy, G.; Selva, J.; Lim, M. Y.-X.; Bodenreider, C.; Yeung, B.; Nosten, F.; Russell, B., The Plasmodium PI (4) K inhibitor KDU691 selectively inhibits dihydroartemisinin-pretreated Plasmodium falciparum ring-stage parasites. *Sci. Rep.* **2017,** *7* (1), 1-9.

51. McNamara, C. W.; Lee, M. C.; Lim, C. S.; Lim, S. H.; Roland, J.; Nagle, A.; Simon, O.; Yeung, B. K.; Chatterjee, A. K.; McCormack, S. L., Targeting Plasmodium PI (4) K to eliminate malaria. *Nature* **2013,** *504* (7479), 248-253.

52. Zeeman, A.-M.; Van Amsterdam, S. M.; McNamara, C. W.; Voorberg-Van Der Wel, A.; Klooster, E. J.; Van Den Berg, A.; Remarque, E. J.; Plouffe, D. M.; Van Gemert, G.-J.; Luty, A., KAI407, a potent non-8-aminoquinoline compound that kills Plasmodium cynomolgi early dormant liver stage parasites in vitro. *Antimicrob. Agents Chemother.* **2014,** *58* (3), 1586-1595.

53. Wurz, R. P.; Sastri, C.; D'Amico, D. C.; Herberich, B.; Jackson, C. L.; Pettus, L. H.; Tasker, A. S.; Wu, B.; Guerrero, N.; Lipford, J. R., Discovery of imidazopyridazines as potent Pim-1/2 kinase inhibitors. *Bioorg. Med. Chem. Lett.* **2016,** *26* (22), 5580-5590.

54. Morris, G. M.; Lim-Wilby, M., Molecular docking. In *Molecular modeling of proteins*, Springer: 2008; pp 365-382.

55. Walker, J. R., Wernimont, A.K., He, H., Seitova, A., Loppnau, P., Sibley, L.D., Graslund, S., Hutchinson, A., Bountra, C., Weigelt, J., Edwards, A.M., Arrowsmith, C.H., Hui, R., El Bakkouri, M., Structural Genomics Consortium (SGC), CRYSTAL STRUCTURE OF PVX_084705 WITH BOUND INHIBITOR. 2015-12-16.

56. Schrödinger Release 2020-2: Canvas, S., LLC, New York, NY, 2020.

57. Bemis, G. W.; Murcko, M. A., The properties of known drugs. 1. Molecular frameworks. *J. Med. Chem* **1996,** *39* (15), 2887-2893.

58. Fraser, C.; Carragher, N. O.; Unciti-Broceta, A., eCF309: a potent, selective and cell-permeable mTOR inhibitor. *MedChemComm* **2016,** *7* (3), 471-477.

59. Manolikakes, G.; Dong, M. S. Z.; Mayr, H.; Li, J.; Knochel, P., Negishi Cross-Couplings Compatible with Unprotected Amide Functions. *Eur. J. Chem.* **2009,** *15* (6), 1324-1328.

60. Yang, Y.; Oldenhuis, N. J.; Buchwald, S. L., Mild and General Conditions for Negishi Cross-Coupling Enabled by the Use of Palladacycle Precatalysts. *Angew. Chem., Int. Ed.* **2013,** *52* (2), 615-619.

61. Zegzouti, H.; Hennek, J.; Alves, J.; Goueli, S., ADP-Glo™ Kinase Profiling Systems for targeted and flexible kinase inhibitor profiling. **2014**.

62. Baker, D. A.; Stewart, L. B.; Large, J. M.; Bowyer, P. W.; Ansell, K. H.; Jiménez-Díaz, M. B.; El Bakkouri, M.; Birchall, K.; Dechering, K. J.; Bouloc, N. S., A potent series targeting the malarial cGMP-dependent protein kinase clears infection and blocks transmission. *Nat. Commun.* **2017,** *8* (1), 1-9.

63. Penzo, M.; de Las Heras-Dueña, L.; Mata-Cantero, L.; Diaz-Hernandez, B.; Vazquez-Muñiz, M.-J.; Ghidelli-Disse, S.; Drewes, G.; Fernandez-Alvaro, E.; Baker, D. A., High-

throughput screening of the Plasmodium falciparum cGMP-dependent protein kinase identified a thiazole scaffold which kills erythrocytic and sexual stage parasites. *Sci. Rep.* **2019,** *9* (1), 1-13.

64. Chaube, U.; Bhatt, H., 3D-QSAR, molecular dynamics simulations, and molecular docking studies on pyridoaminotropanes and tetrahydroquinazoline as mTOR inhibitors. *Mol. Diversity* **2017,** *21* (3), 741-759.

65. Ren, P.; Liu, Y.; Wilson, T. E.; Li, L.; Chan, K., Benzoxazole kinase inhibitors and methods of use. Google Patents: 2014.

66. Walker, J. R., Wernimont, A.K., He, H., Seitova, A., Loppnau, P., Sibley, L.D., Graslund, S., Hutchinson, A., Bountra, C., Weigelt, J., Edwards, A.M., Arrowsmith, C.H., Hui, R., El Bakkouri, M., Structural Genomics Consortium (SGC), Crystal Structure of PVX_084705 with bound 1-tert-butyl-3-(3-chlorophenoxy)-1H-pyrazolo[3,4-d]pyrimidin-4-amine inhibitor **2015**.

67. Ouvry, G.; Clary, L.; Tomas, L.; Aurelly, M.; Bonnary, L.; Borde, E.; Bouix-Peter, C.; Chantalat, L.; Defoin-Platel, C.; Deret, S., Impact of minor structural modifications on properties of a series of mTOR inhibitors. *ACS Med. Chem. Lett.* **2019,** *10* (11), 1561-1567

CHAPTER THREE: Imidazopyridazines

3.1. Introduction

Towards circumventing antimalarial drug resistance,[1, 2] a SoftFocus kinase (SFK) library[3] was subjected to whole-cell phenotypic high-throughput screening (HTS) against human malaria parasite *Plasmodium falciparum* strains using an image-based assay.[4] This library, initiated by the BioFocus group, was tested using the DAPI (4′,6-diamidino-2-phenylindole) staining procedure in a high throughput fashion.[5] Compounds based on the diaryl-imidazopyridazine core (**Figure 3.1**), designated SoftFocus Kinase 52 (SFK52), were among the chemical series identified with antiplasmodium activity.[4]

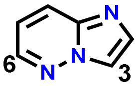

Figure 3.1: Imidazopyridazine core

Of the 488 compounds screened, a total of 153 compounds displayed >80% inhibition against *Pf*NF54 at a concentration of 1.82 μM.[4] An SAR was established by exploring aryl substitutions at positions 3 and 6. Initial *in vitro* ADME data identified 4-methylsulphonylphenyl as the preferred substituent at position 3. At position 6, electron-withdrawing *meta*-substituents on the aromatic ring conferred optimal potency. Further optimization of the identified scaffold led to the identification of the lead compound MMV652103 (**Figure 3.2**), hereafter referred to as the parent compound.

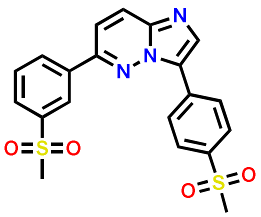

***Pf*NF54 IC$_{50}$ = 7.3 nM**
***Pf*K1 IC$_{50}$ = 6.3 nM**
***In vivo P. berghei* (po) at 4 x 50 mg/kg, 98%, 7 MSD^{a}**
hERG IC$_{50}$ = 0.9 µM
Solubility, pH 6.5 <5 µM
***Pv*PI4K IC$_{50}$ = 0.8 nM**
***Pf*PKG IC$_{50}$ = 120 nM**

Figure 3.2: Parent compound (MMV652103) ^{a}MSD, mean survival days; hERG, human *ether-a-go-go*-related gene; *Pv*PI4K, *P. vivax* phosphatidylinositol 4-kinase; *Pf*PKG, *P. falciparum* cGMP-dependent kinase

3.1.1 Imidazopyridazines as *Pf*CDPK1 and *Pf*PKG inhibitors

Plasmodium kinase inhibition by chemotypes with the imidazopyridazine core has also been reported. Potent 3,6-disubstituted imidazopyridazine-based inhibitors were identified by Chapman et al. via HTS against *P. falciparum* calcium-dependent protein kinase 1 (*Pf*CDPK1).[6] Subsequent SAR exploration using CADD methods yielded lead compounds with promising *in vitro* ADME and antiparasitic activity. When screened against a panel of human kinases (at 1 µM inhibitor concentration), one of these compounds (**Figure 3.3**) exhibited high selectivity and modest *in vivo* efficacy in a *P. berghei* mouse model.

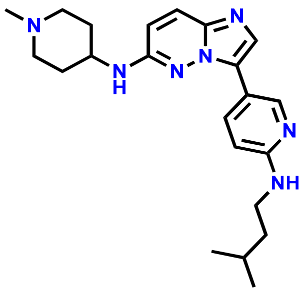

Figure 3.3: Potent *Pf*CDPK1 inhibitor (*Pf*CDPK1 IC$_{50}$ = 0.013 µM) with imidazopyridazine core *In vivo P. berghei* (po) at 4 × 50 mg/kg, 46%, 7 mean survival days

The physicochemical property profile and structural diversity of this series were further explored by introducing alternative heteroaromatic linking motifs.[7] The pyrazole linker replaced the six-membered heteroaromatic ring to further improve ADME parameters such as lowering of LogD. Using a homology model generated for *Pf*CDPK1, Chapman at al. followed a structure-guided design approach to improve the antimalarial potency of the imidazopyridazine series.[8] This resulted in a lead compound with *Pf*CDPK1 IC_{50} in the sub-nanomolar range and improved *in vitro P. falciparum* EC_{50} values (**Figure 3.4**).

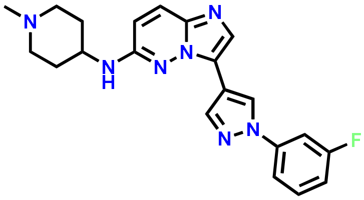

Figure 3.4: *Pf*CDPK1 inhibitor with *Pf*CDPK1 IC_{50} = 0.02 μM

Unfortunately, designed to mitigate ADME issues, especially permeability; aryl linker rings and basic side chain, modifications were accompanied by a loss in antiparasitic potency. Although compound exposure, *in vivo*, was increased in a murine model and *Pf*CDPK1 activity was maintained, efficacy remained modest (**Figure 3.5**).

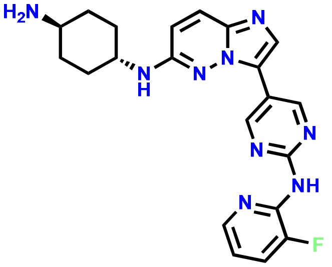

***Pf*CDPK1 IC_{50}:**	**<0.010μM**
***P. falciparum* EC_{50}:**	**0.012μM**
MLM %rem at 30 mins:	**85**
In vivo % reduction in parasitemia (*P. berghei*):	**4**

Figure 3.5: *Pf*CDPK1 inhibitor with imidazopyridazine core. MLM, mouse live microsomes

Considering the results obtained, the effect of targeting *Pf*CDPK1 on *in vivo* parasitemia reduction was questioned. The poor correlation between inhibition of parasite growth and enzyme inhibition indicated that off-target activities contributed to the compounds' antiplasmodium potency.[9] Green et al. used a chemical genetics approach, where the effects of inhibition the *Pf*CDPK1 were studied, to demonstrate that inhibition of the already mentioned protein had no effect on asexual parasite development.[10] This suggested that imidazopyridazines killed parasites via inhibition of other enzymes despite their potent inhibition of *Pf*CDPK1 *in vitro*.[10] Furthermore, a class of late-acting imidazopyridazines was shown to kill parasites via inhibition of *Pf*PKG.[10-12] *Pf*PKG was established as the primary target after observing a significant shift in potency (up to 29-fold) when compounds were screened against a *Pf*PKG T618Q mutant in which the crucial threonine gatekeeper is mutated to a relatively bulky glutamic acid.

3.1.2. Imidazopyridazines as *Pf*PI4K inhibitors

KAI715, a potent compound with an imidazopyridazine core, was identified via cell-based screening against *P. falciparum* asexual blood-stage parasites (**Figure 3.6**).[13] Using forward genetics in which the gene responsible for the mutant phenotype is identified and characterized, the target of **KAI715** was elucidated to determine its mechanism of action. Two resistant clones were yielded by selection with **KAI715**.

The first clone showed resistance in *Pf*PI4K amplification and the second comprised an Asp139Tyr mutation in the small GTPase *Pf*Rab11A (PF3D7_1320600). Consistent with membrane trafficking functions, PI4K regulates and binds Rab11A in *Drosophila spermatocytes*. *Pf*PI4K was thus convincingly identified as the direct target for the imidazopyridazine compound **KAI715** using genetic and chemical evidence.

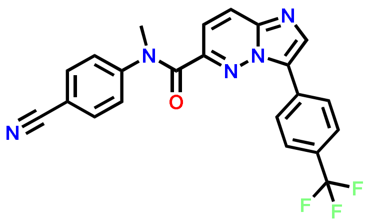

Figure 3.6: KAI715, a *Pf*PI4K inhibitor with *Pf*PI4K IC_{50} = 11 nM

3.1.3. Imidazopyridazines as dual inhibitors of *Pv*PI4K and *Pf*PKG

Imidazopyridazine analogues have so far been shown to target *Plasmodium* PKG and PI4K. To improve the poor solubility of the parent compound (MMV652103), Cheuka et al. synthesized amide-containing analogues.[14] These were then investigated in a single-point assay to determine percent inhibition against both recombinantly expressed *Pf*PKG (at 10 µM inhibitor concentration) and *Pv*PI4K (at 0.1 µM inhibitor concentration). All 22 analogues exhibited potent *Pv*PI4K inhibition with over 86% of compounds showing >90% *Pv*PI4K inhibition at 0.1 µM. This suggested that *Plasmodium* PI4K may be the major target driving the potent whole-cell antiplasmodium activity observed. The imidazopyridazine analogue shown in **Figure 3.7** displayed the highest antiplasmodium activity (*Pf*NF54 IC_{50} = 0.019 µM) and the highest percent inhibition against *Pv*PI4K (99.8%).

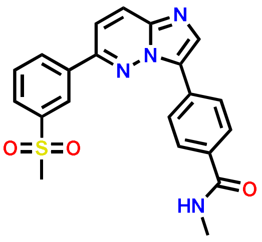

***Pf*NF54 IC_{50}: 0.019 µM**
% *Pv*PI4K inh. @ 0.1µM: 99.8 %
% *Pf*PKG inh. @ 10µM: 75 %

Figure 3.7: Frontrunner imidazopyridazine analogue studied by Cheuka et al.[14]

3.2. Aims and specific objectives

3.2.1. Aims

The probability of several essential targets in a parasite generating resistance mutations at the same time is extremely low.[15] Therefore, polypharmacology has proved to be beneficial in either preventing or slowing the emergence of drug resistance.[16] In the pursuit of dual target inhibition, the overall aim of this project is to develop an SAR of imidazopyridazines as dual inhibitors against *Plasmodium* PI4K and PKG. Greater focus was placed on improving *Plasmodium* PKG inhibition as the imidazopyridazine series investigated by Cheuka et al. already showed potent *Plasmodium* PI4K inhibition.

3.2.2. Specific Objectives

1. Prioritize compounds from the in-house library for *Pf*PKG screening using a chemoinformatics approach (first batch of imidazopyridazine analogues to be screened against *Pf*PKG)
2. Rationalize enzymatic data from the previously prioritized compounds using molecular docking
3. Use the rationale developed to virtually screen the in-house library and select compounds for further *Pf*PKG screening (second batch of imidazopyridazine analogues to be screened against *Pf*PKG).

3.3. Compound prioritization using chemoinformatics

For this part of the project, an in-house library of 334 imidazopyridazine analogues was used. Unfortunately, compounds in this library showed poor solubility. This poses challenges as one of the consequences of poor solubility in enzyme assays is partial inhibition, thus providing unreliable data.[17] To mitigate this issue, a chemoinformatics approach was used to prioritize compounds for *Pf*PKG screening. This provides an appropriate starting point to generate the structure activity relationship (SAR) with regard to *Pf*PKG inhibition. In addition to the properties used in Lipinski's rule of five; various descriptors were selected, due to their role in predicting solubility, and calculated for imidazopyridazine compounds.[18]

1. Aliphatic indicator (Fsp^3)

The concept of the aliphatic indicator was introduced by Yan and Gastigier:[19]

$$Fsp^3 = \frac{number\ of\ sp^3\ carbons}{number\ of\ total\ carbons}$$

This descriptor was also defined as a carbon bond saturation measure by Lovering et al.[20] Fsp^3 increases as compounds progress through the drug development pipeline. In the discovery phase, the average Fsp^3 value is 0.36, and this increases to 0.45 in Phase 3. Marketed drugs have a mean Fsp^3 value of 0.47. A high Fsp^3 value is largely associated with low melting point and high solubility. Lovering and colleagues subsequently demonstrated that compounds with high Fsp^3 values also showed low CYP450 inhibition and promiscuity.[21]

2. Aromatic balance (Ar-sp^3)

Aromatic balance was introduced by Lesson et al. as an additional metric to assess the impact of ion class and time on oral drug molecular properties.[22] The marketed drug data indicated that it is preferred when Ar-sp^3 value is <0 meaning that compounds are more lipophilic.

$$Ar\text{-}\,sp^3 = number\ of\ aromatic\ atoms - number\ of\ sp^3\ carbons$$

Used as a shape descriptor, increasing Ar-sp^3 values are associated with an increase in "flatness". Conversely, low Ar-sp^3 values increase the contribution of aliphatic properties and three-dimensionality. Patented compounds produced by pharmaceutical companies have a high degree of aromaticity.[23] 63% of these patented compounds have more than 2 aromatic rings.

3. Property forecast index (PFI)

The PFI was proposed by Hill and Young who analyzed the solubility data from a GSK compound library:[24]

$$PFI = \ logD_{7.4} + aromatic\ ring\ count$$

Individually, correlation between the two parameters is weak. This descriptor was also extended to include intrinsic clearance, CYP450 inhibition, hERG binding, promiscuity, and permeability. This increased its ability to predict ADME properties.[25] Therefore, compounds with ideal properties are associated with low PFI values and for optimal developability, compounds should have a $PFI \leq 7$. Nakashima et al. demonstrated that compounds with $PFI < 5$ were likely accompanied by high measured thermodynamic solubility.[26]

4. Aromatic indicator (Ar/HA)

In addition to the aliphatic indicator, Yan et al. used the aromatic indicator (also referred to as the aromatic proportion, AP) when building a neural network model to predict aqueous solubility:[19]

$$Ar/HA = \frac{number\ of\ aromatic\ atoms}{number\ of\ heavy\ atoms}$$

Although the contribution of Ar/HA to the model was not clear, when applied to a test set of 496 compounds, the model achieved $r = 0.96$, $r^2 = 0.92$, mean absolute error = 0.4, and SD = 0.59. Delaney then introduced the Ar/HA descriptor in a regression model, which increased its predictive power.[27] It was then suggested that dense crystals with high melting points were formed by aromatic compounds leading to low solubility. Ar/HA was then included in the generation of a recursive partitioning (RP) binary model to classify whether compounds were soluble enough to obtain reliable data from biological screening assays.[28] The algorithm of the model selected molecular weight and Ar/HA descriptor as the most influential factors when categorizing the compounds as either insoluble or soluble.

These described physicochemical descriptors were calculated, for the in-house library, then plotted and visualized as a heatmap to investigate correlations between physicochemical properties (**Figure 3.8**). This 2D visual representation uses colors to identify the correlation between the characteristics using a deep learning algorithm.[29] Links between different molecular characteristics are revealed and evaluated.

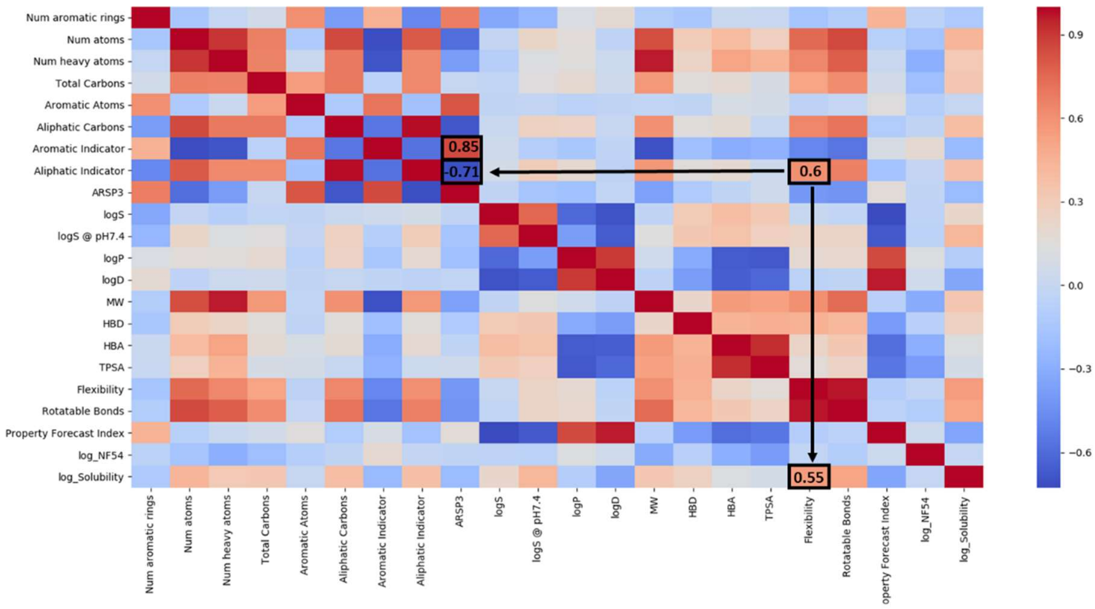

Figure 3.8: Heatmap of the calculated physicochemical properties of SFK52 library compounds. The red color showed positive correlation while the blue color demonstrated negative correlations.

From this heatmap, focus was put on the correlation of solubility to other calculated properties of the compounds. The flexibility of the compound correlates with its solubility and aliphatic indicator (Fsp^3). This implied the role that the number of saturated carbon plays regarding solubility. In the same space, the aromatic balance ($Ar\text{-}sp^3$) is negatively correlated with the aliphatic indicator (Fsp^3), but strongly correlated with the aromatic indicator (Ar/HA).

Distribution curves of compounds in this library were generated for the Property Focus Index (PFI) and the aliphatic indicator (Fsp^3) to understand how many compounds had the ideal value range. Insightfully, the least number of compounds were found in the indicated target class relaying a reason why solubility plagued this library.

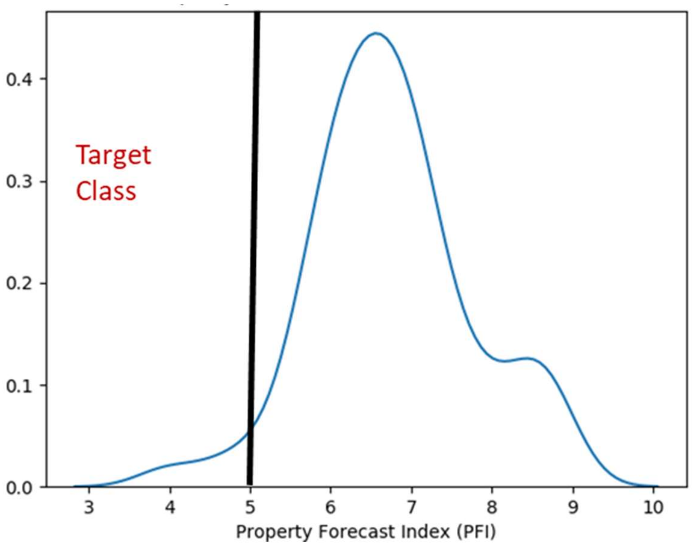

Figure 3.9: Property forecast index (PFI) distribution of imidazopyridazines

As PFI increases, the number of compounds that meet defined target values for solubility, permeability clearance, hERG inhibition, and promiscuity decreases. **Figure 3.9** shows that most compounds had a PFI value of about greater than 5 predicting problems with solubility and promiscuity.

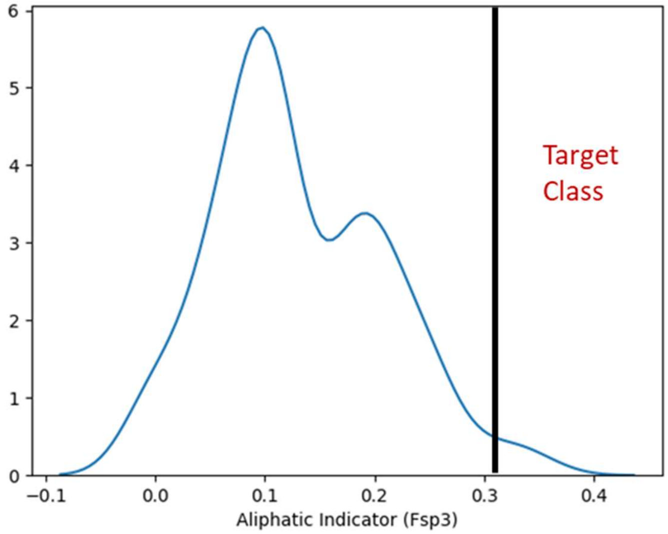

Figure 3.10: Aliphatic indicator (Fsp^3) distribution of imidazopyridazines

Moreover, the distribution curve of Fsp^3 shown in **Figure 3.10** demonstrates that once again majority of the compounds are outside the target aliphatic indicator value. As the Fsp^3 value increases through development phases from 0.36 in discovery to an average of 0.47 in marketed drugs.[21] Additionally, the aromaticity of compounds negatively correlates with their solubility. Therefore, decreasing the number of aromatic rings will influence the solubility and promiscuity of the compounds.

Because of the correlation between flexibility and the aliphatic indicator (Fsp^3), imidazopyridazine analogues with Fsp^3 of >0.3 were selected. Therefore, to create a starting point to build an SAR that is experimentally validated, nine (including matched pairs) compounds were selected for *Pf*PKG screening according to the protocol described in **Section 6.2.4** (**Table 3.1**).

Table 3.1: Whole-cell and enzymatic activity and calculated binding energy data of imidazopyridazine analogues

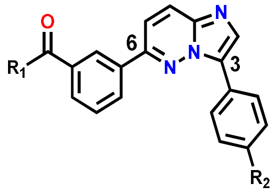

Compound	**R$_1$**	**R$_2$**	**Solubility (µM)^a**	***Pf*PKG (% inh. at 10 µM)^b**	***Pf*PKG IC$_{50}$ (µM)^c**
1	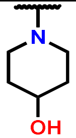	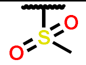	178	96	0.183
2	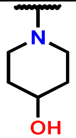	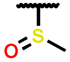	ND	95	2.24
3	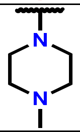	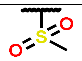	100	94	0.292
4	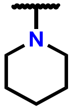	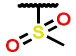	6.3	92	0.432
5	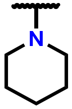	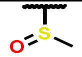	200*	79	1.51
6	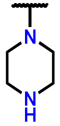	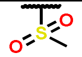	2.2	100	ND
7	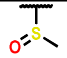	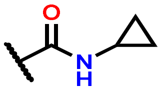	200*^{d}	49	ND
8	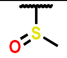	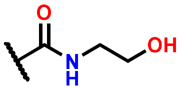	ND	29	ND
9	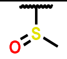	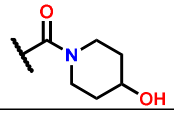	170*^{d}	34	ND

^{a}Determined at pH 6.5 using an HPLC-based miniaturized shake flask method. ^{b}Percent *Pf*PKG inhibition at 10 µM, carried out in triplicate in n = 2 independent experiment. ^{c}*In vitro PfPKG* activity at 10 µM ATP. ^{d}Determined at pH 7.4 using turbidimetric solubility assay *Data from Cheuka et al.[14]

The compounds selected showed high to moderate solubility and varying *Pf*PKG inhibitory activity (29–100%), thus providing a strong basis for SAR studies. Compounds with aliphatic rings on the R_1 position (**1**, **2**, **3**, **4** and **5**) showed 79–100% *Pf*PKG inhibition at 10 µM.

Compounds with a sulphone on R_2 showed 92–100% inhibition at 10 µM, indicating that amide substitution on R_1 increased *Pf*PKG inhibition. Conversely, *Pf*PKG inhibition decreased with amide substituents on R_2 (**7**, **8**, and **9**) to 29–49% inhibition at 10 µM. This trend was also apparent in amidated imidazopyridazine analogues synthesized and tested by Cheuka et al. The sulphoxide at R_2 reduced *Pf*PKG inhibition as observed in matched pairs: **1**, **2** and **4**, **5.**

With a wide range of *Pf*PKG activity demonstrated by the compounds selected, the structural features affecting *Pf*PKG activity were then studied using molecular docking studies.

3.4. Rationalization of *Pf*PKG inhibition using molecular docking

The enzymatic data generated for the prioritized compounds above were used to develop a structure-based rationale driving *Pf*PKG inhibition. This was done by docking the compounds into *Pv*PKG (PDB ID: 5F0A) using the protocol described in **section 6.1.2.**

Compounds with unfavorable docking poses had amide moieties at the third position of the imidazopyridazine core (**Figure 3.11B**). This may be due to the back pocket, as illustrated in **Figure 3.11.** The substituted amide at position 3 may be too bulky, thus disallowing the ligand from properly fitting into the back pocket. These favorable poses also revealed the preferred binding pose of the imidazopyridazine core.

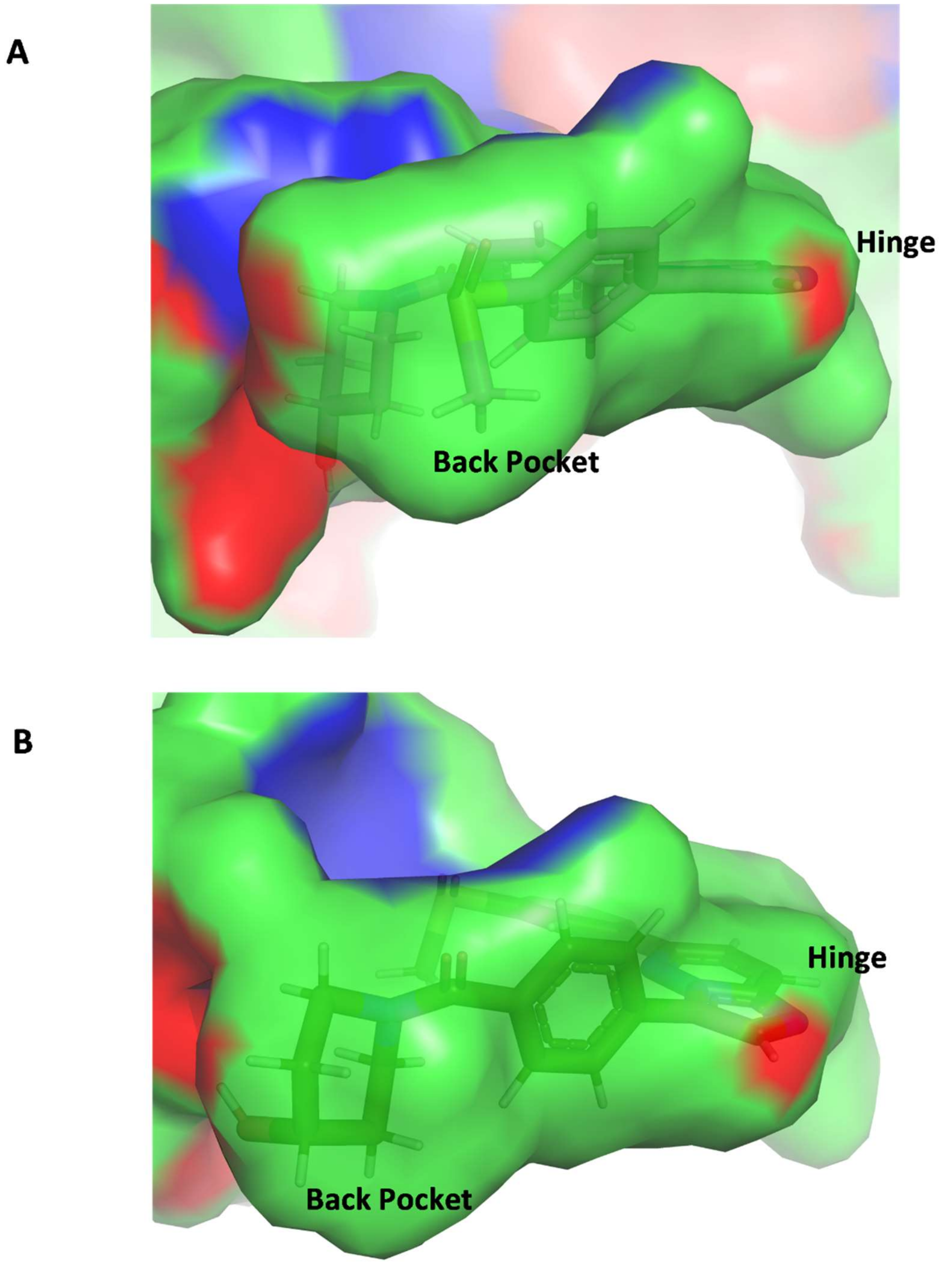

Figure 3.11: The favorable pose of **2** (**A**) and the unfavorable pose of **9** (**B**) when docked into *Pf*PKG (PDB ID: 5F0A). The negatively charged regions (red), positively charged region (green), and hydrophobic regions (green) are represented on the surface.

These discussed structural findings were used to filter out compounds, from the from the 334-compound in-house library, with predicted *Pf*PKG inhibition and were subsequently subjected to enzymatic screening.

3.5. *In silico* binding predictions and *Pf*PKG inhibition data

The structural findings discussed in the previous section were used to virtually filter the original library of 334 compounds. A total of 36 diverse imidazopyridazine analogues, including some matched pairs, were selected, and tested *in vitro* against *Pf*PKG using the protocol described in **Section 6.2.4** (**Table 3.2**).

Table 3.2: Enzymatic activity, docking score, and calculated binding energy data of imidazopyridazine analogues

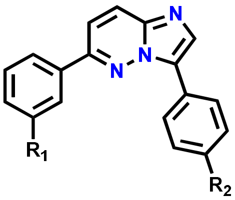

Compound	R1	R2	*Pf*PKG IC_{50} (µM)^{a}	Binding energy (kcal/mol)
10	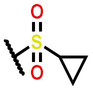	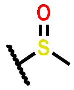	0.463	-69.52
11	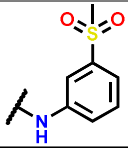	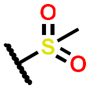	0.017	-61.39
12	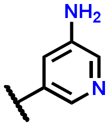	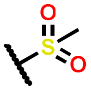	0.675	-50.24
13	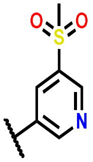	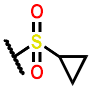	56%*	-60.77
14	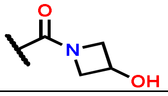	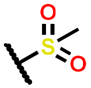	0.134	-65.85
15	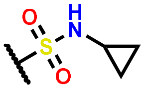	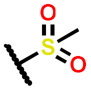	0.016	-51.33
16	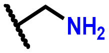	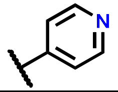	0.043	-46.22
17	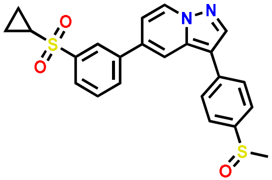		1.06	-62.81
18	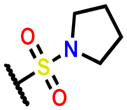	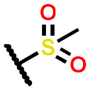	0.053	-57.91
19	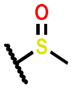	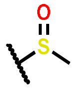	2.56	-59.07

20	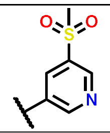	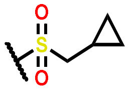	56%*	-68.54
21	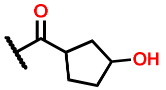	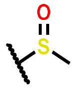	78%*	-66.9
22	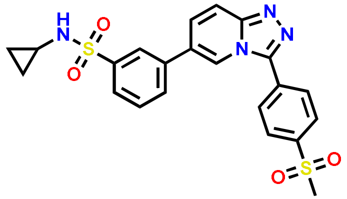		>30	-52.37
23	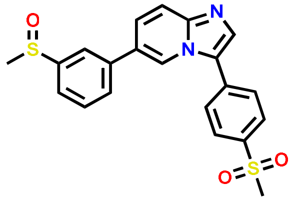		53%*	-57.11
24	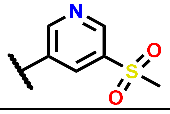	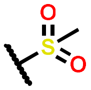	>30	-60.77
25	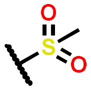	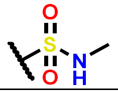	0.077	-63.65
26	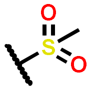	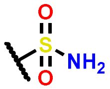	>10	-58.39
27	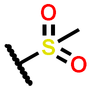	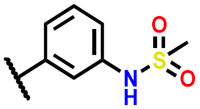	0.366	-64.04
28	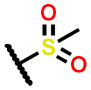	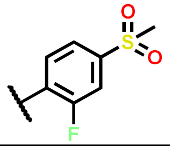	>30	-56.41
29	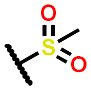	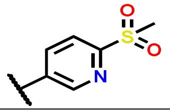	0.007	-58.89
30	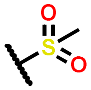	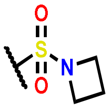	73%*	-51.77
31	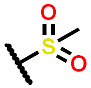	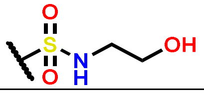	87%*	-68.20
32	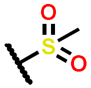	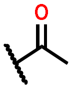	0.15	-61.78
33	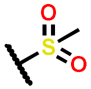	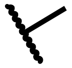	>30	-57.41

34	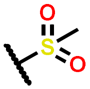	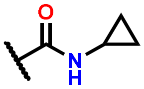	1.404	-67.89
35	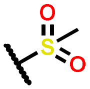	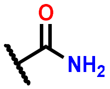	0.086	-60.24
36	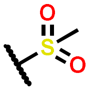	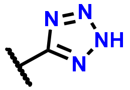	0.709	-40.50
37	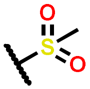	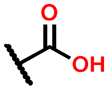	0.418	-46.54
38	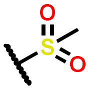	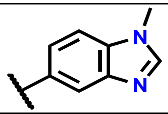	0.986	-50.77
39	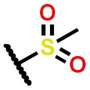	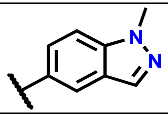	0.032	-49.50
40	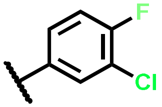	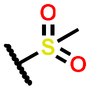	66%*	-58.80
41	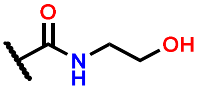	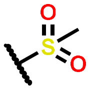	0.208	-55.54
42	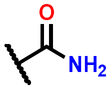	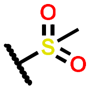	0.414	-48.67
43	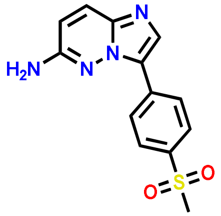		89%*	-46.54
44	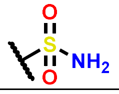	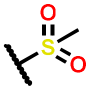	0.102	-50.70
45	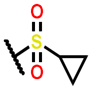	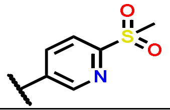	0.008	-53.44
Parent	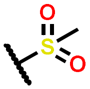	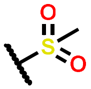	0.12	-57.29

[a]*in vitro PfPKG* activity at 10 µM ATP. *Percent *Pf*PKG inhibition at 10 µM, carried out in triplicate in n = 2 independent experiments.

Most of the compounds exhibited high activity. Twenty of 36 compounds showed *Pf*PKG IC_{50} < 1 µM (range: 0.007–0.986 µM). There were various structural changes on compounds which demonstrated low activity (IC_{50} > 30 µM). Compound **22** had a triazolopyridine core instead of the imidazopyridazine while **28** and **33** had an *ortho*-fluoro on the benzyl and methyl on R_2, respectively. The pyridyl moiety at R_1 of **24** also led to inactivity.

Due to the lack of correlation between enzymatic activity and calculated binding energies (**Figure 3.12**), a qualitative approach was used to gain further insight into the SAR driving *Pf*PKG inhibition.

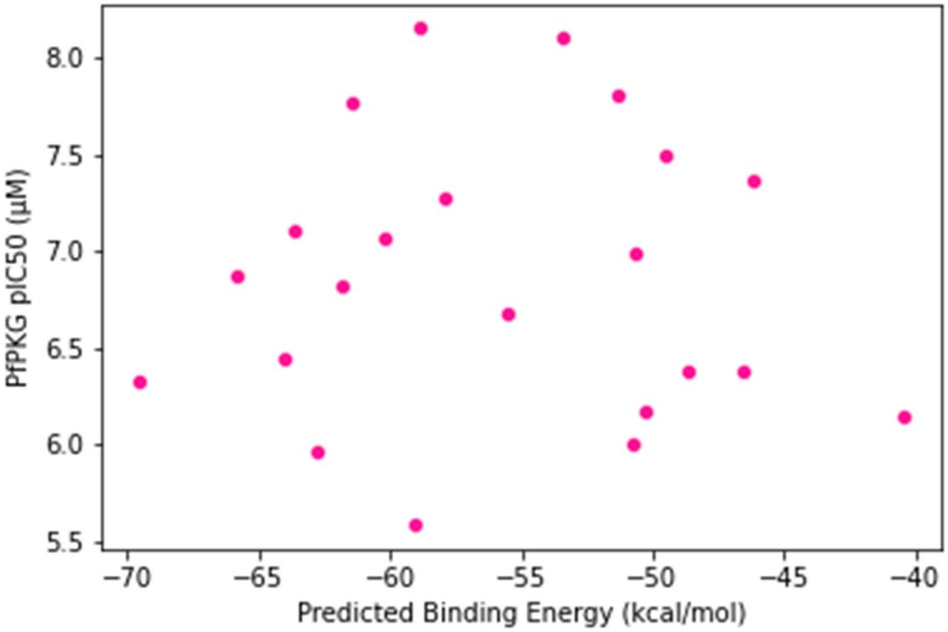

Figure 3.12: Scatter plot of the imidazopyridazine analogues showing the lack of correlation between the *Pf*PKG IC_{50} values and the calculated binding energy.

Therefore, the binding poses of matched pairs were analyzed and compared. The nearly 10-fold shift between the parent compound (*Pf*PKG IC_{50} = 0.12 μM) and **11** (*Pf*PKG IC_{50} = 0.017 μM) may be due to the interaction between the amine linker and the backbone of the isoleucine (**Ile540**) of the glycine-rich loop (**Figure 3.13**). Additional interactions were also observed between the ligand (**11**) and other residues, namely: **Arg542**, **Lys563**, and **Asp675**.

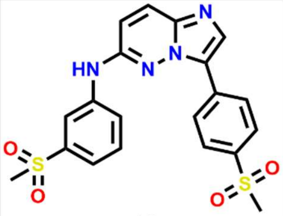

11

***Pf*PKG IC$_{50}$ = 0.017 μM**

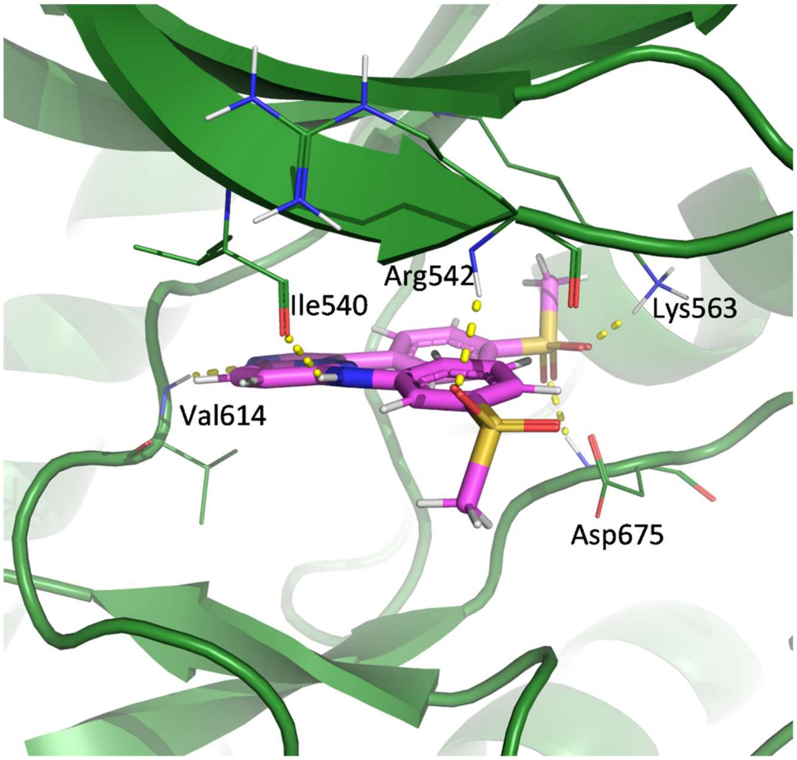

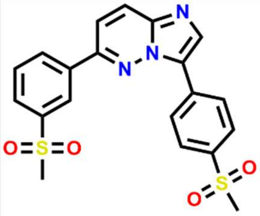

Parent

***Pf*PKG IC$_{50}$ = 0.12 μM**

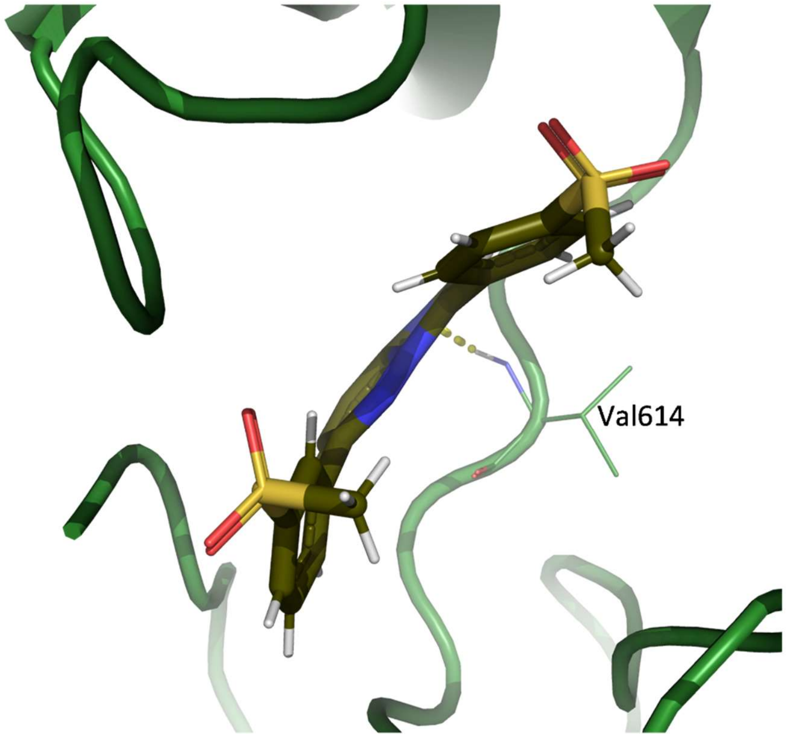

Figure 3.13: 11 (pink) and the parent compound (brown) docked into *Pv*PKG with interacting residues showed as lines

Compounds with amides (**42**; *Pf*PKG IC_{50} = 0.414 µM) and substituted amides (**41** and **14**; *Pf*PKG IC_{50} = 0.208 µM and 0.134 µM, respectively) at R_1 showed comparable *Pf*PKG inhibition activities. **16** had *Pf*PKG IC_{50} = 0.043 µM, which may be due to the interaction between the protonated amine and **Asp675** (**Figure 3.14**).

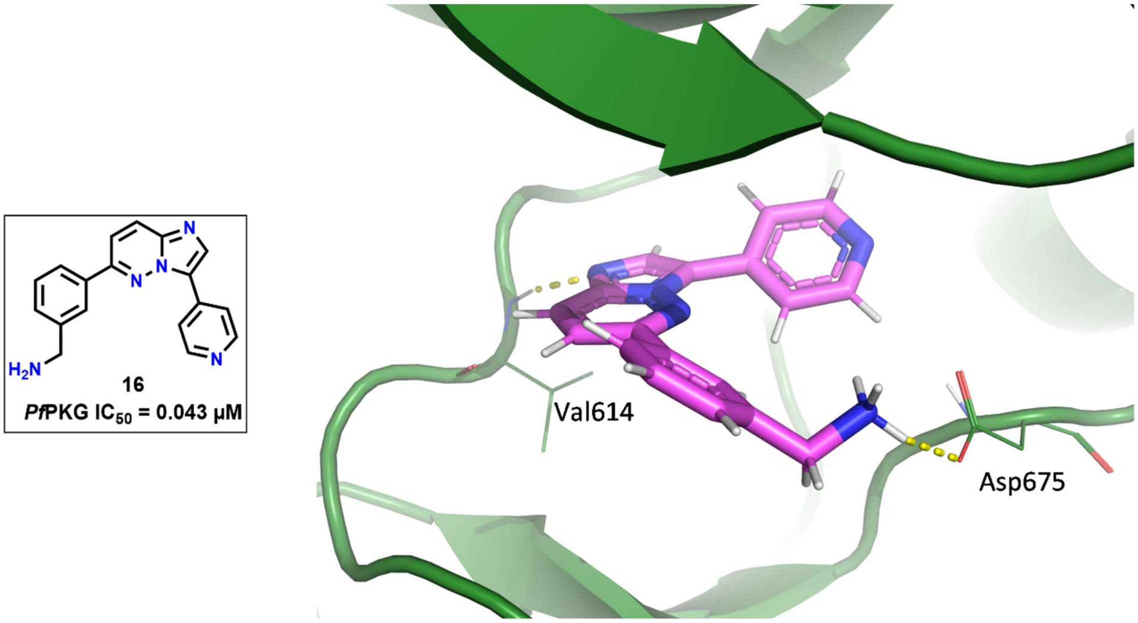

Figure 3.14: 16 (magenta) docked into *Pv*PKG (green) with interacting residues labeled and showed as lines

According to the *Pf*PKG inhibition, the sulphonamide (**44**, *Pf*PKG IC_{50} = 0.102 µM) is preferred over the amide (**42**, *Pf*PKG IC_{50} = 0.414 µM) at R_1. This preference of sulphonamides over amides at R_1 is also apparent in the difference in potency between substituted sulphonamides and substituted amides. Compounds with substituted sulphonamides had lower *Pf*PKG IC_{50} values: **15** (*Pf*PKG IC_{50}: 0.016µM) and **18** (*Pf*PKG IC_{50}: 0.053µM) than those with substituted amides: **14** (*Pf*PKG IC_{50}: 0.134µM) and **41** (*Pf*PKG IC_{50}: 0.208µM). Binding mode analysis of the docking poses of **44** and **42**, showed an additional interaction with **Asp675** and **44** (**Figure 3.15**).

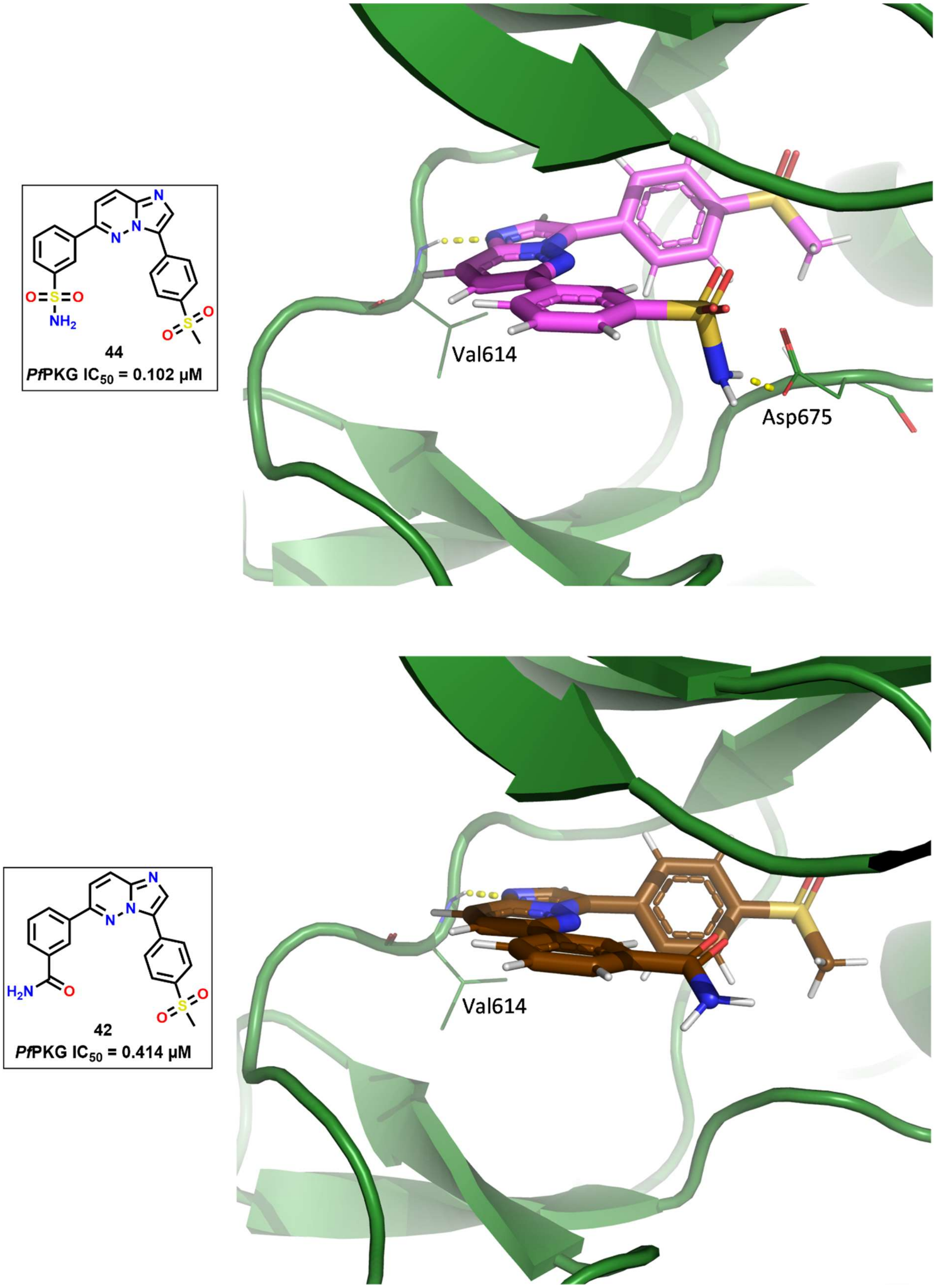

Figure 3.15: **44** (pink) and **42** (brown) docked into *Pv*PKG with interacting residues labeled and showed as lines

Loss of activity was also exhibited when the sulphones of the parent compound were replaced by sulphoxides in **19** (*Pf*PKG IC_{50} = 2.56 µM). According to the binding site analysis of **28** (*Pf*PKG IC_{50} > 30 µM), the addition of the *ortho*-fluoride to the R_2 benzyl moiety caused the core to flip, which may be responsible for the lack of *Pf*PKG activity observed (**Figure 3.16**). The core flip could be due to the size of the back pocket which is tight.

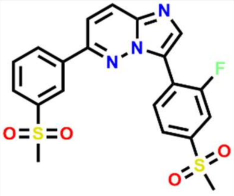

28
***Pf*PKG IC_{50} > 30 µM**

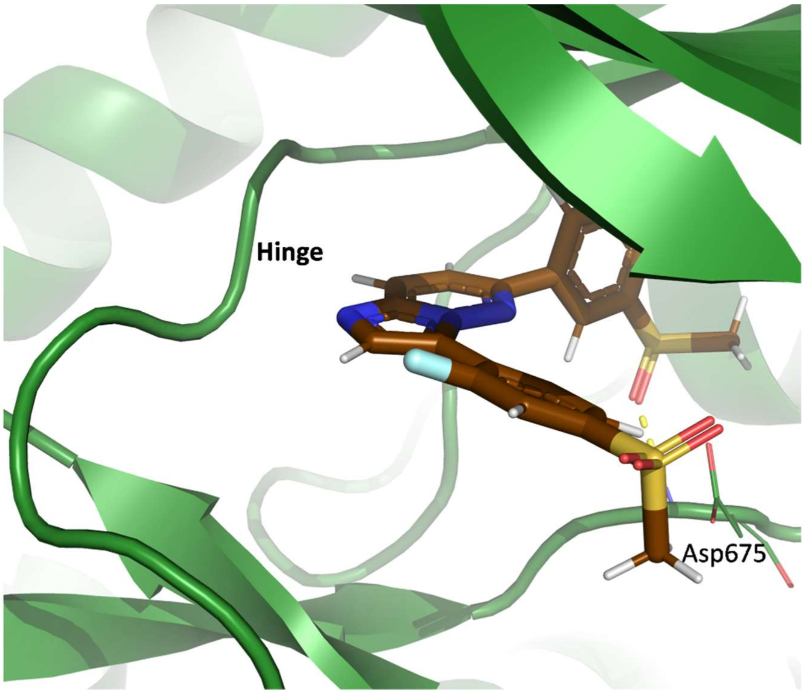

Figure 3.16: 28 (brown) docked into *Pv*PKG with interacting residues labeled and showed as lines

A substantial *Pf*PKG potency gain (>100-fold) was brought about by a subtle change on R_2 from sulphonamide (**26**; *Pf*PKG $IC_{50} > 10$ μM) to N-methyl sulphonamide (**25**; *Pf*PKG IC_{50} = 0.077 μM). This brings into focus the influence the back pocket has on *Pf*PKG inhibition.

As demonstrated by **25**, there could be hydrophobic interactions between the ligand and the back pocket as the only structural difference is on R_2. These hydrophobic interactions are also highlighted when comparing compounds **39** (*Pf*PKG IC_{50} = 0.032 μM) and **38** (*Pf*PKG IC_{50} = 0.986 μM) with the only structural differences being the benzo[*d*]imidazole of **39** and the indazole of **38**. Moreover, **Figure 3.17** also shows that there is a loss of hinge binding interactions with **38** which may also have contributed to the loss of *Pf*PKG inhibition.

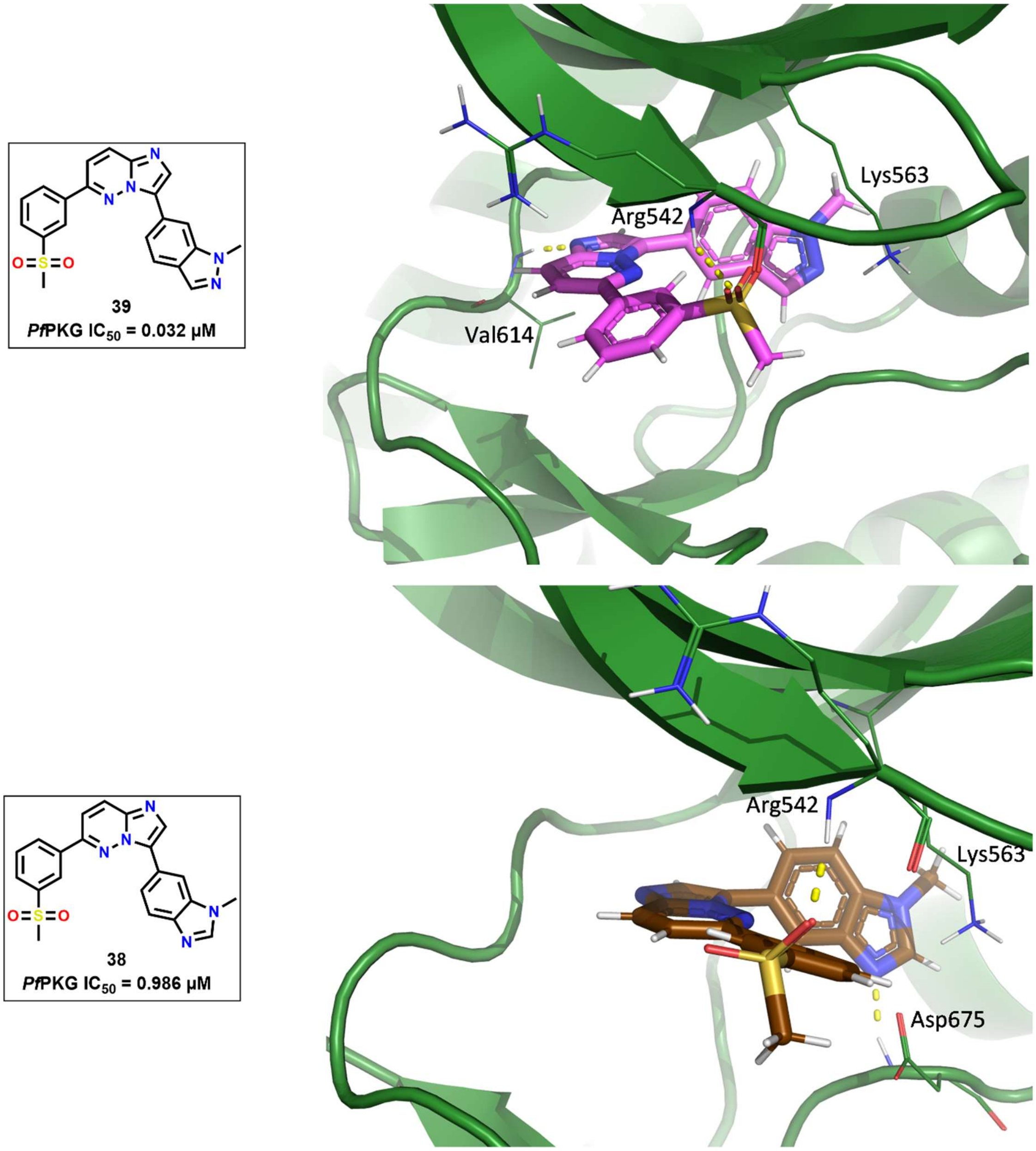

Figure 3.17: 39 (pink) and **38** (brown) docked into *Pv*PKG with interacting residues showed as lines.

Compounds with amide and carbonyl substituents on R_2 (**32**; *Pf*PKG IC_{50} = 0.15 µM, and **35**; *Pf*PKG IC_{50} = 0.086 µM, respectively) showed comparable potency. This could be because they both interact with the backbones of **Asp675** and **Arg542** (**Figure 3.18**).

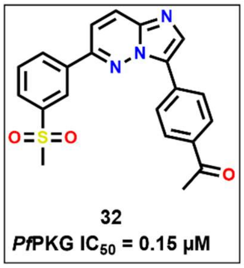

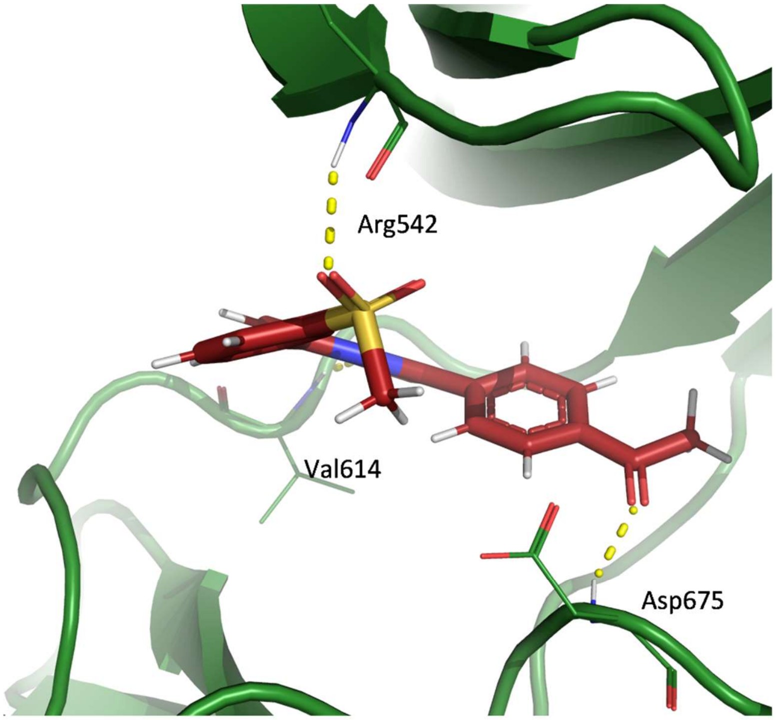

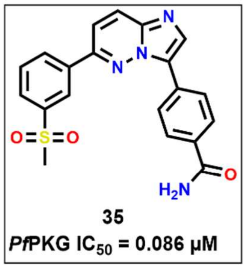

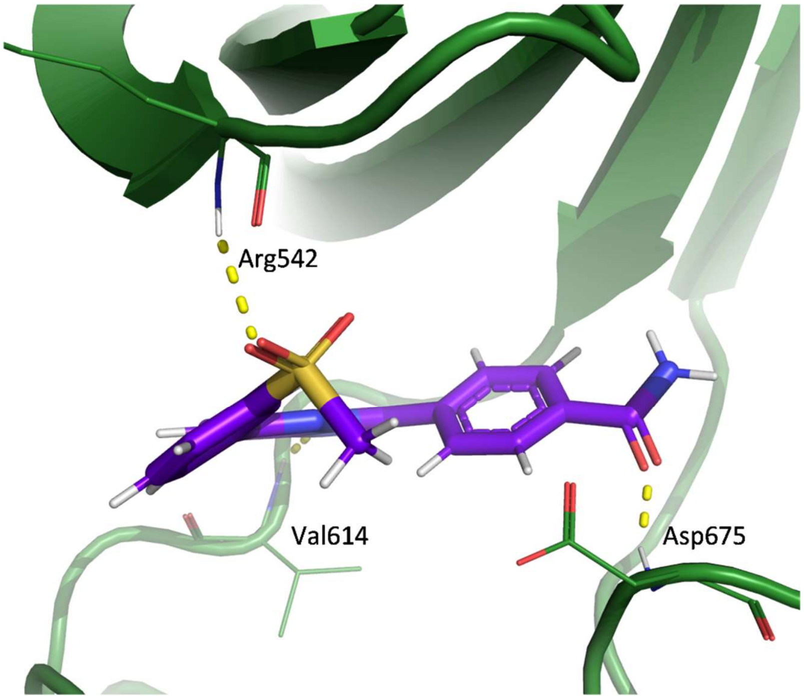

Figure 3.18: 32 (red) and **35** (purple) docked into *Pv*PKG with interacting residues labeled and showed as lines

The compound with bulk amide substituents (**34**; *Pf*PKG IC$_{50}$ = 1.404 µM) showed a decrease in potency associated with a tight back pocket (**Figure 3.19**).

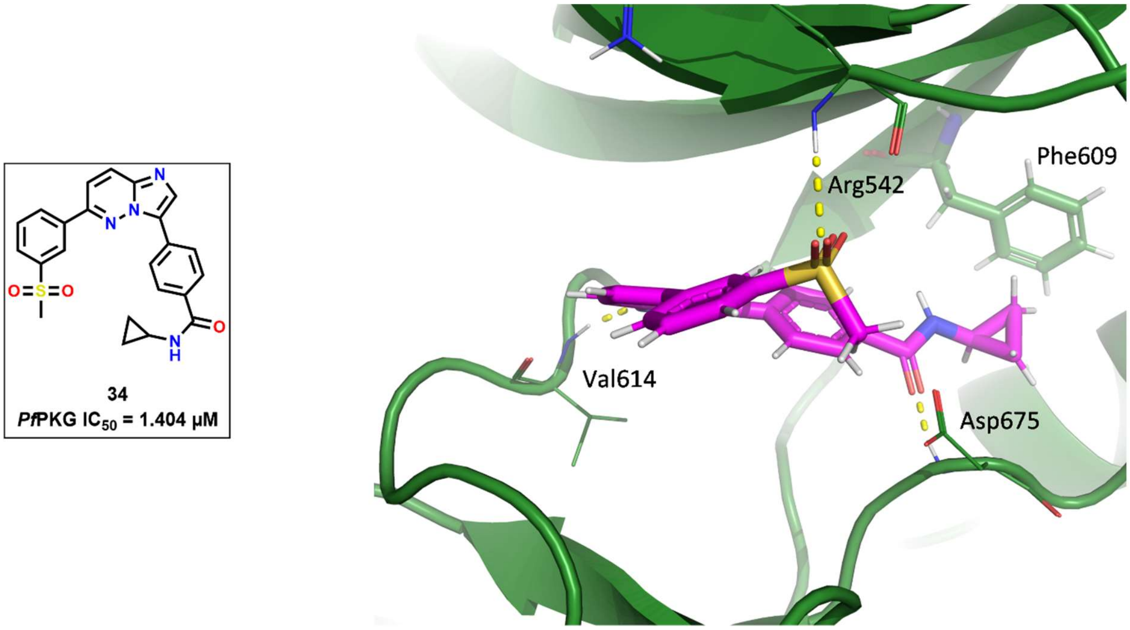

Figure 3.19: 34 docked into *Pv*PKG with interacting residues labeled and shown as lines

With the only structural difference being the cyclopropyl substituent at R$_2$, **29** and **45** showed comparable potency (0.007 µM and 0.008 µM, respectively). However, due to the structural similarity with **29** and the parent compound, their docking poses were quite similar making it difficult to decipher what is driving the >20-fold difference in *Pf*PKG inhibition. This warrants the use of molecular dynamic simulations to gain deeper insight into the interactions involved in driving the observed *Pf*PKG inhibition potency. This is described in the following section.

3.6. Molecular dynamics

There is a subtle structural difference between the parent compound (**Parent**) and **29**, which comprises a pyridyl in place of a phenyl (**Figure 3.20**).

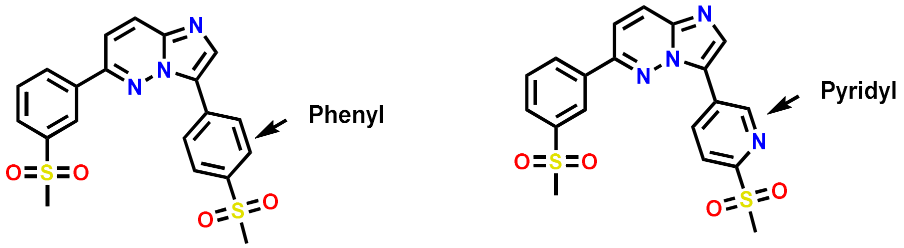

Parent
*Pf*PKG IC_{50} = 0.12 µM

29
*Pf*PKG IC_{50} = 0.007 µM

Figure 3.20: Structure of the parent compound and **29** with corresponding *Pf*PKG IC_{50} values

Molecular dynamic simulations were carried out, using the protocol described in **Section 6.1.3**, to gain deeper insight into the potency shift between the two compounds. Analysis of the back pocket interactions in the simulations revealed that a favorable interaction in that pocket increased *Pf*PKG potency. Focus was placed on the back pocket as this is where the structural difference between the two compounds is found.

Compound **29** formed a very strong and stable interaction between the sulphonyl on R_2 with **Asp675** residue for 99% of the time during the simulation. Conversely, there was very little to no interaction between the R_2 sulphonyl of the parent compound and **Asp675**. The line plot of distances over the simulation time shown in **Figure 3.21** shows the consistency of the interaction formed with the residue.

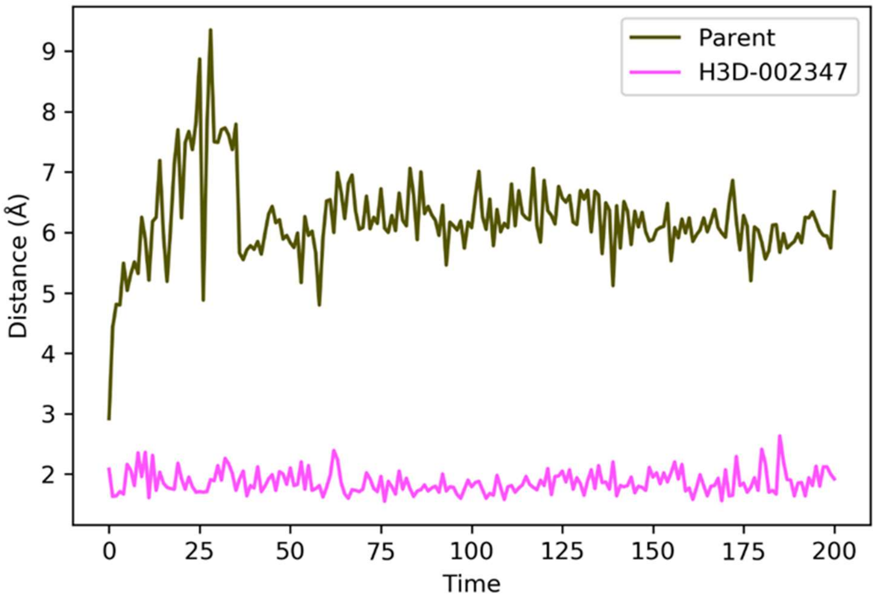

Figure 3.21: Distance between **Asp675** and the parent compound (brown) and **29** (pink)

This computationally validates the influence the **Asp675** residue has on *Pf*PKG inhibition. As seen in the previous section, interaction with this residue also had a positive impact on *Pf*PKG inhibition.

Further analysis of the molecular dynamic simulations of both complexes revealed a conformational difference in the back pocket. In the parent-PKG complex, bulky amino acid residues (**Asn578** and **Asn575**) in the back pocket were located close to the ligand, this could lead to the restricted movement of the methyl group of the R_2 sulphone.

The conformation of the mentioned residues in the PKG-**29** protein-ligand complex widened the space in the back pocket, permitting movement of the methyl group, exposing the R_2 sulphonyl to form a hydrogen-bond with **Asp675**. Differences in the distances from the respective ligands and bulky amino acids (**Asn578** and **Asn575**) are summarized in line plots of distances over the simulation time with respect to each protein-ligand complex (**Figures 3.22** and **3.23**).

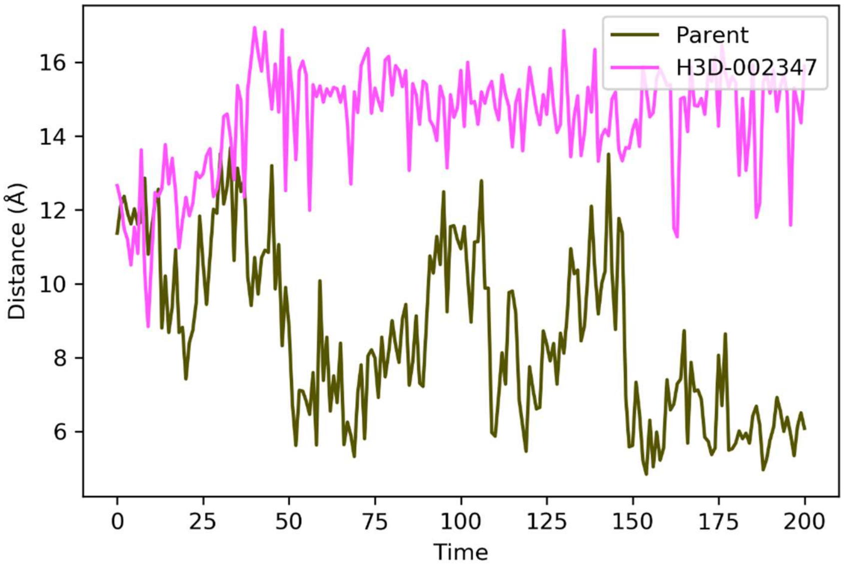

Figure 3.22: Distance between **Asn578** and the parent compound (brown) and **29** (pink)

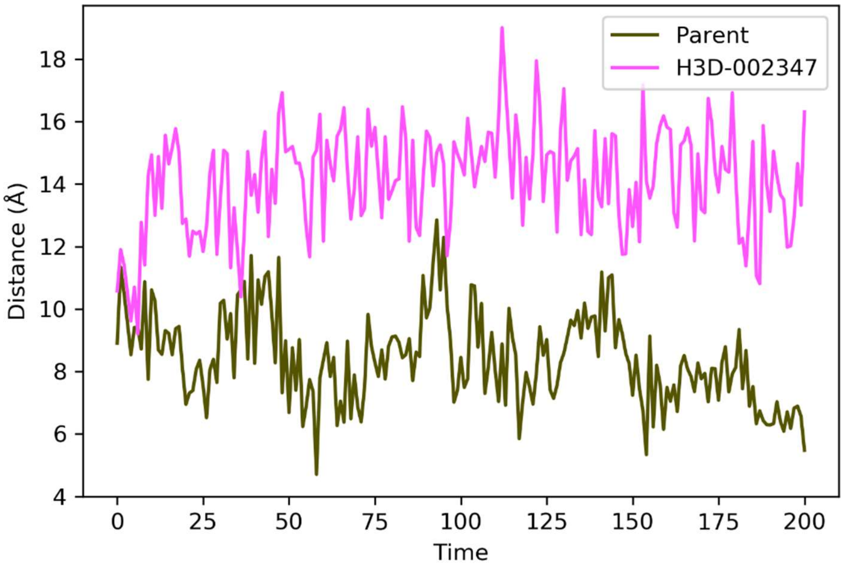

Figure 3.23: Distance between **Asn575** and the parent compound (brown) and **29** (pink)

Pyridyl moieties are often used in medicinal chemistry due to their various characteristics, specifically, hydrogen bond-forming ability, stability, and water solubility improvement.[30] Due to its increased electronegativity, when compared to phenyl, this aromatic heterocyclic moiety forms hydrogen bonds with water molecules.

3.7. Chemical Space Analysis

Chemical space analysis was done using the Platform for Unified Molecular Analysis (PUMA), version 1.[31] The compounds were color-coded according to their respective *Pf*PKG IC_{50} values. Compound **16** (*Pf*PKG $IC_{50} = 0.043$ µM) was located at the top-right of the plot. This may be due to the different R_1 and R_2 substitutes when compared to other analogues which commonly had sulphones on either side. This also showed the corresponding chemical space which can be further explored.

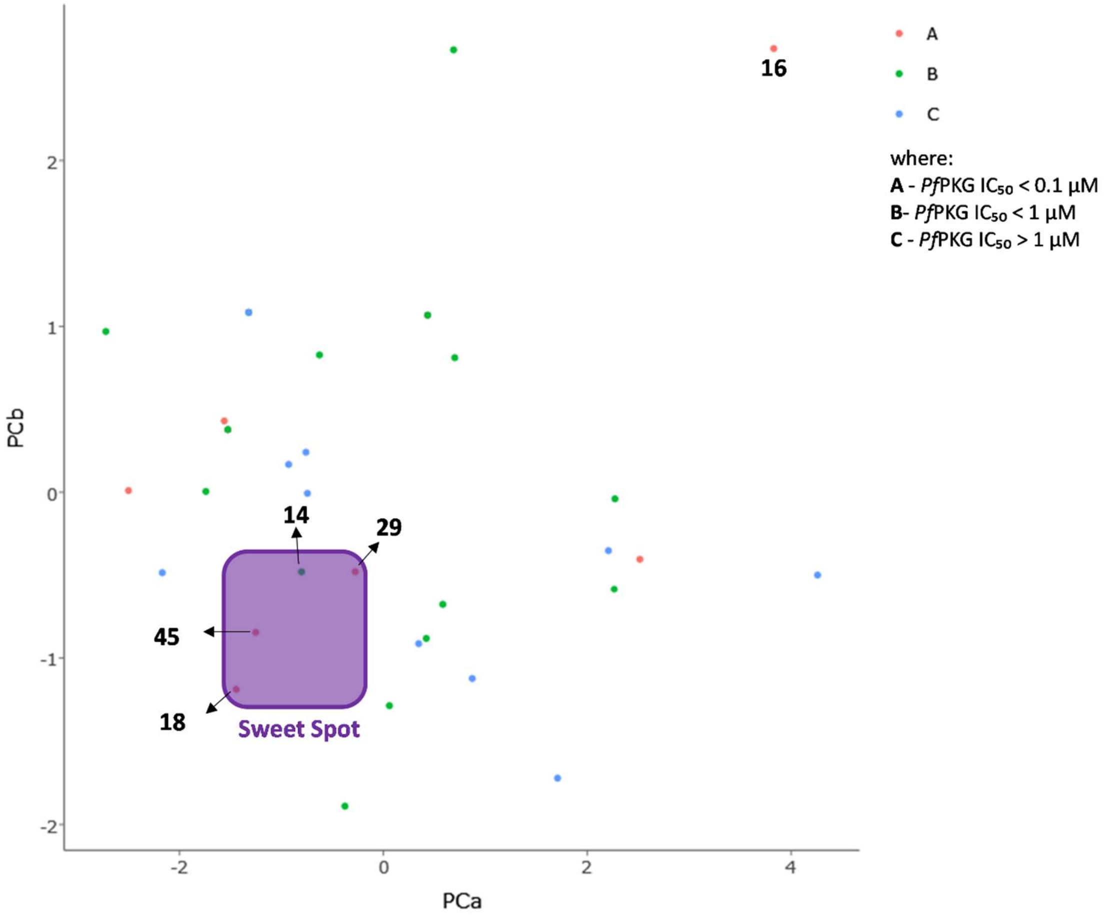

Figure 3.24: Chemical space analysis of the tested Imidazopyridazine analogues.

A sweet spot was also identified within the chemical space. This spot included compounds: **18** (*Pf*PKG IC_{50} = 0.053 µM), **45** (*Pf*PKG IC_{50} = 0.008 µM), **14** (*Pf*PKG IC_{50} = 0.134 µM) and **29** (*Pf*PKG IC_{50} = 0.008 µM). Therefore, targeting this spot during optimization may lead to the discovery of compounds with similar *Pf*PKG IC_{50} values.

3.8. Conclusion and future work

At position 6, substituted sulphonamides improve *Pf*PKG inhibition over substituted amides. As seen with the amine linker. increased interactions at the front pocket, through position 6 substitutions, also improve *Pf*PKG inhibition. **Figure 3.24** summarizes the structural findings observed. Interaction with the aspartic acid residue (**Asp675**) greatly improved *Pf*PKG inhibition activity. The conformation of the hydrophobic pocket may have also played a role *Pf*PKG inhibition.

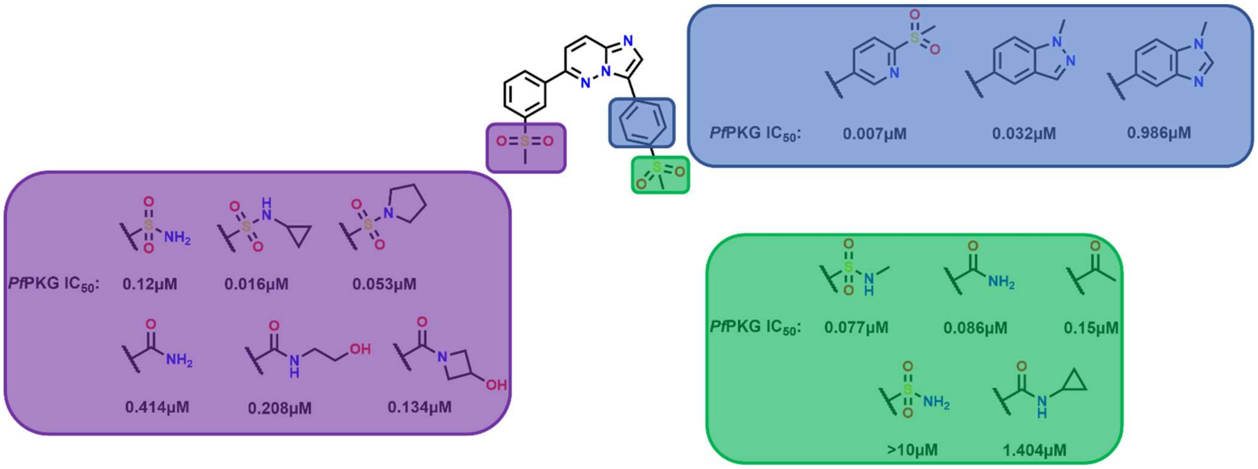

Figure 3.24: Schematic diagram that summarizes the findings discussed of the imidazopyridazine analogues

Incorporation of functional groups that to facilitate interaction with this residue may lead to improved inhibition. Designing 3,6-substituted imidazopyridazine analogues with sulphonamide substitutions at position 6 while maintaining a pyridyl moiety at position 3 may further increase *Pf*PKG inhibition.

3.9. References

1. Dondorp, A. M.; Nosten, F.; Yi, P.; Das, D.; Phyo, A. P.; Tarning, J.; Lwin, K. M.; Ariey, F.; Hanpithakpong, W.; Lee, S. J., Artemisinin resistance in Plasmodium falciparum malaria. *N. Engl. J. Med.* **2009,** *361* (5), 455-467.

2. Uwimana, A.; Legrand, E.; Stokes, B. H.; Ndikumana, J.-L. M.; Warsame, M.; Umulisa, N.; Ngamije, D.; Munyaneza, T.; Mazarati, J.-B.; Munguti, K., Emergence and clonal expansion of in vitro artemisinin-resistant Plasmodium falciparum kelch13 R561H mutant parasites in Rwanda. *Nat. Med.* **2020,** *26* (10), 1602-1608.

3. John Harris, C.; D Hill, R.; W Sheppard, D.; J Slater, M.; FW Stouten, P., The design and application of target-focused compound libraries. *Comb. Chem. High Throughput Screening* **2011,** *14* (6), 521-531.

4. Le Manach, C.; Gonzàlez Cabrera, D.; Douelle, F.; Nchinda, A. T.; Younis, Y.; Taylor, D.; Wiesner, L.; White, K. L.; Ryan, E.; March, C., Medicinal chemistry optimization of antiplasmodial imidazopyridazine hits from high throughput screening of a SoftFocus kinase library: part 1. *J. Med. Chem.* **2014,** *57* (6), 2789-2798.

5. Duffy, S.; Avery, V. M., Development and optimization of a novel 384-well anti-malarial imaging assay validated for high-throughput screening. *Am. J. Trop. Med. Hyg.* **2012,** *86* (1), 84.

6. Chapman, T. M.; Osborne, S. A.; Bouloc, N.; Large, J. M.; Wallace, C.; Birchall, K.; Ansell, K. H.; Jones, H. M.; Taylor, D.; Clough, B., Substituted imidazopyridazines are potent and selective inhibitors of Plasmodium falciparum calcium-dependent protein kinase 1 (PfCDPK1). *Bioorg. Med. Chem. Lett.* **2013,** *23* (10), 3064-3069.

7. Large, J. M.; Osborne, S. A.; Smiljanic-Hurley, E.; Ansell, K. H.; Jones, H. M.; Taylor, D. L.; Clough, B.; Green, J. L.; Holder, A. A., Imidazopyridazines as potent inhibitors

of Plasmodium falciparum calcium-dependent protein kinase 1 (PfCDPK1): Preparation and evaluation of pyrazole linked analogues. *Bioorg. Med. Chem. Lett.* **2013,** *23* (21), 6019-6024.

8. Chapman, T. M.; Osborne, S. A.; Wallace, C.; Birchall, K.; Bouloc, N.; Jones, H. M.; Ansell, K. H.; Taylor, D. L.; Clough, B.; Green, J. L., Optimization of an imidazopyridazine series of inhibitors of Plasmodium falciparum calcium-dependent protein kinase 1 (Pf CDPK1). *J. Med. Chem.* **2014,** *57* (8), 3570-3587.

9. Ansell, K. H.; Jones, H. M.; Whalley, D.; Hearn, A.; Taylor, D. L.; Patin, E. C.; Chapman, T. M.; Osborne, S. A.; Wallace, C.; Birchall, K., Biochemical and antiparasitic properties of inhibitors of the Plasmodium falciparum calcium-dependent protein kinase PfCDPK1. *Antimicrob. Agents Chemother.* **2014,** *58* (10), 6032-6043.

10. Green, J. L.; Moon, R. W.; Whalley, D.; Bowyer, P. W.; Wallace, C.; Rochani, A.; Nageshan, R. K.; Howell, S. A.; Grainger, M.; Jones, H. M., Imidazopyridazine inhibitors of Plasmodium falciparum calcium-dependent protein kinase 1 also target cyclic GMP-dependent protein kinase and heat shock protein 90 to kill the parasite at different stages of intracellular development. *Antimicrob. Agents Chemother.* **2016,** *60* (3), 1464-1475.

11. Mahmud, F.; Lee, P. C.; Wahab, H. A.; Mustaffa, K. M. F.; Leow, C. H.; Rasul, A.; Lai, N. S., ATP gatekeeper of Plasmodium protein kinase may provide the opportunity to develop selective antimalarial drugs with multiple targets. *Asian Pac. J. Trop. Med.* **2020,** *13* (8), 350.

12. Moolman, C.; Sluis, R. v. d.; Beteck, R. M.; Legoabe, L. J., An update on development of small-molecule Plasmodial kinase inhibitors. *Molecules* **2020,** *25* (21), 5182.

13. McNamara, C. W.; Lee, M. C.; Lim, C. S.; Lim, S. H.; Roland, J.; Nagle, A.; Simon, O.; Yeung, B. K.; Chatterjee, A. K.; McCormack, S. L., Targeting Plasmodium PI (4) K to eliminate malaria. *Nature* **2013,** *504* (7479), 248-253.

14. Cheuka, P. M.; Centani, L.; Arendse, L. B.; Fienberg, S.; Wambua, L.; Renga, S. S.; Dziwornu, G. A.; Kumar, M.; Lawrence, N.; Taylor, D., New Amidated 3, 6-Diphenylated Imidazopyridazines with Potent Antiplasmodium Activity Are Dual Inhibitors of Plasmodium Phosphatidylinositol-4-kinase and cGMP-Dependent Protein Kinase. *ACS Infect. Dis.* **2020**.

15. Silver, L. L., Appropriate targets for antibacterial drugs. *Cold Spring Harbor Perspect. Med.* **2016,** *6* (12), a030239.

16. Hooper, D. C.; Jacoby, G. A., Topoisomerase inhibitors: fluoroquinolone mechanisms of action and resistance. *Cold Spring Harbor Perspect. Med.* **2016,** *6* (9), a025320.

17. Strelow, J.; Dewe, W.; Iversen, P. W.; Brooks, H. B.; Radding, J. A.; McGee, J.; Weidner, J., Mechanism of action assays for enzymes. *Assay Guidance Manual [Internet]* **2012**.

18. Lipinski, C. A.; Lombardo, F.; Dominy, B. W.; Feeney, P. J., Experimental and computational approaches to estimate solubility and permeability in drug discovery and development settings. *Adv. Drug Delivery Rev.* **1997,** *23* (1-3), 3-25.

19. Yan, A.; Gasteiger, J., Prediction of aqueous solubility of organic compounds based on a 3D structure representation. *J. Chem. Inf. Comput. Sci.* **2003,** *43* (2), 429-434.

20. Lovering, F.; Bikker, J.; Humblet, C., Escape from flatland: increasing saturation as an approach to improving clinical success. *J. Med. Chem.* **2009,** *52* (21), 6752-6756.

21. Lovering, F., Escape from Flatland 2: complexity and promiscuity. *MedChemComm* **2013,** *4* (3), 515-519.

22. Leeson, P. D.; St-Gallay, S. A.; Wenlock, M. C., Impact of ion class and time on oral drug molecular properties. *MedChemComm* **2011,** *2* (2), 91-105.

23. Ritchie, T. J.; Macdonald, S. J.; Peace, S.; Pickett, S. D.; Luscombe, C. N., Increasing small molecule drug developability in sub-optimal chemical space. *MedChemComm* **2013,** *4* (4), 673-680.

24. Hill, A. P.; Young, R. J., Getting physical in drug discovery: a contemporary perspective on solubility and hydrophobicity. *Drug discovery today* **2010,** *15* (15-16), 648-655.

25. Young, R. J.; Green, D. V.; Luscombe, C. N.; Hill, A. P., Getting physical in drug discovery II: the impact of chromatographic hydrophobicity measurements and aromaticity. *Drug discovery today* **2011,** *16* (17-18), 822-830.

26. Nakashima, S.; Yamamoto, K.; Arai, Y.; Ikeda, Y., Impact of physicochemical profiling for rational approach on drug discovery. *Chem. Pharm. Bull.* **2013,** *61* (12), 1228-1238.

27. Delaney, J. S., ESOL: estimating aqueous solubility directly from molecular structure. *J. Chem. Inf. Comput. Sci.* **2004,** *44* (3), 1000-1005.

28. Lamanna, C.; Bellini, M.; Padova, A.; Westerberg, G.; Maccari, L., Straightforward recursive partitioning model for discarding insoluble compounds in the drug discovery process. *J. Med. Chem.* **2008,** *51* (10), 2891-2897.

29. Waskom, M.; Botvinnik, O.; Hobson, P.; Warmenhoven, J.; Cole, J. B.; Halchenko, Y.; Vanderplas, J.; Hoyer, S.; Villalba, S.; Quintero, E., Seaborn: V0. 6.0 (June 2015). *Zenodo* **2015**.

30. Hamada, Y., *Role of pyridines in medicinal chemistry and design of BACE1 inhibitors possessing a pyridine scaffold*. InTech Rijeka: 2018.

31. Gonzalez-Medina, M.; Medina-Franco, J. L., Platform for unified molecular analysis: PUMA. *J. Chem. Inf. Model.* **2017,** *57* (8), 1735-1740.

32. About the Pandemic Response Box. https://www.mmv.org/mmv-open/pandemic-response-box/about-pandemic-response-box.

33. Reader, J.; van der Watt, M. E.; Taylor, D.; Le Manach, C.; Mittal, N.; Ottilie, S.; Theron, A.; Moyo, P.; Erlank, E.; Nardini, L., Multistage and transmission-blocking targeted

antimalarials discovered from the open-source MMV Pandemic Response Box. *Nat. Commun.* **2021,** *12* (1), 1-15.

34. Le Corre, L.; Girard, A.-L.; Aubertin, J.; Radvanyi, F.; Benoist-Lasselin, C.; Jonquoy, A.; Mugniery, E.; Legeai-Mallet, L.; Le Merrer, Y., Synthesis and biological evaluation of a triazole-based library of pyrido [2, 3-d] pyrimidines as FGFR3 tyrosine kinase inhibitors. *Org. Biomol. Chem.* **2010,** *8* (9), 2164-2173.

CHAPTER FOUR: Pandemic response box (PRB) screening for hit identification of *Plasmodium* PI4K and PKG inhibitors

4.1. Introduction

In target-based drug discovery, the hit identification process is triggered after validation of the target setting the stage for hit identification research. The main objective of this part of the project was to identify hits from the Medicines for Malaria Venture (MMV) Pandemic Response Box (PRB) that target *Plasmodium* PI4K and PKG.

The PRB, which was inspired by the need to catalyze drug discovery in response to emerging pandemics, was assembled by MMV and Drugs for Neglected Diseases Initiative (DND*i*), in collaboration with scientists from both industry and academic settings.[1] Reader et al. tested the activity of these PRB compounds against the asexual blood-stage and sexual stages of *P. falciparum*, leading to the identification of compounds with stage-specific and multi-stage antiplasmodium activity.[2] The human mixed-lineage kinase 3 (MLK3) inhibitor, MMV1580482 and MMV1593539, a *Staphylococcus aureus* pyruvate kinase 1 (PK1), exhibited activity in the asexual stage with *Pf*NF54 IC_{50} of 1.39µM and 0.69µM, respectively. This demonstrates the opportunity for the repositioning of PRB compounds as antimalarials.

4.2. Aim and specific objectives

4.2.1. Aim

The aim of this study was to identify hit compounds with *Plasmodium* PI4K and PKG activity from the PRB through virtual screening. The hits were then experimentally validated through biochemical screening against these targets. To avoid false positives, the antiplasmodium activity data generated by Reader et al.[2] were used to establish target criteria. This ensured that the compounds that underwent virtual screening and eventually enzymatic testing demonstrated antiplasmodium activity and were not just general kinase inhibitors.

4.2.2. Specific Objectives

1. Use antiplasmodium activity data generated against both the asexual and sexual stages to establish target criteria
2. Virtually screen PRB compounds that fit the target criteria using molecular docking and binding mode analysis methods
3. Perform enzymatic screening of the selected compounds against *Plasmodium* PI4K and PKG.

4.3. Compound prioritization

4.3.1 Introduction

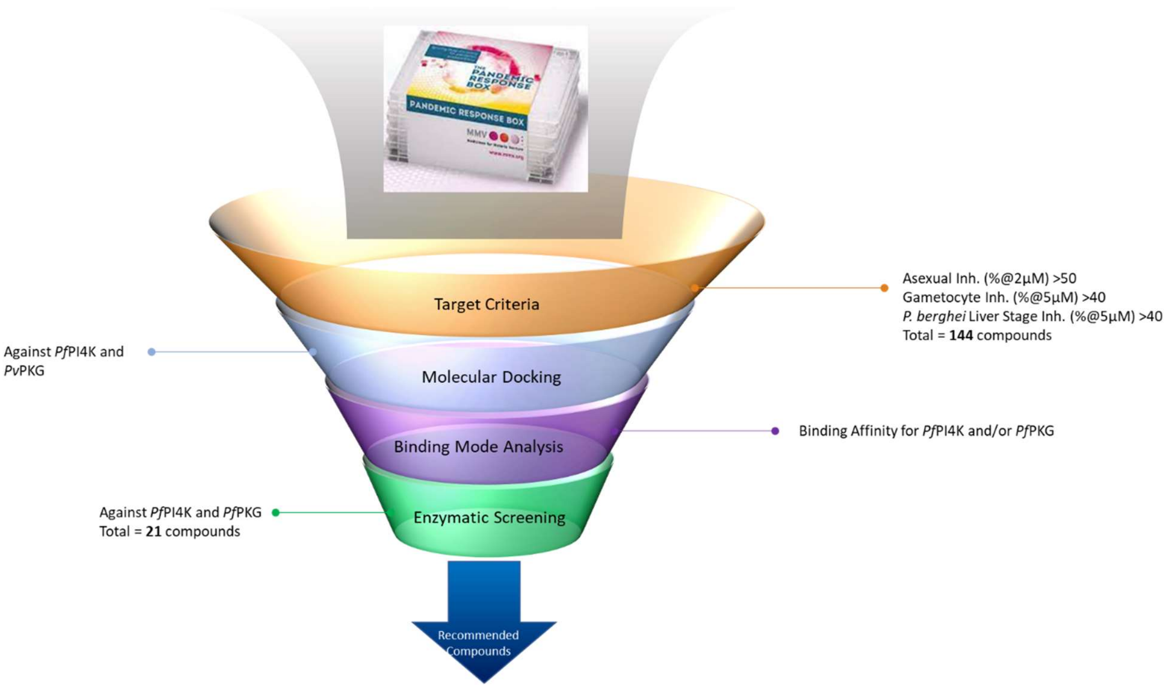

Figure 4.1: Screening cascade followed for pandemic response box compounds

The strategies used to select compounds for enzymatic screening are shown in **Figure 4.1**. Of the 400 PRB compounds, a total of 144 satisfied the established target criteria. These compounds were then progressed to the next step and docked against the *Pf*PI4K homology model and *Pv*PKG crystal structure (PDB ID: 5F0A) using the docking protocol described in **Section 6.1.2**. Binding energies were calculated and the binding modes of the compounds to the two targets were analyzed. This greatly reduced the number of compounds to 21, which were screened against *Pv*PI4K and *Pf*PKG in an ADP-Glo assay described in **Section 6.2.4**. The following sections explain each strategy in detail.

4.3.1. Target criteria

As already mentioned above, in order to reduce the number of false positives, target criteria were established using experimental data generated by Reader et al.[2] This allowed the focus to be on compounds that demonstrated antiplasmodium activity experimentally in either stage of the *Plasmodium* life-cycle. The target criteria used were:

- >50% asexual blood stage inhibition at 2 µM
- >40% gametocyte stage inhibition at 5 µM
- > 40% *P. berghei* liver-stage inhibition at 5 µM

The compounds were then screened using these criteria. A total of 144 compounds fulfilled the established criteria and were progressed to the next step in the workflow.

4.3.2. Compound prioritization via molecular docking

As this is a virtual screening campaign, molecular docking was used to screen out hits from the 144-compound dataset. Since the PRB comprises diverse chemotypes, little focus was placed on the docking score and calculated binding energy as the main objective was to filter out compounds that are not predicted to bind to the targets, *Plasmodium* PI4K and PKG.

The hinge-binding moiety that forms hydrogen bonds with the hinge of the kinase was of main interest when filtering out compounds for screening. This is because the focus on this chapter is on hit identification and not lead optimization as seen in Chapter 2 and SAR building of an already established hit in Chapter 3.

The binding site with the adenine region of ATP forming the hinge interactions is shown in **Figure 4.2**.

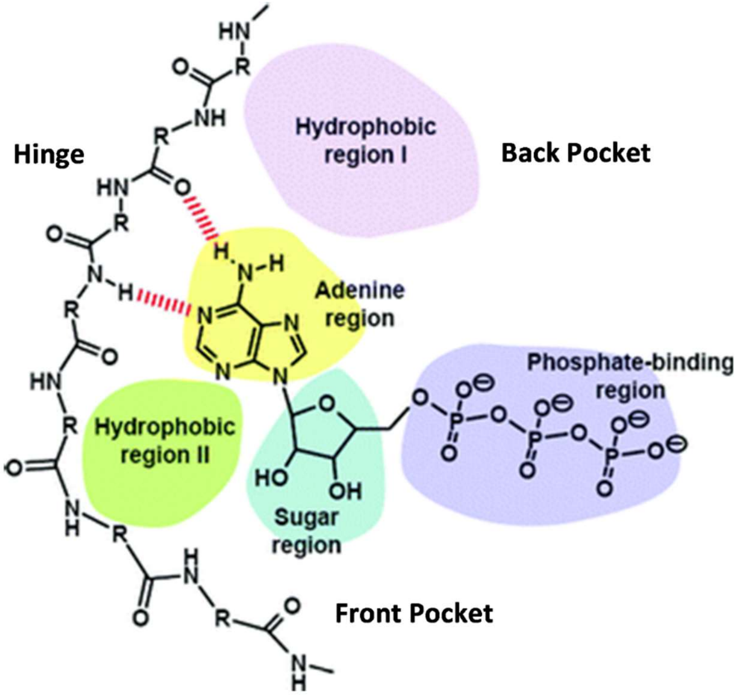

Figure 4.2: The kinase active site with bound ATP. The adenine region forms the hinge interaction with the kinase.[3]

Compounds that formed a hinge interaction with either target were progressed forward. The 21 compounds selected for enzymatic screening are listed in **Table 4.1**. The whole cell data shown are from the published work of Reader at al.[2]

Table 4.1: Compounds prioritized for enzymatic screening

Compound	Compound Structure	*Pf*PI4K Molecular Docking Pose	*Pv*PKG Molecular Docking Pose	% *Pf*NF54 asexual inhibition (2 µM)[a]
MMV000043	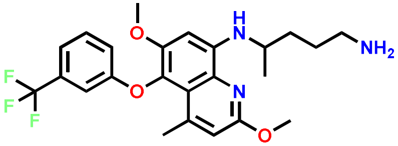	Favorable	Favorable	56.5
MMV1634491	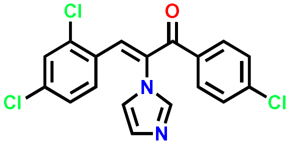	Favorable	Favorable	56.2
MMV1580844	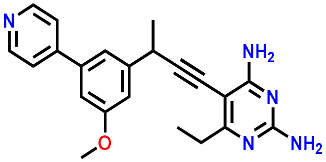	Favorable	Favorable	51.1
MMV1580488	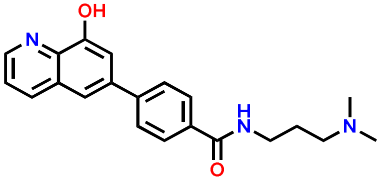	Favorable	Favorable	68.6

MMV1578570	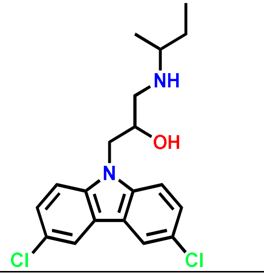	Favorable	Favorable	68.7
MMV1578564	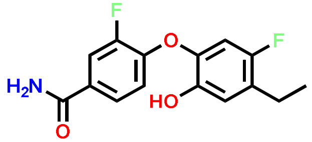	Favorable	Favorable	54.5
MMV1580482	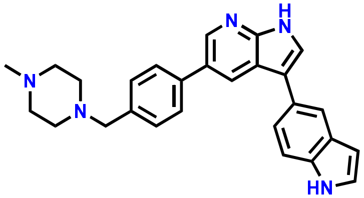	Favorable	Unfavorable	66
MMV1593521	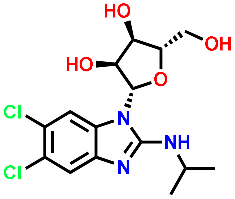	Favorable	Unfavorable	66.8
MMV1581549	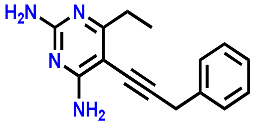	Favorable	Unfavorable	66

MMV1593540	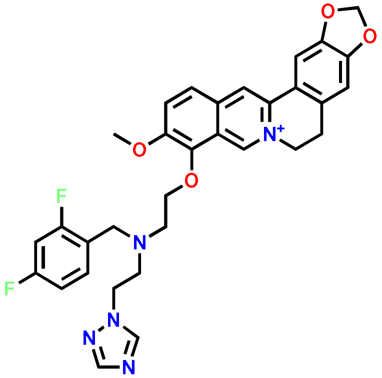	Favorable	Unfavorable	78.3
MMV099714	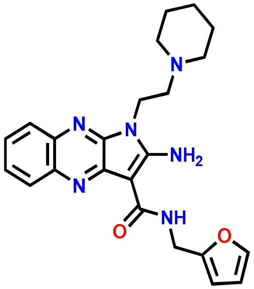	Favorable	Unfavorable	77.4
MMV009948	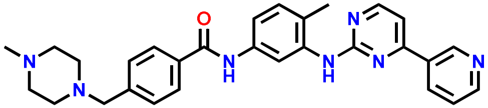	Unfavorable	Favorable	60.6
MMV000725	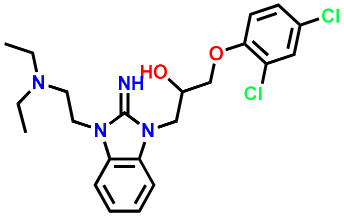	Unfavorable	Favorable	95.4

MMV1557856	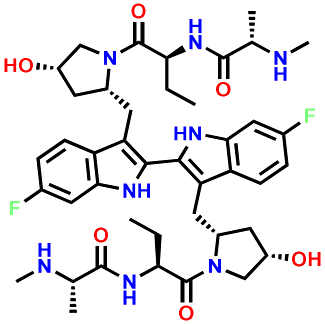	Unfavorable	Favorable	75.7
MMV1580492	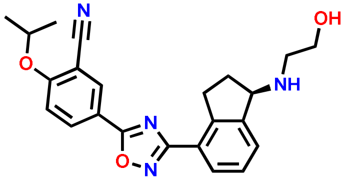	Unfavorable	Favorable	78.4
MMV1634071	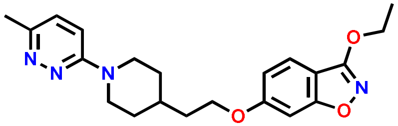	Unfavorable	Favorable	84.1
MMV019724	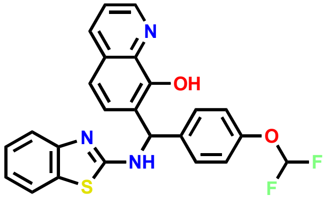	Unfavorable	Favorable	70.5
MMV637659	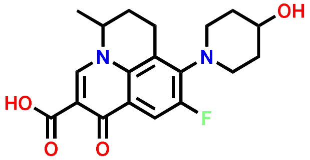	Unfavorable	Favorable	69.7

MMV001438	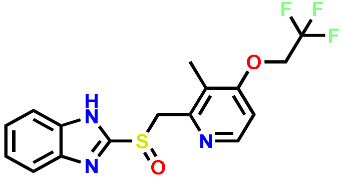	Unfavorable	Favorable	71.5
MMV010036	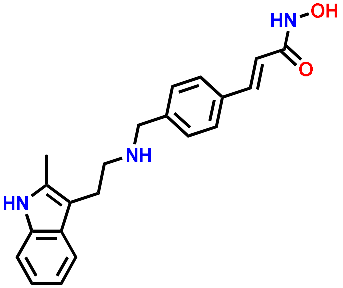	Unfavorable	Favorable	62.2
MMV303733	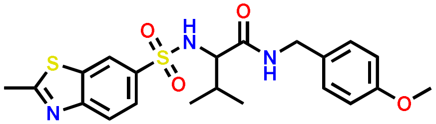	Unfavorable	Favorable	81.6

[a] Data generated by Reader et al.[2]

Most of the compounds were polycyclic in that they contained more than one cyclic component. However, they were structurally diverse, for example, **MMV000043**, **MMV1580488** and **MMV637659** have a quinoline core. There were also compounds with the benzo[d]imidazole core: **MMV1593521**, **MMV000725** and **MMV001438** while **MMV1580844**, **MMV1581549** and **MMV009948** have a pyrimidine core.

4.4. *Pf*PKG inhibition

4.4.1. Introduction

These 21 compounds were tested in biochemical assays against the recombinantly expressed enzyme to assess their *Plasmodium* PKG activity. Single-point assays were first carried out to determine their percentage inhibition. This was followed by generation of dose-response curves to calculate the IC_{50} values of compounds with >70% *Pf*PKG activity. Here, a hit compound was defined as showing >70% *Pf*PKG inhibition at 10 µM.

4.4.2. *In vitro Pf*PKG assay

Compounds were screened against recombinantly expressed *Pf*PKG in an ADP-GLO single-point assay at a concentration of 10 µM. The *Pf*PKG percentage inhibition of each compound is shown in **Table 4.2.**

Table 4.2: *Pf*PKG enzymatic data for PRB compounds

Compound	Compound Structure	% *Pf*PKG inhibition (10 µM)[a]
MMV1580482	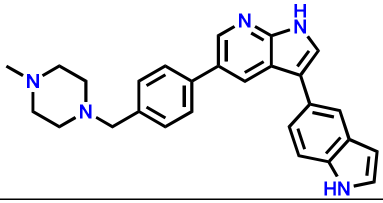	94
MMV1580844	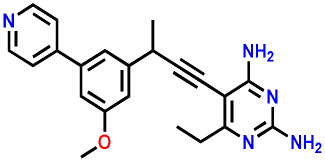	89
MMV009948	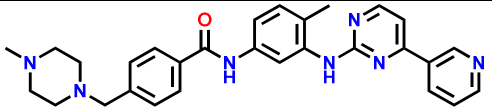	87
MMV000043	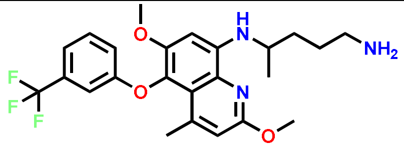	76
MMV1593521	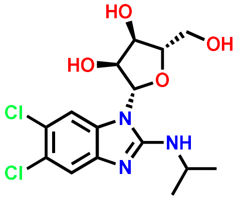	59
MMV1578570	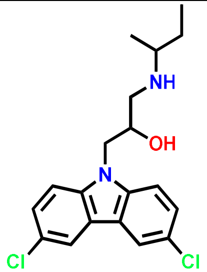	39
MMV1578564	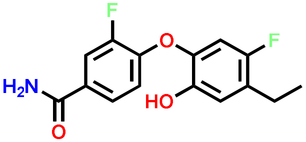	39
MMV1581549	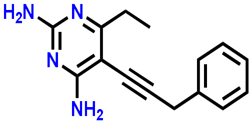	39
MMV1634491	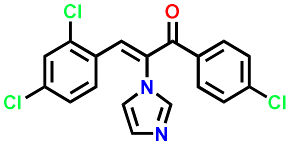	38

MMV1580488	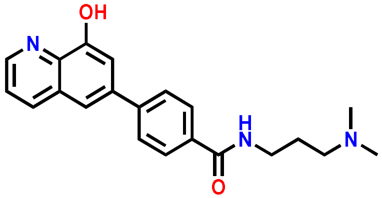	32
MMV1580492	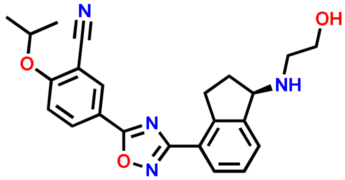	26
MMV010036	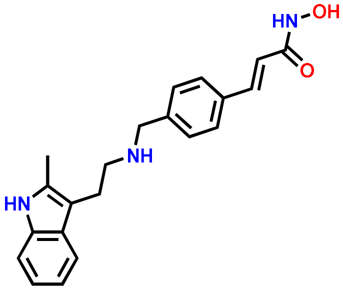	26
MMV1593540	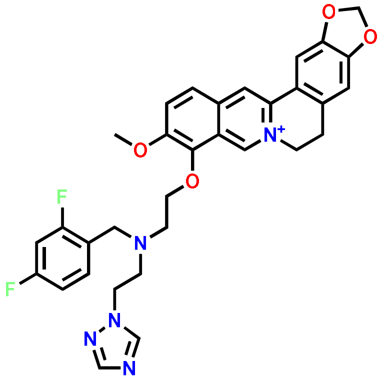	24
MMV303733	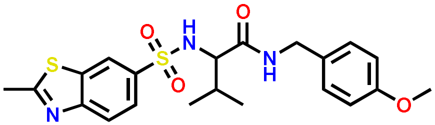	24
MMV637659	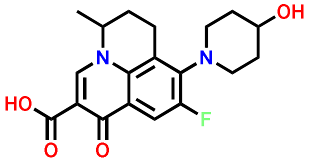	23
MMV1634071	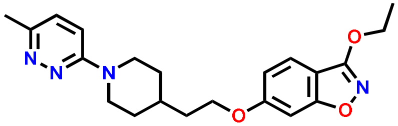	22
MMV019724	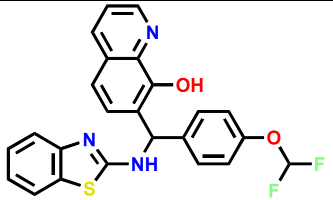	22

MMV001438	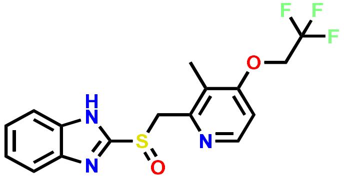	22
MMV099714	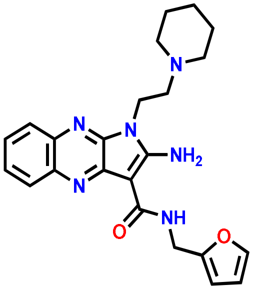	21
MMV1557856	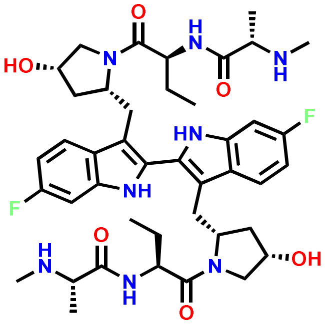	21
MMV000725	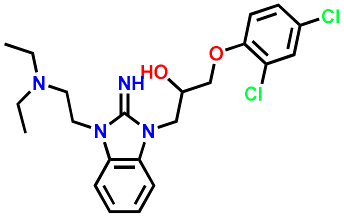	18

[a]*in vitro Pf*PKG percent inhibition at 10 µM ATP, carried out in duplicate in n = 2 independent experiments.

Eleven of the 21 compounds showed *Pf*PKG inhibition < 30%, and only five compounds inhibited *Pf*PKG by 30–50%. As a hit compound was defined as compounds showing >70% *Pf*PKG inhibition at 10 µM, therefore, four of the 21 compounds screened against *Pf*PKG were classed as hits (approximately 20% success hit rate). These were: **MMV1580482**, **MMV1580844**, **MMV009948** and **MMV000043**.

A dose-response curve was generated for these hits to calculate the *Pf*PKG IC_{50} values shown in **Table 4.3**. **MMV009948**, **MMV1580844**, and **MMV1580482** all showed comparable weak *Pf*PKG activity. **MMV000043** was slightly less potent than the rest of the compounds.

Table 4.3: *Pf*PKG IC_{50} values of PRB hit compounds

Compound	Structure	*Pf*PKG IC_{50} (µM)[a]
MMV000043	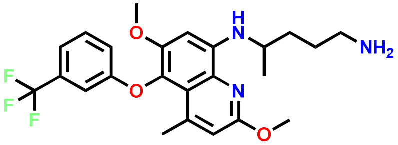	4.67
MMV1580844	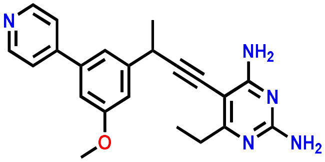	1.92
MMV1580482	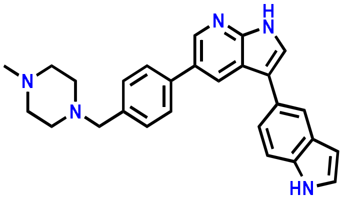	1.02
MMV009948	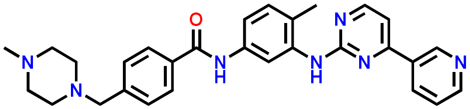	1.52

[a]*in vitro Pf*PKG inhibition at 10 µM ATP, carried out in duplicate in n = 2 independent experiments.

4.4.3. Rationalization of *Pf*PKG inhibition

Once hit compounds were identified, further molecular docking experiments were carried out against *Plasmodium* PKG. This was done to gain further insights into the structural features influencing *Plasmodium* PKG activity with regard to the hit compound. In some instances, the appropriate orientation of the hit compound in the binding site, especially the core, is investigated alongside similar chemotypes that have been co-crystallized with a kinase. Here, the conservative feature of kinase domains is highly exploited.

MMV000043 (tafenoquine): validation of binding pose and PfPKG insights

MMV000043 (tafenoquine) has not been co-crystallized with a kinase or any other target. This particular hit compound belongs to the 8-aminoquinoline group and, to date, no 8-aminoquinolines have been co-crystallized with a kinase.

The predicted binding pose of **MMV000043** had the methoxy on the aminoquinoline core forming the hinge interaction (**Figure 4.3**).

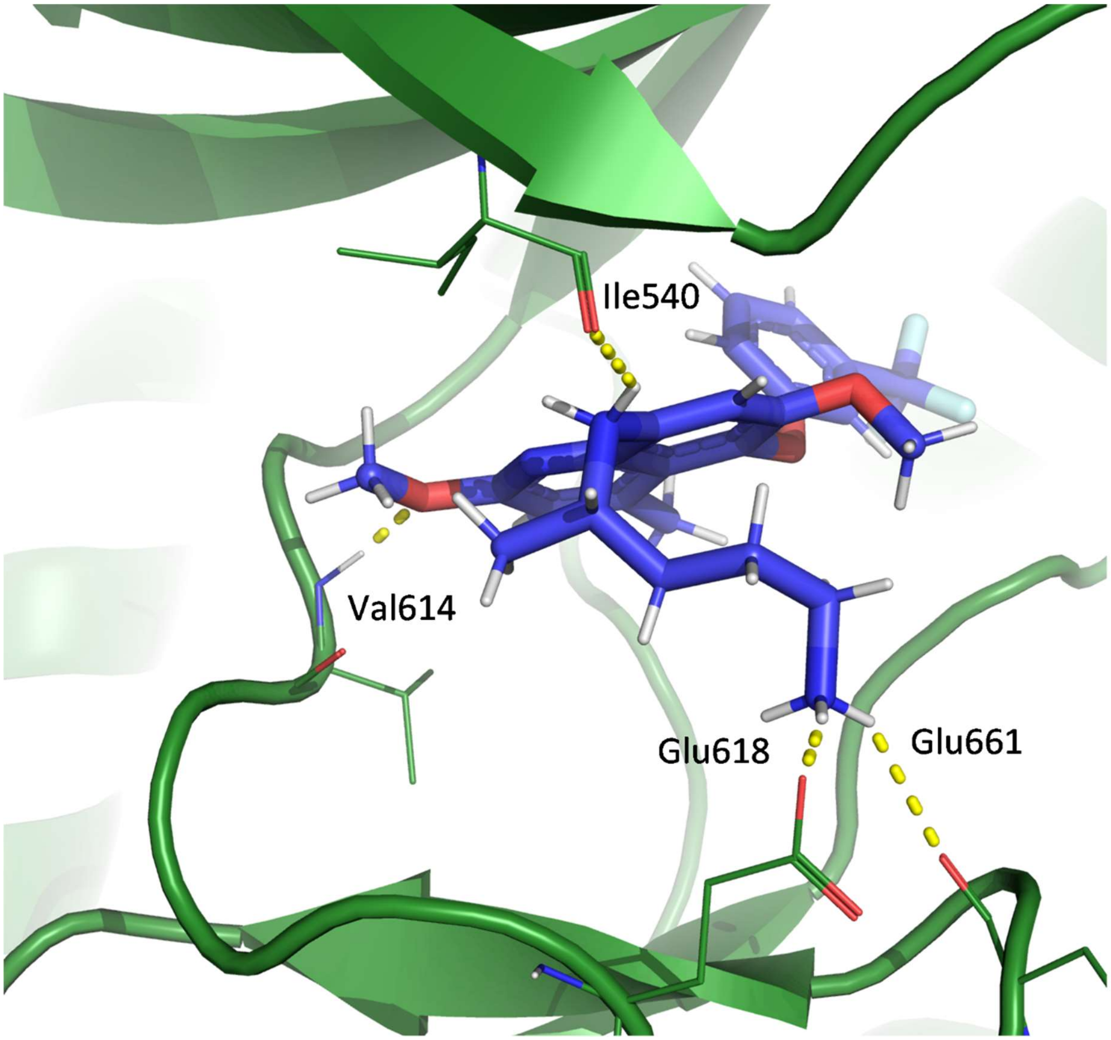

Figure 4.3: MMV000043 (blue) docked into *Pv*PKG (green) with interacting residues shown as lines

Additionally, the amino side-chain formed an interaction with the **Glu618**, **Glu661** and **Ile540** residues. Further studies, both computational and experimental, need to be undertaken on **MMV000043** to validate the influence these formed interactions have on *Pf*PKG inhibition.

MMV1580844: validation of binding pose and PfPKG insights

Molecular docking experiments of **MMV1580844** in *Pv*PKG revealed the pyrimidine-2,4-diamine core to be the hinge binding motif (**Figure 4.4**). A previously crystallized pyrimidine-2,4-diamine analogue also shows this mentioned core interacting with the hinge.[4]

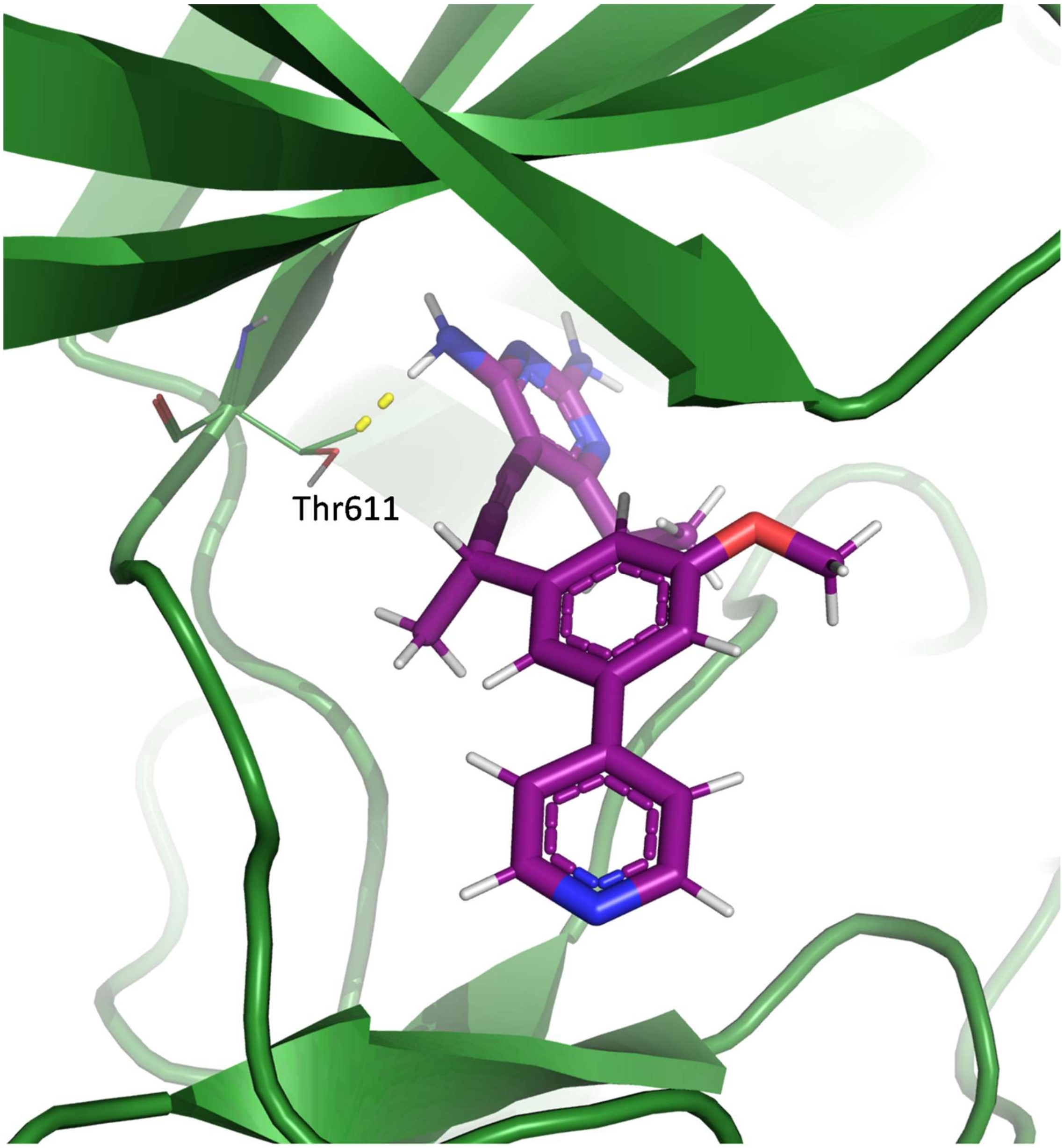

Figure 4.4: MMV1580844 (purple) docked into *Pv*PKG (green) with interacting residues shown as lines

However, not many interactions are formed, and this may explain the moderate *Pf*PKG activity demonstrated by **MMV1580844** (*Pf*PKG IC_{50} = 1.92 μM). This potency may be greatly improved by removing the rigid triple bond linker and optimizing side-chains to form favorable interactions with other amino acid residues.

MMV1580482: validation of binding pose and PfPKG insights

An approved drug was used to orientate the hit compound into the binding site. The reference compound used in this case is the competitive BRAF kinase inhibitor vemurafenib.[5] This marketed drug has a 1H-pyrrolo[2,3-b]pyridine core similar to that of the hit compound **MMV1580482** (**Figure 4.5**).

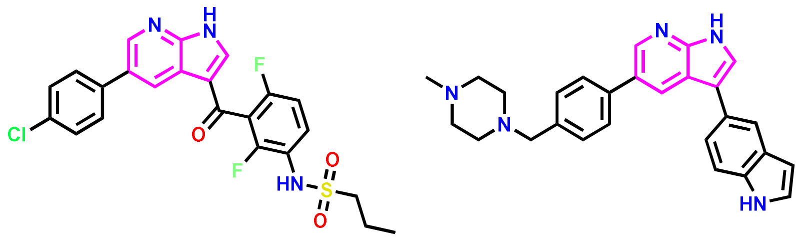

Figure 4.5: Structure of vemurafenib and **MMV1580482**. The 1H-pyrrolo[2,3-b]pyridine core common to both in shown in pink.

As shown in **Figure 4.6**, vemurafenib uses the 1H-pyrrolo[2,3-b]pyridine core as the hinge binding motif. This is also observed in other core analogues co-crystallized with PDB structures 3ETA,[6] 1ZYS,[7] 4W05,[8] 4FK3,[9] and 7ATS.[10]

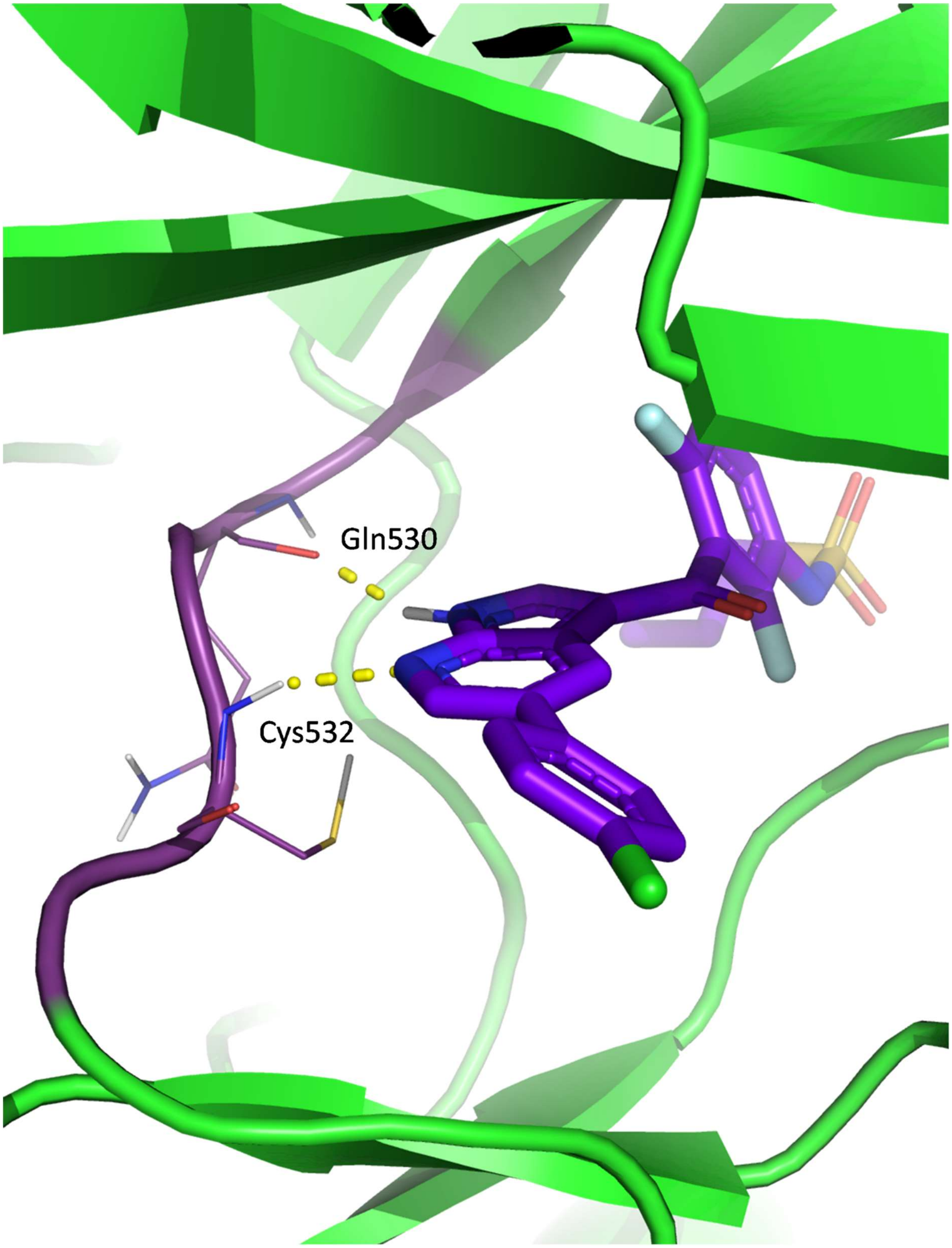

Figure 4.6: Co-crystallized ligand with a 1H-pyrrolo[2,3-b]pyridine core docked into a human kinase (PDB ID: 3OG7). The hinge is colored purple.

This supports the docked pose of **MMV1580482** in *Pv*PKG, as shown in **Figure 4.7**.

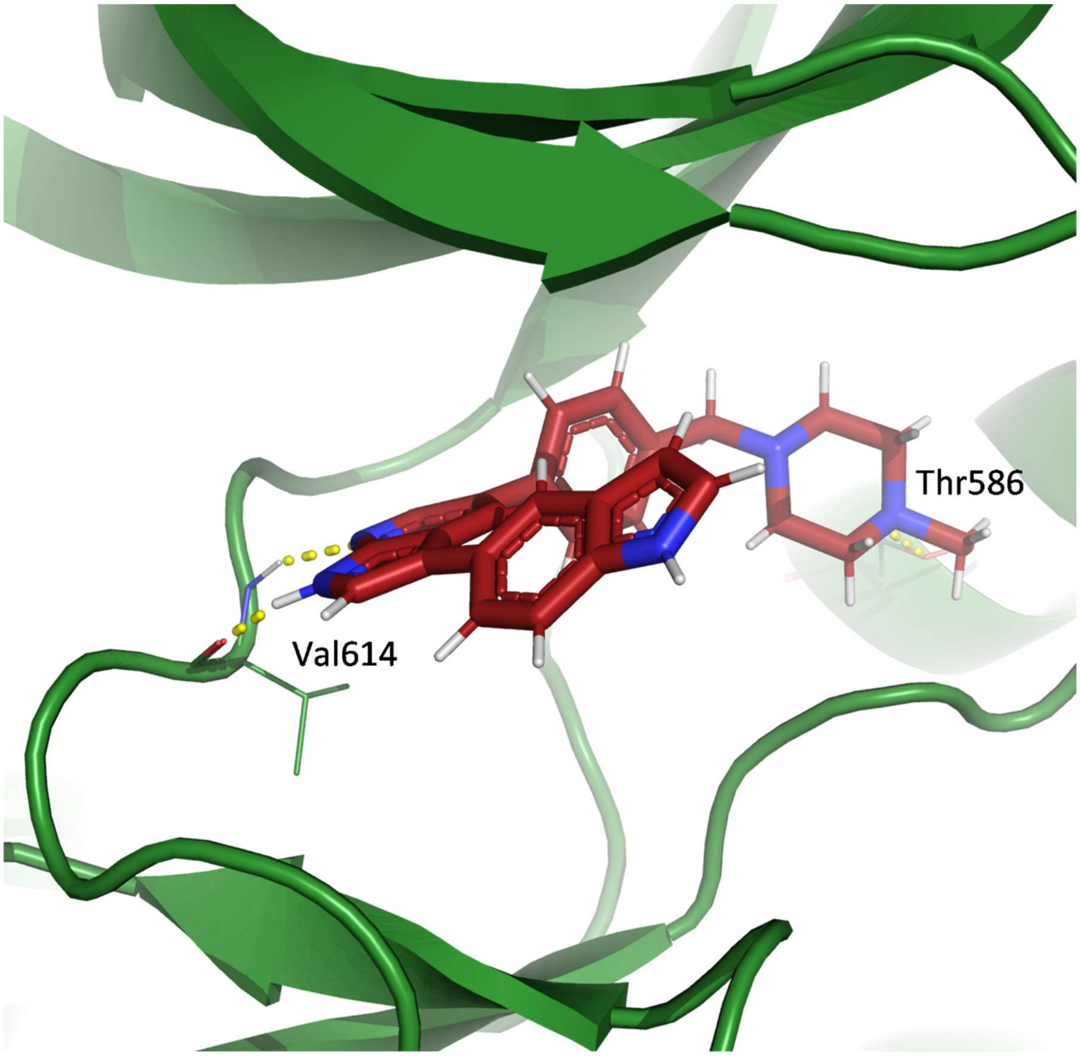

Figure 4.7: MMV1580482 (red) docked into *Pv*PKG (green) with interacting residues shown as lines

Hinge and back pocket interactions are formed when **MMV1580482** (*Pf*PKG IC_{50} = 1.02 µM) is docked into *Pv*PKG. The influence of these interactions on the exhibited Plasmodium PKG IC_{50} should be investigated further.

MMV009948 (imatinib): validation of binding pose and PfPKG insights

Fortunately, **MMV0009948** (imatinib) was previously crystallized with a kinase (**Figure 4.8**). Imatinib is an approved drug that is used in the treatment of chronic myelogenous leukemia (CML) among other malignancies.

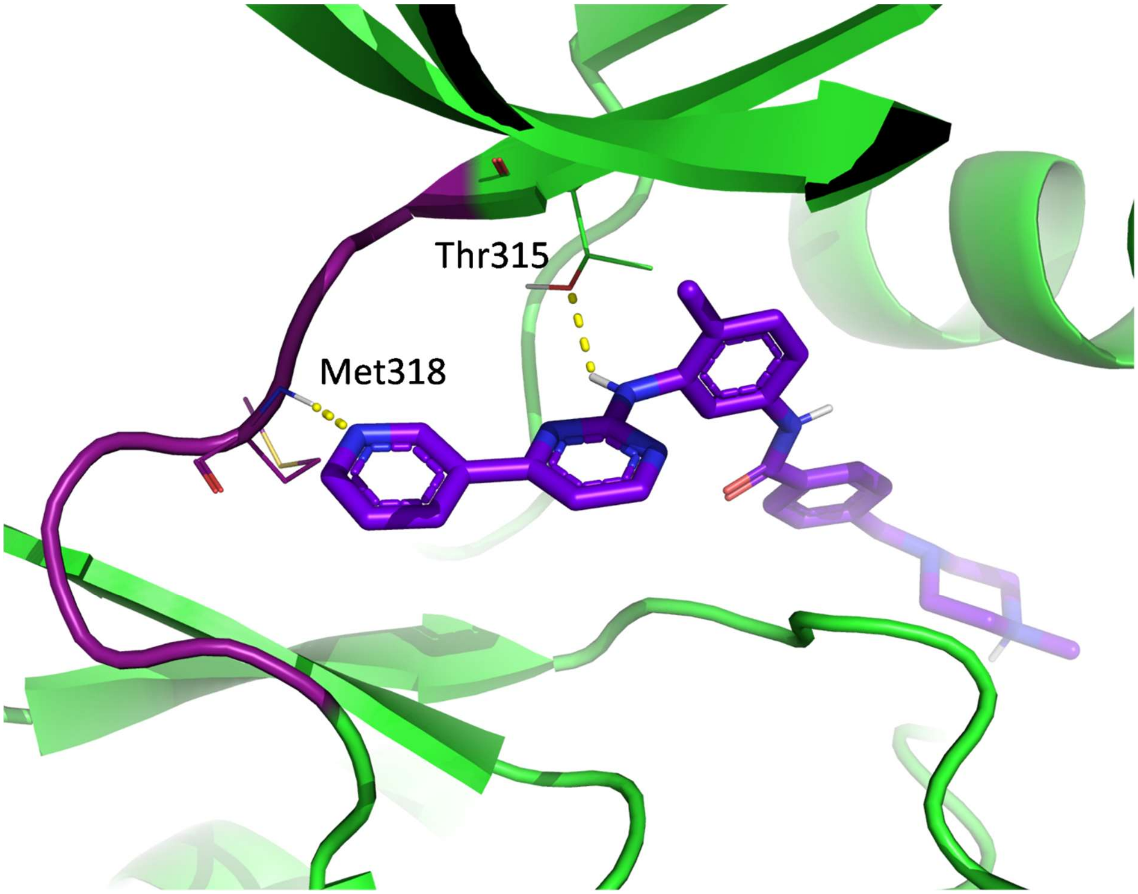

Figure 4.8: MMV009948 (imatinib) co-crystallized with the human Abl kinase (PDB ID: 2HYY). The hinge is colored purple.

With the *Pv*PKG crystal structure in the DFG-in conformation, which greatly reduces the space in the back pocket and forces the predicted “bent” conformation (**Figure 4.9**).

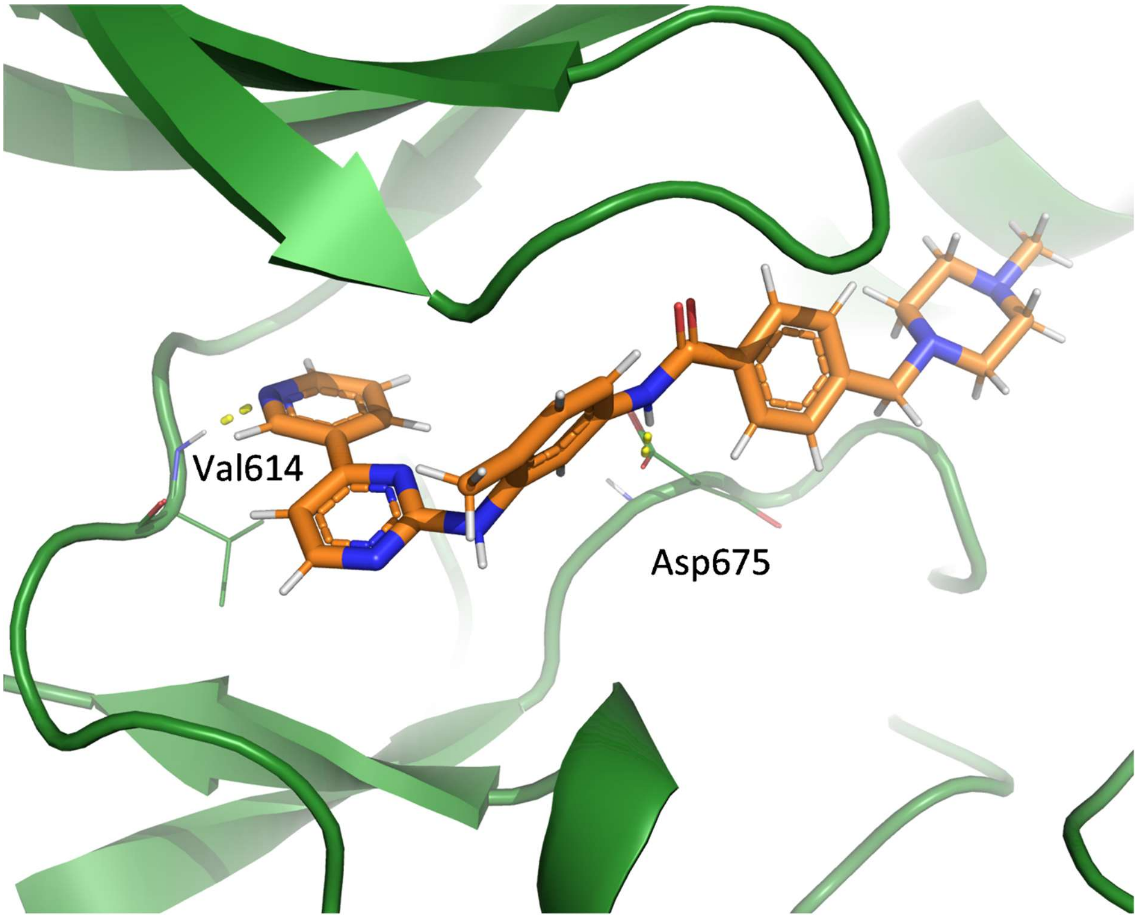

Figure 4.9: MMV009948 (orange) docked into *Pv*PKG (green) with interacting residues shown as lines

Docking studies show **MMV009948** (*Pf*PKG IC$_{50}$ = 1.52 µM) formed interactions with Asp675 and the hinge residue, Val614. However, further studies should be conducted to understand the influence of these interactions regarding this hit.

4.5. *Pv*PI4K inhibition

4.5.1. Introduction

As was done to verify *Plasmodium* PKG inhibition in the previous sections, the 21 compounds selected were also screened against the recombinantly expressed *P. vivax* PI4K. The same workflow was applied: single-point assays were first carried out for all compounds, and this was followed by dose-response curves for compounds showing >70% *Pv*PI4K inhibition.

4.5.2. *In vitro Pv*PI4K assay

The 21 compounds were screened against recombinantly expressed *Pv*PI4K in a fluorescence-based assay following the ADP-GLO protocol (**section 6.2.4**). The enzymatic results are shown in **Table 4.4**.

Table 4.4: *Pv*PI4K enzymatic results for PRB compounds

Compound	Compound Structure	% *Pv*PI4K inhibition (10 µM)^a
MMV1580482	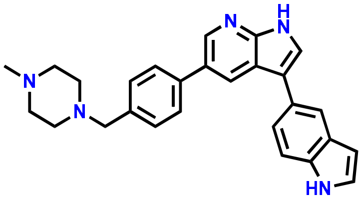	83
MMV1580844	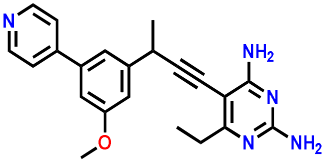	76
MMV1581549	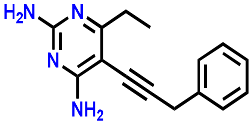	54

MMV1580488	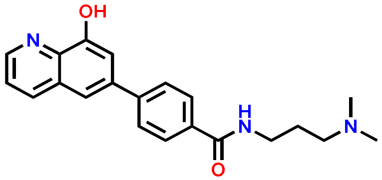	47
MMV009948	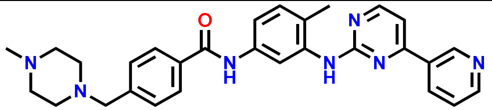	34
MMV1593540	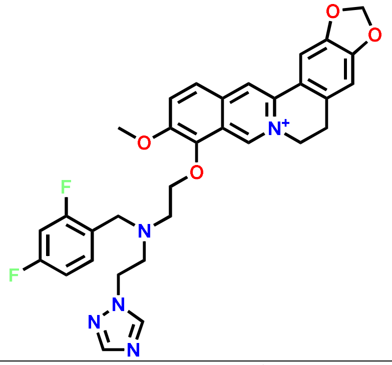	19
MMV099714	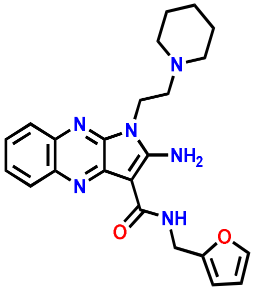	19
MMV1593521	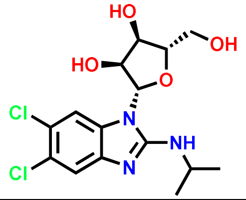	18
MMV000725	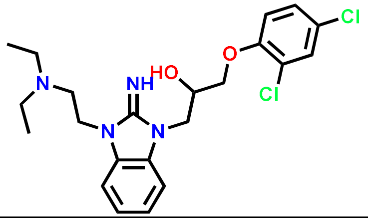	15
MMV1580492	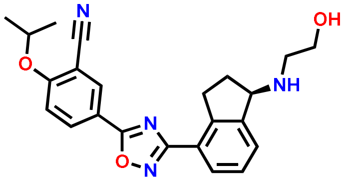	14
MMV637659	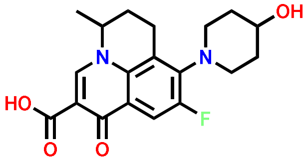	12

MMV1557856	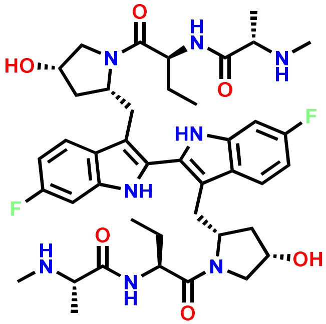	11
MMV019724	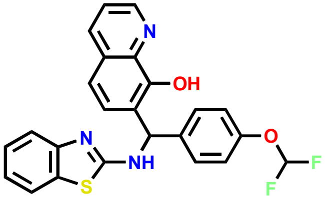	10
MMV303733	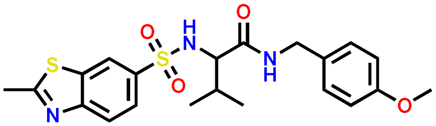	10
MMV1578570	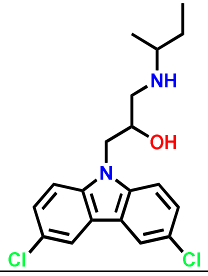	9
MMV1634491	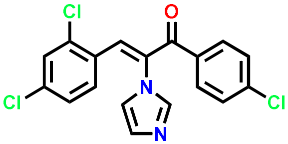	8
MMV1578564	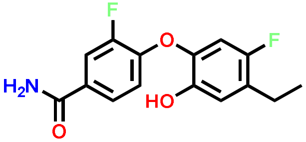	8
MMV1634071	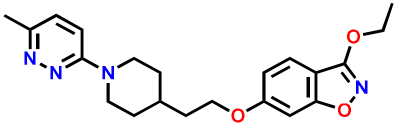	8
MMV010036	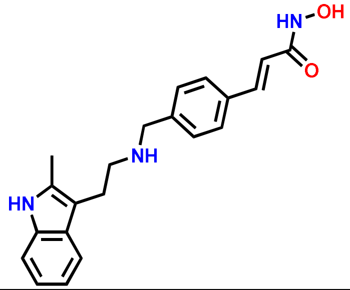	8

MMV000043	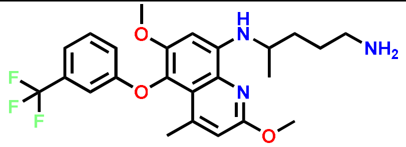	6
MMV001438	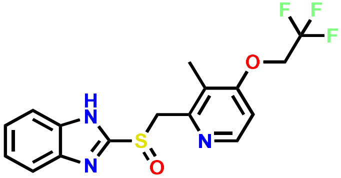	6

[a]*In vitro* *Pv*PI4K inhibition at 10 µM ATP, carried out in duplicate in n = 2 independent experiments.

16 of the 21 compounds showed <20% *Pv*PI4K inhibition. **MMV1581549**, **MMV1580488** and the previously identified *Pf*PKG inhibitor **MMV009948** showed *Pv*PI4K inhibition of 54%, 47% and 34%, respectively. The two remaining compounds (**MMV1580844** and **MMV1580482**) were identified as hit compounds as they demonstrated >70% inhibition of *Pv*PI4K (76% and 83%, respectively) based on the hit criteria established previously for *Pf*PKG inhibition. On this basis both **MMV1580844** and **MMV1580482** were progressed to full dose-response screening in order to generate the *Pv*PI4K IC_{50} values shown in **Table 4.5**.

Table 4.5: PRB hit compounds against *Pv*PI4K

Compound	**Structure**	***Pv*PI4K IC_{50} (µM)[a]**
MMV1580844	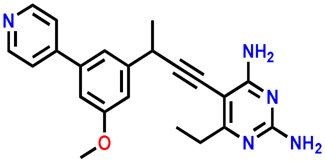	3.71
MMV1580482	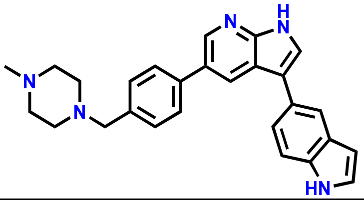	1.66

[a]*In vitro* *Pv*PI4K inhibition at 10 µM ATP, carried out in duplicate in n = 2 independent experiments.

Notably, compounds **MMV1580844** and **MMV1580482**, which exhibited *Pf*PKG activity, also showed *Pv*PI4K potency albeit very weak.

4.5.3. Rationalization of *Pf*PI4K inhibition

To understand the rationale behind the PvPI4K potency exhibited, docking studies were done. These studies were carried out to provide insights into factors driving *Pv*PI4K potency.

MMV1580844: validation of binding pose and PvPI4K insights

Figure 4.10 shows the docking pose of **MMV1580844** in the *Pf*PI4K homology model. As seen in the *Pv*PKG binding site, the pyrimidine-2,4-diamine core is once again the moiety that binds to the hinge section.

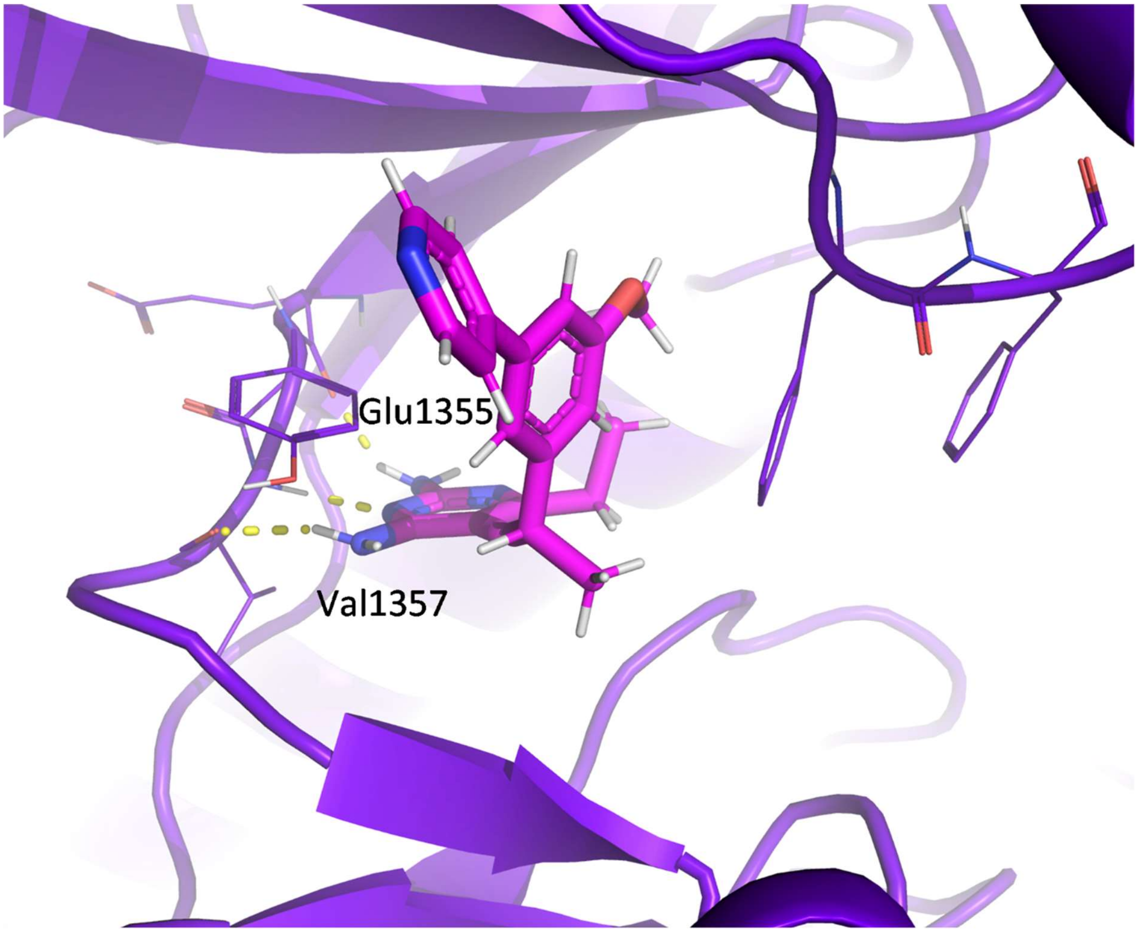

Figure 4.10: MMV1580844 (pink) docked into *Pf*PI4K (purple) with interacting residues shown as lines

MMV1580482: validation of binding pose and PvPI4K insights

The previous section demonstrated that the 1H-pyrrolo[2,3-b]pyridine core was used as the hinge-binding motif.

MMV1580482 interacts with amino acids other than those in the hinge, as shown in **Figure 4.11**. These include the aspartic acid, **Asp1430,** of the DFG-in chain and the serine **Ser921** found in the front pocket of the kinase. These additional interactions may explain the slight difference in *Pf*PI4K potency compared to that of **MMV1580844** and suggests that the number of interactions may influence potency.

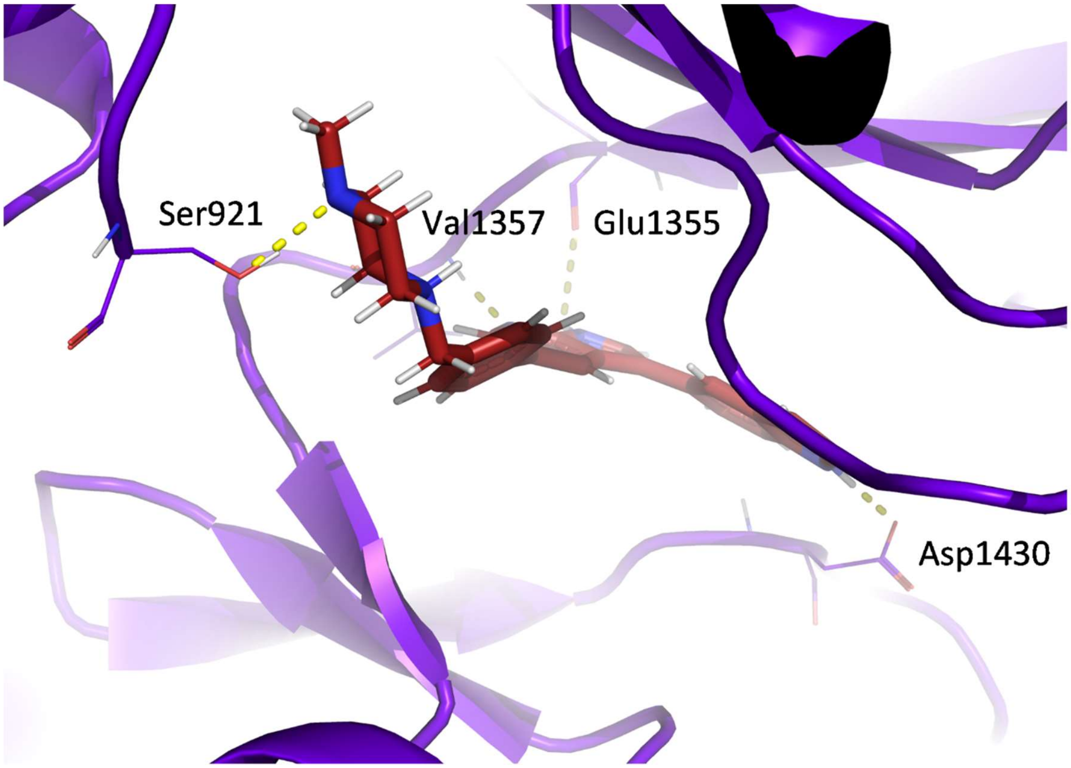

Figure 4.11: MMV1580482 (red) docked into *Pf*PI4K (purple) with interacting residues shown as lines and hydrogen bonds shown in yellow

4.6. Literature review of hit compounds

4.6.1. MMV00043 (tafenoquine)

Tafenoquine, an antimalarial marketed under the brand names Arakoda® and Krintafel® had a *Pf*PKG IC_{50} of 4.67 µM (**Figure 4.12**).[11, 12] The US Food and Drug Administration (FDA) approved tafenoquine for two indications:

1. As a radical treatment to eliminate dormant *P. vivax* and *P. ovale* liver-stage parasites
2. For prophylaxis of malaria.

Arakoda® (100 mg tafenoquine per tablet) is administered for prophylaxis and Krintafel® (150 mg tafenoquine per tablet) is administered for the treatment of malaria. The drug belongs to the 8-aminoquinoline class[13] and is hypothesized to prevent recrudescence of bone marrow, splenic, and any other non-circulating merozoite parasites.[14, 15] However, the molecular target of tafenoquine remains to be elucidated.

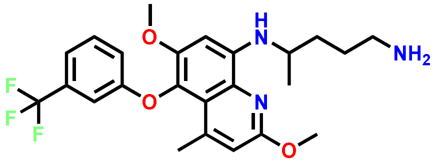

Figure 4.12: Structure of tafenoquine

4.6.2. MMV1580844

Identified as a dual *Pf*PKG and *Pv*PI4K inhibitor, the pyrimidine-2,4-diamine **MMV1580844** is one of the antibacterials included in the PRB (**Figure 4.13**).[16] Interestingly, it was the most potent compound identified by Reader et al. (*Pf*NF54 IC_{50} = 0.0017 µM).[2] Additionally, it exhibited potent liver-stage activity against *P. berghei* parasites (IC_{50} = 0.004 µM).

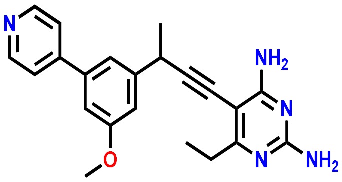

Figure 4.13: Structure of MMV1580844 (*Pf*PKG and *Pv*PI4K IC_{50} = 1.92 µM and 3.71 µM, respectively)

MMV1580844 is known to target dihydrofolate reductase (DHFR) in both yeast and mammalian cells.[17, 18] The DHFR target is essential for the reduction of folate cofactors involved in the biosynthesis of deoxythymidine monophosphate (dTMP).[19] The essentiality of this target makes it a valid target not only for bacterial infections but also for cancer.[20] DHFR is also highly conserved across species. As suggested by Delves et al. and demonstrated by **MMV1580844**, inhibition of *Plasmodium* DHFR translates to asexual and liver-stage potency.[21] Notably, the antimalarial drug, Pyrimethamine has a pyrimidine-2,4-diamine core and has also been shown to inhibit *Plasmodium* DHFR.[22] With regard to kinases, the SAR of the pyrimidine-2,4-diamine core has been studied widely on both *Plasmodium* and human kinases, including the human phosphatidylinositol-5-phosphate-4 kinase, type II beta (PIP5K2β).[23] However, the 2,4-diamines on the pyrimidine ring are usually substituted with bulky moieties. Therefore, the SAR of **MMV1580844**, with free amines, remains unexplored for *Plasmodium* kinase inhibition.

4.6.3. MMV1580482 (URMC-099-C)

The antiviral **MMV1580482** showed activity against the asexual stage (*Pf*NF54 IC_{50} = 1.3 µM; **Figure 4.14**).[2] Its activity against *Pf*PKG and *Pv*PI4K was similar, with IC_{50} = 1.02 µM and 1.66 µM, respectively.

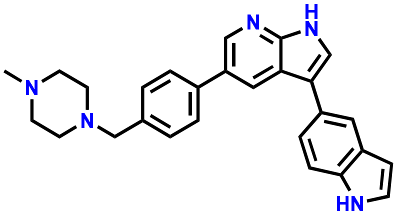

Figure 4.14: Structure of **MMV1580482**

MMV1580482 is a mixed lineage kinase 3 (MLK3) inhibitor and has demonstrated efficacy in antiretroviral therapy. The 1H-pyrrolo[2,3-b]pyridine core has been investigated as a *Plasmodium* kinase inhibitor. The 1H-pyrrolo[2,3-b]pyridine analogues shown in **Figure 4.15**(**A**) were discovered via HTS of approximately 30,000 compounds against *Pf*CLK1 and

*Pf*CLK3 using a time-resolved fluorescence resonance energy transfer (TR-FRET) assay.[24] Mahindra et al later established a SAR leading to the discovery of the core analogue in **Figure 4.15**(**B**).[25] However, this SAR was only established at positions 2 and 4 whereas **MMV1580482** substitutions occur at positions 3 and 5. This highlights the novelty of this hit compound as a dual *Pf*PKG/*Pv*PI4K inhibitor.

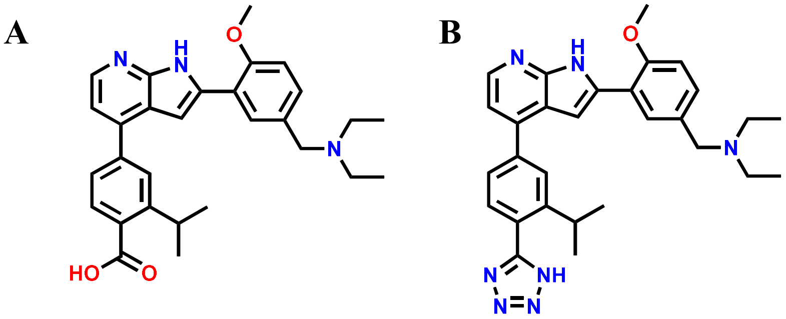

	A	B
*Pf*CLK3 IC_{50} =	40 nM	19 nM
*Pf*3D7 IC_{50} =	180 nM	270 nM

Figure 4.15: Structures of 1H-pyrrolo[2,3-b]pyridine analogues as *Pf*CLK3 inhibitors

4.6.4. MMV009948 (imatinib)

This hit compound showed a *Pf*PKG potency of 1.52 µM. In addition to being included as an antiviral in the PRB, **MMV009948** is an FDA-approved anticancer drug that acts via tyrosine kinase inhibition (**Figure 4.16**).[26] It is marketed under the brand name Gleevec®/Glivec® and is used for the treatment of chronic myeloid leukemia (CML).

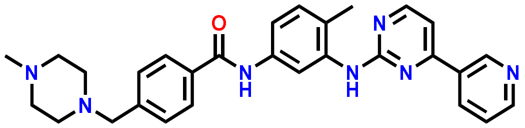

Figure 4.16: Structure of **MMV009948** (imatinib)

According to the crystallized imatinib-ABL2 (PDB ID: 2HYY) complex, the hinge binding motif is the 4-(pyridine-3-yl)pyrimidine moiety (**Figure 4.17**).[27] To date, no SAR has been established with the mentioned moiety relative to *Plasmodium* kinase inhibition.

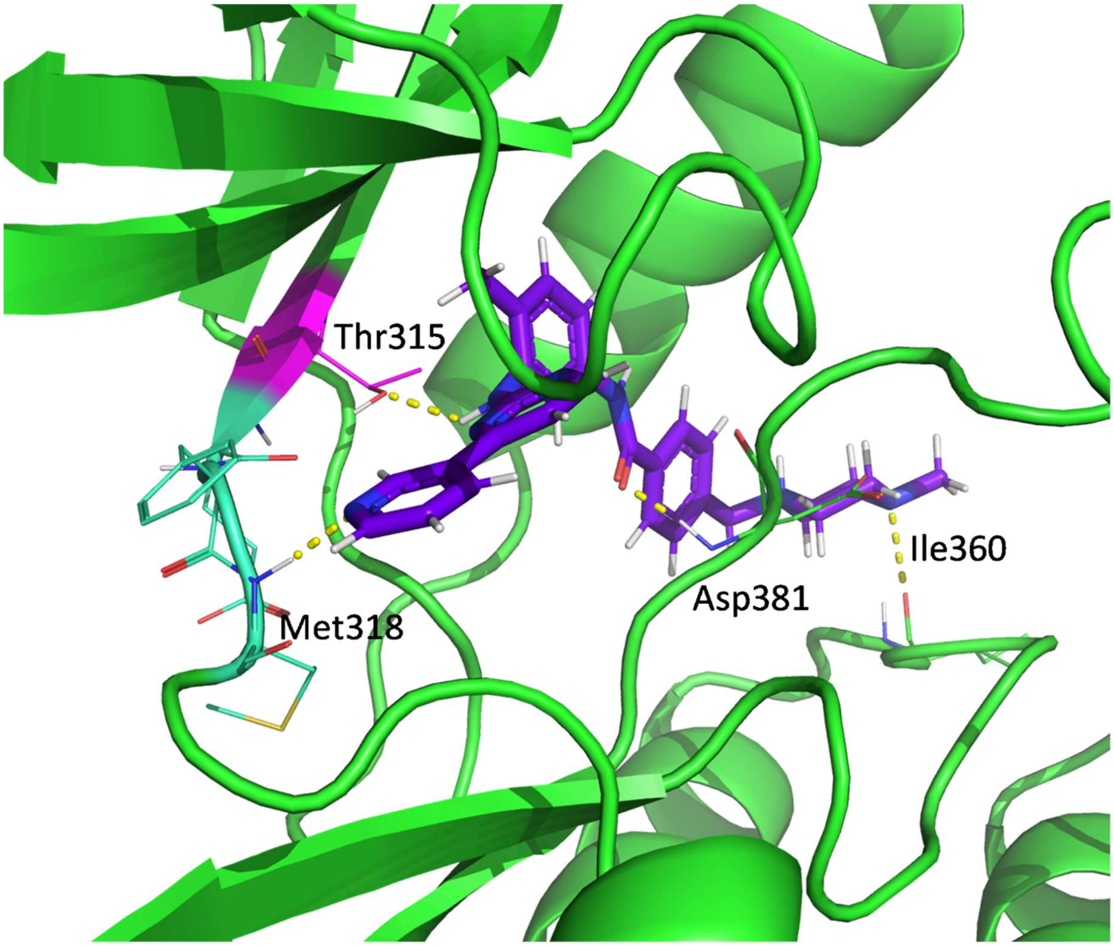

Figure 4.17: Human Abl kinase domain (PDB ID: 2HYY) in complex with MMV009948 (imatinib, purple). The hinge (cyan), gatekeeper (Thr315, magenta), and interacting residues are labelled.

4.7. Conclusion

Four hit compounds showed activity against *Pv*PI4K and/or *Pf*PKG (**MMV000043**, **MMV1580844**, **MMV1580482**, and **MMV009948**), albeit weak. Two hit compounds (**MMV1580844** and **MMV1580482**) demonstrated dual activity against both *Pv*PI4K and *Pf*PKG. The comparable *Pf*PKG potency of **MMV1580844**, **MMV1580482**, and **MMV09948** may be due to the formation of hinge interactions only. However, it is important to note that to effectively inhibit the kinase, the hinge interaction must be complemented by additional interactions in other regions of the ATP active site, such as hydrophobic regions.

*Pf*PKG potency may be increased by introducing lipophilic substituents in the side-chains interacting with the back pocket amino acids of *Pf*PKG. *Pf*PKG potency may be increased by introducing substituents to interact favorably with **Asp675**. In addition to hinge interactions, other interactions in the hydrophobic and ribose pocket may increase *Pv*PI4K potency. Learnings from previous chapters have yielded various strategies that can be used to optimize these hits for respective enzyme inhibition.

Focusing on the novel chemotypes with dual *Pf*PKG/*Pv*PI4K inhibition (**Figure 4.18**): 1H-pyrrolo[2,3-b]pyridine (**MMV1580482**) and pyrimidine-2,4-diamine (**MMV1580844**), several strategies can be used to design the respective analogues.

1H-pyrrolo[2,3-b]pyridine

Pyrimidine-2,4-diamine

Figure 4.18: Novel chemotypes with dual *Pf*PKG/*Pv*PI4K inhibition

As a suggestion, core hopping with known *Pf*PKG and *Pv*PI4K inhibitors may be a good place to start. For example, putting bulky substituents at R_1 while less bulky ones at R_2 of the 1H-pyrrolo[2,3-b]pyridine may cause the core to flip into the correct orientation and may translate to increasing *Pf*PKG inhibition. In this regard core hopping with ML10, fluorophenylmethanesulfonamide at R_2 and the N-(cyclopropylmethyl)pyrimidin-2-amine at R_1 may be a starting point. With regards to the pyrimidine-2,4-diamine core, there is more space to work with because no matter the core flip, the hinge interactions will still be maintained. For selectivity purposes over the human kinases, it is advisable to keep one position bulky.

4.8. References

1. About the Pandemic Response Box. https://www.mmv.org/mmv-open/pandemic-response-box/about-pandemic-response-box.

2. Reader, J.; van der Watt, M. E.; Taylor, D.; Le Manach, C.; Mittal, N.; Ottilie, S.; Theron, A.; Moyo, P.; Erlank, E.; Nardini, L., Multistage and transmission-blocking targeted antimalarials discovered from the open-source MMV Pandemic Response Box. *Nat. Commun.* **2021,** *12* (1), 1-15.

3. Le Corre, L.; Girard, A.-L.; Aubertin, J.; Radvanyi, F.; Benoist-Lasselin, C.; Jonquoy, A.; Mugniery, E.; Legeai-Mallet, L.; Le Merrer, Y., Synthesis and biological evaluation of a triazole-based library of pyrido [2, 3-d] pyrimidines as FGFR3 tyrosine kinase inhibitors. *Org. Biomol. Chem.* **2010,** *8* (9), 2164-2173.

4. Arris, C. E.; Boyle, F. T.; Calvert, A. H.; Curtin, N. J.; Endicott, J. A.; Garman, E. F.; Gibson, A. E.; Golding, B. T.; Grant, S.; Griffin, R. J., Identification of novel purine and pyrimidine cyclin-dependent kinase inhibitors with distinct molecular interactions and tumor cell growth inhibition profiles. *J. Med. Chem.* **2000,** *43* (15), 2797-2804.

5. Flaherty, K. T.; Yasothan, U.; Kirkpatrick, P., Vemurafenib. *Nat. Rev. Drug Discovery* **2011,** *10* (11), 811-813.

6. Patnaik, S.; Stevens, K. L.; Gerding, R.; Deanda, F.; Shotwell, J. B.; Tang, J.; Hamajima, T.; Nakamura, H.; Leesnitzer, M. A.; Hassell, A. M., Discovery of 3, 5-disubstituted-1H-pyrrolo [2, 3-b] pyridines as potent inhibitors of the insulin-like growth factor-1 receptor (IGF-1R) tyrosine kinase. *Bioorg. Med. Chem. Lett.* **2009,** *19* (11), 3136-3140.

7. Stavenger, R.; Zhao, B.; Zhou, B.; Brown, M.; Lee, D.; Holt, D., Pyrrolo [2, 3-b] pyridines inhibit the checkpoint kinase Chk1. 2016.

8. Thevakumaran, N.; Lavoie, H.; Critton, D. A.; Tebben, A.; Marinier, A.; Sicheri, F.; Therrien, M., Crystal structure of a BRAF kinase domain monomer explains basis for allosteric regulation. *Nat. Struct. Mol. Biol.* **2015,** *22* (1), 37-43.

9. Tsai, J.; Lee, J. T.; Wang, W.; Zhang, J.; Cho, H.; Mamo, S.; Bremer, R.; Gillette, S.; Kong, J.; Haass, N. K., Discovery of a selective inhibitor of oncogenic B-Raf kinase with potent antimelanoma activity. *Proc. Natl. Acad. Sci.* **2008,** *105* (8), 3041-3046.

10. Mathea, S., Chatterjee, D., Preuss, F., Yamamoto, S., Tawada, M., Nomura, I., Takagi, T., Ahmed, M., Little, W., Mueller-Knapp, S., Knapp, S, The LIMK1 Kinase Domain Bound To LIJTF500127. 2020.

11. Freedman, D. O., Tafenoquine: integrating a new drug for malaria prophylaxis into travel medicine practice. Oxford University Press: 2019; Vol. 26, p tay140.

12. Ratner, M., FDA approves first single-dose antimalarial. *Nat. Biotechnol.* **2018,** *36* (9), 785-786.

13. Lu, K.-Y.; Derbyshire, E. R., Tafenoquine: A Step toward Malaria Elimination: Published as part of the Biochemistry series "Biochemistry to Bedside". *Biochemistry* **2020,** *59* (8), 911-920.

14. Markus, M. B., Killing of Plasmodium vivax by Primaquine and Tafenoquine. *Trends Parasitol.* **2019,** *35* (11), 857-859.

15. Markus, M. B., Safety and Efficacy of Tafenoquine for Plasmodium vivax Malaria Prophylaxis and Radical Cure: Overview and Perspectives. *Ther. Clin. Risk Manage.* **2021,** *17*, 989.

16. Fernández-Villa, D.; Aguilar, M. R.; Rojo, L., Folic acid antagonists: antimicrobial and immunomodulating mechanisms and applications. *Int. J. Mol. Sci.* **2019,** *20* (20), 4996.

17. Frey, K. M.; Viswanathan, K.; Wright, D. L.; Anderson, A. C., Prospective screening of novel antibacterial inhibitors of dihydrofolate reductase for mutational resistance. *Antimicrob. Agents Chemother.* **2012,** *56* (7), 3556-3562.

18. Lamb, K. M.; G-Dayanandan, N.; Wright, D. L.; Anderson, A. C., Elucidating features that drive the design of selective antifolates using crystal structures of human dihydrofolate reductase. *Biochemistry* **2013,** *52* (41), 7318-7326.

19. Hawser, S.; Lociuro, S.; Islam, K., Dihydrofolate reductase inhibitors as antibacterial agents. *Biochem. Pharmacol.* **2006,** *71* (7), 941-948.

20. McGuire, J. J., Anticancer antifolates: current status and future directions. *Curr. Pharm. Des.* **2003,** *9* (31), 2593-2613.

21. Delves, M.; Plouffe, D.; Scheurer, C.; Meister, S.; Wittlin, S.; Winzeler, E. A.; Sinden, R. E.; Leroy, D., The activities of current antimalarial drugs on the life cycle stages of Plasmodium: a comparative study with human and rodent parasites. *PLoS Med.* **2012,** *9* (2), e1001169.

22. McGregor, I. A.; Smith, D. A., Daraprim in treatment of malaria. *Br. Med. J.* **1952,** *1* (4761), 730.

23. Voss, M. D.; Czechtizky, W.; Li, Z.; Rudolph, C.; Petry, S.; Brummerhop, H.; Langer, T.; Schiffer, A.; Schaefer, H.-L., Discovery and pharmacological characterization of a novel small molecule inhibitor of phosphatidylinositol-5-phosphate 4-kinase, type II, beta. *Biochem. Biophys. Res. Commun.* **2014,** *449* (3), 327-331.

24. Alam, M. M.; Sanchez-Azqueta, A.; Janha, O.; Flannery, E. L.; Mahindra, A.; Mapesa, K.; Char, A. B.; Sriranganadane, D.; Brancucci, N. M.; Antonova-Koch, Y., Validation of the protein kinase PfCLK3 as a multistage cross-species malarial drug target. *Science* **2019,** *365* (6456).

25. Mahindra, A.; Janha, O.; Mapesa, K.; Sanchez-Azqueta, A.; Alam, M. M.; Amambua-Ngwa, A.; Nwakanma, D. C.; Tobin, A. B.; Jamieson, A. G., Development of Potent Pf CLK3 Inhibitors Based on TCMDC-135051 as a New Class of Antimalarials. *J. Med. Chem.* **2020,** *63* (17), 9300-9315.

26. Peng, B.; Lloyd, P.; Schran, H., Clinical pharmacokinetics of imatinib. *Clin. Pharmacokinet.* **2005,** *44* (9), 879-894.

27. Cowan-Jacob, S. W.; Fendrich, G.; Floersheimer, A.; Furet, P.; Liebetanz, J.; Rummel, G.; Rheinberger, P.; Centeleghe, M.; Fabbro, D.; Manley, P. W., Structural biology contributions to the discovery of drugs to treat chronic myelogenous leukaemia. *Acta Crystallogr., Sect. D: Biol. Crystallogr.* **2007,** *63* (1), 80-93.

CHAPTER FIVE: Summary, conclusions, and recommendations for future work

5.1. Summary and conclusion

The aim of this study was to use CADD to rationally design and accelerate the identification of *P. falciparum* kinase inhibitors. The first objective of this study was to design and synthesize novel analogues of the anticancer human mTOR inhibitor MLN0128 as dual *Pf*PI4K/*Pf*PKG inhibitors. Structural information regarding the target and off-target involved were obtained through the PDB (*Pv*PKG and mTOR) and homology modeling (*Pf*PI4K). Using structure-based drug design methods, several strategies were used to design potent yet selective dual *Pf*PI4K/*Pf*PKG inhibitors. Selected compounds were prioritized for synthesis according to ease of synthesis.

There was lack of correlation between enzymatic activity and calculated binding energies of the compounds with respect to both targets. Binding mode analysis of matched pairs was therefore used to obtain structural insights into factors influencing enzymatic potency of identified inhibitors. Compound **46h** (**Figure 5.1**) had an IC_{50} of 1.8 nM against *Pv*PI4K, thus demonstrating very high potency. The MLN0128 analogue that exhibited the highest *Pf*PKG inhibition was **46b** (**Figure 5.1**) with an IC_{50} of 0.12 µM. There was poor correlation between both enzymatic activities and whole-cell activity. Interestingly, **46b** (0.66 µM) and **46g** (0.4 µM) (**Figure 5.1**), the most potent *Pf*PKG inhibitors, also exhibited high whole-cell activity against the CQ-sensitive strain *Pf*NF54. High selectivity was also maintained against the HuPI4KIIIβ and moderate selectivity was achieved against the mTOR kinase.

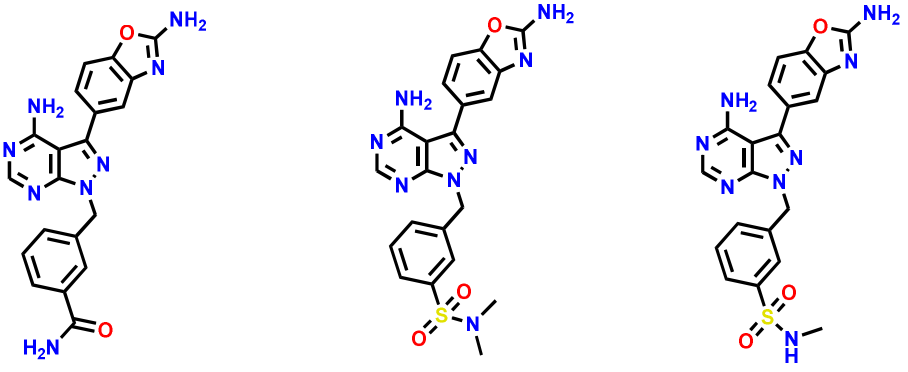

46b
*Pv*PI4K IC_{50} (μM): 0.004
*Pf*PKG IC5$_0$ (μM): 0.12
mTOR IC50 (μM): 0.002
HuPI4KIIIβ IC50 (μM): >10
*Pf*NF54 IC50 (μM): 0.66
*Pf*K1 IC50 (μM): 0.54
Solubility (μM): 15

46g
*Pv*PI4K IC_{50} (μM): 0.004
*Pf*PKG IC5$_0$ (μM): 0.18
mTOR IC50 (μM): 0.004
HuPI4KIIIβ IC50 (μM): >10
*Pf*NF54 IC50 (μM): 0.4
Solubility (μM): <5

46h
*Pv*PI4K IC_{50} (μM): 0.002
*Pf*PKG IC5$_0$ (μM): 0.22
mTOR IC50 (μM): 0.008
HuPI4KIIIβ IC50 (μM): >10
*Pf*NF54 IC50 (μM): 3.52
Solubility (μM): 5

Figure 5.1: Front-runner MLN0128 analogues with associated biological data

Another objective was to use *in silico* tools to accelerate the identification of 3,6-substituted imidazopyridazine (SFK52) analogues that, in addition to being *Pv*PI4K inhibitors, are potent *Pf*PKG inhibitors. Using various statistical-based physicochemical properties, compounds were prioritized for *Pf*PKG enzymatic screening. Enzymatic data were rationalized using molecular docking against the *Plasmodium* PKG crystal structure and findings were then used to virtually screen an in-house compound library to identify potent *Pf*PKG inhibitors. This led to the identification of several potent SFK52 analogues with sub-100 nanomolar *Pf*PKG inhibition. Further *in silico* binding predictions were used to explain the enzymatic inhibition data. Molecular dynamic simulations were carried out for **29** (*Pf*PKG IC_{50} = 0.007 μM) and the parent compound (*Pf*PKG IC_{50} = 0.12 μM) to gain further insight into factors driving increased *Pf*PKG potency (**Figure 5.2**). Dual *Plasmodium* PI4K/PKG potency with sub-nanomolar enzyme inhibition is challenging to achieve.

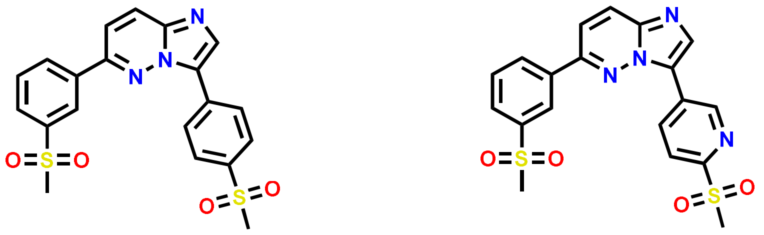

Parent
*Pf*PKG IC_{50} = 0.12 μM

29
*Pf*PKG IC_{50} = 0.007 μM

Figure 5.2: Parent compound and front-runner SFK52 analogue with associated biological activity.

The final objective of this study was to virtually screen the PRB for potential *Pf*PI4K and/or *Pf*PKG inhibitors. Of the 400 compounds in the PRB, 21 were selected for enzymatic screening after virtual screening using the *Pv*PKG crystal structure and the *Pf*PI4K homology model. Four hits were identified against *Pf*PKG (approximately 20% success rate) and two against *Pv*PI4K (approximately 10% success rate). This led to the discovery of **MMV1580844** and **MMV1580482** as dual *Pv*PI4K and *Pf*PKG inhibitors (**Figure 5.3**).

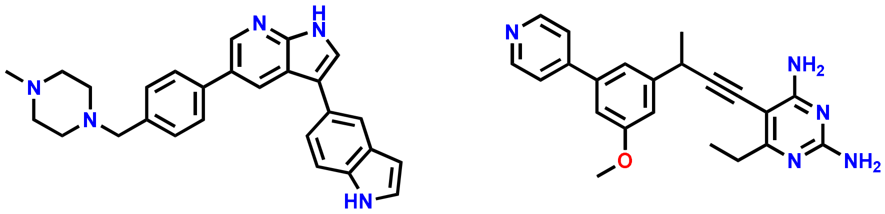

MMV1580482
*Pf*PKG IC5$_0$ (μM): 1.02
*Pv*PI4K IC_{50} (μM): 1.66

MMV1580844
*Pf*PKG IC5$_0$ (μM): 1.92
*Pv*PI4K IC_{50} (μM): 3.71

Figure 5.3: Front-runner Pandemic Response Box compounds that exhibited dual *Pf*PKG/*Pv*PI4K inhibition.

In conclusion, this project identified structural features that can improve *Plasmodium* PI4K and PKG inhibition with strategies to improve selectivity against human kinases also observed.

5.2. Recommendations for future work

Regarding MLN0128 analogues, *meta*-hydrogen bond-donating groups, for example **46b,** were shown to increase enzymatic potency (**Figure 5.4**).

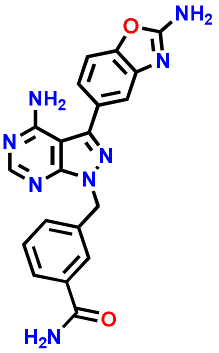

46b
*Pv*PI4K IC_{50} (µM): 0.004
*Pf*PKG IC5$_0$ (µM): 0.12
mTOR IC50 $_($µM): 0.002
HuPI4KIIIβ IC50 ($_{µM}$): >10
*Pf*NF54 IC50 ($_{µM)}$: 0.66
*Pf*K1 IC50 (µM$_{):}$ 0.54
Solubility (µM): 15

Figure 5.4: MLN0128 analogue, **46b**, with its associated biological data.

Specifically, designing compounds with *meta* substituents that interact with **Asp675** may lead to an increase in *Pf*PKG inhibition (**Figure 5.5A**). Selectivity over mTOR may be achieved by adding an additional linker between the amine and the benzoxazole moiety. This increases bulkiness and disrupts the amine acid interaction with **Asp2357**, which plays a great role in selectivity (**Figure 5.5B**).

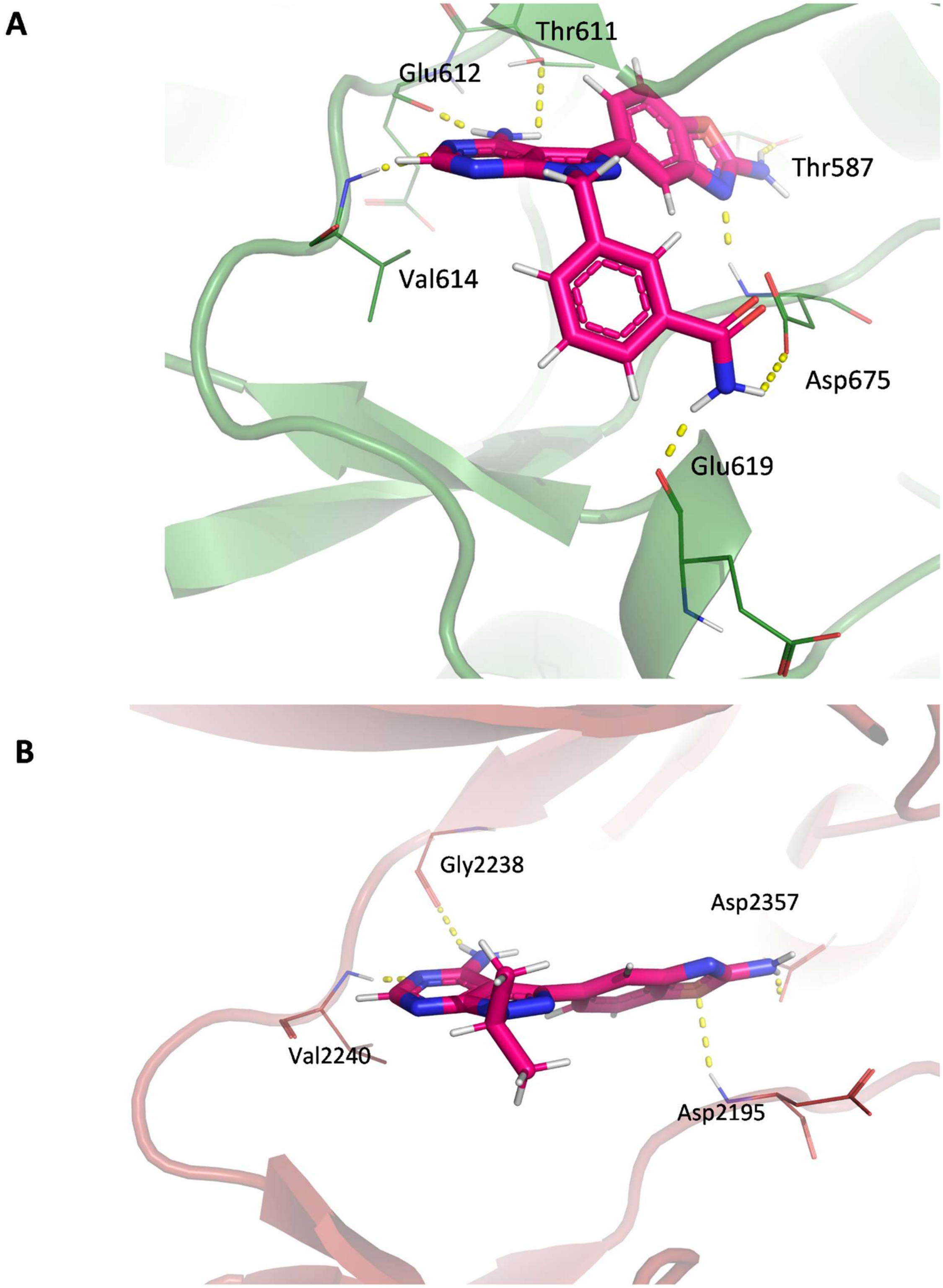

Figure 5.5: 46b docked into *Pv*PKG (**A**) and **MLN0128** docked into mTOR (**B**) showing important amino acid interactions.

Concerning SFK52 analogues, observing from **15** and **29** (**Figure 5.6**), *Pf*PKG inhibition may be increased by maintaining the pyridine moiety at position 3 and adding substituted sulphonamides at position 6.

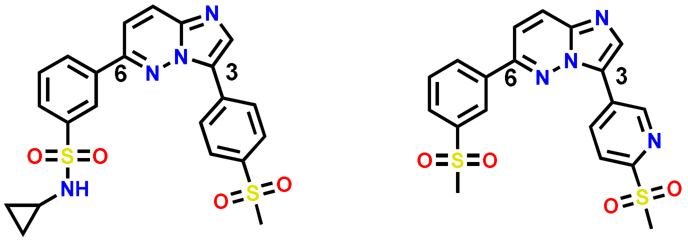

H3D-000359
*Pf*PKG IC_{50} = 0.016 µM

H3D-002347
*Pf*PKG IC_{50} = 0.007 µM

Figure 5.6: Front-runner SFK52 analogues with associated biological data

Optimization of the novel chemotypes (1H-pyrrolo[2,3-b]pyridine and pyrimidine-2,4-diamine) may lead to increased dual *Pf*PKG/*Pv*PI4K potency compared to that of the original hits (**Figure 5.7**). This process may be guided by findings in previous chapters, specifically, amino acid interactions that favor enzyme inhibition.

1H-pyrrolo[2,3-b]pyridine

Pyrimidine-2,4-diamine

Figure 5.7: Novel chemotypes that exhibited dual *Pf*PKG/*Pv*PI4K inhibition.

CHAPTER SIX: Materials and methods

6.1. *In silico* methods

6.1.1. Homology modeling

The *pfpi4k* protein sequence was retrieved in FASTA format from the PlasmoDB (accession code: PF3D7_0509800).[1] Using BLAST,[2] HuPI4KIIIβ (PDB ID: 4D0L)[3] was identified as a suitable template. In Schrödinger Suite 2018-3,[4] the Prime module[5] was used to build the homology model.

6.1.2. Molecular docking

Protein structures were prepared using the “protein preparation” wizard protocol available in Schrödinger Suite 2019-2.[6] Hydrogen atoms were added to the available 3D crystal structures of *Pv*PKG (PDB ID: 5F0A) and human mTOR (PDB ID: 4JT5). Hydrogen atoms were minimized to avoid contacts, keeping the heavy atoms fixed at their original positions. All water molecules were removed. Protein structures were optimized based on the OPLS3e force field.[7] Ligands, water molecules, and other co-crystallized agents were deleted. The ProtAssign script was used to optimize intramolecular contacts. The imperf script was used to perform restrained minimization of the protein, with maximum root-mean-square deviation (RMSD) = 0.3Å.

A docking grid was then generated using the “receptor grid generation” module of Maestro. The grid encloses a box centered on the native ligand. A scaling factor of 1.0 was set for van der Waal’s radii of receptor atoms with a partial atomic charge <0.25. Protonation states, tautomers, stereochemistry, and any desired geometric restraints (distances, dihedrals, and angles) of the ligands were generated during ligand preparation. Partial charges were calculated and applied to the ligands together with an energy minimization protocol with a suitable force field. Using the Glide extra precision setting, compounds were then docked against the generated docking grid.[8] Using the Prime MMGBSA tool, compounds with a favorable docked pose were rescored using the OPLS3e force field,[7] the VSGB implicit solvent,[9] hierarchical sampling, and a 5.0-Å radius.

6.1.3. Molecular dynamics (MD)

Schrödinger's MD code, developed by D.E Shaw Research, was used to carry out MD simulations.[10] In all simulation runs, normal temperature and pressure (NPT) conditions were applied (pressure: 1 atm; temperature: 293.15 K). The duration of the simulations was 200 ns with a relaxation time of 1 ps for complexes of interest. OPLS3e force field parameters were used. A cut-off radius of 9.0 Å was applied to Coulomb interactions. The boundaries of the orthorhombic period box were set 10 Å away from protein atoms. The transferrable intermolecular potential with the four points model (TIP4P) explicitly described the water molecules.[11, 12] Using default software settings, the salt concentration of NaCl of 0.15 M was used, followed by the system being built using the System Builder module.[13] For temperature control, the Nosé-Hoover chain coupling scheme was used.[14] In addition, for pressure control, the Martyna-Tuckerman-Klein chain coupling scheme with a coupling constant of 2.0 ps was used.[15] A RESPA integrator in which long-range forces were updated every three steps and short-range forces were updated every step was used to calculate non-bonded forces. For analysis, trajectories were saved at 50 ps intervals. The Simulation Interaction Diagram tool was used to analyze the interactions and behavior of the protein and ligand. The RMSD of the protein-ligand complex was monitored to determine the stability of the MD simulations.

6.2. Biological methods

6.2.1. *In vitro* antiplasmodium assays

The antiplasmodium asexual blood-stage activity of the compounds was tested using the *P. falciparum* chloroquine-sensitive strain NF54 and the multidrug-resistant strain K1. With slight variations, the parasites were cultured and maintained according to the method described by Trager and Jensen, and a parasite lactate dehydrogenase assay was used to determine antiplasmodium activity.[16]

Stock solutions of the compounds were prepared in 100% DMSO at 20 mg/mL and stored at -20 °C prior to analysis. With the highest starting concentration at 6 µM, subsequent dilutions were prepared in medium on the day of the assay. Ten concentration points (0.012–100 µg/mL) were prepared from serial dilutions in complete medium. The concentration resulting in 50% inhibition of parasite growth (IC_{50}) was determined by performing a dose-response analysis within the mentioned range.

With an initial concentration of 1000 ng/mL, artesunate and chloroquine were used as controls in all assays using a similar dilution approach. The final concentration of DMSO did not affect parasite growth. Data were normalized based on controls and mean IC_{50} values were calculated from $n \geq 2$ biological repeats. These assays were carried out by the *in vitro* parasitology team at H3D, UCT.

6.2.2. Turbidimetric-based kinetic solubility

Stock solutions (10 mM) were prepared by dissolving compounds and controls in DMSO. A pre-dilution Nunc™ 96-well fluorescence plate was prepared with serial dilutions of the stock solution (0.125–8 mM) in triplicate. Secondary dilutions in PBS (0.01 M, pH 7.4) and DMSO were prepared in a second plate in triplicate such that each well contained 200 µL compound solution (concentration range: 0–200 µM).

A SpectraMax 340 PC microplate reader (Molecular Devices, Sunnydale, CA, USA) was used to measure absorbance at 620 nM after 2-h incubation at room temperature. Concentration-absorbance curves were then exported and plotted in Microsoft Excel®. The limit of solubility of a compound was determined as the point of deflection (in PBS) from the baseline (DMSO plot). The controls for this assay were reserpine and hydrocortisone, which represent poorly and highly soluble compounds, respectively, and these were treated similarly.

6.2.3. Kinetic Solubility using the HPLC-based DMSO "dry-down" method

To minimize the impact of solvent-enhanced solubility which occurs when using the turbidimetric method, this approach was also used to determine kinetic solubility. Stock solutions (10 mM) were prepared by dissolving compounds in 100% DMSO. For each compound, calibration curves were constructed using low (11 µM), medium (100 µM), and high (220 µM) concentrations using HPLC with UV detection.

First, solutions of high and medium concentrations were prepared by adding 4.4-µL and 2-µL aliquots of the stock solution to 195.6 µL and 198 µL DMSO in wells A and B, respectively, of a 96-well plate. The low concentration solution was made up in well C by taking a 10-µL aliquot from well A (high concentration) and adding 190 µL DMSO. To mitigate the effects of solubility enhancement due to DMSO, each test sample (4 µL of the 10 mM stock solution) was placed in wells D, E, and F, in triplicate, and DMSO was removed by freeze-drying under Genevac®. Phosphate buffer (200 µL) was then added to wells containing the dry compounds. The plates were covered and placed on a shaker for 24 h at 37 °C, before centrifuging at 23 °C using a digitor 21R® centrifuge at 3500 rpm for 15 min. The supernatant was transferred to another 96-well plate for HPLC analysis combined with UV detection. The concentration of the dissolved samples was determined by comparing the standard curve constructed using samples in wells A, B, and C with the average peak areas produced by the samples in well D, E, and F. These assays were carried out by the ADME (Absorption, Distribution, Metabolism, Excretion) team at H3D, UCT.

6.2.4. Kinase inhibition assays

Assay selection

The Kinase-Glo® luminescent kinase assay platform (Promega Corporation) measures kinase activity by quantifying the amount of ATP remaining after a kinase reaction.[17] The assay procedure involves adding a single reagent directly to a completed kinase reaction. The remaining ATP is then used as a substrate in the luciferase reaction, which produces one photon of light per turnover (**Figure 6.1**). The luminescent signal generated correlates with the amount of ATP present and is inversely proportional to kinase activity.

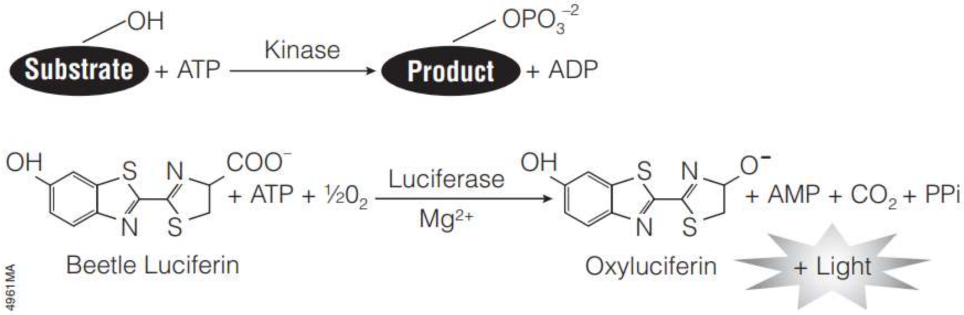

Figure 6.1: Kinase-Glo® reaction mechanism.

The kinase reaction is first conducted under appropriate conditions. The ATP remaining when Kinase-Glo® Reagent is added is used as a substrate by Ultra-Glo™ luciferase to catalyze the mono-oxygenation of luciferin. The luciferase reaction produces one photon of light per turnover and luminescence is inversely related to kinase activity.

Kinase-Glo® and other ATP-depletion kits with the same principles are commonly used for High-Throughput Screening (HTS). Despite their universal applicability, shortcomings relating to high background and large substrate turnover have limited their use for kinases with slow turnover in Mechanism-of-Action (MoA) studies. To circumvent this problem, Zegzouti and colleagues (Promega) developed a novel method that retains the advantages and eliminates the drawbacks of the Kinase-Glo® assay.**[18]** The simple "mix-and-read" cocktails of the ADP-Glo™ kinase assay contain two major components and are added to a complete kinase reaction in two steps (**Figure 6.2**).

In the first step, ADP-Glo™ reagent is added. This reagent contains an enzyme to remove unreacted ATP. In the second step, a kinase detection reagent is added. This component contains a mixture of enzymes that convert ADP (product of the kinase reaction) back into ATP. Luciferase and its substrate then convert ATP to AMP in a two-step reaction that gives off light. The kinase detection reagent also contains an inhibitor of the enzyme in ADP-Glo™ reagent, thus preventing it from degrading newly converted ATP from ADP.

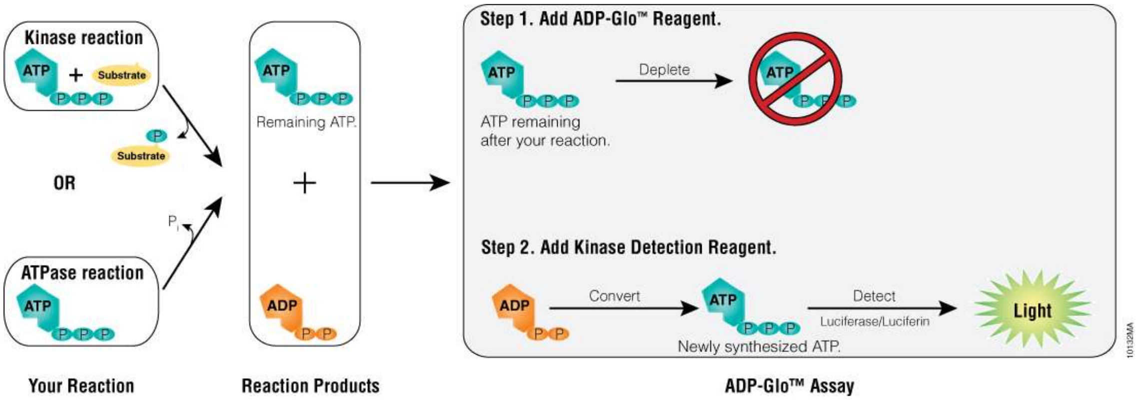

Figure 6.2: ADP-Glo™ kinase assay.

The first step involves depletion of unconsumed ATP after the kinase/ATPase reaction. ADP is converted into ATP that is detected via a luciferase/luciferin reaction in the second step. The luminescent signal measured is proportional to the amount of ADP produced and the kinase activity.

Along with extremely low background and increased signal (**Figure 6.3**), ADP-Glo™ demonstrated the following advantages over the Kinase-Glo® assay: extreme sensitivity (0.1 pmol ADP), broad ATP concentration (1–5 mM), and applicability to all kinases. This assay may therefore be used for HTS profiling as well as MoA studies. ADP-Glo™ was thus the assay selected for testing both *Pf*PKG and *Pf*PI4K inhibitors.

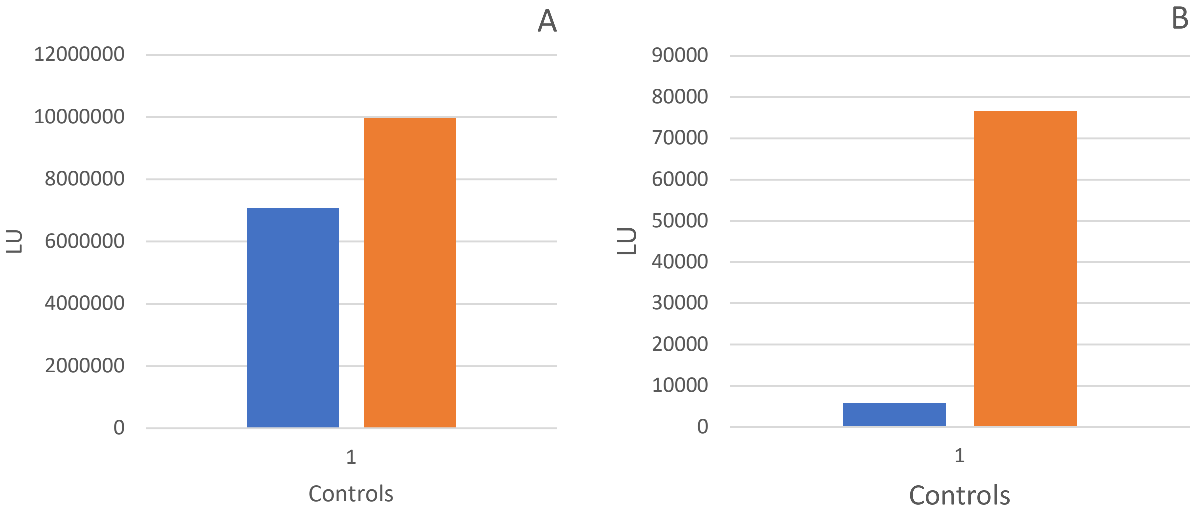

Figure 6.3: Comparison of positive (orange) and negative (blue) controls for Kinase-Glo® (A) and ADP-Glo™ (B) assays. The high signal-to-background ratio of ADP-Glo^{TM} is preferred.

Assay optimization

i) *Pf*PKG

Identifying a kinase concentration that guarantees a sufficiently high signal and strong linearity between signal and kinase activity is paramount to assay optimization. In addition to preparing a standard curve, enzyme titration assays were carried out to determine the optimal enzyme concentration to use for inhibitor screening. A standard curve is necessary to determine the amount of enzyme to use in the assay. A standard curve was therefore prepared to estimate the amount of ADP produced in the kinase reaction and to represent luminescence corresponding to the conversion of ATP to ADP based on the ATP concentration used. These conversion curves represent the amounts of ATP and ADP produced at a specified conversion percentage in a reaction. Appropriate volumes of ATP and ADP stock solutions were combined to create the standard samples used to generate the ATP-to-ADP conversion curve. The 96-well plate set-up used to generate the standard curve is shown in **Table 6.1**.

Table 6.1: ATP/ADP standard curve dilutions

% Conversion	**40%**	**20%**	**10%**	**5%**	**2.5%**	**0**
ADP (µL)	40	20	10	5	2.5	0
ATP (µL)	60	80	90	95	97.5	100

ATP, adenosine triphosphate; ADP, adenosine diphosphate.

Based on work previously reported by Baker et al.,[19] GRTGRRNSI-NH2 (PKA) was used as the substrate for the *Pf*PKG kinase reaction. The assay buffer used contained 25 mM HEPES buffer (pH 7.4), 0.01% bovine serum albumin (BSA), 0.01% Triton-X, 20 mM $MgCl_2$, 2 mM dithiothreitol (DTT), and 8 µM cGMP (Sigma, G6129). To determine the optimal *Pf*PKG enzyme concentration, a two-fold serial dilution was prepared using 10 µM ATP, 20 µM GRTGRRNSI-NH2 (PKA), and assay buffer (total volume = 40 µL). As a control, the last well did not contain any enzyme. The solution was incubated at 22 ºC and after 30 min, 5-µL aliquots of the kinase reaction were transferred to a 384-well plate and mixed with an equal volume of the ADP-Glo™ reagent. After 40 min incubation, 10 µL kinase detection reagent was added to the aliquots. Luminescence was measured after 30-min incubation using a PerkinElmer EnSpire multimode plate-reader. The appropriate enzyme concentration to be used in the assays was calculated using the relative luminescence unit (RLU) signal for 10% to 15% conversion (**Figure 6.4**). The ATP-to-ADP standard curve was used to determine the RLU signal associated with 10% ATP conversion at a specified enzyme concentration. According to these results, the linear region was maintained, and the assays were henceforth performed using a final *Pf*PKG concentration of 1 nM.

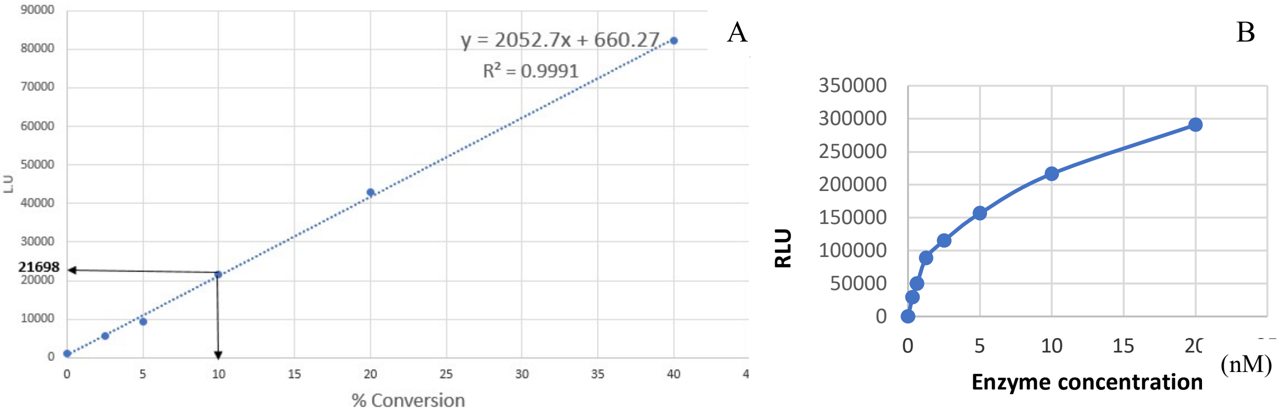

Figure 6.4: A, ATD/ADP conversion standard curve; B, *Pf*PKG enzyme titration

MLN0128 was titrated across an assay plate to determine its IC_{50} with concentrations ranging from 1 µM to 0.98 nM. The last two wells included controls with 100% enzyme activity and no enzyme activity, respectively. A two-fold serial dilution of MLN0128 was prepared with 10 µM ATP, 20 µM GRTGRRNSI-NH2 (PKA), and assay buffer (total volume = 40 µL). The incubation was performed at 22 ºC and after 30 min, 5-µL aliquots of the kinase reaction were transferred to a 384-well plate and mixed with an equal volume of ADP-Glo™ reagent. After 40 min incubation, 10 µL kinase detection reagent was added to the aliquots. Luminescence was measured after 30 min incubation using a PerkinElmer EnSpire multimode plate-reader. The *Pf*PKG IC_{50} determined (20 nM) was comparable to that recorded at the GSK/Cellzome facility, further validating the assay protocol developed for screening *Pf*PKG inhibitors (**Figure 6.5**).

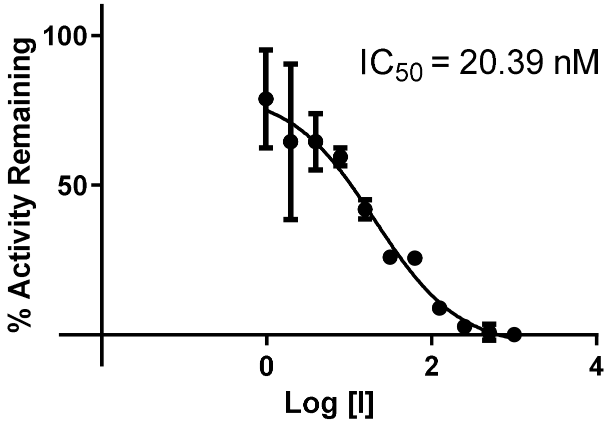

Figure 6.5: IC_{50} of MLN0128 against *Pf*PKG

Compounds of interest were then screened against *Pf*PKG using the assay protocol developed. The compounds were tested at a range of concentrations (10 µM–0.17 nM). To determine the IC_{50} of the target compounds, three-fold serial dilutions were prepared using 10 µM ATP, 20 µM GRTGRRNSI-NH2 (PKA), and assay buffer (total volume = 40 µL). The solution was incubated at 22 ºC and after 30 min, 5-µL aliquots of the kinase reaction were transferred to a 384-well plate and mixed with an equal volume of ADP-Glo™ reagent. After 40 min incubation, 10 µL kinase detection reagent was added to the aliquots. Luminescence was measured after 30 min incubation using a PerkinElmer EnSpire multimode plate-reader. The assay was repeated at least twice.

ii) *Pv*PI4K

Due to challenges in expressing and purifying *Pf*PI4K, *Pv*PI4K was used. The *Pv*PI4K assay conditions were optimized using the same methods described for *Pf*PKG assays. The final enzyme concentration used for the *Pv*PI4K assay was 6 nM. The protocols of both *Pv*PI4K and *Pf*PKG inhibition assays are similar. The assay buffer components are: 25 mM HEPES buffer (pH 7.4), 0.01% BSA, 0.01% Triton-X, 20 mM $MgCl_2$, 2 mM dithiothreitol (DTT), and 2M NaCl. The substrate used for this kinase was L-alpha-phosphatidylinositol substrate (Avanti Polar Lipid, cat. 840042P) at a concentration of 110 µM.

The IC_{50} values of the target compounds were then determined by screening, in three-fold serial dilutions, within the concentration range of 100–0.1 nM. The kinase reaction was then incubated at 22 ºC and after 30 min, 5-µL aliquots of the kinase reaction were transferred to a 384-well plate and mixed with an equal volume of ADP-Glo™ reagent. After 40 min incubation, 10 µL kinase detection reagent was added to the aliquots. Luminescence was measured after 30 min incubation using a PerkinElmer EnSpire multimode plate-reader. The assay was repeated at least twice. The same protocol was used for the human lipid kinase inhibition assay (HuPI4KIIIβ) performed by Reaction Biology Corporation but using the ADP-Glo Lipid Kit.

6.2.5. RBC HotSpot kinase assay protocol

The mTOR kinase inhibition assay was performed according to previously developed methods.[20] The base reaction buffer contained 20 mM HEPES (pH 7.5), 10 mM $MgCl_2$, 1 mM EGTA, 0.01% Brij35, 1% DMSO, 2 mM DTT, 0.1mM Na_3VO_4, and 0.02 mg/mL BSA. The substrate was added to freshly prepared reaction buffer and the required co-factors were added. The mTOR kinase was then added to the substrate solution and mixed gently.

The compounds (10-point serial dilution starting at 10 µM) in 100% DMSO were added to the kinase reaction using acoustic liquid handling technology (nanolitre range; Echo550, Beckman Coulter) and incubated at 22 °C for 20 min. The reaction was initiated by adding ^{33}P-ATP to the mixture before incubating for a further 2 h at 22 °C. Kinase inhibition was then detected using the P81 filter-binding method. These assays were outsourced to Reaction Biology Corporation.

6.3. Chemistry

6.3.1. Reagents, solvents, and equipment

All reagents and chemicals used were purchased from various commercial sources and used without further purification. The solvents used in the reactions were anhydrous, with the exception of formamide. Reactions were monitored via analytical TLC and LC-MS. TLC plates were sourced from Merck (TLC Silica gel 60 F254 aluminium-backed) and were developed in a 100-mL beaker covered with either a watch glass or aluminium foil. The plates were visualized under UV at 254 and 366 nm.

An Agilent LC-MS instrument comprising an Agilent 1260® Infinity Binary Pump, Agilent 1260® Infinity Diode Array Detector, Agilent 1290® Infinity Column Compartment, Agilent 1260® Infinity Autosampler, Agilent 6120® Quadrupole LC-MS, and Peak Scientific® Genius 1050 Nitrogen Generator was used for compound purity verification and reaction monitoring. A Kinetex® Core C18 2.6-µm column (50 × 3 mm) column maintained at 35–40 °C was used. The chromatographic mobile phase was comprised 10 mM aqueous ammonium acetate (NH_4Ac) containing 0.4% acetic acid while the organic phase comprised 10 mM NH_4Ac in methanol containing 0.4% acetic acid (**Table 6.2**). The mass spectra were acquired using electrospray ionization (ESI) and/or atmospheric pressure chemical ionization (APCI) in the positive ionization mode unless otherwise stated. The final compounds were subjected to purity verification via LC-MS to ensure acceptable purity (≥95%). All yields reported are isolated and correspond to individual synthetic steps in a scheme.

Table 6.2: HPLC gradient used for determining the purity and mass (mass-to-charge, m/z) of compounds via LC-MS

Time (min)	10 mM ammonium acetate buffer in water	10 mM ammonium acetate buffer in methanol (90%)	Flow (mL/min)
0	85	15	0.7
0.3	85	15	0.7
1.2	0	100	0.7
4.5	0	100	0.7

^{1}H-NMR and ^{13}C-NMR spectra were acquired on either Bruker AV 400 (^{1}H, 400.0 MHz; ^{13}C, 101 MHz) or Varian Mercury 300 (^{1}H, 300.1 MHz) spectrometers. NMR samples were dissolved in deuterated DMSO (DMSO-d$_6$). Chemical shifts (δ) are reported in parts per million (ppm) and rounded to two decimal places. Coupling constants (*J*) are reported in Hertz (Hz) and rounded to one decimal place. Abbreviations used in assigning ^{1}H-NMR signals are: d (doublet), dd (doublet of doublets), dt (doublet of triplets) m (multiplet), q (quartet), s (singlet), t (triplet), or td (triplet of doublets). Purification and characterization of certain selected intermediates and analogues are reported in ESI.

6.3.2. Synthesis and Characterization

Compound 36: 1H-pyrazolo[3,4-d]pyrimidine-4-amine

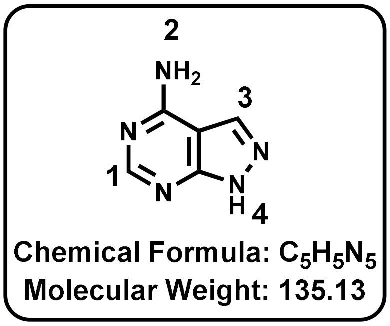

5-Amino-1H-pyrazole-4-carbonitrile (3 g, 27.75 mmol) in formamide (15 mL) was heated to 180 °C and stirred for 8 h. Upon cooling, the reaction mixture formed a precipitate that was filtered out to yield the desired intermediate **36** as a white solid (3.7 g, 27.38 mmol, 98% yield; TLC; R$_f$=0.57; 20%MeOH/DCM). ^{1}H NMR (400 MHz, DMSO-*d6*) δ = 13.33 (s, 1H, H^4), 8.14

(s, 1H, H^1), 8.09 (s, 1H, H^3), and 7.56 ppm (s, 2H, H^2). ^{13}C NMR (101 MHz, DMSO-*d6*) δ = 158.46, 156.25, 155.23, 133.09, and 100.05 ppm. HPLC-MS (APCI/ESI): t_R = 0.132 min, *m/z* $[M+H]^+$= 136.1.

Compound 37: 3-Iodo-1H-pyrazolo[3,4-d]pyrimidin-4-amine

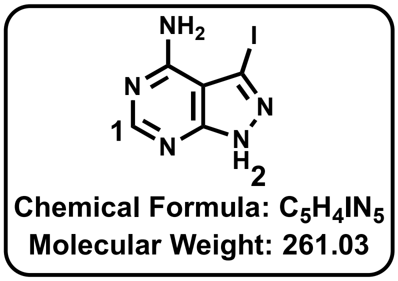

1H-Pyrazolo[3,4-*d*] pyrimidine-4-amine (**2**; 1.5 g, 11.1 mmol) and *N*-iodosuccinimide (3.75 g, 16.65 mmol, 1.5 eq) in *N,N*-dimethylformamide (15 mL) was heated for 8 h at 80 °C. Upon cooling, the reaction mixture formed a precipitate that was filtered out to produce intermediate **37** as a pale brown solid (2.253 g, 8.6312 mmol, 77.76% yield; R_f=0.7; 20%MeOH/DCM). ^1H NMR (400 MHz, DMSO-d_6) δ = 13.78 (s, 1H, H^2), 8.18 (s, 1H, H^1). ^{13}C NMR (101 MHz, DMSO- d_6) δ = 158.05, 156.48, 155.50, 103.00, and 90.02 ppm. HPLC-MS (APCI/ESI): t_R = 0.575 min, *m/z* $[M+H]^+$= 262.0.

Compound 38a: ***4-(Bromomethyl)benzamide***

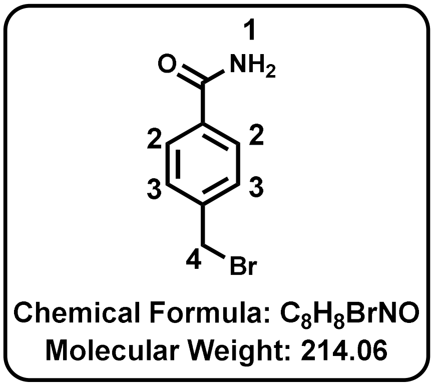

4-(Bromomethyl) benzonitrile (1 g, 5.102 mmol) in concentrated sulfuric acid (4.6 mL) was heated at 50 °C for 1 h. The reaction mixture was quenched with water to form a precipitate that was filtered out to yield intermediate **38a** as a white solid (863.2 mg, 79% yield; R_f =0.52; 50% ethyl acetate/hexane). ^{1}H NMR (300 MHz, DMSO-d_6) δ = 7.97 (s, 1H, H^1), 7.86 (d, *J* = 8.27 Hz, 2H, H^2), 7.52 (d, *J* = 8.27 Hz, 2H, H^3), 7.38 (s, 1H, H^1), and 4.74 ppm (s, 2H, H^4). ^{13}C NMR (101 MHz, DMSO-d_6) δ = 167.89, 141.53, 134.62, 129.53 (2C), 128.31 (2C), and 33.99 ppm.

Compound 38b: ***3-(bromomethyl)benzamide***

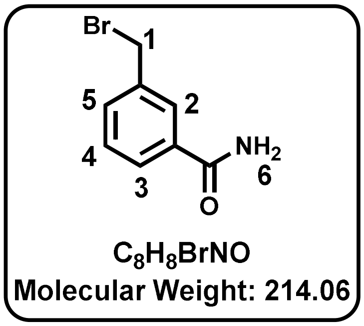

3-(Bromomethyl) benzonitrile (750 mg, 2.5510 mmol) in concentrated sulfuric acid (2.7 mL) was heated at 50 °C for 1 h. The reaction mixture was quenched with water to form a precipitate that was filtered out to yield intermediate **38b** as a white solid (528 mg, 64% yield; Rf =0.52; 50% ethyl acetate/hexane). ^{1}H NMR (600 MHz, DMSO-d_6) δ 7.95 (s, 1H, H^6), 7.91 (t, *J* = 1.42

Hz, 1H, H^2), 7.77 (dt, J = 7.7, 1.4 Hz, 1H, H^3), 7.56 (dt, J = 7.6, 1.4 Hz, 1H, H^5), 7.40 (t, J = 7.6 Hz, 1H, H^4), 7.35 (s, 1H, H^6), 4.70 (s, 2H, H^1). ^{13}C NMR (151 MHz, DMSO-*d*$_6$) δ 167.80, 138.64, 135.17, 132.41, 129.08, 128.93, 127.67 and 63.14 ppm.

Compound 39: 2-((4-amino-3-iodo-1H-pyrazolo[3,4-d] pyrimidin-1-yl)methyl)benzonitrile

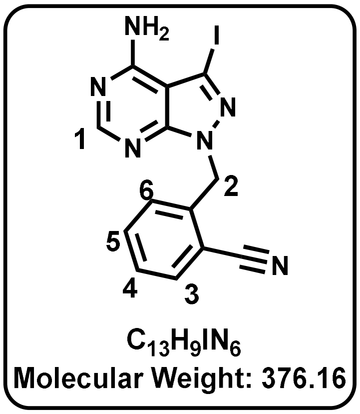

3-Iodo-1H-pyrazolo[3,4-d]pyrimidin-4-amine (200 mg, 0.7663 mmol, 1 eq.) and 2-(Bromomethyl) benzonitrile (181 mg, 0.9195 mmol, 1.2 eq.) in DMF (2.3 mL) was treated with K_2CO_3 (212 mg, 1.5326 mmol, 2 eq.), heated to 30 °C, and stirred for 2 h. The reaction mixture was extracted with ethyl acetate. The organic layer was separated, washed with brine, dried with anhydrous sodium sulphate, and concentrated under reduced pressure. It was then purified by chromatography on silica gel eluting with DCM/MeOH (10/1) to obtain the intermediate **39** as a brown solid (94.5 mg, 31% yield; R_f =0.5; 10%MeOH/DCM). ^{1}H NMR (600 MHz, DMSO-*d*$_6$) δ 8.21 (s, 1H, H^1), 7.84 (dd, *J* = 7.7 and 1.4 Hz, 1H, H^3), 7.62 (td, *J* = 7.7, 1.4 Hz, 1H, H^4), 7.47 (td, *J* = 7.7 Hz, 1.2 Hz, 1H, H^5), 7.20 (dd, *J* = 7.2, 1.2 Hz, 1H, H^6), 5.64 (s, 2H, H^2). ^{13}C NMR (151 MHz, DMSO-*d*$_6$) δ 158.22, 156.85, 154.39, 140.27, 134.10, 133.71, 129.40, 129.19, 117.44, 111.23, 103.62, 90.79 and 48.58 ppm. HPLC-MS (APCI/ESI): purity = 98%, t_R = 2.280 min, *m/z* $[M+H]^+$ = 377.

Compound 40: 2-((4-amino-3-iodo-1H-pyrazolo[3,4-d]pyrimidin-1-yl)methyl)benzamide

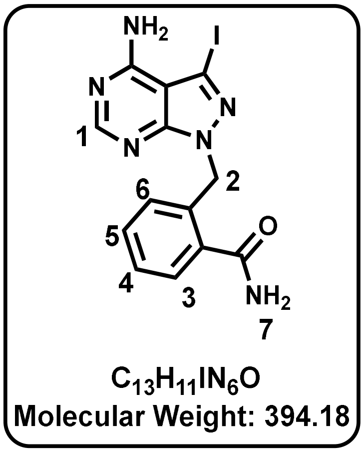

2-((4-amino-3-iodo-1H-pyrazolo[3,4-d] pyrimidin-1-yl)methyl)benzonitrile (400 mg, 0.5319 mmol, 1 eq.) and Potassium hydroxide (1.2 g, 21.4 mmol, 40 eq.) in Ethanol/Water (1 mL, 1:1) was heated at 80 °C for 2 h. The reaction mixture was extracted with ethyl acetate. The organic layer was separated, washed with brine, dried with anhydrous sodium sulphate, and concentrated under reduced pressure. It was then purified by chromatography on silica gel eluting with DCM/MeOH (10/1) to obtain the intermediate **40** as a red-brick solid (116.9 mg, 30% yield; R_f =0.3; 10%MeOH/DCM). ^{1}H NMR (600 MHz, DMSO-*d*$_6$) δ 8.17 (s, 1H, H^1), 7.95 (s, 1H, H^7), 7.54 – 7.46 (m, 2H, H^3 and H^7), 7.31 – 7.26 (m, 2H, H^4 and H^5), 6.65 (dd, *J* = 7.3, 1.2 Hz, 1H, H^6), 5.68 (s, 2H, H^2). ^{13}C NMR (151 MHz, DMSO-*d*$_6$) δ 170.45, 158.21, 156.74, 154.33, 135.60, 135.57, 130.48, 128.18, 127.66, 127.60, 103.59, 90.06 and 48.09 ppm.

General Procedure for Synthesis of Compounds 41a-c

4-(bromomethyl)benzenesulphonyl chloride (2 g, 7.4349 mmol, 1 eq.) in anhydrous THF, in the presence of DIPEA (1.6 mL, 8.9219 mmol, 1.2 eq.) was cooled to 0 °C. The relevant amine solution (1.1 eq.) was added to the reaction mixture which was stirred at 0 °C for 2 h. The reaction mixture was extracted with ethyl acetate. The organic layer was separated, washed with brine, dried with anhydrous sodium sulphate, and concentrated under reduced pressure. It was then purified by chromatography on silica gel eluting with Ethyl acetate/ Hexane (1/1) to obtain the required intermediate.

Compound 41a: 4-(bromomethyl)benzenesulphonamide

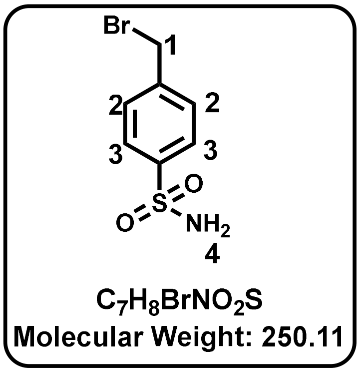

As a white solid (808.1 mg, 43% yield; R_f =0.68 50%Ethyl Acetate/Hexane). ^{1}H NMR (600 MHz, DMSO-*d$_6$*) δ 7.77 (d, *J* = 8.6 Hz, 2H, H^3), 7.59 (d, *J* = 8.3 Hz, 2H, H^2), 7.33 (s, 2H, H^4), 4.72 (s, 2H, H^1). ^{13}C NMR (151 MHz, DMSO-*d$_6$*) δ 142.33, 132.92, 130.19 (2C), 126.49 (2C) and 62.69 ppm.

Compound 41b: 4-(bromomethyl)-N-methylbenzenesulphonamide

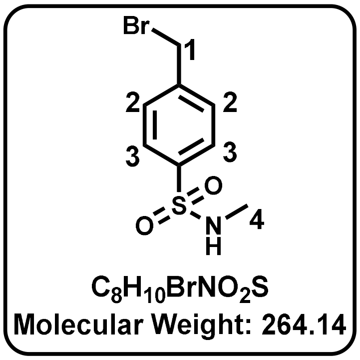

As a white solid (816.6 mg, 41% yield; R_f =0.55 50%Ethyl Acetate/Hexane). ^{1}H NMR (600 MHz, DMSO-*d$_6$*) δ 7.69 (d, *J* = 8.3 Hz, 2H, H^3), 7.49 (d, *J* = 8.0 Hz, 2H, H^2), 4.54 (s, 2H, H^1), 2.35 (d, J = 5.0 Hz, 3H, H^4). ^{13}C NMR (151 MHz, DMSO-d_6) δ 137.89, 129.93, 127.17 (2C), 127.01 (2C), 62.64 and 29.08 ppm.

Compound 41c: 4-(bromomethyl)-N,N-dimethylbenzenesulphonamide

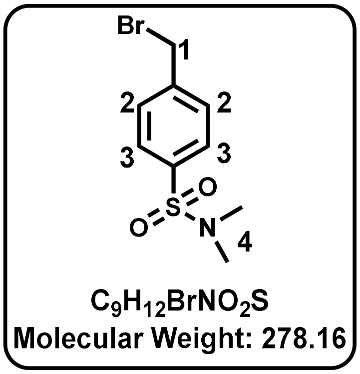

As a white solid (656.5 mg, 32% yield; R_f =0.43 30%Ethyl Acetate/Hexane). ^1H NMR (600 MHz, DMSO-d_6) δ 7.71 (d, J = 8.2 Hz, 2H, H^3), 7.67 (d, J = 8.2 Hz, 2H, H^2), 4.75 (s, 2H, H^1), 2.58 (s, 6H, H^4). ^{13}C NMR (151 MHz, DMSO-d_6) δ 143.57, 134.97, 130.55 (2C), 128.37 (2C), 56.62 and 37.99 (2C) ppm.

General Procedure for Synthesis of Compounds 42a, b

The respective benzoic acid (800 mg, 1 eq.) in THF (9 mL) was cooled then treated with Lithium Aluminium Hydride (1.6 eq.) and stirred for 3 h at 0 °C. The reaction mixture was heated quenched with distilled water and extracted with ethyl acetate. The organic layer was separated, dried with anhydrous sodium sulphate, and concentrated under reduced pressure. It was then purified by chromatography on silica gel eluting with DCM/MeOH (10/1) to obtain the required intermediate.

Compound 42a: 3-(hydroxymethyl)-N-methylbenzenesulfonamide

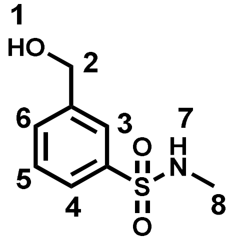

Chemical Formula: $C_8H_{11}NO_3S$
Molecular Weight: 201.24

As a brown liquid (623 mg, 83% yield; R$_f$ =0.53; 10%MeOH/DCM). ^{1}H NMR (400 MHz, DMSO-d_6) δ 7.77 (broad s, 1H, H^3), 7.64 (t, *J* = 5.8 Hz, 1H, H^5), 7.57 – 7.55 (m, 2H, H^4 and H^6), 7.41 (q, *J* = 5.0 Hz, 1H, H^7), 5.41 (t, *J* = 5.7 Hz, 1H, H^1), 4.60 (d, *J* = 4.7 Hz, 2H, H^2), 2.42 (d, *J* = 4.4 Hz, 3H, H^8). ^{13}C NMR (101 MHz, DMSO-d_6) δ 142.40, 138.81, 133.15, 128.36, 127.79, 127.09, 49.06 and 29.13 ppm.

Compound 42b: 3-(hydroxymethyl)-N,N-dimethylbenzenesulfonamide

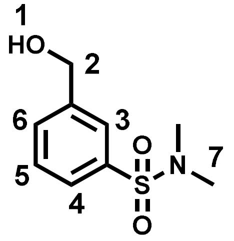

Chemical Formula: $C_9H_{13}NO_3S$
Molecular Weight: 215.27

As a brown liquid (567.7 mg, 75.6% yield; R$_f$ =0.66; 10%MeOH/DCM). ^{1}H NMR (400 MHz, DMSO-d_6) δ 7.71 (broad s, 1H, H^3), 7.62 – 7.60 (m, 2H, H^4 and H^6), 7.54 (t, *J* = 7.7 Hz, 1H, H^5), 5.47 (t, *J* = 5.81 Hz, 1H, H^1), 4.62 (s, 2H, H^2), 2.60 (s, 6H H^7). ^{13}C NMR (101 MHz, DMSO-d_6) δ 144.69, 133.72, 131.26, 128.59, 126.22, 125.44, 62.59 and 38.04 (2C) ppm.

General Procedure for Synthesis of Compounds 43a, b

The respective hydroxymethyl (900 mg) in DCM was treated with thionyl chloride (1.9 eq.) and stirred for 8 h at 25 °C. The reaction mixture was quenched with saturated sodium bicarbonate solution then extracted with ethyl acetate. The organic layer was separated, dried with anhydrous sodium sulphate, and concentrated under reduced pressure. It was then purified by chromatography on silica gel eluting with DCM/MeOH (10/1) to obtain the required intermediate.

Compound 43a: 3-(chloromethyl)-N-methylbenzenesulfonamide

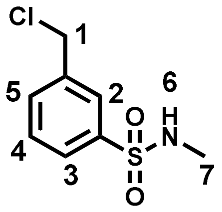

Chemical Formula: $C_8H_{10}ClNO_2S$
Molecular Weight: 219.68

As a yellow liquid (745 mg, 76% yield; R*f* =0.45; 10%MeOH/DCM. ^{1}H NMR (400 MHz, DMSO-*d*$_6$) δ 7.77 (broad s, 1H, H^2), 7.65 (t, J = 6.1 Hz, 1H, H^4), 7.58 – 7.54 (m, 2H, H^3 and H^5), 7.39 (q, *J* = 5.1 Hz, 1H, H^6), 4.60 (s, 2H, H^1), 2.42 (d, *J* = 5.0 Hz, 3H, H^7). ^{13}C NMR (101 MHz, DMSO-*d*$_6$) δ 144.44, 139.72, 130.61, 129.36, 125.38, 124.74, 62.70 and 29.12 ppm.

Compound 43b: 3-(chloromethyl)-N,N-dimethylbenzenesulfonamide

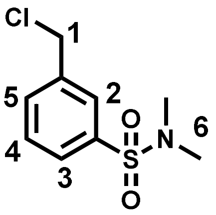

Chemical Formula: $C_9H_{12}ClNO_2S$
Molecular Weight: 233.71

As a yellow liquid (225.7 mg, 42% yield; R_f =0.63; 10%MeOH/DCM. ^{1}H NMR (400 MHz, DMSO-*d*$_6$) δ 7.79 (broad s, 1H, H^2), 7.71 (t, *J* = 7.7 Hz, 1H, H^4), 7.64 – 7.60 (m, 2H, H^3 and H^5), 4.62 (s, 2H, H^1), 2.62 (s, 6H, H^6). ^{13}C NMR (101 MHz, DMSO-*d*$_6$) δ 144.67, 131.25, 129.52, 127.84, 126.24, 125.45, 62.60 and 38.04 (2C) ppm.

General Procedure for Synthesis of Compounds 45a-g

3-Iodo-1H-pyrazolo[3,4-d]pyrimidin-4-amine (200 mg, 0.7663 mmol, 1 eq.) and respective bromomethyl (1.2 eq.) in DMF (2.3 mL) was treated with K_2CO_3 (212 mg, 1.5326 mmol, 2 eq.), heated to 30 °C, and stirred for 2 h. The reaction mixture was extracted with ethyl acetate. The organic layer was separated, washed with brine, dried with anhydrous sodium sulphate, and concentrated under reduced pressure. It was then purified by chromatography on silica gel eluting with DCM/MeOH (10/1) to obtain the required intermediate.

Compound 45a: 4-((4-Amino-3-iodo-1H-pyrazolo[3,4-d]pyrimidin-1-yl)methyl)benzamide

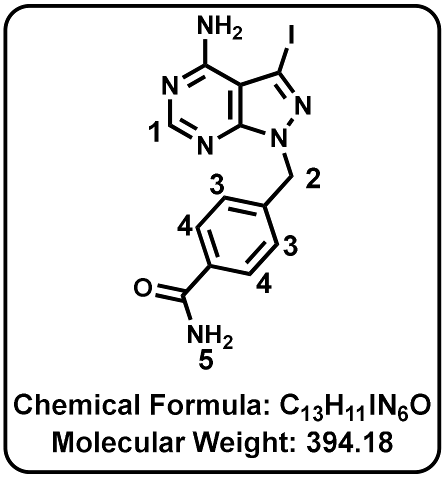

As a brown solid (94.5 mg, 31% yield; R_f =0.37; 20%MeOH/DCM). ^{1}H NMR (400 MHz, DMSO-d_6) δ = 8.25 (s, 1H, H^1), 7.89 (s, 1H, H^5), 7.81 (d, J = 8.3 Hz, 2H, H^4), 7.33 – 7.25 (m, 3H, H^{3,5}), and 5.54 ppm (s, 2H, H^2). ^{13}C NMR (101 MHz, DMSO-d_6) δ = 168.00, 158.23, 156.81, 154.11, 140.33, 134.26, 128.26 (2C), 127.83 (2C), 103.65, 90.08, and 50.18 ppm. HPLC-MS (APCI/ESI): t_R = 2.083 min, *m/z* $[M+H]^+$= 395.1.

Compound 45b: 3-((4-amino-3-iodo-1H-pyrazolo[3,4-d]pyrimidin-1-yl)methyl)benzamide

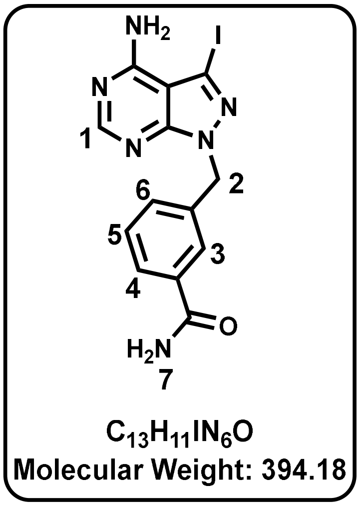

As a brown solid (143.62 mg, 47% yield; R*f* =0.14; 10%MeOH/DCM). ^{1}H NMR (400 MHz, DMSO-*d₆*) δ 8.26 (s, 1H, H^{1}), 7.95 (s, 1H, H^{7}), 7.79 (dt, *J* = 7.3, 1.7 Hz, 1H, H^{4}), 7.77 (t, *J* = 1.9 Hz, 1H, H^{3}), 7.40 (t, *J* = 7.3 Hz, 1H, H^{5}), 7.37 (dt, *J* = 7.7, 1.7 Hz, 1H, H^{6}), 7.32 (s, 1H, H^{7}), 5.53 (s, 2H, H^{2}). ^{13}C NMR (101 MHz, DMSO-*d₆*) δ 168.02, 158.21, 156.77, 154.07, 137.43, 135.15, 130.92, 129.00, 127.42, 127.11, 103.64, 90.06 and 50.33 ppm. HPLC-MS (APCI/ESI): purity = 98%, t_R = 2.154 min, *m/z* [M+H]$^{+}$ = 396

Compound 45c: 4-((4-amino-3-iodo-1H-pyrazolo[3,4-d]pyrimidin-1-yl)methyl)benzenesulphonamide

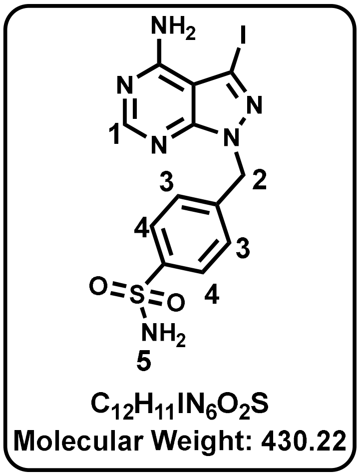

As a yellow solid (135.1 mg, 41% yield; R$_f$ =0.14; 10%MeOH/DCM). ^{1}H NMR (600 MHz, DMSO-d_6) δ 8.20 (s, 1H, H^1), 7.74 (d, J = 8.0 Hz, 2H, H^4), 7.35 (d, J = 8.7 Hz, 2H, H^3), 7.27 (s, 2H, H^5), 5.53 (s, 2H, H^2). ^{13}C NMR (151 MHz, DMSO- d_6) δ 158.21, 156.83, 154.09, 143.88, 141.06, 128.47 (2C), 126.47 (2C), 103.63, 90.36 and 49.97 ppm.

Compound 45d: 4-((4-amino-3-iodo-1H-pyrazolo[3,4-d]pyrimidin-1-yl)methyl)-N-methylbenzenesulphonamide

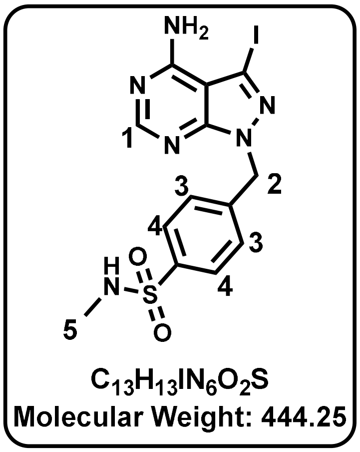

As a yellow solid (149.7 mg, 44% yield; R$_f$ =0.74; 10%MeOH/DCM). ^{1}H NMR (600 MHz, DMSO-d_6) δ 8.21 (s, 1H, H^1), 7.70 (d, J = 8.4 Hz, 2H, H^4), 7.37 (d, J = 7.8 Hz, 2H, H^3), 5.55

(s, 2H, H[2]), 2.35 (d, *J* = 5.0 Hz, 3H, H[5]). ^{13}C NMR (151 MHz, DMSO-d_6) δ 158.22, 156.86, 154.14, 141.73, 139.13, 128.66 (2C), 127.50 (2C), 103.63, 90.46, 49.90 and 29.09 ppm. HPLC-MS (APCI/ESI): purity = 98%, t_R = 2.099 min, *m/z* [M+H]$^+$ = 444.9

Compound 45e: 4-((4-amino-3-iodo-1H-pyrazolo[3,4-d]pyrimidin-1-yl)methyl)-N,N-dimethylbenzenesulphonamide

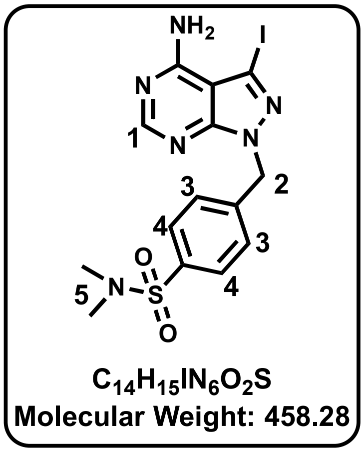

As a yellow solid (164.9 mg, 47% yield; R$_f$ =0.58; 10%MeOH/DCM). ^{1}H NMR (600 MHz, DMSO-d_6) δ 8.21 (s, 1H, H[1]), 7.68 (d, *J* = 8.6 Hz, 2H, H[4]), 7.41 (d, *J* = 8.3 Hz, 2H, H[3]), 5.58 (s, 2H, H[2]), 2.55 (s, 6H, H[5]). ^{13}C NMR (151 MHz, DMSO-d_6) δ 158.24, 156.89, 154.19, 142.40, 134.71, 128.69 (2C), 128.39 (2C), 103.63, 90.56, 49.84 and 37.95 (2C) ppm. HPLC-MS (APCI/ESI): purity = 98%, t_R = 2.189 min, *m/z* [M+H]$^+$ = 458.9

Compound 45f: 3-((4-amino-3-iodo-1H-pyrazolo[3,4-d]pyrimidin-1-yl)methyl)-N,N-dimethylbenzenesulfonamide

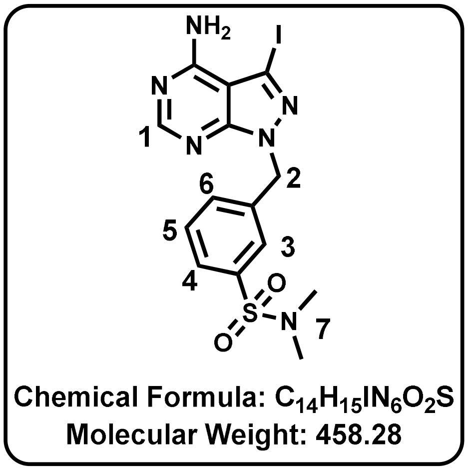

Chemical Formula: $C_{14}H_{15}IN_6O_2S$
Molecular Weight: 458.28

As a yellow solid (153.4 mg, 44% yield; R_f =0.67; 10%MeOH/DCM). ^{1}H NMR (400 MHz, DMSO-*d*$_6$) δ 8.25 (s, 1H, H^1), 7.67 (dt, *J* = 7.8, 1.8 Hz, 1H, H^4), 7.64 (broad t, *J* = 1.7 Hz, 1H, H^3), 7.61 (t, *J* = 7.6 Hz, 1H, H^5), 7.54 (dt, *J* = 7.6, 1.6 Hz, 1H, H^6), 5.64 (s, 2H, H^2), 2.56 (s, 6H, H^7). ^{13}C NMR (101 MHz, DMSO-*d*$_6$) δ 158.25, 156.86, 154.19, 138.72, 135.60, 132.60, 130.27, 127.20, 127.06, 103.69, 90.37, 49.96 and 37.95 (2C) ppm. HPLC-MS (APCI/ESI): purity = 99%, t_R = 2.243 min, *m/z* [M+H]$^+$ = 458.9

Compound 45g: 3-((4-amino-3-iodo-1H-pyrazolo[3,4-d]pyrimidin-1-yl)methyl)-N-methylbenzenesulfonamide

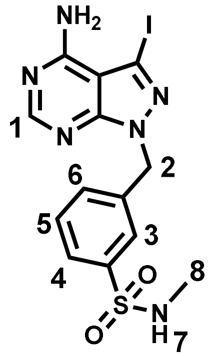

Chemical Formula: $C_{13}H_{13}IN_6O_2S$
Molecular Weight: 444.25

As a yellow solid (115.6 mg, 34% yield; R_f =0.63; 10%MeOH/DCM). ^{1}H NMR (400 MHz, DMSO-d_6) δ 8.26 (s, 1H, H^1), 7.70 (dt, *J* = 7.9, 1.3 Hz, 1H, H^4), 7.67 (broad t, *J* = 1.9 Hz, 1H, H^3), 7.58 (t, *J* = 7.7 Hz, 1H, H^5), 7.50 (dt, *J* = 7.7, 1.5 Hz, 1H, H^6), 7.44 (q, *J* = 5.1 Hz, 1H, H^7), 5.60 (s, 2H, H^2), 2.40 (d, *J* = 4.9 Hz, 3H, H^8). ^{13}C NMR (101 MHz, DMSO-d_6) δ 158.25, 156.87, 154.16, 140.27, 138.55, 132.05, 130.14, 126.37, 126.11, 103.67, 90.37, 50.00 and 29.09 ppm. HPLC-MS (APCI/ESI): purity = 99%, t_R = 2.099 min, *m/z* $[M+H]^+$ = 444.9

Compound 44: 5-(4,4,5,5-Tetramethyl-1,3,2-dioxaborolan-2-yl)benzo[d]oxazol-2-amine

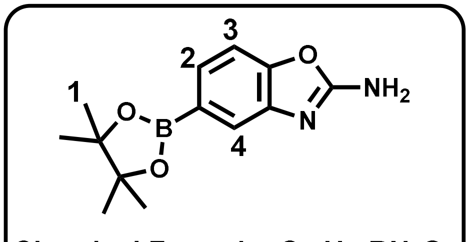

Chemical Formula: $C_{13}H_{17}BN_2O_3$
Molecular Weight: 260.10

5-Bromobenzo[d]oxazol-2-amine (**7**; 500 mg, 2.347 mmol, 1 eq.) and bis(pinacolato)diborate (720 mg, 2.8353 mmol, 1.2 eq.) in dioxane (4 mL) was purged with N_2 gas. The reaction mixture was then treated with potassium acetate (700 mg, 7.041 mmol, 3 eq.) and $PdCl_2$(dppf)-DCM (160 mg, 0.1876 mmol, 0.08 eq.). The resulting reaction mixture was heated to 100 °C and stirred for 8 h. After cooling to room temperature, the solution was diluted with EtOAc and filtered through a pad of celite. The solution was then concentrated under reduced pressure and purified by chromatography on silica gel eluting with hexane/EtOAc (1/1) to yield the boronic ester intermediate **9** (Figure 20) as a pale brown solid (531 mg, 40% yield; R_f =0.41; 20% MeOH/DCM). ^{1}H NMR (400 MHz, DMSO-d_6) δ = 6.82 (d, J = 1.2, 1H, H^4), 6.68 (dd, J = 8.0 and 1.1 Hz, 1H, H^2), 6.47 (d, J = 8.0, 1H, H^3), 0.55 (s, 12H, H^1). ^{13}C NMR (101 MHz, DMSO-d_6) δ 162.55, 149.84, 141.27, 126.90, 123.40, 120.30, 107.09, 82.86 (2C), and 22.97 ppm (4C). HPLC-MS (APCI/ESI): t_R = 2.428 min, *m/z* $[M+H]^+$ = 261.1.

General Procedure for Synthesis of Compounds 46a-h

The respective pyrazolopyrimidine reactant (200 mg, 1 eq.) and 5-(4,4,5,5-tetramethyl-1,3,2-dioxaborolan-2-yl)benzo[d]oxazol-2-amine (1.2 eq.) in dioxane:water (1.8:0.6 mL, 1:4) was purged with N_2 gas. The reaction mixture was then treated with sodium carbonate (5 eq.) and tetrakis(triphenylphosphine)palladium (0.08 eq.). The resulting reaction mixture was heated to

100 °C and stirred for 8 h. After cooling to room temperature, the solution was diluted with DCM/MeOH (1:1) and filtered through a pad of celite. The solution was then concentrated under reduced pressure and purified by chromatography on silica gel eluting with DCM/MeOH (20/1) to yield the final product.

Compound 46a/SK34: 4-((4-Amino-3-(2-aminobenzo[d]oxazol-5-yl)-1H-pyrazolo[3,4-d]pyrimidin-1-yl)methyl)benzamide

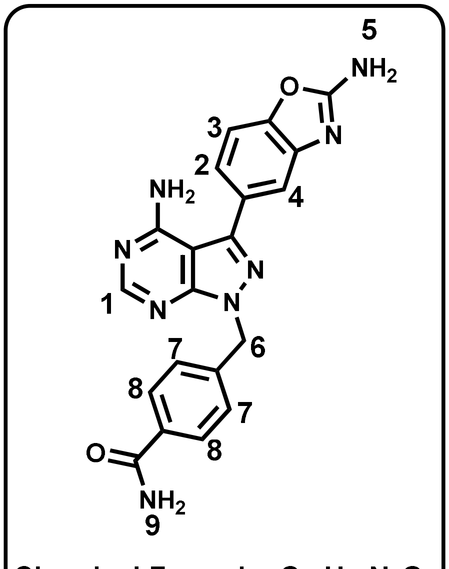

Chemical Formula: $C_{20}H_{16}N_8O_2$
Molecular Weight: 400.40

As a pale brown solid (72.7 mg, 36% yield; m.p. 279-281 °C; R_f=0.31; 20%MeOH/DCM). ^{1}H NMR (400 MHz, DMSO-*d₆*) δ = 8.29 (s, 1H, H^1), 7.89 (s, 1H, H^9), 7.82 (d, *J* = 8.0 Hz, 2H, H^8), 7.51 (s, 2H, H^5), 7.47 (d, *J* = 8.1 Hz, 1H, H^3), 7.42 (d, *J* = 1.6 Hz, 1H, H^4), 7.35 (d, *J* = 8.4 Hz, 2H, H^7), 7.29 (s, 1H, H^9), 7.25 (dd, *J* = 8.2, 1.7 Hz 1H, H^2), and 5.62 ppm (s, 2H, H^6). ^{13}C NMR (101 MHz, DMSO-*d₆*) δ = 168.06, 163.93, 158.69, 156.49, 154.83, 148.88, 145.24, 144.90, 140.75, 134.12, 128.83, 128.23 (2C), 127.81 (2C), 120.94, 115.49, 109.34, 97.90, and 49.95 ppm. HPLC-MS (APCI/ESI): purity = 96%, t_R = 2.154 min, *m/z* [M+H]$^+$ = 401.1.

Compound 46b/SK77: 3-((4-amino-3-(2-aminobenzo[d]oxazol-5-yl)-1H-pyrazolo[3,4-d]pyrimidin-1-yl)methyl)benzamide

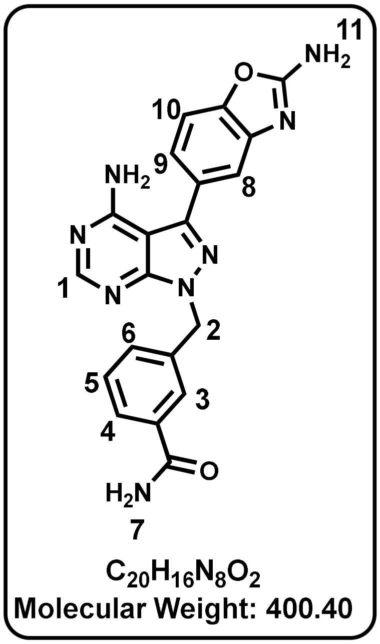

$C_{20}H_{16}N_8O_2$

Molecular Weight: 400.40

As a pale white solid (23.2 mg, 12% yield; m.p. 295-297 °C; R_f=0.36; 20%MeOH/DCM). ^{1}H NMR (600 MHz, DMSO-d_6) δ 8.25 (s, 1H, H^1), 7.92 (s, 1H, H^7), 7.79 (t, J = 1.9 Hz, 1H, H^3), 7.73 (dt, J = 7.1 and 1.8 Hz, 1H, H^4), 7.47 (s, 2H, H^{11}), 7.42 (d, J = 8.1 Hz, 1H, H^{10}), 7.40 – 7.35 (m, 3H, H^5, H^6, H^8), 7.29 (s, 1H, H^7), 7.20 (dd, J = 8.1 and 1.8 Hz, 1H, H^9), 5.56 (s, 2H, H^2). ^{13}C NMR (151 MHz, DMSO-d_6) δ 168.05, 163.87, 158.65, 156.45, 154.74, 148.82, 145.16, 144.85, 137.79, 135.06, 130.89, 128.86, 128.80, 127.41, 126.95, 120.91, 115.45, 109.32, 97.84 and 50.03 ppm. HPLC-MS (APCI/ESI): purity = 96%, t_R = 2.154 min, m/z $[M+H]^+$ = 401.1.

Compound 46c/SK126: 2-((4-amino-3-(2-aminobenzo[d]oxazol-5-yl)-1H-pyrazolo[3,4-d]pyrimidin-1-yl)methyl)benzamide

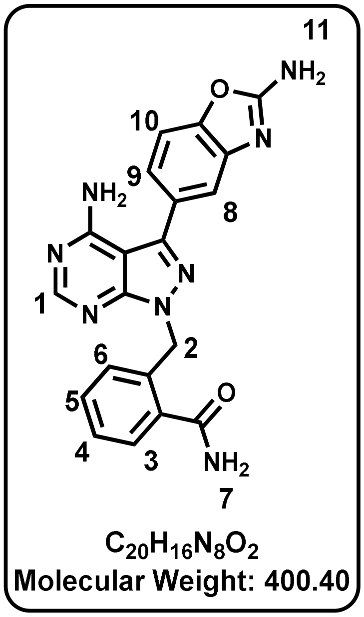

As a pale white solid (32 mg, 16% yield; m.p. 296-298 °C; R_f=0.4; 20%MeOH/DCM). ^{1}H NMR (600 MHz, DMSO-d_6) δ 8.21 (s, 1H, H^1), 8.02 (s, 1H, H^7), 7.53 – 7.49 (m, 2H, H^3 and H^7), 7.48 (s, 2H, H^{11}), 7.43 (d, *J* = 8.1 Hz, 1H, H^{10}), 7.39 (d, *J* = 1.7 Hz, 1H, H^8), 7.31 – 7.27 (m, 2H, H^4 and H^5), 7.22 (dd, *J* = 8.1 and 1.7 Hz, 1H, H^9), 6.77 – 6.73 (m, 1H, H^6), 5.75 (s, 2H, H^2). ^{13}C NMR (151 MHz, DMSO-d_6) δ 170.57, 163.88, 158.68, 156.42, 155.02, 148.83, 145.19, 144.86, 135.94, 135.65, 130.44, 128.82, 128.16, 127.65, 127.54, 120.94, 115.50, 109.31, 97.82 and 47.86 ppm. HPLC-MS (APCI/ESI): purity = 99%, t_R = 2.209 min, *m/z* $[M+H]^+$ = 401

Compound 46d/SK201: 4-((4-amino-3-(2-aminobenzo[d]oxazol-5-yl)-1H-pyrazolo[3,4-d]pyrimidin-1-yl)methyl)benzenesulphonamide

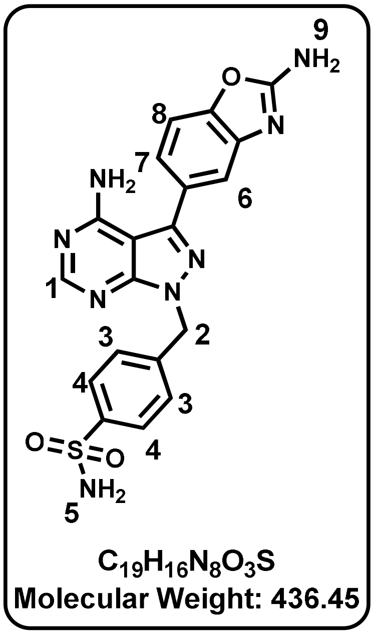

$C_{19}H_{16}N_8O_3S$
Molecular Weight: 436.45

As a pale white solid (12.1 mg, 4% yield; m.p. 235-237 °C; R_f=0.4; 20%MeOH/DCM). ^{1}H NMR (600 MHz, DMSO-d_6) δ 8.24 (s, 1H, H^1), 7.74 (d, J = 8.5 Hz, 2H, H^4), 7.48 (s, 2H, H^9), 7.43 – 7.41 (m, 3H, H^3, H^8), 7.38 (d, J = 1.8 Hz, 1H, H^6), 7.25 (s, 2H, H^5), 7.20 (dd, J = 8.1 and 1.8 Hz, 1H, H^7), 5.60 (s, 2H, H^2). ^{13}C NMR (151 MHz, DMSO-d_6) δ 163.88, 158.67, 156.51, 154.81, 148.85, 145.35, 144.86, 143.75, 141.46, 128.74, 128.46 (2C), 126.44 (2C), 120.92, 115.48, 109.32, 97.88 and 49.75 ppm.

Compound 46e/SK148: 4-((4-amino-3-(2-aminobenzo[d]oxazol-5-yl)-1H-pyrazolo[3,4-d]pyrimidin-1-yl)methyl)-N-methylbenzenesulphonamide

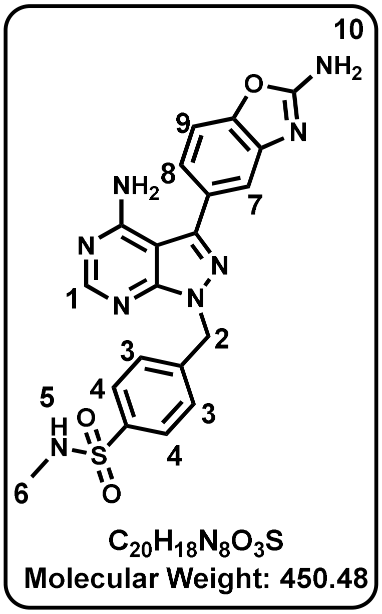

$C_{20}H_{18}N_8O_3S$
Molecular Weight: 450.48

As a pale white solid (52 mg, 26% yield; m.p. 273-275 °C; R_f=0.54; 20%MeOH/DCM). ^{1}H NMR (600 MHz, DMSO-*d₆*) δ 8.24 (s, 1H, H^1), 7.70 (d, *J* = 8.1 Hz, 2H, H^4), 7.48 (s, 2H, H^{10}), 7.45 (d, *J* = 8.6 Hz, 2H, H^3), 7.42 (d, *J* = 7.9 Hz, 1H, H^9), 7.39 (d, *J* = 1.7, 1H, H^7), 7.36 (q, *J* = 5.0 Hz, 1H, H^5), 7.21 (dd, *J* = 8.1 and 1.7 Hz, 1H, H^8), 5.62 (s, 2H, H^2), 2.35 (d, *J* = 5.0 Hz, 3H, H^6). ^{13}C NMR (151 MHz, DMSO-*d₆*) δ 163.89, 158.69, 156.54, 154.86, 148.86, 145.41, 144.87, 142.15, 138.99, 128.72, 128.64 (2C), 127.47 (2C), 120.93, 115.49, 109.33, 97.86 and 49.68, 29.09 ppm. HPLC-MS (APCI/ESI): purity = 99%, t_R = 2.236 min, *m/z* $[M+H]^+$ = 451

Compound 46f/SK162: 4-((4-amino-3-(2-aminobenzo[d]oxazol-5-yl)-1H-pyrazolo[3,4-d]pyrimidin-1-yl)methyl)-N,N-dimethylbenzenesulphonamide

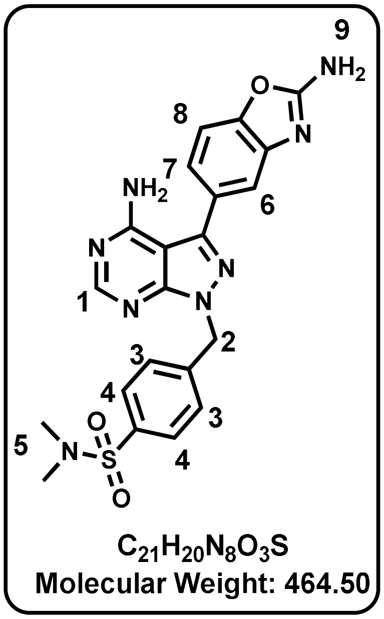

$C_{21}H_{20}N_8O_3S$
Molecular Weight: 464.50

As a pale white solid (95.2 mg, 47% yield; m.p. 290-291 °C; R_f=0.58; 20%MeOH/DCM). ^{1}H NMR (600 MHz, DMSO-*d*$_6$) δ 8.25 (s, 1H, H^1), 7.69 (d, *J* = 8.5 Hz, 2H, H^4), 7.48 – 7.47 (m, 4H, H^3, H^9), 7.43 (d, *J* = 8.1 Hz, 1H, H^8), 7.39 (d, *J* = 1.7, 1H, H^6), 7.21 (dd, *J* = 8.1 and 1.7 Hz, 1H, H^7), 5.65 (s, 2H, H^2), 2.55 (s, 6H, H^5). ^{13}C NMR (151 MHz, DMSO-*d*$_6$) δ 163.89, 158.70, 156.57, 154.92, 148.87, 145.47, 144.88, 142.83, 134.56, 128.70, 128.67 (2C), 128.36 (2C), 120.92, 115.48, 109.34, 97.84, 49.60 and 37.95 (2C) ppm. HPLC-MS (APCI/ESI): purity = 99%, t_R = 2.271 min, *m/z* [M+H]$^+$ = 465

Compound 46g/SK183: 3-((4-amino-3-(2-aminobenzo[d]oxazol-5-yl)-1H-pyrazolo[3,4-d]pyrimidin-1-yl)methyl)-N,N-dimethylbenzenesulfonamide

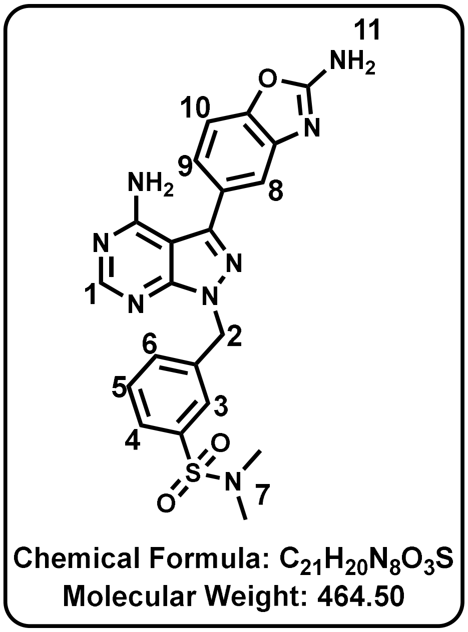

Chemical Formula: $C_{21}H_{20}N_8O_3S$
Molecular Weight: 464.50

As a pale white solid (45 mg, 11% yield; m.p. 242-245 °C; R_f=0.8; 20%MeOH/DCM). ^{1}H NMR (600 MHz, DMSO-d_6) δ 8.24 (s, 1H, H^1), 7.64 (broad t, J = 1.3 Hz, 1H, H^3), 7.63 – 7.60 (m, 1H, H^4), 7.58 – 7.57 (m, 2H, H^5 and H^6), 7.48 (s, 2H, H^{11}), 7.43 (d, J = 8.2 Hz, 1H, H^{10}), 7.36 (d, J = 1.2 Hz, 1H, H^8), 7.19 (dd, J = 1.7, 8.1 Hz, 1H, H^9), 5.66 (s, 2H, H^2), 2.50 (s, 6H, H^7). ^{13}C NMR (151 MHz, DMSO-d_6) δ 163.90, 158.68, 156.53, 154.90, 148.86, 145.45, 144.87, 139.10, 135.40, 132.58, 130.21, 128.69, 127.06, 127.00, 120.84, 115.40, 109.35, 97.86, 49.65 and 37.91 (2C) ppm. HPLC-MS (APCI/ESI): purity = 99%, t_R = 2.296 min, m/z $[M+H]^+$ = 465.1

Compound 46h/SK194: 3-((4-amino-3-(2-aminobenzo[d]oxazol-5-yl)-1H-pyrazolo[3,4-d]pyrimidin-1-yl)methyl)-N-methylbenzenesulfonamide

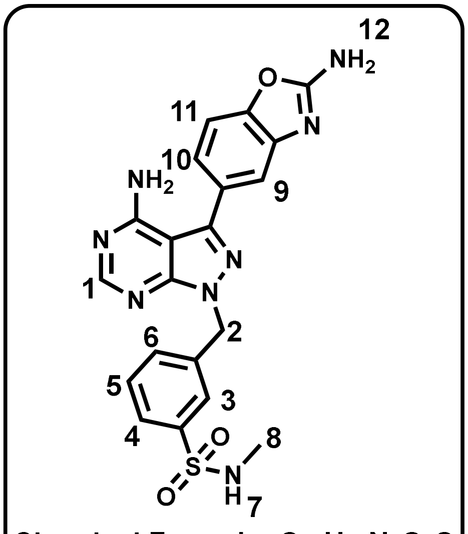

Chemical Formula: $C_{20}H_{18}N_8O_3S$
Molecular Weight: 450.48

As a pale white solid (25.2 mg, 5% yield; m.p. 261-263 °C; R$_f$=0.7; 20%MeOH/DCM). ^{1}H NMR (600 MHz, DMSO-d_6) δ 8.25 (s, 1H, H^{1}), 7.68 (broad t, *J* = 1.7 Hz, 1H, H^{3}), 7.65 (dt, *J* = 7.2, 1.9 Hz, 1H, H^{4}), 7.55 (overlapping t, *J* = 7.7 Hz, 1H, H^{5}), 7.53 – 7.52 (m, 1H, H^{6}), 7.48 (s, 2H, H^{12}), 7.43 (d, *J* = 8.1 Hz, 1H, H^{11}), 7.41 (overlapping q, *J* = 5.2 Hz, 1H, H^{7}), 7.37 (d, *J* = 1.7 Hz, 1H, H^{9}), 7.20 (dd, *J* = 1.8, 8.1 Hz, 1H, H^{10}), 5.63 (s, 2H, H^{2}), 2.34 (d, *J* = 5.0 Hz, 3H, H^{8}). ^{13}C NMR (151 MHz, DMSO-d_6) δ 163.89, 158.68, 156.53, 154.85, 148.86, 145.41, 144.87, 140.13, 138.92, 132.03, 130.07, 128.72, 126.22, 126.08, 120.89, 115.45, 109.34, 97.86, 49.69 and 29.06 ppm. HPLC-MS (APCI/ESI): purity = 99%, t$_R$ = 2.156 min, *m/z* [M+H]$^+$ = 451

6.4. References

1. McNamara, C. W.; Lee, M. C.; Lim, C. S.; Lim, S. H.; Roland, J.; Nagle, A.; Simon, O.; Yeung, B. K.; Chatterjee, A. K.; McCormack, S. L., Targeting Plasmodium PI (4) K to eliminate malaria. *Nature* **2013,** *504* (7479), 248-253.

2. Johnson, M.; Zaretskaya, I.; Raytselis, Y.; Merezhuk, Y.; McGinnis, S.; Madden, T. L., NCBI BLAST: a better web interface. *Nucleic Acids Res.* **2008,** *36* (suppl_2), W5-W9.

3. Burke, J. E.; Inglis, A. J.; Perisic, O.; Masson, G. R.; McLaughlin, S. H.; Rutaganira, F.; Shokat, K. M.; Williams, R. L., Structures of PI4KIIIβ complexes show simultaneous recruitment of Rab11 and its effectors. *Science* **2014,** *344* (6187), 1035-1038.

4. Prime, S., LLC, New York, NY, 2018.

5. Jacobson, M. P.; Pincus, D. L.; Rapp, C. S.; Day, T. J.; Honig, B.; Shaw, D. E.; Friesner, R. A., A hierarchical approach to all-atom protein loop prediction. *Proteins: Struct., Funct., Bioinf.* **2004,** *55* (2), 351-367.

6. Schrödinger Release 2020-2: Protein Preparation Wizard; Epik, S., LLC, New York, NY, 2016; Impact, Schrödinger, LLC, New York, NY, 2016; Prime, Schrödinger, LLC, New York, NY, 2020.

7. Harder, E.; Damm, W.; Maple, J.; Wu, C.; Reboul, M.; Xiang, J. Y.; Wang, L.; Lupyan, D.; Dahlgren, M. K.; Knight, J. L., OPLS3: a force field providing broad coverage of drug-like small molecules and proteins. *J. Chem. Theory Comput.* **2016,** *12* (1), 281-296.

8. Schrödinger Release 2020-2: Maestro, S., LLC, New York, NY, 2020.

9. Li, J.; Abel, R.; Zhu, K.; Cao, Y.; Zhao, S.; Friesner, R. A., The VSGB 2.0 model: a next generation energy model for high resolution protein structure modeling. *Proteins: Struct., Funct., Bioinf.* **2011,** *79* (10), 2794-2812.

10. Bowers, K. J.; Chow, D. E.; Xu, H.; Dror, R. O.; Eastwood, M. P.; Gregersen, B. A.; Klepeis, J. L.; Kolossvary, I.; Moraes, M. A.; Sacerdoti, F. D. In *Scalable algorithms for*

molecular dynamics simulations on commodity clusters, SC'06: Proceedings of the 2006 ACM/IEEE Conference on Supercomputing, IEEE: 2006; pp 43-43.

11. Jorgensen, W. L.; Chandrasekhar, J.; Madura, J. D.; Impey, R. W.; Klein, M. L., Comparison of simple potential functions for simulating liquid water. *J. Chem. Phys.* **1983,** *79* (2), 926-935.

12. Neria, E.; Fischer, S.; Karplus, M., Simulation of activation free energies in molecular systems. *J. Chem. Phys.* **1996,** *105* (5), 1902-1921.

13. Desmond Molecular Dynamics System, D. E. S. R., New York, NY, 2021. Maestro-Desmond Interoperability Tools, Schrödinger, New York, NY, 2021. New York, NY, , 2021.

14. Martyna, G. J.; Klein, M. L.; Tuckerman, M., Nosé–Hoover chains: The canonical ensemble via continuous dynamics. *J. Chem. Phys.* **1992,** *97* (4), 2635-2643.

15. Martyna, G. J.; Tobias, D. J.; Klein, M. L., Constant pressure molecular dynamics algorithms. *J. Chem. Phys.* **1994,** *101* (5), 4177-4189.

16. Trager, W.; Jensen, J. B., Human malaria parasites in continuous culture. *Science* **1976,** *193* (4254), 673-675.

17. Worzella, T.; Larson, B., A Glowing Profile to Meet Screening Needs.

18. Zegzouti, H.; Hennek, J.; Alves, J.; Goueli, S., ADP-Glo™ Kinase Profiling Systems for targeted and flexible kinase inhibitor profiling. **2014**.

19. Penzo, M.; de Las Heras-Dueña, L.; Mata-Cantero, L.; Diaz-Hernandez, B.; Vazquez-Muñiz, M.-J.; Ghidelli-Disse, S.; Drewes, G.; Fernandez-Alvaro, E.; Baker, D. A., High-throughput screening of the Plasmodium falciparum cGMP-dependent protein kinase identified a thiazole scaffold which kills erythrocytic and sexual stage parasites. *Sci. Rep.* **2019,** *9* (1), 7005.

20. Anastassiadis, T.; Deacon, S. W.; Devarajan, K.; Ma, H.; Peterson, J. R., Comprehensive assay of kinase catalytic activity reveals features of kinase inhibitor selectivity. *Nat. Biotechnol.* **2011,** *29* (11), 1039-1045.